Accurate fault location on overhead distribution lines using superimposed components

Aslan, Y.

Award date:
1996

Awarding institution:
University of Bath

ACCURATE FAULT LOCATION ON OVERHEAD DISTRIBUTION LINES USING SUPERIMPOSED COMPONENTS

Submitted by Y. ASLAN, B.Sc., M.A.(Ed)
for the degree of
Doctor of Philosophy
at the University of BATH
1996

ProQuest LLC
789 East Eisenhower Parkway
P.O. Box 1346
Ann Arbor, MI 48106-1346

SYNOPSIS

This thesis describes an alternative approach to accurately locating faults on overhead radial distribution lines with or without remote infeed source . The fault location algorithm is based on an interactive approach and in order to locate the actual fault point, the fault is first assumed to be at a point close to the local end. The most accurate fault is then found interactively by systematically varying the assumed fault position until such time as the fault-path current(s) in the healthy phase(s) attain a minima. It utilises superimposed phase signals and special filtering techniques are utilised to accurately extract the fundamental phasors from the measured fault voltage and current signals. In the algorithm, the presence of multiple load taps and remote source infeed are taken into consideration.

The algorithm has been tested using CAD techniques. However, important aspects of practical fault recorders such as VT and CT responses, analogue interface effects and quantisation errors, have been considered.

Finally, the developed fault location technique has been evaluated using simulated data from practical 11 kV and 33 kV overhead radial distribution lines with and without remote source. Effect of fault resistance, fault type and location, remote source, local end source capacity, fault cycle and dynamic loads on accuracy have been investigated. A sensitivity analysis of the algorithm including the effect of load and source capacity estimation errors and line length settings have also been carried out in order to demonstrate the robustness of the developed fault location algorithm to such practical constraints.

ACKNOWLEDGEMENTS

The author wishes to express his sincere thanks to DR. R. K. AGGARWAL for his continuous support, guidance, supervision and encouragement throughout the course of this work and during the preparation of the thesis. He would like also to thank Professor A. T. JOHNS for his interest in this work and many useful suggestions and also for the facilities provided in the Power System Research Laboratory. Thanks are extended to the Power and Energy Systems Group at the University of Bath for their support and encouragement in many aspects of the work.

He would like to thank his family and particularly his wife and son for their support and patience during the course of this work.

Finally, the author would like to acknowledge the support of the University of Dumlupınar and Turkish Government for providing the opportunity and financial support to carry out the Ph.D research at the University of Bath.

Contents

List of Tables

List of Figures

List of Principal Symbols

Z_0, Z_1, Z_2	Sequence impedances of the distribution line
I_0, I_1, I_2	Sequence currents
V_a, V_b , V_c	Three-phase-earth voltages
V_{af}	Voltage at the fault point for phase 'a'
R_f	Fault resistance
V_{select}, I_{select}	Selected voltage and current
I_{comp}	Compensating current
I_a, I_b, I_c	Three-phase fault currents at the local end
D	Distance to the fault
I_f	Fault current
Z_{app}, X_{app}, R_{app}	Apparent impedance, reactance and resistance
z_1	The positive sequence impedance of the transmission line (in ohm/unit length)
Z_{aa},...,Z_{cc},	Elements of line [Z] matrix
I_{pre},I_{post}	Pre-fault and post-fault currents
V_{pre},V_{post}	Pre-fault and post-fault voltages
$V_{fa(ss)}$,$V_{fb(ss)}$,$V_{fc(ss)}$	Three-phase pre-fault phase-earth voltages at the assumed fault point.
β	Distance between assumed fault point and local end.

Z_s, Z_m	Line self and mutual impedances
$I_{Sa(ss)}$, $I_{Sb(ss)}$, $I_{Sc(ss)}$	Three-phase pre-fault steady-state currents at the local end
$V_{Sa(ss)}$,$V_{Sb(ss)}$,$V_{Sc(ss)}$	Three-phase pre-fault phase-earth voltages at the local end
V_{fa}, V_{fb}, V_{fc}	Three-phase post-fault phase-earth voltages at the assumed fault point
V_{Sa}, V_{Sb}, V_{Sc}	Three-phase-earth post-fault voltages at the local source terminals
I_{Sa}, I_{Sb}, I_{Sc}	Three-phase post-fault currents at the local source terminals
V'_{fa}, V'_{fb}, V'_{fc}	Three-phase superimposed voltages to earth at the assumed fault point
I'_{Sa}, $I'_{Sb,}$ I'_{Sc}	Three-phase superimposed fault currents from local end
I'_{Ra}, I'_{Rb}, I'_{Rc}	Three-phase superimposed fault currents from remote end
I'_{fa}, I'_{fb}, I'_{fc}	Three-phase superimposed fault-path currents at the assumed fault position
L	Length of distribution line
Z_{sr},Z_{mr}	Source serial and mutual impedances
Z_{sr},Z_{mr}	Line serial and mutual impedances
α	Distance between the actual fault point and the local end
r_a,r_e	Resistance of the conductor and resistance of the earth return path
D_e	Equivalent spacing of the earth return path
D_s	Geometric mean radius of a single conductor
D_{ab}, D_{ac}, D_{bc}	Distance between 'a', 'b' and 'c' phase conductors
$[Y_{SR}]$	Remote source admittance matrix
V_R	Busbar voltage at the remote end of the line
VA_R	Symmetrical short circuit level at the remote end busbar

Z_{S1}, Z_{S0}	Positive and zero components of the source impedance
Z_L	Load impedance
V_L	Line voltage at the load point
M	Transformer rating
P_f	Load power factor
V_T	Voltage of a load at the tap point
I_T	Current of the load at the tap point
I_L	Current at the load terminals
l	Length of the tapped line
Z_{Lab}, Z_{Lbc}, Z_{Lca}	Load impedance connected between three terminals
Y_{Lab},Y_{Lbc},Y_{Lca}	Load admittance between three load terminals
$[Y_{Labc}]$	Three-phase load admittance matrix
V_{TN}	Voltage vector representation at tapping point N
V_{LN}	Voltage vector representation at N^{th} load
[Z]	Line series impedance matrix per unit length
$[Y_{LN}]$	Load admittance matrix representation for load tap L_N
$[Z_{LN}]$	Load impedance matrix representation for load tap L_N
$[I_{LN}]$	Load current at load tap L_N
$[I_{TN}]$	Load current at tap N
$[Y_{EN}]$	Equivalent admittance matrix looking into load tap L_N from tap N
V_S , I_S	Voltage and currents recorded at the sending end
I_{01}, I_{12}, I_{23},...	Currents between tap points
l_{01}, l_{12}, l_{23},...	Length of the line sections between tap points

Z_{01}, Z_{12}, Z_{23},...	Impedance between tap points
$[I'_R]$	Superimposed receiving end currents
$[V'_f]$	Superimposed fault voltages at the assumed fault point
$[Y_{ER}]$	Equivalent admittance matrix looking into receiving-end from assumed fault position
$[Y_{ES}]$	Equivalent admittance matrix looking into sending-end from assumed fault position
$[Y_{SR}]$	Equivalent source admittance representing source at receiving-end
$[Y_{SS}]$	Equivalent source admittance representing source at sending-end
[U]	Unit matrix
X/R	Reactance to resistance ratio

ABBREVIATIONS

CT	Current Transformer
VT	Electromagnetic Voltage Transformer
EMTP	Electromagnetic Transient Program
DFT	Discrete Fourier Transform
CAD	Computer Aided Design
DFR	Digital Fault Recorder
EHV	Extra High Voltage
SCADA	Supervisory Control and Data Acquisition
TACS	Transient Analysis of Control Systems

Types of fault:

a-e	phase 'a' to earth fault
b-e	phase 'b' to earth fault
a-b-e	phase 'a' to 'b' to earth fault
a-b	phase 'a' to 'b' fault
abc	three phase fault

INTRODUCTION

1.1 The Importance of Fault Locators for Distribution Systems

Distribution systems constitute the major link between the substation and the customers. Because of simplicity of construction and maintenance advantages, low cost in instalment, etc., the majority of distribution systems are overhead systems [1]. However, more faults occur on distribution systems than on either transmission systems or in the generating facilities. Some of the factors that contribute to this are the relatively high degree of exposure of a distribution system, the natural hazards, the type of construction used, etc. [2]. The major causes of faults on overhead distribution circuits are wind and trees, lightning, and equipment or wiring failures. Other common causes are human error, glaze, snow and foreign objects. Operating experience shows that in overhead distribution systems, 70-80% of all faults are transient in nature [3]. Most utilities employ reclosers and/or fuses with source circuit breakers to handle transient faults. Permanent faults, however, require a location of faulty line section, isolation and possible re-scheduling of the network before normal power delivery may be resumed [4]. Transient faults may not cause any malfunctions in normal utility equipments but certainly may cause data losses and malfunctions in computer based and electronic switching equipment [5].

Overhead radial distribution lines are attractive from an economic and maintenance point of view but in the presence of a shunt fault, all the customers are affected unless the faulted section is isolated from the main feeder by means

of fuses or sectionalizers etc. In recent years with the privatization of power and distribution companies, it has become essential for them to provide to the customers a high quality service without any outages, hence the need to locate permanent and transient faults as quickly as possible. The importance of fault locators is more obvious where foot patrols are relied upon, particularly on relatively long lines and when the visibility is very poor because of tree growth, etc. Also, locators can help where maintenance is divided between different companies or divisions within a company, and the weak spots that are not obvious may be found because a more through inspection can be focused in the limited area defined by the fault locator.

At present, a common method of locating transient and permanent faults on distribution lines is through patrolling a line on foot, in a car, or by a helicopter for eye inspection; the distribution system is then sectionalized to locate and isolate the faults. This is very time consuming, has to be carried out during daylight, and at times in the presence of adverse weather conditions such us snow, storm or heavy rain which can pose danger to personnel [6].

In recent years, the rapid increase in digital technology has led to faster and more powerful computers at low costs. It has therefore become more economic and attractive for power companies to locate faults on distribution lines by using digital equipments rather than patrolling them on foot or by using helicopters. However, in order to expedite repairs in the case of permanent faults and also identify weak spots in the systems under transient faults thereby preventing future potential problems, there is a requisite for power companies to employ accurate fault locators at substations; this would cut down inspection and service restoration times, minimise outage times and provide a high quality of supply to customers.

A digital fault location technique can be implemented as a stand-alone device i.e., an independent device using data from digital protection relays, or an algorithm

using data from digital fault recorders located at a substation [7]. Digital fault recorders record data from the line in an on-line mode. In the event of a fault, the voltage and current information is sent to a fault locator to process the data in an off-line mode. The required system data such as line, load, and source parameters and physical network configuration at the time a fault occurs is obtained from a database.

An area of power systems where changes have taken place in recent years is that of connection of private generation, sometimes also known as *'co-generation'* (Customer Owned Generation), into a distribution system. The growth in this area arises from increasing concern regarding possible energy shortage, escalating fuel and labour costs, and also the desire to obtain a power supply security higher than that provided by the electricity supply authority [8].

Many researchers have developed digital fault location techniques with a major emphasis on transmission lines and little work has been done in distribution lines [9-12]. Distribution feeders include single-phase, two-phase and three-phase laterals, off a main three-phase primary distribution feeder. In distribution systems, the presence of remote infeed due, for example to the aforementioned private generation to improve the system capacity, introduces difficulties to the conventional fault location techniques, particularly those based on apparent impedance methods which make use of current and voltage samples at a single location.

Conventional fault location techniques developed to date for distribution systems, do not consider practical interface errors, load estimation errors and the possible presence of remote source associated with private generation. Moreover, in conventional fault location algorithms based on apparent impedance measurements, the presence of remote infeed source causes under or over distance measurements [13-16].

1.2 Radial Distribution Lines

Radial lines are simple, very low cost and therefore the most common form of lines that are used in distribution systems. Radial distribution systems branch into various primary laterals which in turn separate into sublaterals. In such systems, three, two and single phase loads are tapped off from the main feeder and the current magnitude is highest in the conductors that leave the substation. The magnitude of current diminishes towards the end of the system. Usually as the current decreases, the size of the feeder conductor is also reduced [1].

The reliability and service continuity of distribution systems is relatively low in comparison to a transmission system. A fault occurrence at any location on a radial distribution system causes a power outage for every consumer on the system unless the fault can be isolated from the source by a disconnecting device such as a fuse, sectionalizer, recloser or circuit breaker [2]. The present practice to locate a fault is such that on the occurrence of a fault, each feeder is opened and closed in turn until the faulty circuit is identified. Sectionalizing then takes place on the feeder until the fault is located. During this process, the supply to the consumers may be interrupted.

1.3 Objectives of This Work

The main objectives of the work presented in this thesis are:

- To present the basis of a new digital fault location technique for locating faults on overhead distribution systems based on superimposed components. In this technique, by the use of superimposed components rather than total values, the effects of source capacity and line preloading conditions on accuracy are virtually eliminated [17]. The technique

developed is an interactive approach which utilises fault voltages and currents at one end of a typical distribution system, with or without remote infeed and takes into account the presence of three-phase, two-phase and single-phase load taps and non-homogenous line structures. In order to attain a high degree of accuracy in the location of a fault, post-fault currents and voltages obtained from one end of a typical distribution system are filtered using *Discrete Fourier Transform* (DFT) techniques to essentially extract the power frequency components.

- To test the proposed fault locating technique, using the well proven *Electro Magnetic Transients Program* (EMTP) software; this is used to simulate the overhead distribution systems with load taps. The overhead distribution lines employed in this work are based on a single circuit 11 kV horizontal construction line currently used on the UK distribution system.

- Simulation results using a number of different distribution system configurations with load taps are presented. The technique takes into account the effects of transducers (CTs and VTs) and hardware errors such as the effect of interface modules, anti-aliasing filters and quantisation, so that the information processed through the fault locator algorithm is very close to a real-life situation.

- The proposed algorithm is extensively tested for a practical distribution system with load taps and for different fault conditions. The effects of fault resistance, dynamic loads, load type, presence of remote infeed, fault type, fault distance, source and load estimation errors on accuracy of fault location are investigated.

1.4 Scope of the Thesis

Chapter 2

In this chapter, a review of the fault locator techniques developed to date for distribution lines are presented. These can be essentially divided into three categories: (i) the first one based on the phenomenon of travelling waves and high frequency components. (ii) The second category based on using fundamental frequency voltages and currents at the terminals of a line. The advantages and drawbacks of each technique are also discussed.

Chapter 3

This chapter describes in detail the basis of an alternative approach, as developed in this work, to locate faults on overhead radial distribution lines. The various stages of the fault location technique including the implementation of the fault location algorithm are described in detail. These include emulation of the hardware interfaces, fault inception time identification, extraction of fundamental phasors, calculation of superimposed components and the fundamental principle of the fault location technique.

Chapter 4

This chapter concentrates on extending the principle to a practical distribution system with load taps and remote infeed source; in particular, the effects of load taps are taken into consideration for a typical distribution system.

Chapter 5

In this chapter, the parameters relating to the distribution systems studied are explained.These include physical dimensions of the distribution system, overhead conductors, load and source configuration. Also in this chapter, the procedure for automatically scanning a particular distribution system for fault location (once the system conditions are known), is explained.

Chapter 6

Chapter 6 is divided into three main parts.The first part is concerned with the testing of the algorithm on experimental distribution systems. The second part presents the performance evaluation of the fault locator algorithm under different fault conditions. In this part the effect of fault resistance, source capacity, fault position, fault cycle, dynamic loads, remote infeed source and non-algorithmic errors originating from remote source and load estimation on accuracy are investigated. In the third part, sensitivity analysis is carried out for the fault locator algorithm, this includes an investigation into the non-algorithmic errors introduced by load and remote source capacity estimations.

Chapter 7

Chapter 7 presents a summary of the work presented in this thesis and the conclusions. It also includes suggestions for future work.

LITERATURE REVIEW OF FAULT LOCATOR TECHNIQUES FOR DISTRIBUTION LINES

2.1 Introduction

In EHV transmission lines, fault location has been recognized as an essential requirement and relatively little work has been done in distribution lines. The fault location algorithms developed for transmission lines are not suitable for distribution networks due to significant differences in physical structures and dimensions between the two systems [16].

The fault locating techniques reviewed in this chapter can be divided into three categories: (i) those based on travelling waves and high frequency components, (ii) those based on fundamental frequency currents and voltages, and (iii) those based on knowledge-based approaches.

2.2 Fault Location Techniques Based on Travelling Waves and High Frequency Components

Clarke and Horn have introduced a directional fault indicator for overhead distribution systems using a new sensor [18]. The overhead line mounted sensor relies on a newly developed single phase integrated current and voltage transformer. The sensor developed for this application requires only one high voltage interface per phase for both current and voltage measurements. The signals are guided from the sensor's aluminum casing via a screened and armoured cable to the central logic circuits which are mounted in a box on the overhead line pole.

By measuring the phase angle between the resultant voltage and current vectors, the direction of the fault is detected. The units are installed on the overhead lines and poles at regular intervals. The sensors have been designed for a voltage range between 12 kV and 36 kV. However, since the sensors have to be installed at regular intervals throughout the distribution line, the installation costs are very high. Another drawback of this method is that the fault location process is not centralized and after the occurrence of a fault, in order to localize the faulted section, a crew has to be sent out to inspect the sensor units. This poses additional problems for the power companies.

Another technique is reported in references [19-20] to locate faults on 11 kV distribution systems. In this technique, high frequency components rather than the power frequency components, are used. These are injected by the fault at the fault point and propagate in both directions along the line. The locators are inserted at strategic and regular intervals along the distribution line to observe the high frequency components caused by a fault and to provide information for directional fault finding. In this technique, by using line traps, any high frequency components over a specific band of frequencies are confined to the protected line and by using a pair of stack tuner circuits which are tuned to the same frequency band, the high frequency components are extracted for further processing essentially to deduce the direction of the fault. This method is complex and requires specially tuned filters. However, directional fault locators can be useful in inter-meshed distribution networks, but in longer radial distribution lines, the initial costs would be prohibitively high.

2.3 Fault Location Techniques Based on Fundamental Frequency Components

A technique has been developed by Girgis [13] for location of faults in rural overhead distribution systems. It is based on the concept of apparent impedance

and the current and voltage information is obtained at a single location. In this technique, the load taps are taken into account and voltages and currents are updated at tap points. Essentially, the method is based upon the classification of a fault type and a voltage-current pair is then selected to compute the apparent impedance from fault information; Z_1 and Z_2 line sequence impedances, are assumed equal. Briefly,

for an 'a'-earth fault the voltage at the fault point is:

$$V_{af} = V_a - ((I_1+I_2)\ Z_1 + I_0Z_0) \tag{2.1}$$

thus,

$$V_a = (I_a+kI_0)Z_1 + 3I_0R_f \tag{2.2}$$

where,

$$k = (Z_0-Z_1)/Z_1 \tag{2.3}$$

As mentioned before, this method is based upon apparent impedance, which is the ratio of selected voltage to the selected current according to fault type and faulted phases. Hence the impedance seen at the fault-locator end is given by:

$$Z_{app} = (V_{select})/(I_{select}) = R_{app}+JX_{app} \tag{2.4}$$

Thus, for a single line to ground fault on phase 'a', say:

$$V_{select} = V_a \tag{2.5}$$

and,

$$I_{select} = I_a + K\ I_0 \tag{2.6}$$

hence,

$$Z_{app} = Z_1 + (3I_0R_f)/(I_a + kI_0) \tag{2.7}$$

For single line to ground fault, the compensating current is assumed to be proportional to the total zero sequence current.

Hence,

$$Z_{app} = Dz_1 + (3I_{comp}R_f)/(I_a + kI_0) \tag{2.8}$$

Equation (2.8) is then written in terms of real and imaginary components. Finally by using the imaginary part, fault resistance has been eliminated and distance to the fault calculated.

In this fault location technique, by using EMTP accurate results are obtained. However, in this technique, the possible presence of remote infeed source, transducer and hardware errors and load estimation errors are not considered.

Another digital fault location and diagnosis technique is developed by Zhu et al in reference [16] which is based on fundamental frequency voltage and current samples measured at the locator end. In this technique, the presence of load taps are taken into account for a radial system. The fault distance algorithm is based on an iterative solution to the equations which describe the steady-state fault condition. For a single-line-to-ground fault on phase 'a', say, where voltages and currents at the sending-end of the faulted line segment are assumed to be known and allowing for the mutual couplings among different phases, the following relationship exists for the faulted phase:

$$V_a = D(Z_{aa} I_a + Z_{ab} I_b + Z_{ac} I_c) + I_f R_f \tag{2.9}$$

The voltages at the fault point can be expressed in terms of the phase currents and the fault distance:

$$\begin{bmatrix} V_a' \\ V_b' \\ V_c' \end{bmatrix} = \begin{bmatrix} V_a \\ V_b \\ V_c \end{bmatrix} - D \begin{bmatrix} Z_{aa} & Z_{ab} & Z_{ac} \\ Z_{ba} & Z_{bb} & Z_{bc} \\ Z_{ca} & Z_{cb} & Z_{cc} \end{bmatrix} \begin{bmatrix} I_a \\ I_b \\ I_c \end{bmatrix} \tag{2.10}$$

In order to calculate the fault distance, the following iterative approach is used:

i. The iteration begins by assuming an initial fault current I_f. A reasonable estimate is given by:

$$I_f = I_a - I_{pre} \tag{2.11}$$

ii. With the known fault current, the fault distance and the fault resistance can be calculated by separating equation (2.9) into real and imaginary parts and then solving the two resultant equations.

iii. Once the calculated fault distance is known, the voltage vector at the fault point is calculated using equation (2.10)

iv. Then with the calculated voltage vector at the fault point, the remote-end current infeed is obtained by applying the radial power flow algorithm.

v. Using equation (2.11) to update the fault current, a new iteration begins by going to step ii. This process is repeated until the calculated fault distance converges.

In this fault location algorithm, satisfactory results are obtained for a radial

distribution system. However, in the simulations, presence of dynamic loads and effects of remote infeed source are not considered.

Another fault location technique to estimate shunt faults on radial overhead distribution lines has been proposed by Das et al [15]. This method uses the fundamental frequency components of voltages and currents measured at the line terminals and in this technique, non-homogenous line structure, capacitor banks, and dynamic load taps are taken into account. In this technique, when a fault is detected, the fundamental frequency components of the pre-fault voltage and current phasors at the terminals are recorded. The sequence voltages and currents at the locator terminal before and during the fault are calculated and the type of fault is determined.

By using the line parameters, the type of fault and the phasors of the sequence voltages and currents, the fault is firstly located crudely between two nodes. By taking into account the loads, the exact location of the fault is then calculated in an iterative manner.

Again in this technique, the presence of remote end infeed sources, load estimation errors and errors originating from interface and quantization are not taken into consideration. In the tests performed, satisfactory results have been achieved for fault resistances between 5 Ω and 25 Ω, but the effects of lower and higher fault resistances are not investigated.

Another technique is developed by Austria distribution authority to locate faults on composite distribution systems [21]. Such systems comprise of both overhead lines and underground cables. In this technique, the impedance measured by the digital distance relay is used to locate the fault. However, the fault arc resistance, the nonlinear structure of distribution lines, presence of sub-feeders on a distribution line produce an error on the fault location.

Considering the presumptions above, in radial networks the error introduced by the fault arc resistance is eliminated by evaluating the measured reactance of the fault impedance only. A table of reactances, corresponding to points along the line, is generated and stored in a PC. During the fault, the impedance measured by the distance relay is fed to the computer. The computer selects from a list all the line sections that are possible fault locations and displays them on the screen. If the reactance measured by the relay lies between the reactance at the beginning and at the end of a line section, this section is a probable fault point. However, the method has been limited to radial systems with remote end open. Furthermore, only postfault voltages and currents are used and the effects of load taps are not considered. This leads to unacceptably high errors especially in the presence of high capacity loads. Another disadvantage of the technique is that the presence of remote infeed introduces unacceptable errors and during the fault, remote infeed is disconnected to convert the system into radial system. In some cases, an error as high as 12% has been recorded.

Another fault point locating and sectional isolating technique has been developed by Kakimoto et al [22] to locate phase-to-earth fault point at each pole and isolate the faulted section by controlling pole switches with no outage of unfaulted section by using ground-current sensors. In this technique, phase-earth faults are located at the base of each distribution pole. This is achieved by a simple method of installing a sensor in the grounding conductor, and the faulted section is isolated by high-speed control using optical cables with no power interruption to the unfaulted sections.

This technique is although accurate for phase-earth faults, it is restricted to the faults involving earth which occur at poles. The installation cost is very high since there is a requirement to install current sensors at each pole and use fibre optic cables for communication between poles and substation.

2.4 Knowledge-based Approaches

Other recent efforts have focused on developing fault location techniques using knowledge-based approaches [23-24]. Such techniques often rely on external information such as SCADA alarms, substation and feeder switch status, feeder measurements, load voltage sensors, etc. In many distribution systems, knowledge-based approaches may not be feasible since measurements are usually only available at the substation and information about the operation of feeder protective devices is normally unknown.

FAULT LOCATION TECHNIQUE AS APPLIED TO A PLAIN DISTRIBUTION LINE

3.1 Introduction

In view of the large number of variables present in a distribution system, the problem of accurate fault location on such systems appears, at first, to be intractable. Figure 3.1 shows a distribution system with a remote-end infeed source and a shunt fault created at point 'X'. The influential and unknown parameters are, distance to fault, fault resistance, and the presence of remote infeed source.

This chapter describes the basis of an alternative approach to accurately locating faults on overhead radial distribution lines with remote infeed source. The underlying principles of the technique presented are essentially the same as those developed for plain transmission lines [25], except that the algorithm has been significantly modified to specifically deal with the much higher complexity. The technique also takes into account the practical limitations of the hardware such as interface and quantization errors in the design process. The technique is based on utilising the fault voltage and current samples as obtained at a single location of a typical radial distribution system with remote source; these are then filtered after the analog to digital conversion process by using digital filtering techniques to obtain power frequency components of voltage and current samples. Superimposed

voltage and current components rather than total values are used to minimise the effects of source impedance on the accuracy.

3.2 The Fault Location Technique As Applied To a Plain Feeder

3.2.1 Unsymmetrical Faults

Figure 3.2 shows a block diagram of the different stages involved in the fault location process. The starting point is the digitized voltage and current samples at the terminals of the distribution system which includes a number of cycles of pre-fault and post-fault data. Figure 3.3 shows typical digitized voltage and current waveforms from a faulted distribution system. As seen from the block diagram, the fault location algorithm is implemented as the final stage in the fault location process.

In essence, this technique works on the principle of determining (from pre-fault and post-fault values of voltage and current measured) the superimposed voltage at any assumed fault point. This voltage is then "back injected" at the assumed fault point to check fault path currents in the unfaulted phases. Only when the fault point is correct does the sound phase injected currents at the fault point attain a near zero value.

The fundamental principle can best be illustrated with reference to the simple example shown in Figure 3.4 which is a plain feeder with no taps. A fault position is assumed at 'β' and in order to find superimposed components at this assumed fault point, pre-fault (steady-state) and post-fault voltages and currents at this assumed fault point are calculated as a first step.

Assuming a lumped parameter model of the line (this is simply to simplify the explanation), the pre-fault steady-state voltage $V_{fa,b,c(ss)}$ at the assumed fault point 'β' is related to the measured pre-fault voltages and currents ($V_{Sa,b,c(ss)}$ and $I_{Sa,b,c(ss)}$) as:

$$\begin{bmatrix} V_{fa(ss)}(\beta) \\ V_{fb(ss)}(\beta) \\ V_{fc(ss)}(\beta) \end{bmatrix} = -\beta \begin{bmatrix} Z_s & Z_m & Z_m \\ Z_m & Z_s & Z_m \\ Z_m & Z_m & Z_s \end{bmatrix} \begin{bmatrix} I_{Sa(ss)} \\ I_{Sb(ss)} \\ I_{Sc(ss)} \end{bmatrix} + \begin{bmatrix} V_{Sa(ss)} \\ V_{Sb(ss)} \\ V_{Sc(ss)} \end{bmatrix} \qquad (3.1)$$

where Z_s and Z_m are the line self and mutual impedances/unit length respectively.

The post-fault voltages at the assumed fault point 'β' are:

$$\begin{bmatrix} V_{fa}(\beta) \\ V_{fb}(\beta) \\ V_{fc}(\beta) \end{bmatrix} = -\beta \begin{bmatrix} Z_s & Z_m & Z_m \\ Z_m & Z_s & Z_m \\ Z_m & Z_m & Z_s \end{bmatrix} \begin{bmatrix} I_{Sa} \\ I_{Sb} \\ I_{Sc} \end{bmatrix} + \begin{bmatrix} V_{Sa} \\ V_{Sb} \\ V_{Sc} \end{bmatrix} \qquad (3.2)$$

Where $I_{Sa,b,c}$ and $V_{Sa,b,c}$ are the post-fault line currents and voltages to earth at the sending end of the system respectively.

The superimposed voltages to earth (which is simply the difference between the post-fault and pre-fault values) at a prospective fault distance 'β' are given by:

$$\begin{bmatrix} V_{fa}/ \\ V_{fb}/ \\ V_{fc}/ \end{bmatrix} = \begin{bmatrix} V_{fa} - V_{fa(ss)} \\ V_{fb} - V_{fb(ss)} \\ V_{fc} - V_{fc(ss)} \end{bmatrix} \qquad (3.3)$$

By injecting the superimposed fault voltages at the assumed fault point 'β', superimposed fault path currents are obtained. First of all, the superimposed currents at the measuring end P (which are simply the difference between the measured post-fault and pre-fault values) are given by:

$$\begin{bmatrix} I_{Sa}/ \\ I_{Sb}/ \\ I_{Sc}/ \end{bmatrix} = \begin{bmatrix} I_{Sa} - I_{Sa(ss)} \\ I_{Sb} - I_{Sb(ss)} \\ I_{Sc} - I_{Sc(ss)} \end{bmatrix} \tag{3.4}$$

With reference to the superimposed system model shown in Figure 3.5, these are also the superimposed currents fed into the fault from end P. Again with reference to Figure 3.5, the superimposed currents at the remote end Q (which are also the superimposed currents fed into the fault from Q) are given by:

$$\begin{bmatrix} I_{Ra}/ \\ I_{Rb}/ \\ I_{Rc}/ \end{bmatrix} = \left[(L-\beta) \begin{bmatrix} Z_s & Z_m & Z_m \\ Z_m & Z_s & Z_m \\ Z_m & Z_m & Z_s \end{bmatrix} + \begin{bmatrix} Z_{sr} & Z_{mr} & Z_{mr} \\ Z_{mr} & Z_{sr} & Z_{mr} \\ Z_{mr} & Z_{mr} & Z_{sr} \end{bmatrix} \right]^{-1} \begin{bmatrix} V_{fa}/ \\ V_{fb}/ \\ V_{fc}/ \end{bmatrix} \tag{3.5}$$

Where L is the total length of the line, Z_{sr} and Z_{mr} are the remote end Q source self and mutual impedances respectively and $V'_{fa,b,c}$ the superimposed voltages at the prospective fault point 'β' are obtained from Equation 3.3. Thus the superimposed fault path currents at the assumed fault point 'β' are:

$$\begin{bmatrix} I_{fa}/ \\ I_{fb}/ \\ I_{fc}/ \end{bmatrix} = \begin{bmatrix} I_{Sa}/ + I_{Ra}/ \\ I_{Sb}/ + I_{Rb}/ \\ I_{Sc}/ + I_{Rc}/ \end{bmatrix} \tag{3.6}$$

Essentially, the assumed fault position 'β' is shifted in an interactive fashion to find the minimum value of fault path currents in the healthy phases and this point corresponds to the actual fault point 'α' as shown in Figure 3.4.

3.2.2 Symmetrical Three Phase Faults

Three phase faults in distribution systems are very rare and they are usually caused by human errors such as after the restoration of a line, forgetting to remove grounding clamps. However, in the technique described herein, like other types of fault, in the presence of three-phase faults, it is not possible to check the healthy phase fault path currents since all three phases are faulted. For a symmetrical 3-phase fault, the system produces an impedance at the installation location of the locator equipment which is proportional to the distance from fault location regardless of the fault resistance [21]. Thus by using post-fault voltage and current values for all the phases, the apparent impedance seen at the locator end can be calculated. Hence:

$$Z_{app}=\frac{V_{post}}{I_{post}} \tag{3.7}$$

The magnitude of the impedance is then given by:

$$Z_{app}=(R_{app}+X_{app})^{\frac{1}{2}} \tag{3.8}$$

where X_{app} is the total reactance to the fault point; thus:

$$Distance = X_{app}/X_1 \tag{3.9}$$

where X_1 is the positive phase sequence reactance of the distribution line per km.

In this method, the presence of remote infeed source and the presence of multiple load taps are not taken into consideration. This approximation is justified by virtue of the fact that in three phase faults since the fault resistance between the phases is very low, the presence of remote infeed source does not affect the accuracy. Moreover, in the presence of multiple loads, the load impedance is normally much greater than the fault resistance. This effectively means that even for faults towards the far end of system, results obtained are within reasonable accuracy.

3.3 Feeder Model

A three-phase overhead distribution feeder without ground wire can be represented by its impedance matrix [26], which considers the unequal mutual coupling and the unequal distance between the different phases, as shown in Equation 3.10:

$$[Z_{abc}] = \begin{bmatrix} Z_{aa} & Z_{ab} & Z_{ac} \\ Z_{ba} & Z_{bb} & Z_{bc} \\ Z_{ca} & Z_{cb} & Z_{cc} \end{bmatrix} \qquad (3.10)$$

This is in ohms/unit length, where:

$$Z_{aa} = Z_{bb} = Z_{cc} = [(r_a + r_e) + j(2\pi f)k \ln(D_e/D_s)] \qquad (3.11)$$

These are the self-impedances (in ohms/unit length), where r_a is the resistance of a single conductor 'a', r_e is the resistance of Carson's [27] equivalent (and fictitious) earth return conductor. It is a function of frequency and can be expressed as:

$$r_e = 9.869\times10^{-4}f \quad \Omega/km \tag{3.12}$$

The quantity D_s is the geometric mean radius (GMR) of the phase conductor, k is constant (2×10^{-4} if the length is in km), D_e is equivalent spacing of the earth return path which is a function of both the earth resistivity ρ and the frequency f and can be expressed as:

$$D_e = 658.4(\rho/f)^{1/2} \quad m \tag{3.13}$$

And mutual impedances between phases can be given as:

$$Z_{ab} = Z_{ba} = [r_e + j\omega k \ln(D_e/D_{ab})] \tag{3.14}$$

$$Z_{ac} = Z_{ca} = [r_e + j\omega k \ln(D_e/D_{ac})] \tag{3.15}$$

$$Z_{bc} = Z_{cb} = [r_e + j\omega k \ln(D_e/D_{bc})] \tag{3.16}$$

These are the mutual impedances (in ohm/unit length).

The admittance matrix for each feeder is the inverse of the impedance matrix:

$$[Y_{abc}] = [Z_{abc}]^{-1} \tag{3.17}$$

The feeders are considered as overhead lines throughout the simulations. In order to obtain the most general results as is possible, a line model was chosen whose characteristics are close to those of the three normal phase arrangements on the distribution posts. The line model is calculated with the EMTP line constant routine the *KC Lee* option, which enables the line elements to be considered as

distributed and gives a good degree of accuracy for fault transient simulation studies. Moreover, in the simulations the lines are assumed to be untransposed as is the case in practice.

3.4 Fault Type Simulation

The relative number of the occurrences of different fault types depend upon various factors, e.g., circuit configuration, the height of ground wires, voltage class, method of grounding, relative insulation levels to ground and between phases, number of stormy days per year and atmospheric conditions. In distribution systems, the majority of faults are single line to ground faults (70%), line to line faults (15%), double to ground faults (10%) and three phase faults (5%) [1].

The four most common fault types that are studied in herein are as shown in Figure 3.6(a)-3.6(d). These are:

- Single line-to-ground (or phase-to-earth) fault (SLGF).
- Line-to-line (or phase-to-phase) ungrounded fault (LLF).
- Double line-to-ground (or phase-to-phase earth) fault (DLGF).
- Three-phase grounded or ungrounded fault (3ϕ).

In the fault studies, the fault resistance, particularly for those faults involving ground, is varied from 1 Ω to 200 Ω throughout the simulations.

3.5 Source Configuration

Although the majority of low voltage distribution systems comprise of radial feeders with remote end open, there can be cases where a line section is terminated by a primary substation. The source admittance matrix $[Y_{SR}]$ is defined

in terms of the symmetrical short circuit level and ratio of Z_{s0}/Z_{s1}. In this case $[Y_{SR}]$ takes the usual form:

$$[Y_{SR}] = \begin{bmatrix} (Z_{s1}+Z_n) & (Z_n) & (Z_n) \\ (Z_n) & (Z_{s1}+Z_n) & (Z_n) \\ (Z_n) & (Z_n) & (Z_{s1}+Z_n) \end{bmatrix}^{-1} \tag{3.18}$$

where,

$$Z_{S1} = V_R^2/VA_R \tag{3.19}$$

and

$$Z_n = (Z_{S0} - Z_{S1})/3 \tag{3.20}$$

where Z_n is the neutral impedance, V_R is the busbar voltage at the remote end of the line, VA_R is the symmetrical short circuit level at the remote end busbar, Z_{S1} is the positive phase sequence source impedance, Z_{S0} is the zero phase sequence source impedance.

It should be noted that the source admittance matrix $[Y_{ss}]$ for the local end P is calculated in exactly the same way.

3.6 Fault Inception Time Identification

In the fault recorder, after the digitisation stage, the microprocessor continuously executes a monitoring routine and current and voltage samples from the near end of the distribution line, are continuously measured and stored in the RAM memory of the computer. During this process the oldest information is

overwritten. In the stored data any changes in current and voltage samples due to a fault should be identified before the application of the fault location algorithm. Since recorded voltage and current samples include both pre-fault and post-fault data, it is necessary to determine the time at which the fault has occurred.

In the presence of a fault, current and voltage waveforms are distorted and magnitude and phase angle may change with respect to pre-fault conditions. Figure 3.7 shows the flowchart for identification of the fault inception time. In this process, the first three consecutive current samples of the second cycle are compared with the corresponding three sample of the previous cycle. Any significant change more than a predefined a threshold level indicates the time at which fault has occurred. If this criteria is not satisfied for current samples, then the same process is applied to voltage samples.

However, in the inception of the fault, it is not always possible to detect the fault at precisely the right sample. In the fault inception time identification algorithm developed; in some cases, the fault inception time identified can be 'out' by one or two samples from the time the fault actually occurred; however, this delay (or advance) is manifested in all the signals and therefore there is no effect on accuracy.

3.7 Extraction of Fundamental Phasors

Figure 3.8 shows the effect of transducer/digital filtering on voltage and current waveforms for a typical distribution system. Figure 3.8(a) and 3.8(b) show the voltage and current waveforms with one cycle pre-fault for an 'a'-earth fault for a typical system. As can be seen from the waveforms, after the fault the voltage waveforms are distorted by high frequency components while in current waveforms, DC off-set is more prominent. In the fault location process, in order

to achieve a high degree of accuracy, it is vitally important to extract power frequency voltage and current phasors from the post-fault waveforms which can contain transients ranging from high frequencies down to DC levels. After the A/D conversion, special filtering techniques have to be employed to extract power frequency voltage and current components before further processing. Although in distribution systems, due to lower *X/R* ratio, transients are significantly less in comparison with transmission systems, for better accuracy in fault location and to obtain accurate measurement of the magnitude and angle of the phasors, it is essential to employ digital filtering techniques.

In Figures 3.9(a) and 3.9(b), the input and output voltage and current waveforms of *Discrete Fourier Transform* (DFT) filter are shown. As seen from the input samples, the transients are attenuated by the transducers, low pass filters etc. but nonetheless the waveforms recorded by fault recorders can contain undesirable frequencies which can affect the accuracy significantly. From output samples, it is clearly seen that the DFT technique is very efficient in rejecting high frequency components and effectively attenuates the DC offset components [17]. Figure 3.10 shows the frequency response of DFT filter used.

The method used here is based on one cycle of information and the general DFT equation which gives both magnitude and phase of the fundamental phasor $X_{v,i}(\omega)$ is given as:

$$X_{v,i}(\omega)=(2/N)\sum_{n=0}^{n=N-1}[X_{v,i}(n)\{\cos(\omega n\Delta t) - j\sin(\omega n\Delta t)\}] \qquad (3.21)$$

N	-	number of samples in a cycle
Δt	-	time step length
ω	-	frequency of the phasor to be extracted
$X_{v,i}(n)$	-	sampled voltage or current waveforms

The algorithm uses the peak and angle outputs from the filtering routine to compute the distance to the fault. In order to increase the accuracy of fault location, the first cycle of post-fault data is ignored since the transients are more prominent in the first cycle.

The DFT technique is also applied to pre-fault components in order to obtain the magnitude and phase angle of the phasors for superimposed components calculations and to filter out any possible high frequency harmonics which are quite common in distribution systems due to electronic switching and arc-creating loads.

3.8 Superimposed Components

A fault occurring on a distribution line can be considered as superimposing an equal and opposite voltage to the fault point. The post-fault voltage and current components can thus be considered as the sum of pre-fault and superimposed voltage and current components and are given at the fault point as:

$$V_{post} = V_{pre} + \Delta V_f \tag{3.22}$$

$$I_{post} = I_{pre} + \Delta I_f \tag{3.23}$$

Superimposed components ΔV_f and ΔI_f are simply the difference between pre-fault and post-fault component values.

The difference between pre-fault and post-fault components are given as;

$$V_a' = \Delta V_f = V_{pre} - V_{post} \tag{3.24}$$

$$I_a' = \Delta I_f = I_{pre} - I_{post} \tag{3.25}$$

With the use of superimposed voltage and current quantities rather than total values, errors originating from preloading are virtually eliminated.

3.9 VTs and CTs

The fault locator input quantities are derived from the power system via instrument transformers; the response of these transformers is therefore of primary importance in assessing the overall fault locator performance. In the development of the fault locator, the effect of voltage and current transformers are incorporated into the simulation via the impulse responses of these devices.

In distribution systems, usually up to 33 kV, wound type electromagnetic voltage transformers (VTs) are used. The transient response of voltage transformers is generally good since the errors due to voltage drops in the winding resistances and leakage inductances are small under unsaturated conditions. In the distribution system simulated, a three phase wound voltage transformer with a voltage rating of 11/0.11 kV is used. Figures 3.11(a) and 3.11(b) show the frequency and phase responses of the voltage transformer used, respectively.

To get the current data from the distribution system; 300/5 A current transformers are used for each phase and the outputs of current transformers are connected to appropriate resistances to get equivalent ±10 V reference level for the A/D converter. CTs have a much wider bandwidth of typically 10 kHz. For this reason, the CT is considered ideal.

3.10 Digital Fault Recorder (DFR)

The voltage and current waveform values at the line terminals during the fault is the raw data from which the physical location of the fault can be determined. These values are stored as waveform samples and/or computed phasors by modern

microprocessor-based digital fault recorders (DFRs) installed in the substations [28].

Digital fault recorders have been used by the power supply industry for many years to continuously monitor sections of power systems to provide a record of fault conditions. The complete fault recorder scheme is as shown in Figure 3.12. In practice, on fault inception, the fault recorder is triggered and the captured data provides a number of cycles of both pre-fault and fault data. This enables engineering staff to look at the conditions leading up to the fault, protection operation and how the control systems on the circuit responded, e.g. breaker operating times etc. The DFR has permitted a precise knowledge of the protection's behaviour and of its functional performances [14]. There is an ever increasing demand for power companies to install digital fault recorders as the length of power lines and short circuit currents are increasing.

With the introduction of powerful and cheaper microprocessors, more advanced fault recorders have been developed. These units, apart from monitoring the system and presenting the information in a more convenient form, have the capability of further data processing. Hence by using the DFR and utilizing the recorded fault data, in distribution lines the distance to fault can be calculated accurately.

3.10.1 Interface Modules

The three phase currents and voltages enter through input transformers which provide galvanic isolation from the instrument transformers, as well as transforming the signals to a level suitable to the electronics. Input signals from VT and CT can contain high frequencies under fault conditions as shown in Figure 3.8. There is thus a need to actively remove any frequency components which are greater than half the sampling frequency [29]. This is achieved through the use of anti-aliasing filters. In order to prevent aliasing, a second order

Butterworth low pass filter is used, which is flat in pass band and has a cut-out frequency of 1.5 kHz as shown in Figure 3.13. The filter is based on a *Sallen and Key* circuit as shown in Figure 3.14 and the simulation of the filter is carried out by using TACS which is a subsection of EMTP.

3.10.2 Sampling and Analog to Digital Conversion

The filter outputs are switched in sequence by the multiplexer and fed into the sample and hold circuit in preparation for conversion to a digital value proportional to the instantaneous value of the AC wave.

The analog to digital conversion is achieved via a 12-bit A/D converter and a sampling frequency of 4 kHz is used throughout. In this respect, it should be mentioned that in applications which require a lower sampling rate due, for example, to hardware limitations and/or cost considerations, the fault locator algorithm was also tested for sampling rates of 2 kHz and 1 kHz; the performance attained was little different from that achieved with the 4 kHz sampling rate. Before the conversion, ±10 V reference voltage level is obtained from voltage and current transformers. The $\pm 2^{11}$ conversion process leads to a quantisation level of approximately 4.8 mV. Analog to digital conversion introduces further errors due to quantisation.

3.10.3 Microcomputer

Data acquisition and processing are carried out by a microcomputer. During the steady-state conditions, a 16 bit microprocessor initiates a sampling operation at 4 kHz and stores the data in the rotating buffer. Following the inception of a fault; it freezes this buffer, providing pre-fault information for voltage and current magnitudes and fills the RAM with new available samples as post-fault information [30]. The captured data is then transferred to another computer (such

as a PC) to process the data in order to deduce the distance to the fault. The same computer can be used to access the printer memory and convert the captured voltage and current data into graphical form for printing.

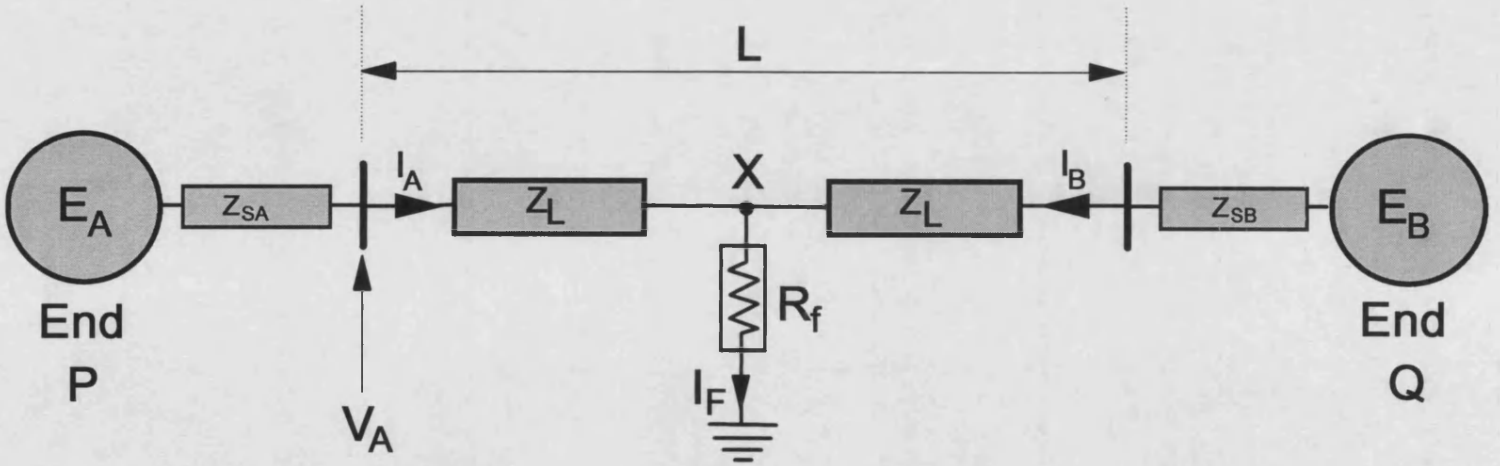

Figure 3.1 Plain distribution system with remote source infeed.

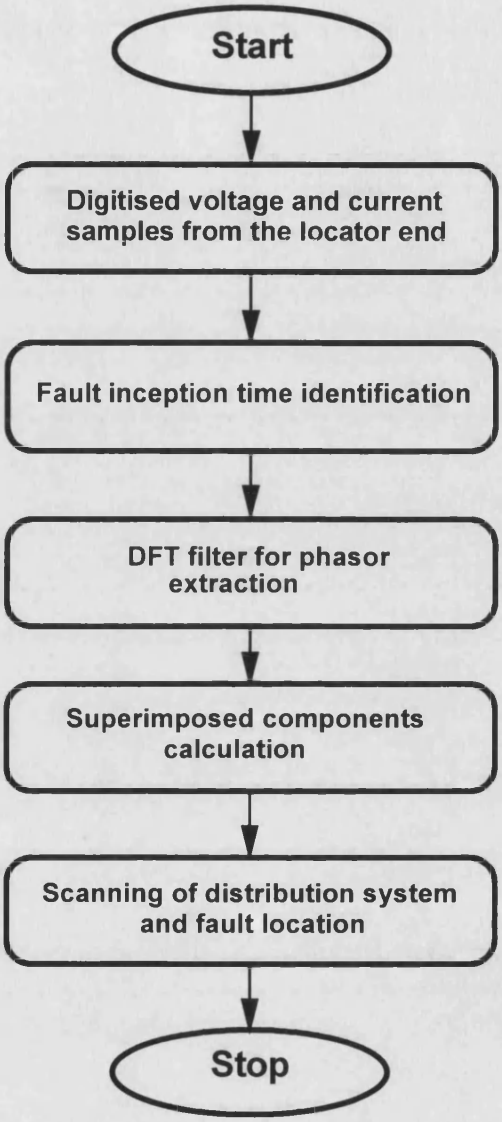

Figure 3.2 Schematic of the complete fault location algorithm.

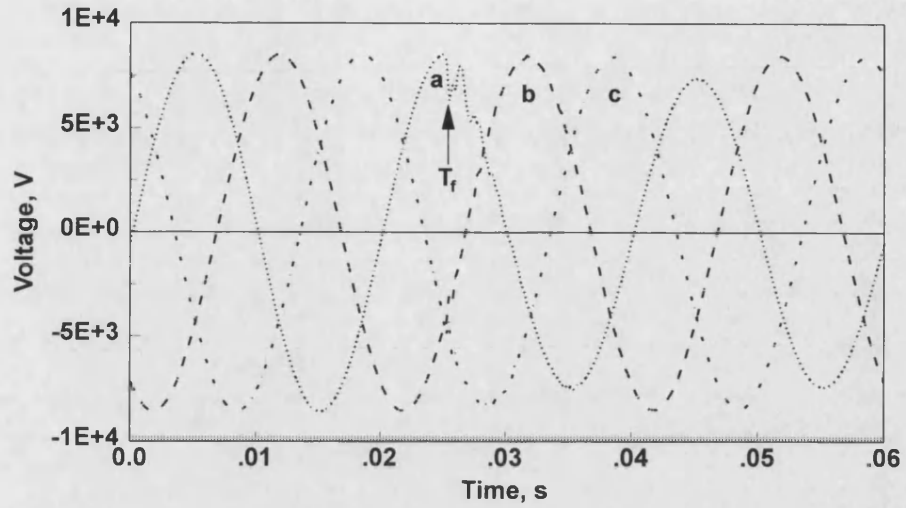

(a)

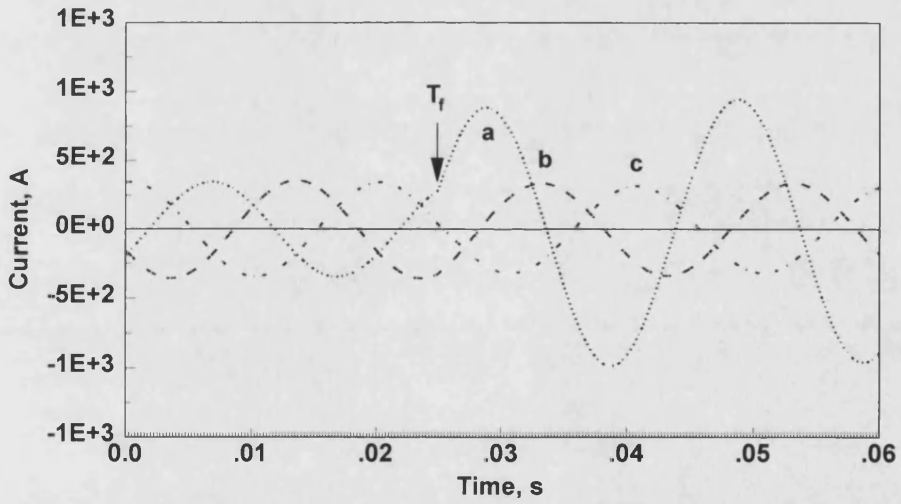

(b)

Figure 3.3 Typical digitized distribution system voltage and current waveforms for an 'a'-earth fault (T_f=Fault inception time).

(a) Voltage waveforms
(b) Current waveforms

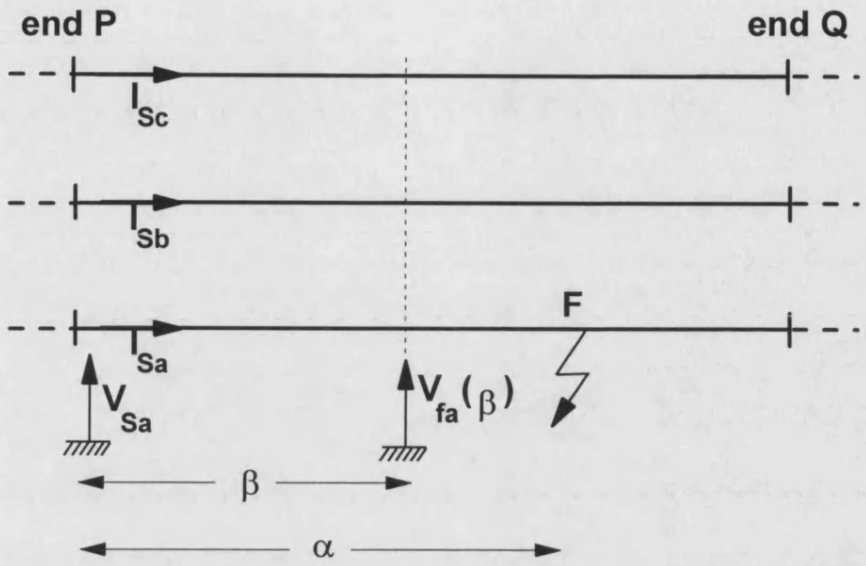

Figure 3.4 Simplified faulted system model

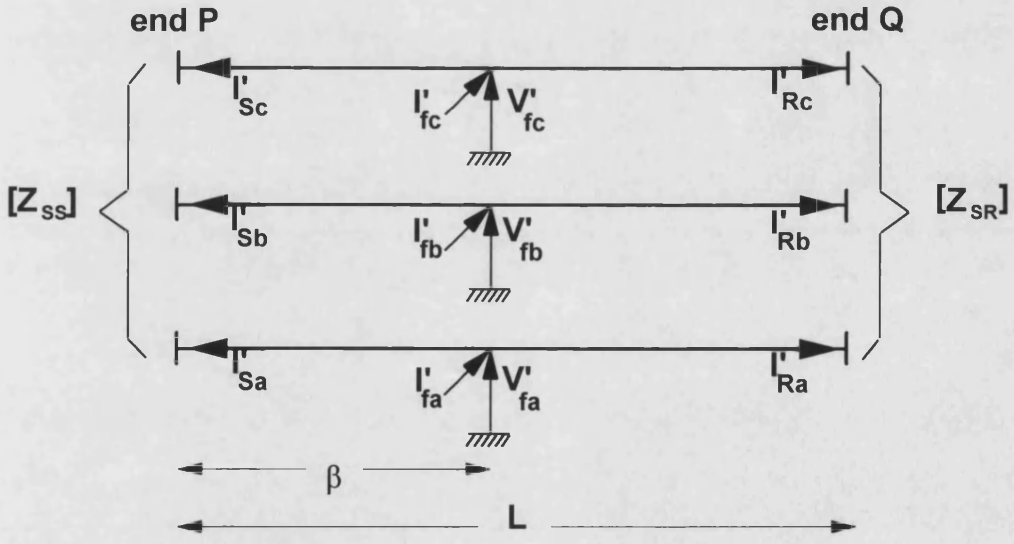

Figure 3.5 Superimposed - component circuit

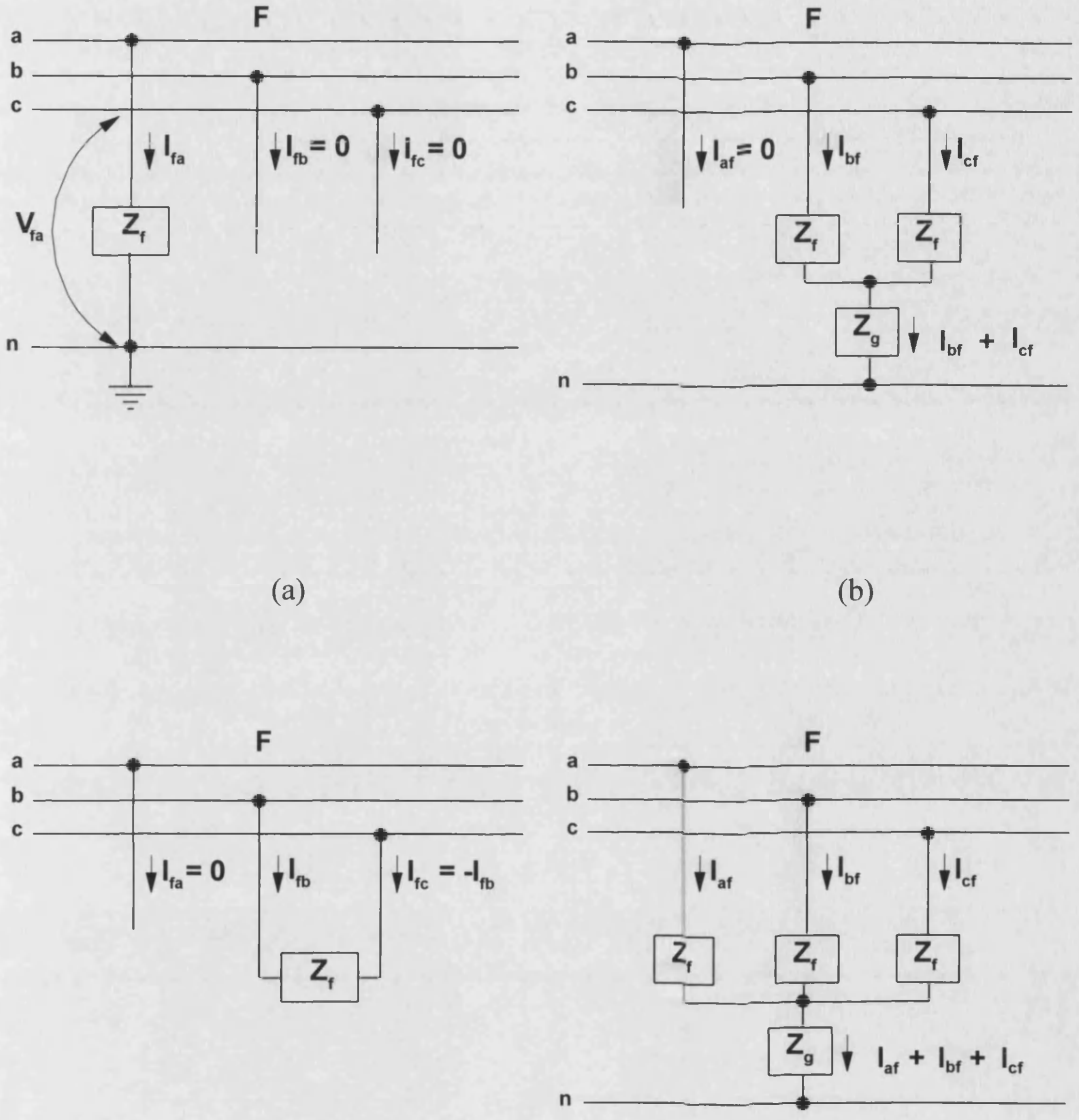

Figure 3.6 Fault types

(a) Single line-to-ground fault
(b) Double-line-to-ground fault
(c) Line-to-line fault
(d) Three phase fault

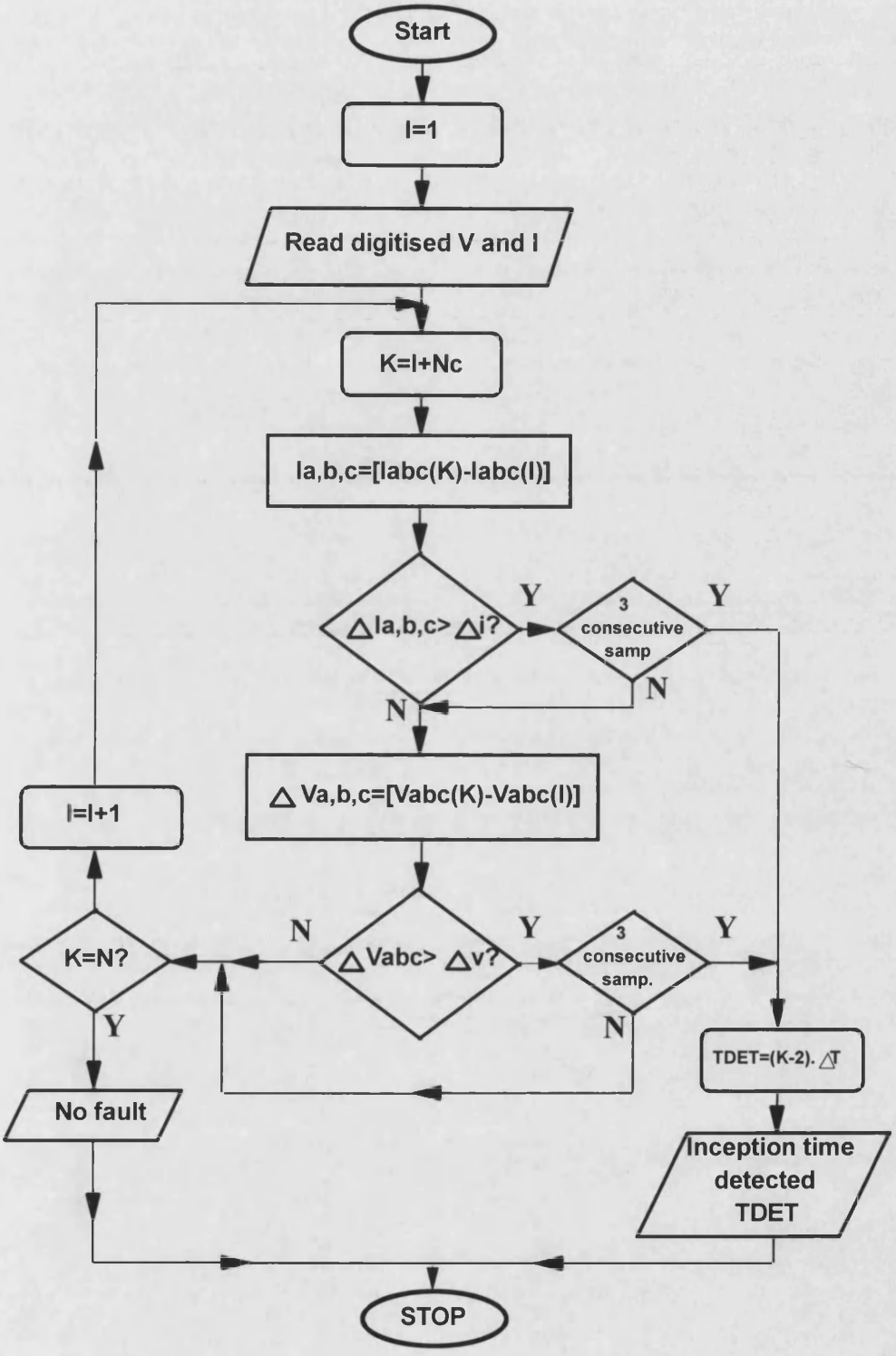

Figure 3.7 Flowchart of fault inception time identification (N-total number of samples, Nc-number of samples in a cycle, Δv, Δi-threshold level for V and I, ΔT-time interval.

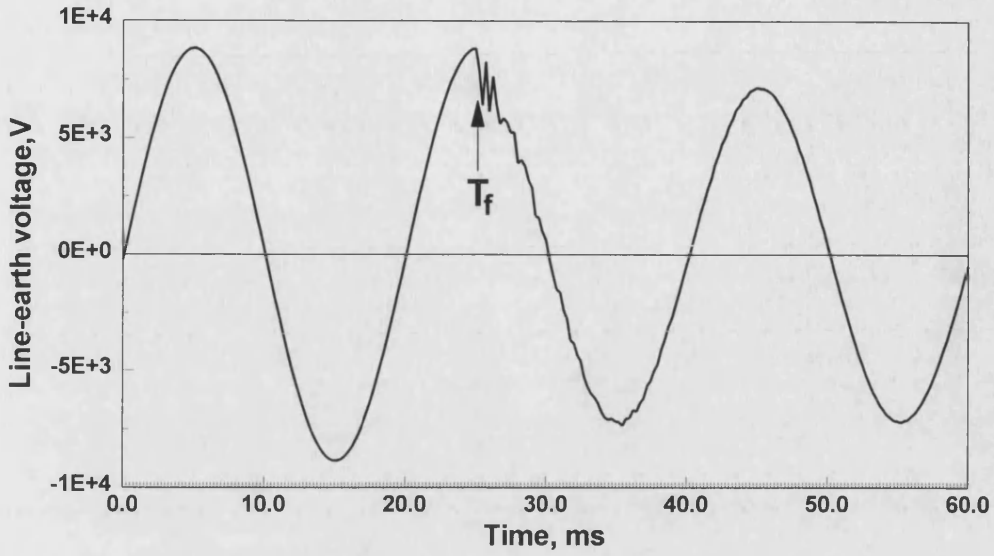

(a)

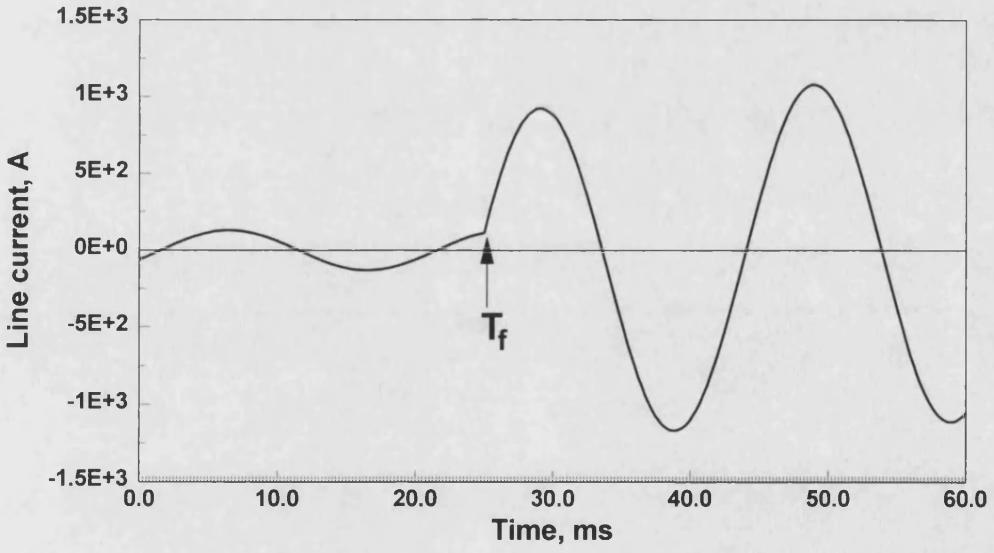

(b)

Figure 3.8 Typical primary system voltage and current waveforms for an 'a'-earth fault (T_f= Fault inception time).

(a) Voltage waveforms
(b) Current waveforms

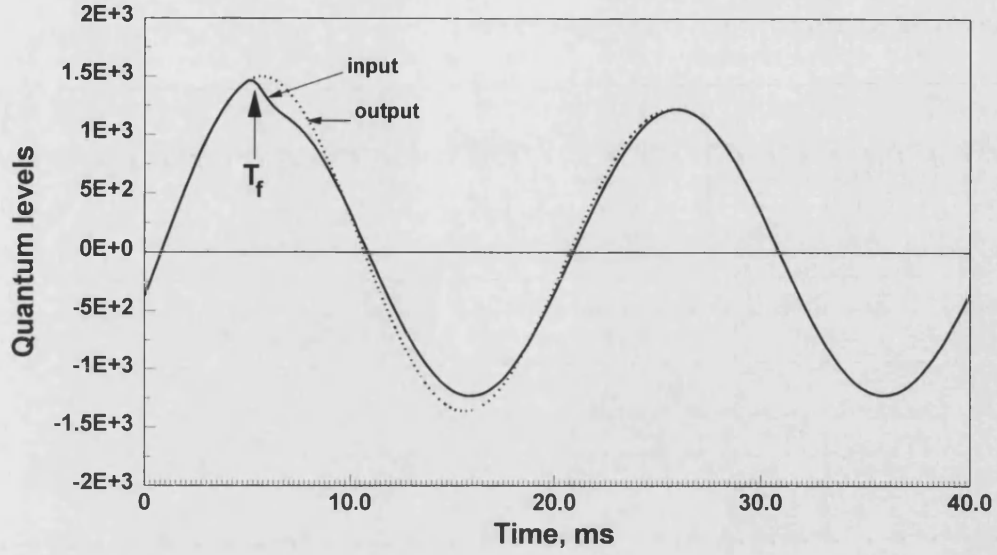

(a)

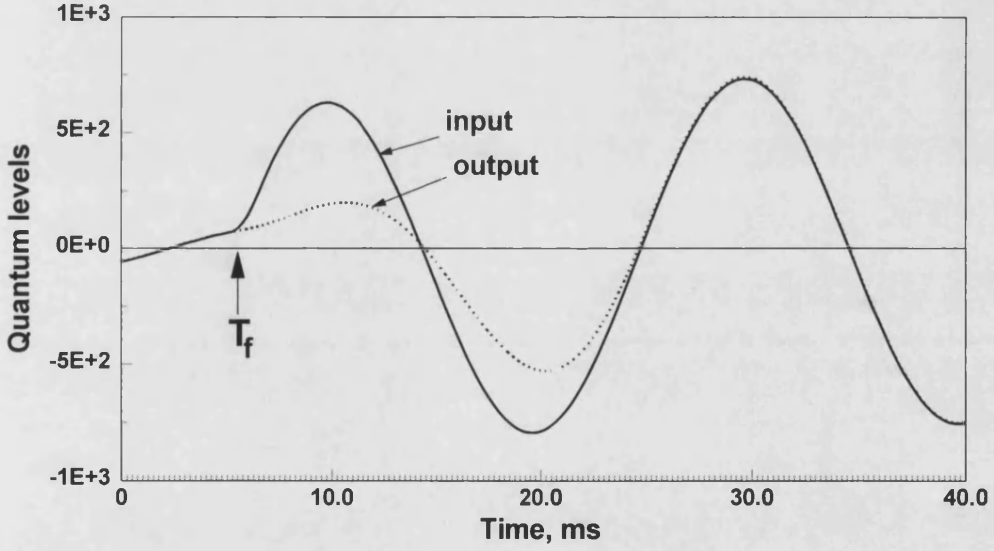

(b)

Figure 3.9 Input and output waveforms of DFT filter for an 'a'-earth fault (T_f= Fault inception time).

(a) Voltage waveforms
(b) Current waveforms

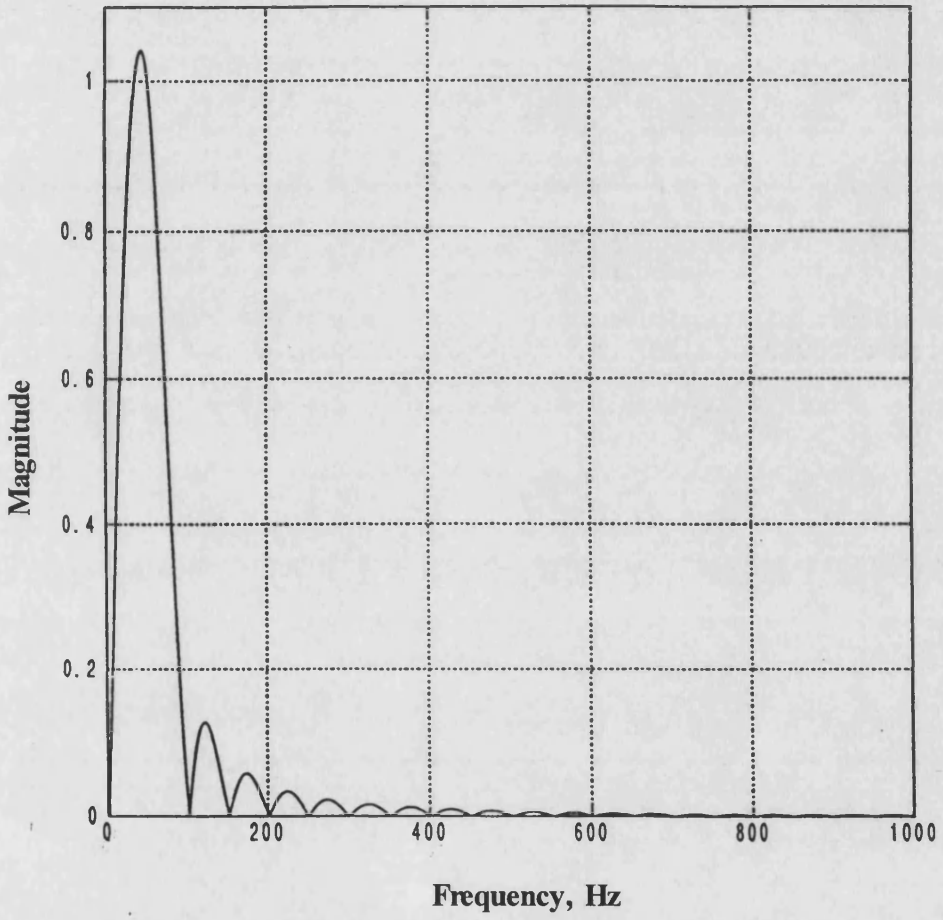

Figure 3.10 Frequency response of DFT filter

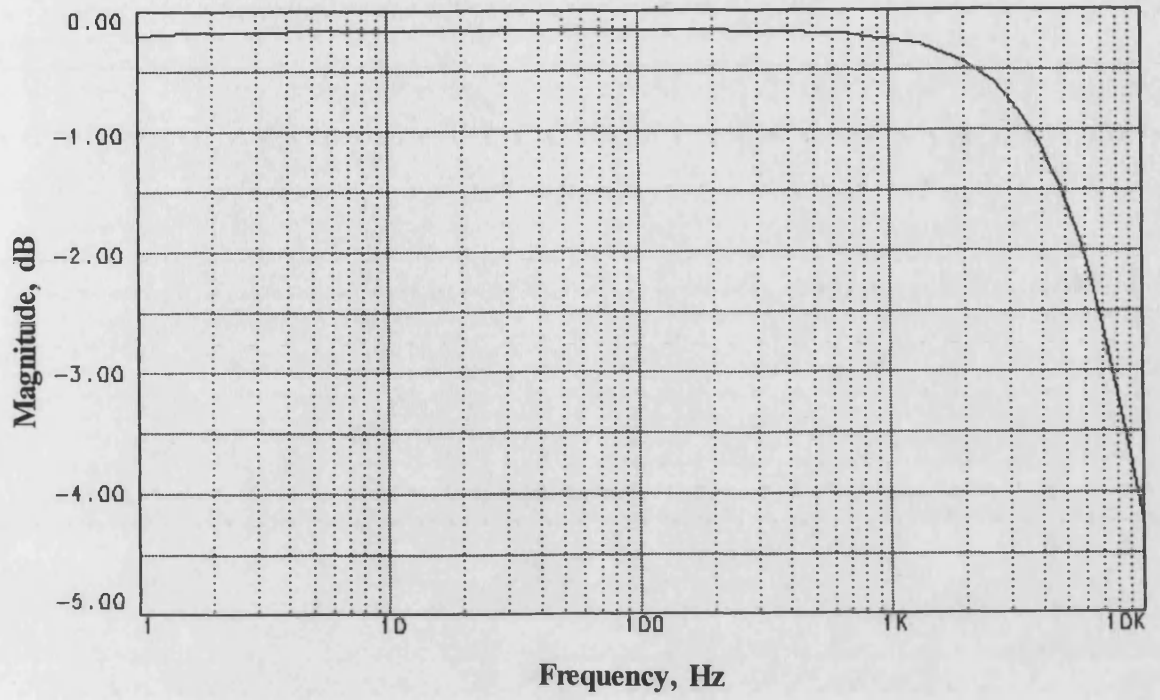

(a)

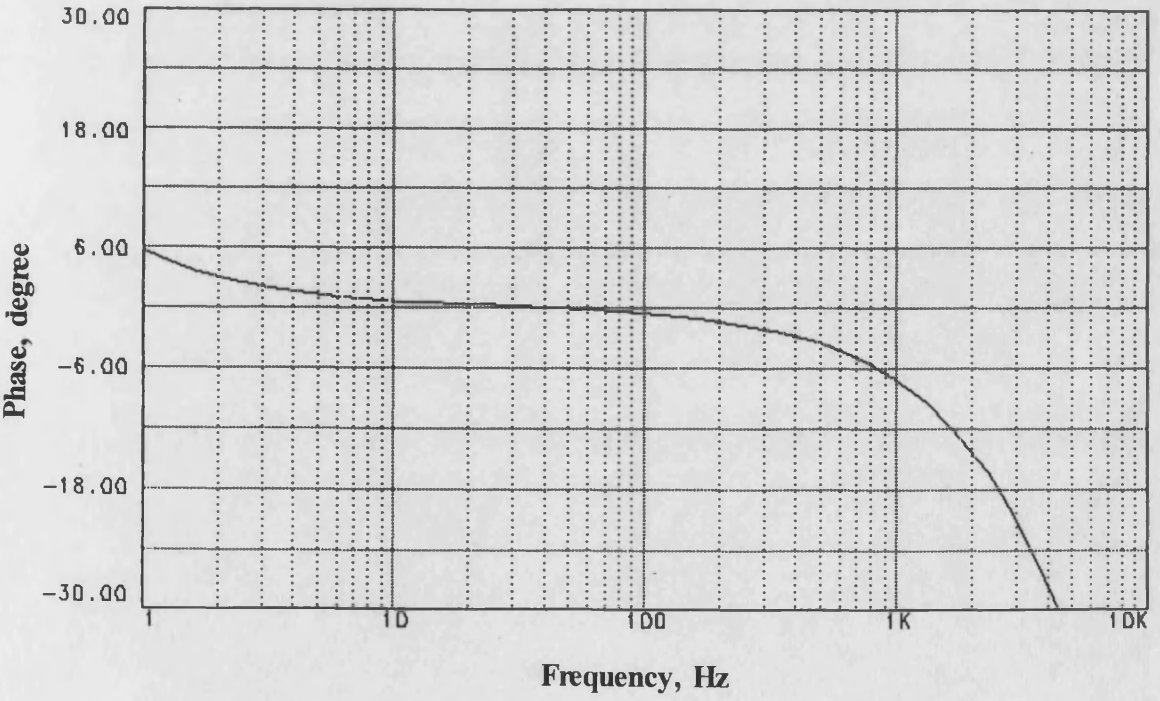

(b)

Figure 3.11 Frequency and phase response of voltage transformer.

(a) Frequency response
(b) Phase response

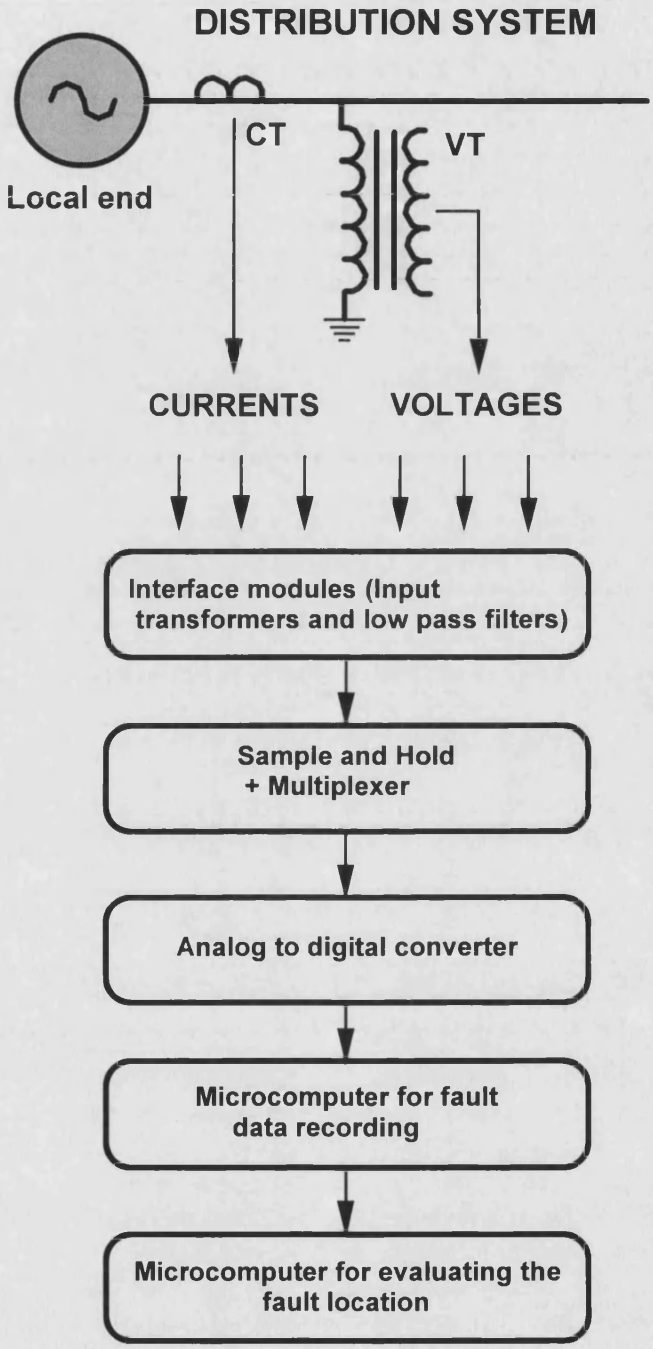

Figure 3.12 Block schematic of the digital fault recorder

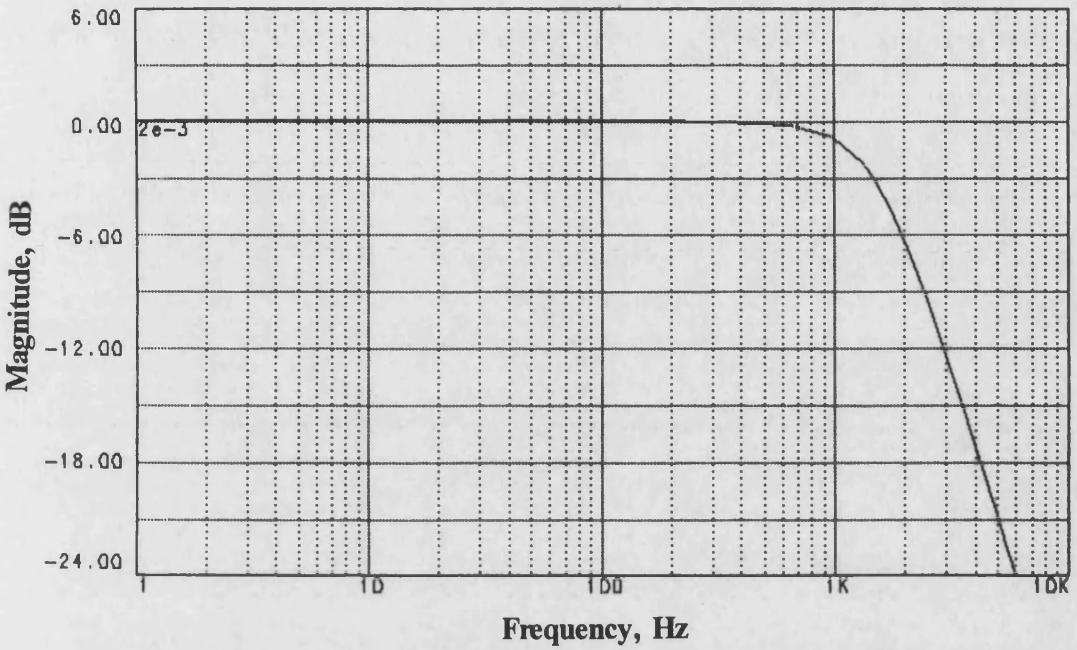

Figure 3.13 Frequency response of low-pass filter.

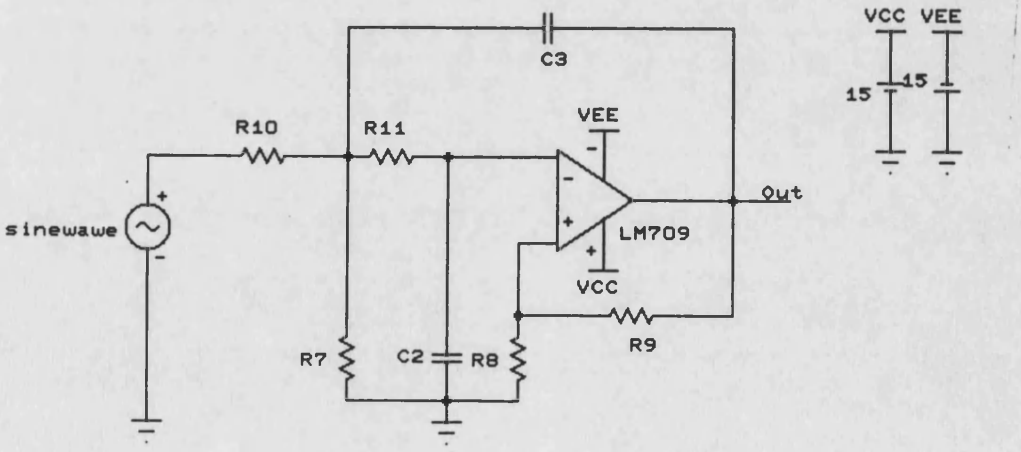

Figure 3.14 Circuit diagram of low-pass filter.

EXTENSION OF PRINCIPLE TO A SYSTEM WITH MULTIPLE LOAD TAPS

4.1 Introduction

The basis of the fault location technique developed in this thesis is explained for a plain feeder in Chapter 3. Although the computational process for a feeder with multiple taps is considerably more complex than that shown for the plain feeders, the same principle can be applied. The accuracy attainable will nonetheless be dependent upon the extent to which the system model representing the load taps and the remote infeed corresponds to the real system.

In conventional techniques, fault location estimates are influenced by the system being non-homogeneous, by pre-fault load current, fault resistance and remote infeed source. In particular, the influence of pre-fault load is considerably greater than the variations in system *X/R* ratios and when fault resistance is also present, considerable difficulties exist when attempting to obtain a precise location of fault [31]. For accurate fault location in radial distribution lines, the inclusion of loads at intermediate taps and the different line section impedances within the fault location algorithm improves the accuracy of the fault location estimate [32].

In the implementation of the algorithm for a practical distribution system, the presence of three phase, two phase and single phase load taps, and the presence of remote source are taken into account. In order to locate the actual fault point, the fault is first assumed to be at a point close to the local end (in this case end

P). The most accurate fault location is then found interactively by systematically varying the assumed fault position until such time as the fault-path current(s) in the healthy phases(s) attain a minima. At every assumed fault point, superimposed fault path currents are calculated as is explained in this chapter.

4.2 Load Representations

In a typical distribution system, it is common to have a mix of 3-phase and single phase loads terminating a length of a tap. In the case of a single-phase load tap, it is adequate to take the nominal transformer rating M and from that assume a load power factor p_f which in practice, varies typically from about 0.8-0.95. Thus with reference to Figure 4.1(a), the impedance referred to the primary of the transformer will be given by:

$$Z_L = \left[|V_L|^2 / M\right] \angle \cos^{-1} p_f \tag{4.1}$$

where V_L is the line voltage at the load point.

For a 3-phase load tap, in the majority of cases the load impedance can be approximated by a Δ-delta connected impedance between phases, as shown in Figure 4.1(b), which is given by:

$$Z_L = \left[3|V_L|^2 / M\right] \angle \cos^{-1} p_f \tag{4.2}$$

From a computational point of view, it is more convenient to consider a general case for setting up the matrix to represent the load tap. Thus with reference to Figure 4.1(c), the matrix relationship relating the main-line tap point and the load at the end of the tap is given by:

$$\begin{bmatrix} V_T \\ I_T \end{bmatrix} = \begin{bmatrix} U & lZ \\ 0 & U \end{bmatrix} \begin{bmatrix} V_L \\ I_L = I_T \end{bmatrix} \tag{4.3}$$

where l is the length of the tap line. For the purposes of simplifying the explanation, the impedance matrix Z here is assumed to be the same as that for the main line as shown in Equation 3.1 and ideal line transposition is assumed throughout.

In setting up the load impedance, the variation of the load with time of the day is taken into account. Although this can only be done approximately, pre-fault voltages and currents can be utilised to establish, to a fair degree of accuracy, the active power fed to the feeder at the measuring point. This can be calculated from:

$$P_{ss} = \sqrt{3}\ |V_{Lss}|\ |I_{Lss}|\ \cos\Phi \tag{4.4}$$

where V_{Lss} and I_{Lss} are the pre-fault line voltage and line current at the measuring end respectively; ϕ is the angle between V_{Lss} and I_{Lss}.

If the line losses are neglected, then P_{ss} is the actual summated load power. To determine the maximum total load, the sum of the rated load powers on the feeder is taken into account:

$$P_{Lmax} = (M_1+M_2+...+M_N)\cos\Phi \tag{4.5}$$

Where N is the number of load taps and M is the nominal transformer rating as defined in Equations 4.1 and 4.2.

The power factor for all the load taps is assumed to be the same. The *load level* is then defined as:

$$L_{level} = P_{ss}/P_{Lmax} \tag{4.6}$$

From this, an approximate level of an active load can be defined at each load tap; for example, for load tap 1 of rating M_1 the load impedance (assuming a single phase load) is given as:

$$Z_{LI} = \left[|V_{LI}|^2 / L_{level}\ M_1\right] \angle \cos^{-1} p_f \tag{4.7}$$

The other load impedances are likewise derived.

4.2.1 Load Admittance Matrices

In the evaluation of loads, according to the connection and impedance of the load, a more convenient form of load admittance matrix is created.

4.2.1.1 Delta Connected Loads

Figure 4.2(a) shows a delta connected load. In this circuit:

$$Z_{Lab} = Z_{Lbc} = Z_{Lca} = Z_L \tag{4.8}$$

and

$$Y_{Lab} = Y_{Lbc} = Y_{Lca} = Y_L = 1/Z_L \tag{4.9}$$

With reference to Figure 4.2(a), the load currents can be written as:

$$\begin{bmatrix} I_a \\ I_b \\ I_c \end{bmatrix} = \begin{bmatrix} (Y_{Lab} + Y_{Lca}) & -Y_{Lab} & -Y_{Lca} \\ -Y_{Lab} & (Y_{Lab} + Y_{Lbc}) & -Y_{Lbc} \\ -Y_{Lca} & -Y_{Lbc} & (Y_{Lbc} + Y_{Lca}) \end{bmatrix} \begin{bmatrix} V_a \\ V_b \\ V_c \end{bmatrix} \tag{4.10}$$

Hence from the equations, (4.8 - 4.10) the admittance matrix, for a delta connected load is written as:

$$[\ Y_{Labc}\ ] = 1/Z_L \begin{bmatrix} 2 & -1 & -1 \\ -1 & 2 & -1 \\ -1 & -1 & 2 \end{bmatrix} \tag{4.11}$$

4.2.1.2 Loads Connected Between Phase 'a' and Phase 'b'

Figure 4.2(b) shows a load connected between phase 'a' and phase 'b'. In this circuit:

$$Z_{Lab} = Z_L \tag{4.12}$$

and

$$Y_{Lab} = Y_L = 1/Z_L \tag{4.13}$$

With reference to Figure 4.2(b), the line currents for 'a' and 'b' phases can be written as:

$$\begin{bmatrix} I_a \\ I_b \\ I_c \end{bmatrix} = \begin{bmatrix} Y_{Lab} & -Y_{Lab} & 0 \\ -Y_{Lab} & Y_{Lab} & 0 \\ 0 & 0 & 0 \end{bmatrix} \begin{bmatrix} V_a \\ V_b \\ V_c \end{bmatrix} \tag{4.14}$$

Thus from equations (4.12) - (4.14), the admittance matrix for a load connected phase 'a' and phase 'b' is written as:

$$[\ Y_{Lab}\ ] = 1/Z_L \begin{bmatrix} 1 & -1 & 0 \\ -1 & 1 & 0 \\ 0 & 0 & 0 \end{bmatrix} \tag{4.15}$$

4.2.1.3 Loads Connected Between Phase 'a' and Phase 'c'

Figure 4.2(c) shows a load connected between phase 'a' and phase 'c'. In this circuit:

$$Z_{Lac} = Z_L \tag{4.16}$$

and

$$Y_{Lac} = Y_L = 1/Z_L \tag{4.17}$$

With reference to Figure 4.2(c), the line currents for 'a' and 'c' phases can be written as:

$$\begin{bmatrix} I_a \\ I_b \\ I_c \end{bmatrix} = \begin{bmatrix} Y_{Lac} & 0 & -Y_{Lac} \\ 0 & 0 & 0 \\ Y_{Lac} & 0 & Y_{Lac} \end{bmatrix} \begin{bmatrix} V_a \\ V_b \\ V_c \end{bmatrix} \tag{4.18}$$

Hence, from equations (4.16) - (4.18), the admittance matrix for a load connecting phase 'a' and phase 'c' is written as:

$$[\ Y_{Lac}\ ] = 1/Z_L \begin{bmatrix} 1 & 0 & -1 \\ 0 & 0 & 0 \\ -1 & 0 & 1 \end{bmatrix} \tag{4.19}$$

4.2.1.4 Loads Connected Between Phase 'b' and Phase 'c'

Figure 4.2(d) shows a load connected between phase 'b' and phase 'c'. In this circuit:

$$Z_{Lbc} = Z_L \tag{4.20}$$

and

$$Y_{Lbc} = Y_L = 1/Z_L \tag{4.21}$$

With reference to Figure 4.2(d), the line currents for 'b' and 'c' phases can be written as:

$$\begin{bmatrix} I_a \\ I_b \\ I_c \end{bmatrix} = \begin{bmatrix} 0 & 0 & 0 \\ 0 & Y_{Lbc} & -Y_{Lbc} \\ 0 & -Y_{Lbc} & Y_{Lbc} \end{bmatrix} \begin{bmatrix} V_a \\ V_b \\ V_c \end{bmatrix} \tag{4.22}$$

Hence from equations (4.20) - (4.22), the load admittance matrix for a load connected between phase 'b' and phase 'c' is written as:

$$[\, Y_{Lbc} \,] = 1/Z_L \begin{bmatrix} 0 & 0 & 0 \\ 0 & 1 & -1 \\ 0 & -1 & 1 \end{bmatrix} \tag{4.23}$$

4.2.1.5 Star Connected Loads

Figure 4.3 shows a star connected load. In this circuit:

$$Z_{La} = Z_{Lb} = Z_{Lc} = Z_L \tag{4.24}$$

and

$$Y_{La} = Y_{Lb} = Y_{Lc} = Y_L = 1/Z_L \tag{4.25}$$

By referring to Figure 4.3 for star connected loads, the line currents for 'a', 'b' and 'c' phases can be written as:

$$\begin{bmatrix} I_a \\ I_b \\ I_c \end{bmatrix} = \begin{bmatrix} Y_{La} & 0 & 0 \\ 0 & Y_{Lb} & 0 \\ 0 & 0 & Y_{Lc} \end{bmatrix} \begin{bmatrix} V_a \\ V_b \\ V_c \end{bmatrix} \tag{4.26}$$

Hence from equations (4.24) - (4.26), the matrix representing the load admittance for a star connected three phase load is written as:

$$[\, Y_{Labc} \,] = 1/Z_L \begin{bmatrix} 1 & 0 & 0 \\ 0 & 1 & 0 \\ 0 & 0 & 1 \end{bmatrix} \tag{4.27}$$

The values of the diagonal elements represent the admittance of that phase. The value of any diagonal element may equal zero if that phase is not present at the load tap. Hence for a single phase load connected phase 'a' to ground the load admittance matrix is given by:

$$[\, Y_{La} \,] = 1/Z_L \begin{bmatrix} 1 & 0 & 0 \\ 0 & 0 & 0 \\ 0 & 0 & 0 \end{bmatrix} \tag{4.28}$$

For a single phase load connected between phase 'b' to ground tap admittance matrix is given by:

$$[\, Y_{Lb} \,] = 1/Z_L \begin{bmatrix} 0 & 0 & 0 \\ 0 & 1 & 0 \\ 0 & 0 & 0 \end{bmatrix} \tag{4.29}$$

And for a single phase load connected between phase 'c' to ground tap admittance matrix is given by:

$$[\ Y_{Lc}\ ] = 1/Z_L \begin{bmatrix} 0 & 0 & 0 \\ 0 & 0 & 0 \\ 0 & 0 & 1 \end{bmatrix} \tag{4.30}$$

4.3 Evaluation of Load Taps

In this fault location technique, the presence of single phase, two phase and three phase loads and the type of load connection is taken into account. In the calculation of superimposed components at the assumed fault point, the overall admittance of the lateral seen at the tap point, including the line impedance between the main feeder and the load point, and the admittance of the load is calculated as a first step in the fault location process. Secondly, the load current is calculated by using the overall admittance of the lateral, seen at the tap point, and the voltage at this point.

4.3.1 Calculation of Load Tap Currents

In the calculation of the superimposed fault-path currents at the assumed fault point, load tap currents are taken into account. With reference to Figure 4.4; the voltage at the tap point is given by:

$$[V_{TN}] = [V_{LN}] + l_N\ [Z]\ [I_{LN}] \tag{4.31}$$

and the load current (ignoring the charging current of the line) is given by:

$$[I_{LN}] = [I_{TN}] = [Y_{LN}]\ [V_{LN}] \tag{4.32}$$

where

$$[Y_{LN}] = [Z_{LN}]^{-1} \tag{4.33}$$

hence

$$[V_{TN}] = [V_{LN}] + l_N [Z] [Y_{LN}] [V_{LN}] \tag{4.34}$$

Thus the voltage at the tap point can be rewritten as:

$$[V_{TN}] = [[U] + l_N [Z] [Y_{LN}]] [V_{LN}] \tag{4.35}$$

This then gives:

$$[V_{LN}] = [[U] + l_N [Z] [Y_{LN}]]^{-1} [V_{TN}] \tag{4.36}$$

By substituting equation 4.36 into equation 4.32, the tap current is:

$$[I_{LN}] = [I_{TN}] = [Y_{LN}] [[U]+l_N [Z] [Y_{LN}]]^{-1} [V_{TN}] \tag{4.37}$$

4.3.2 The Admittance at the Tap Point

In the evaluation of load admittance at the tap point, the impedance of the line section, which is between the main feeder and the load admittance, is taken into account. With reference to Figure 4.4, the equivalent admittance of the load at the tap point is given by:

$$[Y_{EN}] = [I_{TN}] / [V_{TN}] \tag{4.38}$$

From the previous section, the tap currents are given by:

$$[I_{LN}] = [I_{TN}] = [Y_{LN}] [[U] + l_N [Z] [Y_{LN}]]^{-1} [V_{TN}] \tag{4.39}$$

By substituting equation 4.39 into equation 4.38, we get:

$$[Y_{EN}] = [Y_{LN}] [[U] + l_N [Z] [Y_{LN}]]^{-1} \tag{4.40}$$

By referring to Figure 4.4, $[Y_{EN}]$ is the equivalent admittance matrix looking into l_N from tap point N to load tap terminating in L_N. The equivalent admittance matrices for the other loads can be likewise derived.

4.4 Calculation of Superimposed Fault Path Currents at the Assumed Fault Point

Figure 4.5 shows a typical distribution system comprising of four load taps and a remote source with a fault created at 'X'. In the fault location process, initially a fault point is assumed at point 'β'. In order to calculate the superimposed fault path currents at the assumed fault point, as seen from the Figure 4.6, firstly the superimposed sending end currents from assumed fault point 'β' towards the end P, and then the superimposed receiving end currents from the assumed fault point 'β' towards the end Q are calculated.

The superimposed fault path currents at the assumed fault point are:

$$\begin{bmatrix} I_{fa}/ \\ I_{fb}/ \\ I_{fc}/ \end{bmatrix} = \begin{bmatrix} I_{Ra}/ + I_{Sa}/ \\ I_{Rb}/ + I_{Sb}/ \\ I_{Rc}/ + I_{Sc}/ \end{bmatrix} \tag{4.41}$$

In the evaluation of superimposed components at the assumed fault point, in order to simplify the distribution system model and mathematical calculations, the system is divided into two parts at the assumed fault point 'β', as shown in Figure 4.7.

4.4.1 Superimposed Sending end Currents at the Assumed Fault Point

In the evaluation of pre-fault and post-fault currents at the assumed fault point,

the load tap currents are taken into consideration. In the current calculations, the charging currents of the lines are neglected. With reference to Figure 4.8 the current recorded at the end P is:

$$[I_s] = [I_{12}] + [I_{L1}] \tag{4.42}$$

The current in the line section between tap point 1 and tap point 2 is:

$$[I_{12}] = [I_s] - [I_{L1}] \tag{4.43}$$

and the load current is:

$$[I_{L1}] = [Y_{E1}]\,[V_{T1}] \tag{4.44}$$

Hence

$$[I_{12}] = [I_s] - [Y_{E1}]\,[V_{T1}] \tag{4.45}$$

Similarly, the current in the line section between tap point 2 and tap point 3 is:

$$[I_{23}] = [I_{12}] - [Y_{E2}]\,[V_{T2}] \tag{4.46}$$

By simply using pre-fault (steady-state) and post-fault currents, which are obtained from the measuring end P, for any fault between tap point 2 and tap point 3, the sending-end pre-fault and post-fault currents are obtained in Equation 4.46.

Hence the superimposed currents (i.e.those fed into the fault from end P) at the assumed fault point 'β' are:

$$\begin{bmatrix} I_{Sa}/ \\ I_{Sb}/ \\ I_{Sc}/ \end{bmatrix} = \begin{bmatrix} I_{23_{post_a}}/ - I_{23_{pre_a}}/ \\ I_{23_{post_b}}/ - I_{23_{pre_b}}/ \\ I_{23_{post_c}}/ - I_{23_{pre_c}}/ \end{bmatrix} \tag{4.47}$$

4.4.2 The Superimposed Receiving end Currents at the Assumed Fault Point

In order to calculate superimposed receiving end fault path currents (i.e. those fed into the fault from end Q) at the assumed fault point, initially the superimposed fault voltages at the assumed fault point 'β' and the impedance at this point looking into end Q have to be calculated.

The superimposed receiving end currents I'_R at the assumed fault point are given by:

$$[I'_R] = [V'_f]\ [Y_{ER}] \tag{4.48}$$

Where V_f' is the superimposed fault voltage at the assumed fault point and Y_{ER} is the equivalent admittance matrix looking into the remote source Q from the assumed fault point.

4.4.2.1 The Superimposed Voltages at the Assumed Fault Point

As mentioned before, in the fault location technique, the pre-fault and post-fault voltages are obtained at the substation of a radial distribution system. In the evaluation of pre-fault and post-fault load tap currents and in order to find the superimposed fault voltages at the assumed fault point, the pre-fault and post-fault voltages at every tap point are calculated. To do this, the series impedance for each line section is calculated from a knowledge of line configurations and these are then used to determine the voltage drop for each line section.

With reference to Figure 4.8, the recorded voltages at the locator end are given by:

$$[V_S] = [V_{TI}] + l_{01}\ [Z_{01}]\ [I_S] \tag{4.49}$$

Hence the voltages at the first tap point are:

$$[V_{T1}] = [V_S] - l_{01}\,[Z_{12}]\,[I_S] \tag{4.50}$$

The voltages at the second tap point are:

$$[V_{T2}] = [V_{T1}] - l_{12}\,[Z_{12}]\,[I_{12}] \tag{4.51}$$

In the calculation of the pre-fault and post-fault voltages at the assumed fault point 'β', the voltage drop on the line section between load tap and the actual fault point is taken into account. With reference to Figure 4.8, the voltages at the assumed fault point are given by:

$$[V_f] = [V_{T2}] - l_{2\beta}\,[Z_{23}]\,[I_{23}] \tag{4.52}$$

By using pre-fault voltages and currents from the measuring end P in the equations described above, the pre-fault voltages are then calculated at the assumed fault point. To find the post-fault voltages at the assumed fault point, the same process is repeated by using post-fault voltages and currents from the measuring end P. Finally, to obtain the superimposed voltages at the fault point, the differences between pre-fault and post-fault voltages are calculated.

The superimposed fault voltages at the assumed fault point are then given by:

$$\begin{bmatrix} V_{fa}/ \\ V_{fb}/ \\ V_{fc}/ \end{bmatrix} = \begin{bmatrix} V_{fa} - V_{fa(ss)} \\ V_{fb} - V_{fb(ss)} \\ V_{fc} - V_{fc(ss)} \end{bmatrix} \tag{4.53}$$

4.4.2.2 Evaluation of the Driving Matrix $[Y_{ER}]$

As seen from Section 4.4.2, in order to calculate $[I_R']$, the superimposed receiving-

end fault currents at the assumed fault point, it is necessary to calculate the impedance at the assumed fault point looking into end Q. Figure 4.9 shows the receiving-end side of the distribution system studied. It can be seen that each leg is terminated in an effective load impedance and it was shown in Section 4.2.1 as to how these could be derived as a matrix Y_L for either 3-phase or single-phase taps. With reference to Figure 4.9, the admittance at the tap point 4 is given as:

$$[Y_{4R}] = [Y_{E4}] + [Y_{45}] \tag{4.54}$$

where

$$[Y_{E4}] = [Y_{L4}] \left[[U] + l_4 [Z_4] [Y_{L4}]\right]^{-1} \tag{4.55}$$

$[Y_{E4}]$ is the equivalent admittance matrix looking into tap line l_4 from tap point 4 to load tap terminated in load L_4; it is derived using the same methodology as described in Section 4.3.2. Likewise:

$$[Y_{45}] = [Y_{SR}] \left[[U] + l_{45} [Z_{45}] [Y_{SR}]\right]^{-1} \tag{4.56}$$

$[Y_{45}]$ is the equivalent admittance matrix looking into main line l_{45} from tap point 4 to the remote source which in turn is represented by the admittance $[Y_{SR}]$.

The admittance at the third tap point:

$$[Y_{3R}] = [Y_{E3}] + [Y_{34}] \tag{4.57}$$

where $[Y_{E3}]$ is the equivalent admittance matrix looking into tap line l_3 from tap point 3 to load tap terminated in load L_3, given by:

$$[Y_{E3}] = [Y_{L3}] \left[[U] + l_3 [Z_3] [Y_{L3}]\right]^{-1} \tag{4.58}$$

and $[Y_{34}]$ is the equivalent admittance matrix looking into main line l_{34} from tap point 3, given by:

$$[Y_{34}] = [Y_{4R}] \left[[U] + l_{34} [Z_{34}] [Y_{R4}]\right]^{-1} \quad (4.59)$$

With reference to Figure 4.9, for an assumed fault position between tap point 2 and tap point 3 at 'β', to calculate the admittance at the assumed fault point looking into end Q, the line impedance between the assumed fault point and tap point 3 is added to the admittance at the tap point 3.

Hence the admittance matrix at the assumed fault point looking into end Q is given by:

$$[Y_{ER}] = [Y_{3R}] \left[[U] + (l_{23} - l_{2\beta}) [Z_{23}] [Y_{R3}]\right]^{-1} \quad (4.60)$$

4.4.2.3 Evaluation of the Driving Matrix $[Y_{ES}]$

With reference to Figure 4.8 the admittance at tap point 1 is:

$$[Y_{1S}] = [Y_{EI}] + [Y_{10}] \quad (4.61)$$

where

$$[Y_{EI}] = [Y_{LI}] \left[[U] + l_1 [Z_1] [Y_{LI}]\right]^{-1} \quad (4.62)$$

and

$$[Y_{10}] = [Y_{SS}] \left[[U] + l_{01} [Z_{01}] [Y_{SS}]\right]^{-1} \quad (4.63)$$

Now $[Y_{1S}]$ terminates tap point 2, so that with reference to Figure 4.8, $[Y_{2S}]$ is given by:

$$[Y_{2S}] = [Y_{E2}] + [Y_{21}] \quad (4.64)$$

where

$$[Y_{E2}] = [Y_{L2}] \left[[U] + l_2 [Z_2] [Y_{L2}]\right]^{-1} \quad (4.65)$$

and

$$[Y_{21}] = [Y_{1S}] \left[[U] + l_{12} [Z_{12}] [Y_{1S}]\right]^{-1} \quad (4.66)$$

Finally $[Y_{2S}]$ terminates tap point 3, so that with reference to Figure 4.8 , $[Y_{ES}]$ is given by:

$$[Y_{ES}] = [Y_{2S}] \left[[U] + l_{2\beta} [Z_{23}] [Y_{2S}]\right]^{-1} \quad (4.67)$$

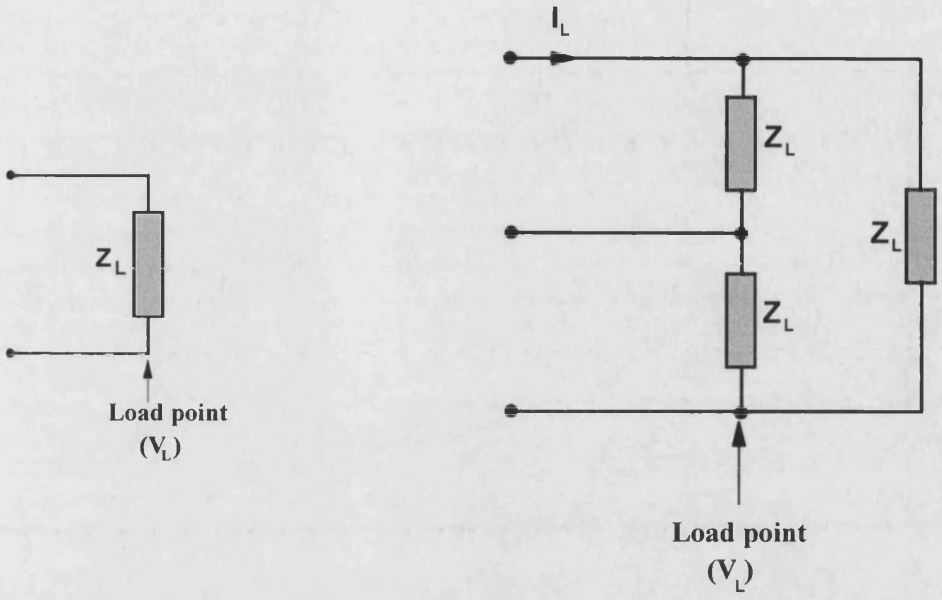

(a)

(b)

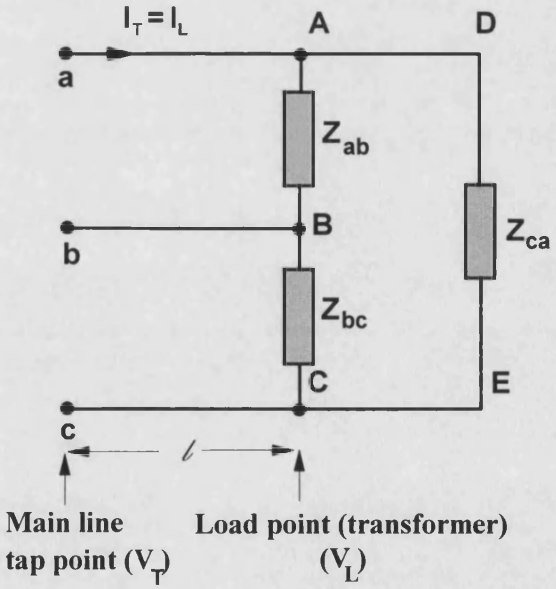

(c)

Figure 4.1 Load-tap representation

(a) Single-phase tap
(b) 3-phase tap
(c) General load-tap representation

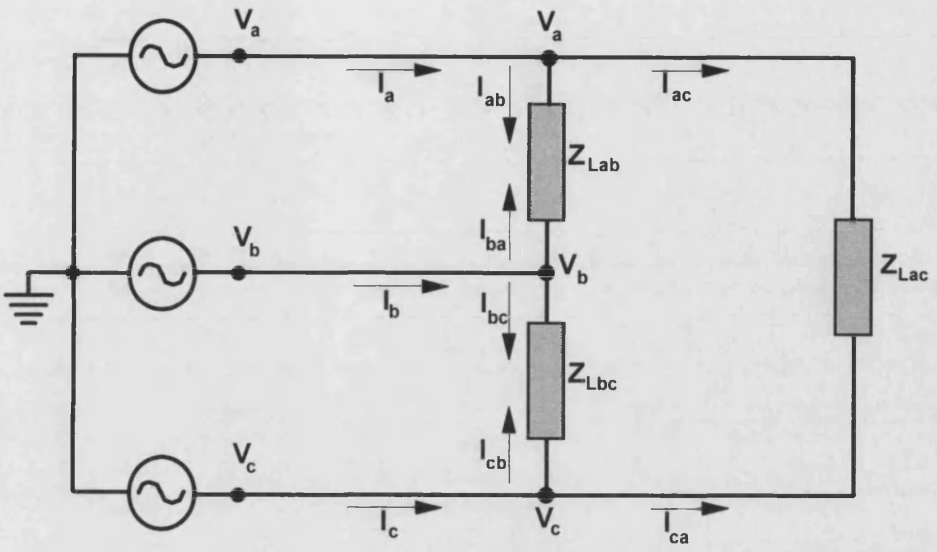

(a)

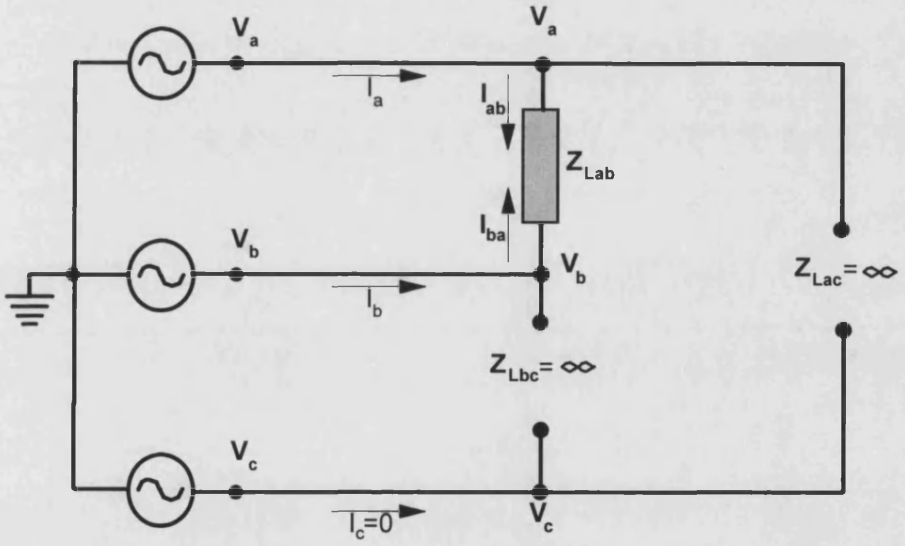

(b)

Figure 4.2 Load connections

(a) Delta connected three phase load
(b) Load connected between phase 'A' and phase 'B'

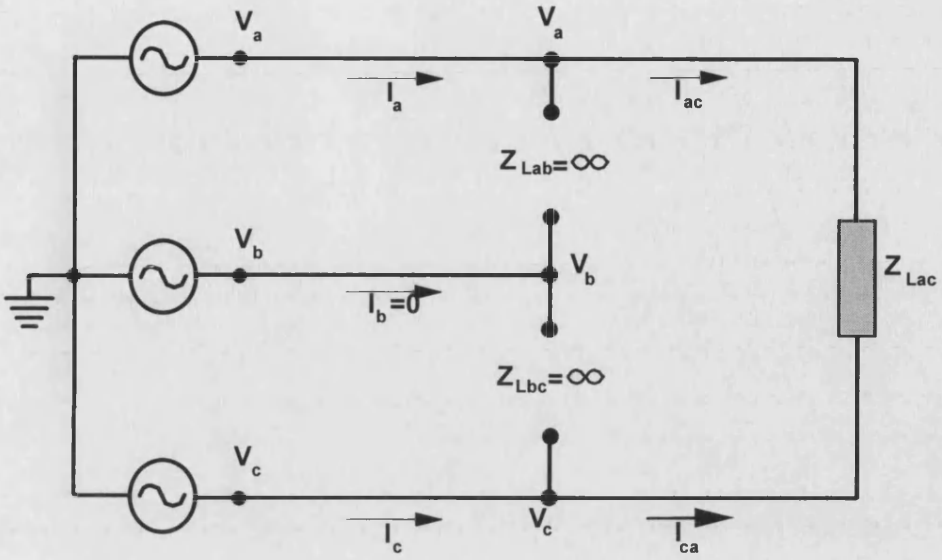

(c)

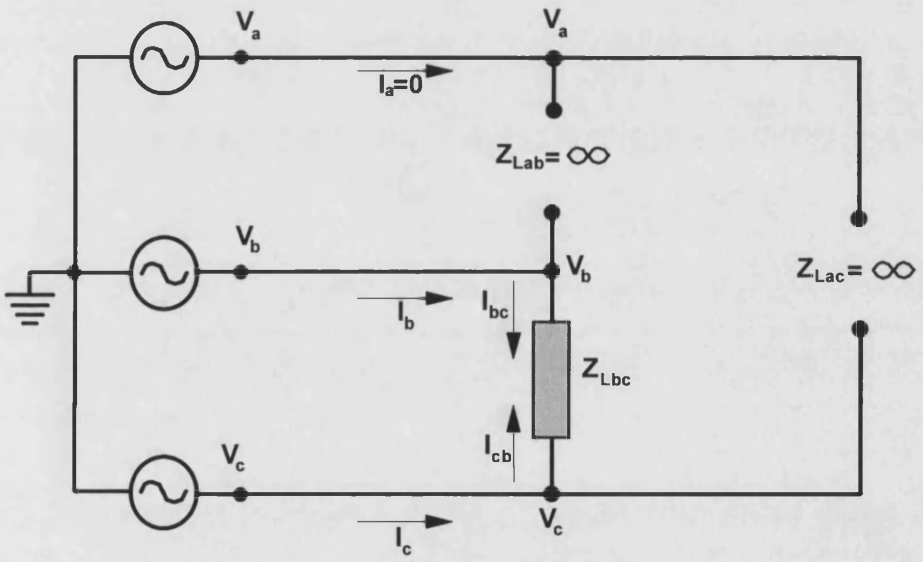

(d)

Figure 4.2 Load connections

(c) Load connected between phase 'A' and phase 'C'
(d) Load connected between phase 'B' and phase 'C'

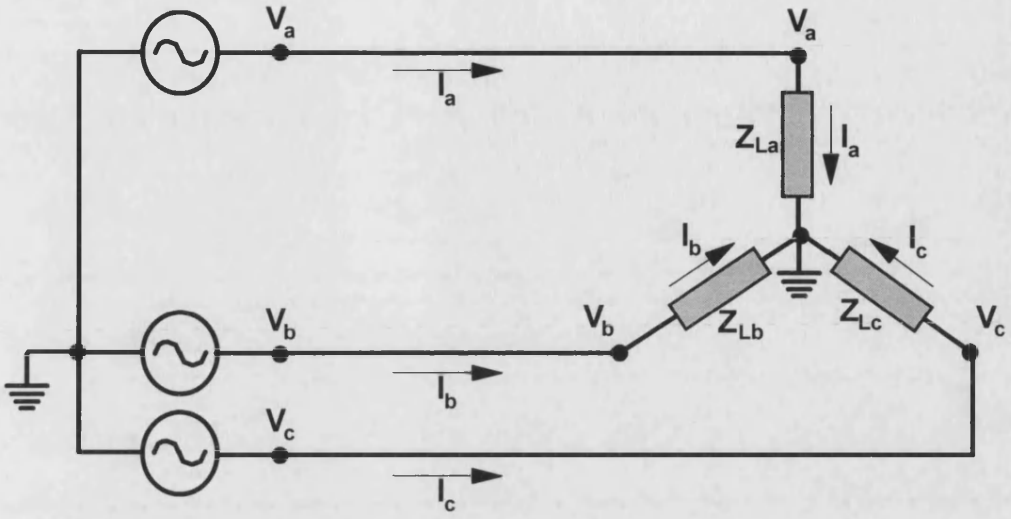

Figure 4.3 Star connected three phase load

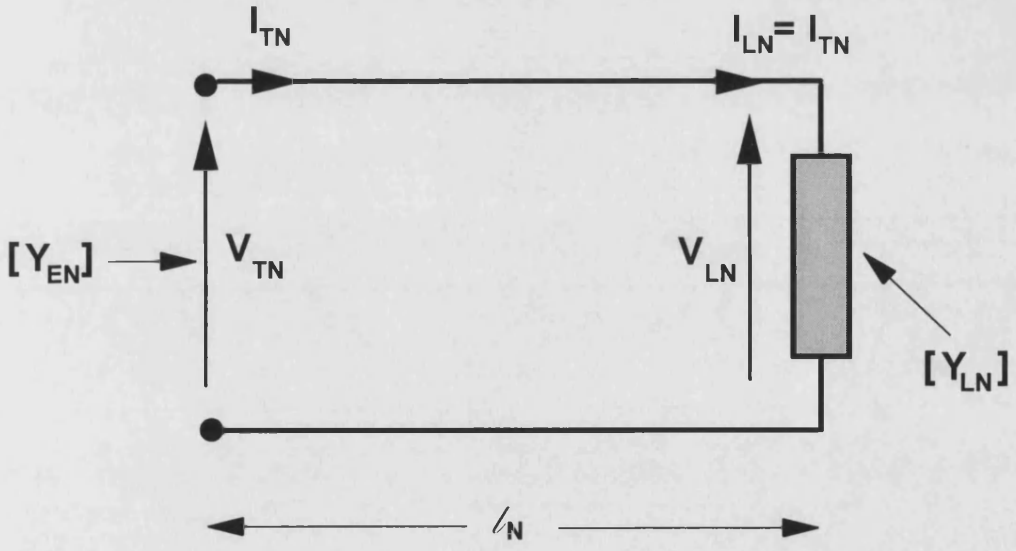

Figure 4.4 General load tap circuit

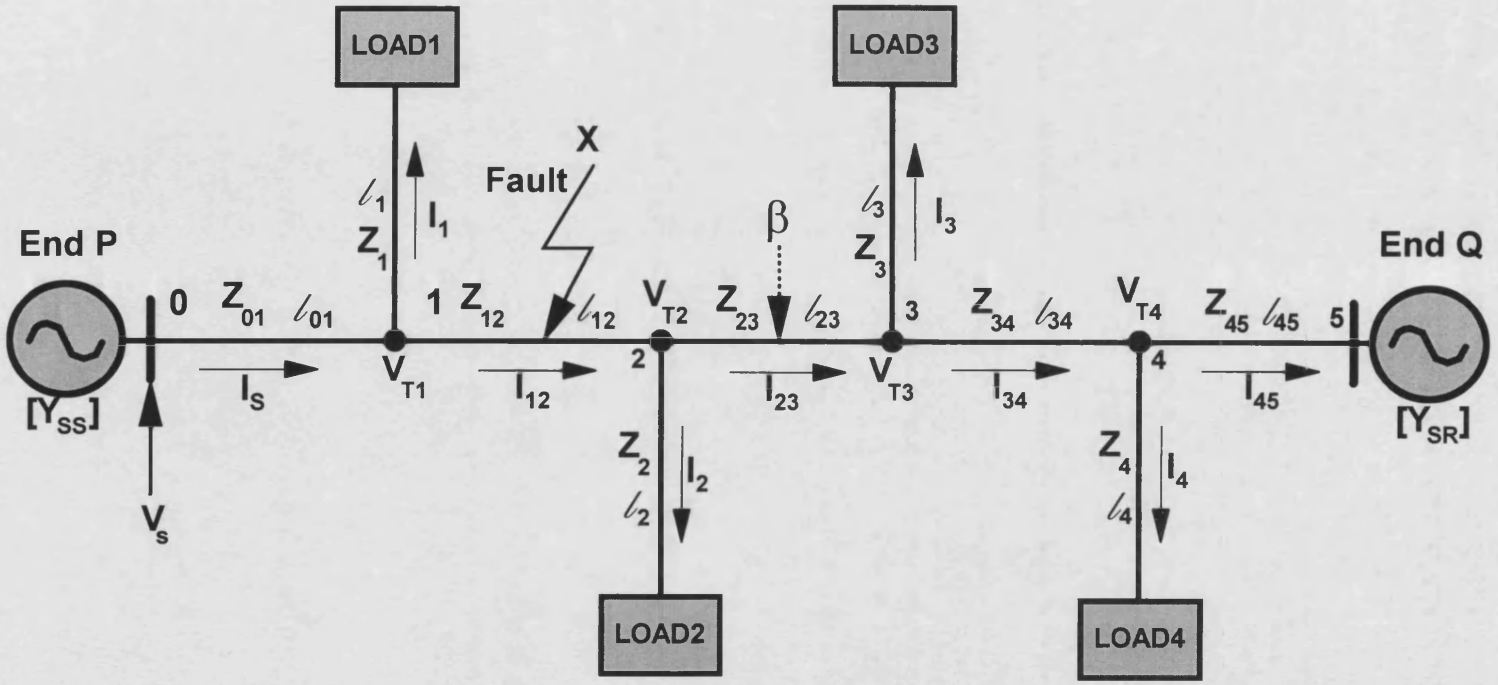

Fig 4.5 A typical distribution system with a fault at 'X'

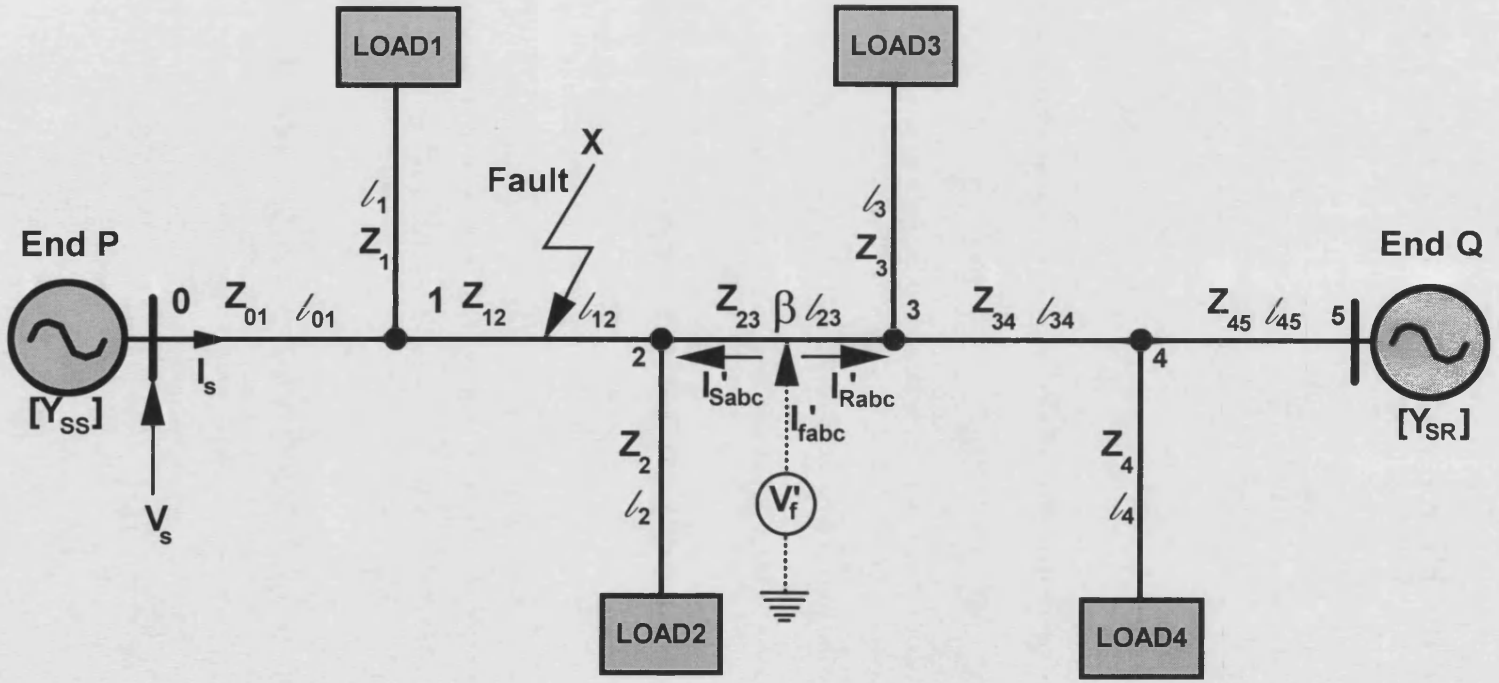

Fig 4.6 Injection of superimposed components at the assumed fault position

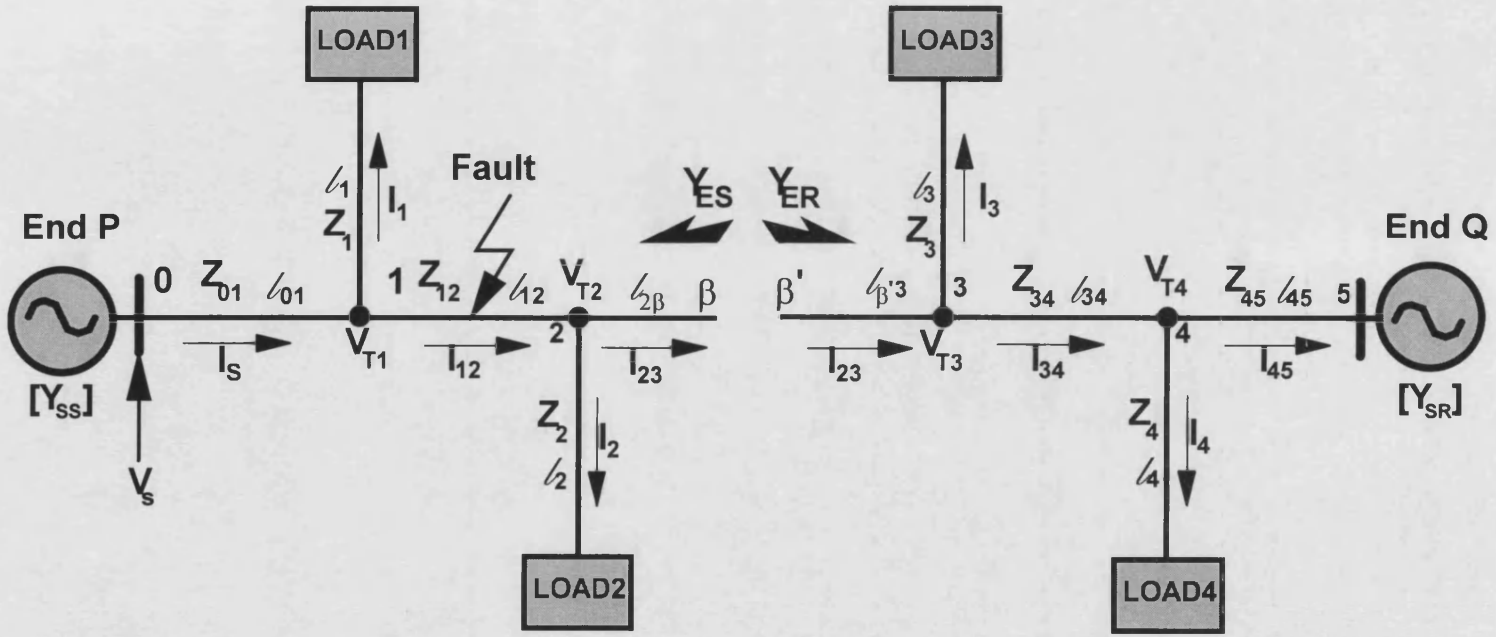

Figure 4.7 Distribution system splitted at the assumed fault position

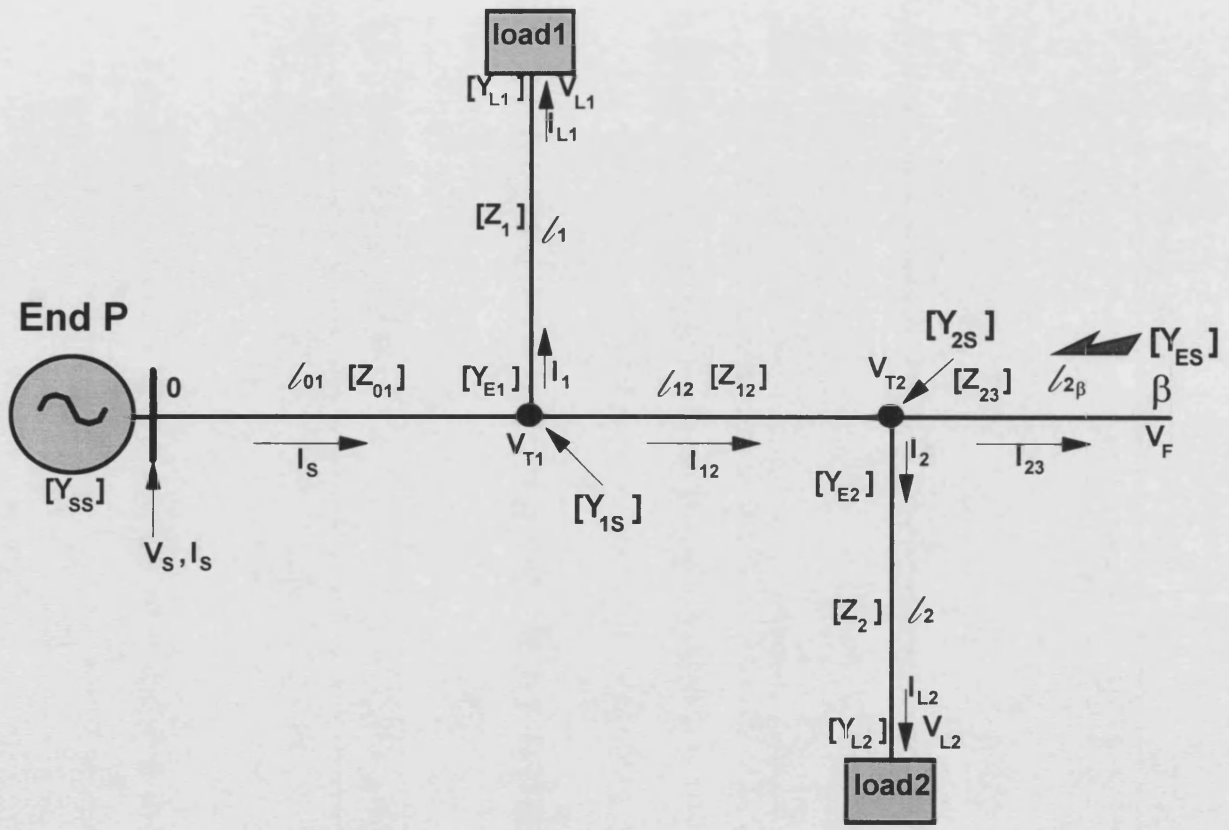

Figure 4.8 Sending-end side of the distribution system

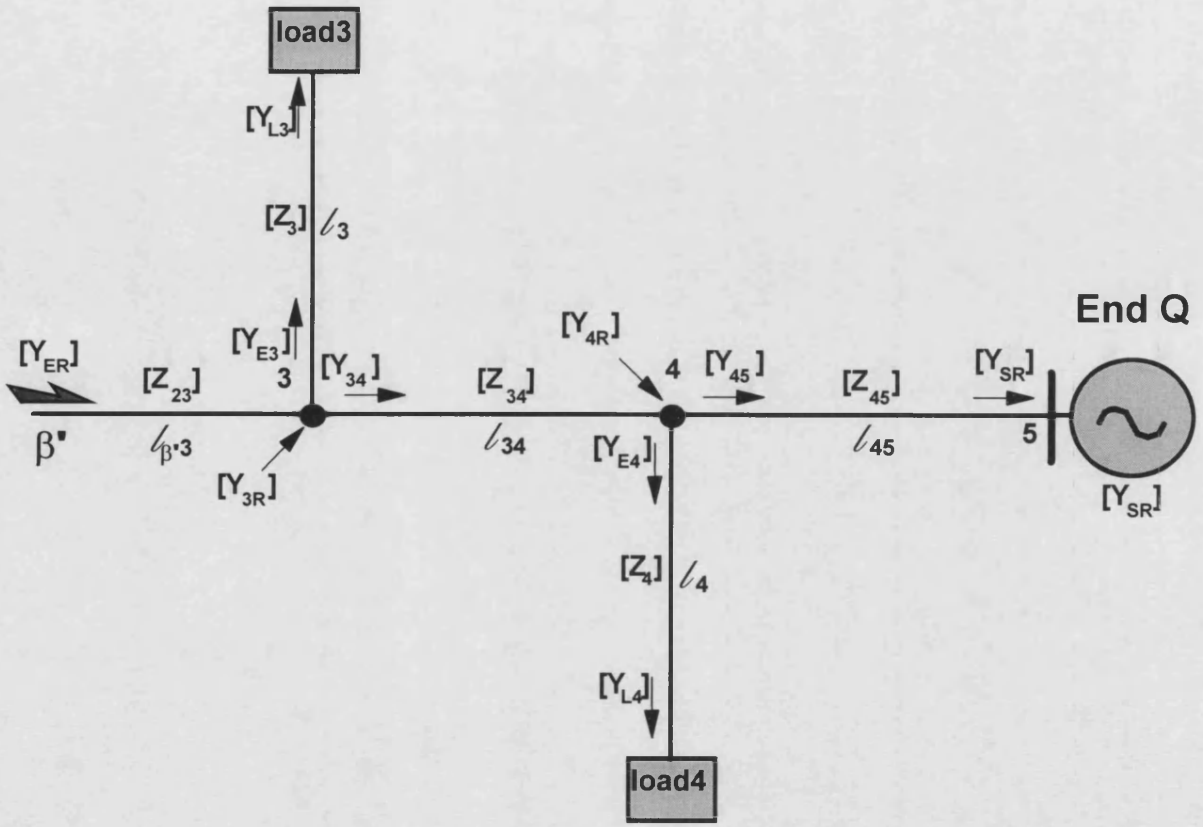

Figure 4.9 Receiving-end side of the distribution system

AUTOMATION OF THE INTERACTIVE PROCESS AND SYSTEM PARAMETERS

5.1 Introduction

This chapter has been divided into two main parts. In the first part, the automation of the interactive process for the purposes of deducing the fault position on the distribution system is described in detail. In the second part, the practical assumptions made and variables that are employed such as distance between load taps, length of tap lines, the type and diameter of conductors used, source and load configurations, etc., are explained.

5.2 The Automation Process

In the fault location algorithm, current and voltage samples are continuously monitored at the locator end (end P in Figure 5.1), and upon the inception of a fault, a predefined number of voltage and current samples are captured which contain both pre-fault and post-fault information. As mentioned previously in Chapter 3, in the execution of the fault location program, filtered pre-fault and post-fault voltage and current magnitudes and phase angles are obtained through the employment of DFT filters. Meanwhile the necessary parameters relating to a particular distribution system such as length of the feeder and tap lines, distance between load taps, load and source information etc. are obtained from a database; this data is then used to set up the distribution system model on a computer.

The fault location algorithm developed is an interactive approach and as

mentioned in Chapter 3, at the assumed fault point, fault-path currents are checked to find the minimum values. In order to facilitate and expedite the actual location of a fault, the implementation of the fault location algorithm is fully automated; this involves scanning distribution system at 50 meter intervals, initially assuming a fault position at end P. The assumed fault position is systematically increased towards the end of the system and at every assumed fault point, superimposed fault voltages are evaluated and then back injected to check the fault path currents. This process of course involves re-calculating the impedance matrices on each side of the assumed fault point, every time it changes. The fault path currents obtained for each assumed fault position are then written into an output file for further inspection. This data is then interrogated automatically in order to ascertain the minimum values of the fault path currents; the point at which this occurs is then the actual fault position as predicted by the fault locator algorithm.

The developed fault location algorithm can accurately locate the faults in a distribution system comprising of up to 10 load taps. Of course, it can be modified to cater for a larger number of taps, if necessary. The location of fault in a distribution system with 10 load taps takes approximately 30 seconds to be calculated on a 486 IBM compatible PC.

5.2.1 Three Phase Faults

Figure 5.2 shows typical waveforms for a three phase fault at tap 3 (8.4 km from end P) for the system shown in Figure 5.1(a) with the remote end open. In the fault location process as mentioned in Section 5.2 above, fault path currents are written into an output file for further inspection for all types of fault. Figure 5.3 shows fault path currents generated by the algorithm for a three phase fault occurs at tap 3 on the system shown in Figure 5.1(a). As clearly evident from the figure, all the fault path currents are very high and there is no minimum point at the actual fault position by virtue of all the phases being faulted. As discussed in the previous Section 3.2.2, in the case of three-phase faults, a different algorithm is

activated. Once it has been established, right at the out-set, that all the three phase currents measured at the fault location end have high values, comparable to each other.

5.3 Distribution System Configurations

The algorithm is initially tested on a simple distribution system with remote source as shown in Figure 5.4. At this stage for simplicity no load taps are connected to the main feeder. In the second stage, the technique is tested for a more realistic system with three load taps with and without remote source as shown in Figures 5.5(a) and 5.5(b) respectively. Finally the algorithm is implemented on a typical practical distribution system.

The practical distribution system studied in this work is an overhead system with single phase and three phase loads tapped off at various locations from the main feeder as shown in Figure 5.1(a). Since the studies also relate to remote source infeed, the termination of the remote-end with a substation is taken into account as shown in Figure 5.1(b). For an 11 kV distribution system, the length of the main feeder is 23.9 km with 7 load taps. The technique is also tested on 33 kV distribution systems with no remote source and with remote source as shown in Figure 5.6(a) and Figure 5.6(b) respectively. The length of the main feeder for 33 kV system is 27.5 km with four load taps. For both distribution systems studied, the system frequency is taken as 50 Hz and average earth resistivity is assumed as 100 Ωm.

5.3.1 Overhead Distribution Lines

The overhead distribution lines simulated in this work are based on a single circuit horizontal construction lines currently used on the UK 11 kV distribution system as shown in Figure 5.8(a). In the system studied, hard drawn copper and

aluminum-alloy conductors are simulated with no earth wires. For 33 kV system single circuit vertical construction aluminum-alloy lines with an earth wire are simulated. The line construction is shown in Figure 5.8(b).

5.3.1.1 The Main Feeder

For the 11 kV system, the main feeder comprises of hard drawn copper conductors with a cross diameter of 11.0 mm and impedance of (0.18 + j0.35) ohm/km. With reference to Figure 5.7, the line matrix for an untransposed feeder is:

$$Z_{MAIN} = \begin{bmatrix} Z_{aa} & Z_{ab} & Z_{ac} \\ Z_{ba} & Z_{bb} & Z_{bc} \\ Z_{ca} & Z_{cb} & Z_{cc} \end{bmatrix} \tag{5.1}$$

The series line parameters at power frequency are given by:

$$Z_{MAIN} = \begin{bmatrix} (0.228+j0.763) & (0.048+j0.431) & (0.048+j0.387) \\ (0.048+j0.431) & (0.228+j0.763) & (0.048+j0.431) \\ (0.048+j0.387) & (0.048+j0.431) & (0.228+j0.763) \end{bmatrix} \tag{5.2}$$

For the 33 kV system, the main feeder comprises of aluminum-alloy conductors with a cross diameter of 17.7 mm and impedance of (0.15+j0.38) ohm/km are simulated. For the earth wire, aluminum-alloy conductor with a cross diameter of 14.2 mm and resistance of 0.27 ohm/km is simulated. With reference to Equation 5.1 and Figure 5.7, the series line parameters at power frequency for a equivalent three conductor system in which the effect of earth wire has been taken into account is thus given by:

$$Z_{MAIN} = \begin{bmatrix} (0.220+j0.563) & (0.071+j0.187) & (0.073+j0.224) \\ (0.075+j0.177) & (0.216+j0.575) & (0.075+j0.177) \\ (0.072+j0.224) & (0.071+j0.187) & (0.211+j0.593) \end{bmatrix} \quad (5.3)$$

5.3.1.2 Laterals

For the lines between loads and taps, aluminum-alloy conductors with a cross diameter of 9.9 mm and an impedance of (0.54 + j0.364) ohm/km are simulated. With reference to Figure 5.7 and Equation 5.1 the line matrix for the laterals is:

$$Z_{TAP} = \begin{bmatrix} (0.598+j0.780) & (0.048+j0.431) & (0.048+j0.387) \\ (0.048+j0.431) & (0.598+j0.780) & (0.048+j0.431) \\ (0.048+j0.387) & (0.048+j0.431) & (0.598+j0.780) \end{bmatrix} \quad (5.4)$$

5.3.2 Loads

In the distribution system studied, primary sides of the three phase transformers are assumed as delta connected. However, dynamic loads such as three phase induction motors are assumed as star connected.

5.3.2.1 Static Loads

The static loads are considered as series R-L with a typical power factor assumed to be 0.9 lagging; the calculation of these loads are explained in some detail in Chapter 4. The diversity factor for all the loads is taken to be 0.5.

5.3.2.2 Dynamic Loads

Many components of power systems respond to disturbances dynamically; i.e., responses to disturbances do not occur instantaneously but require a finite time. Motor loads form a large portion of the total load taps on a distribution system and constitute the major dynamics during certain disturbances. According to tests carried out to investigate the effects of large voltage variations such as those that occur during the system faults, transients that last from three to six cycles have been observed in the load response to rapid voltage changes [33]. In general the dynamic response of motors is slow and the transients injected into the system by such dynamic loads during faults can be filtered out through the DFT filters. However, it is still important to establish the effect on accuracy in the presence of such loads.

In this work, dynamic loads have been represented as induction machines since the vast majority of the dynamic load taps are of this nature. The data relating to a typical induction motor used in this work is:

Asynchronous Motor

Nominal working voltage	:	11 kV
Nominal Power	:	1.0 MVA
Type of connection	:	Three phase, star connected
Power factor	:	0.84 lagging

5.3.3 Pole Configurations

In the UK, 11 kV distribution systems comprise of wooden poles. The pole configuration is such that the conductors are located one meter from each other with a height of 12 meters from the ground as shown in Figure 5.8(a). For the 33 kV distribution system, poles with one earth wire are used as shown in Figure 5.8(b).

5.3.4 Source Configuration

The sources are star connected and the neutral point is earthed with a solid conductor or with an impedance as shown in Figures 5.9(a) and 5.9(b) respectively. The data relating to the sources is:

	Source End P for 11 kV System	**Source End P for 33 kV System**
Short circuit level (SCL)	: 58 MVA	250 MVA
Nominal voltage	: 11 kV	33 kV
X/R	: 10	30
Z_{s0}/Z_{s1}	: 0.5	0.5

	Source End Q for 11 kV System	**Source End Q for 33 kV System**
Short circuit level (SCL)	: 10 MVA	10 MVA
Nominal voltage	: 11 kV	33 kV
X/R	: 10	10
Z_{s0}/Z_{s1}	: 1.0	1.0

The source capacity was modelled using a series impedance is given by:

$$Z = |V_L|^2/MVA \tag{5.5}$$

and

$$Z = R + jX \tag{5.6}$$

where

$$X = Z \sin(\tan^{-1}(X{:}R\ ratio)) \tag{5.7}$$

$$R = X/(X{:}R\ ratio) \tag{5.8}$$

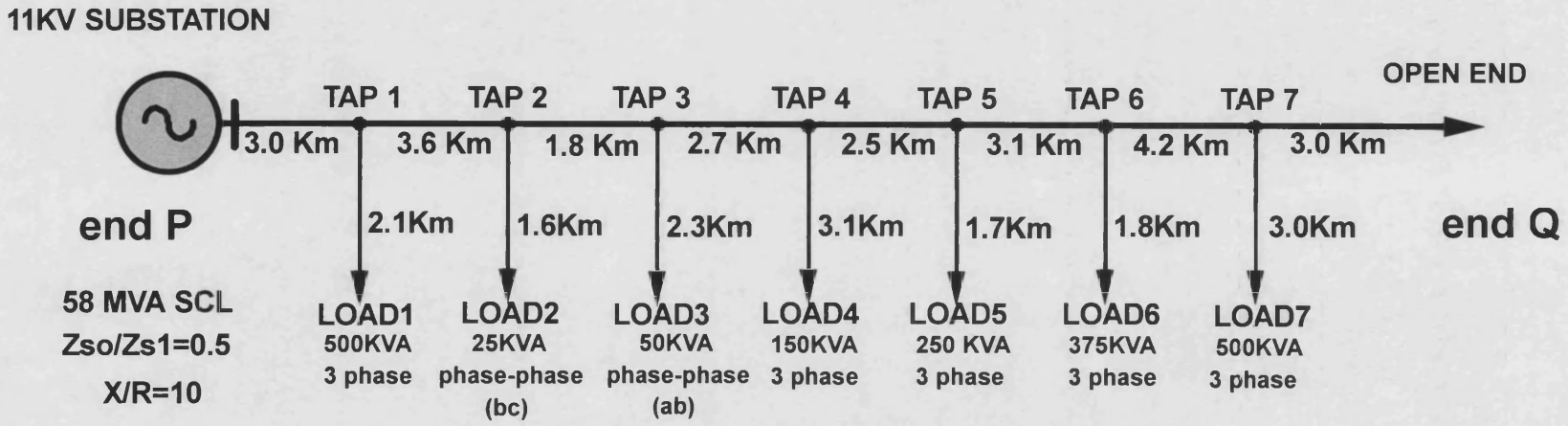

Figure 5.1(a) Typical 11 kV radial distribution system with no remote source.

For all load taps, power factor P_f=0.9 lagging.

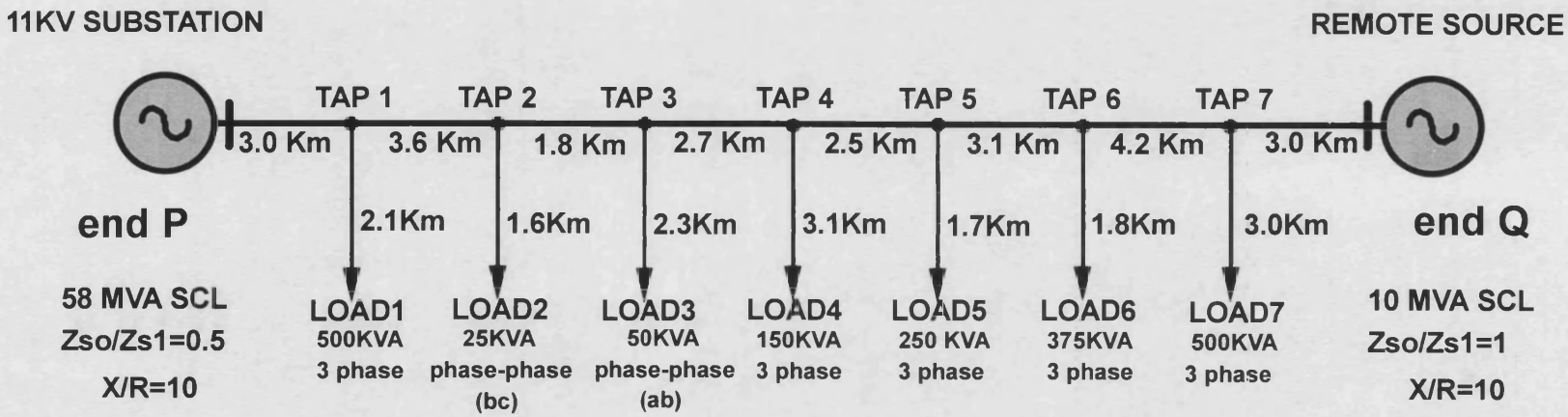

Figure 5.1(b) Typical 11 kV radial distribution system with remote source.

For all load taps, power factor P_f=0.9 lagging.

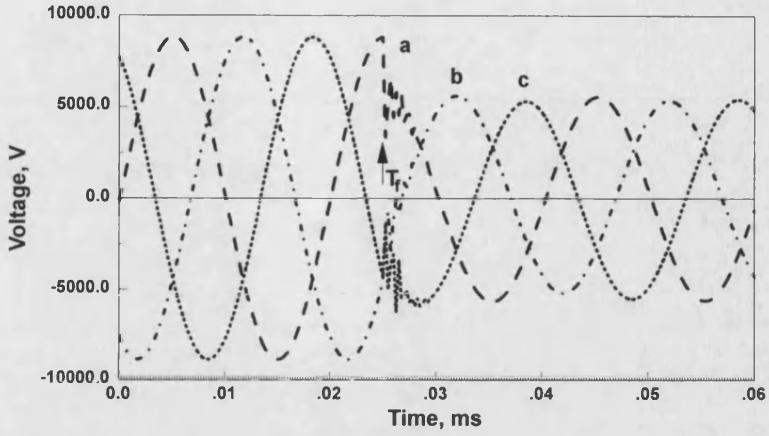

(a)

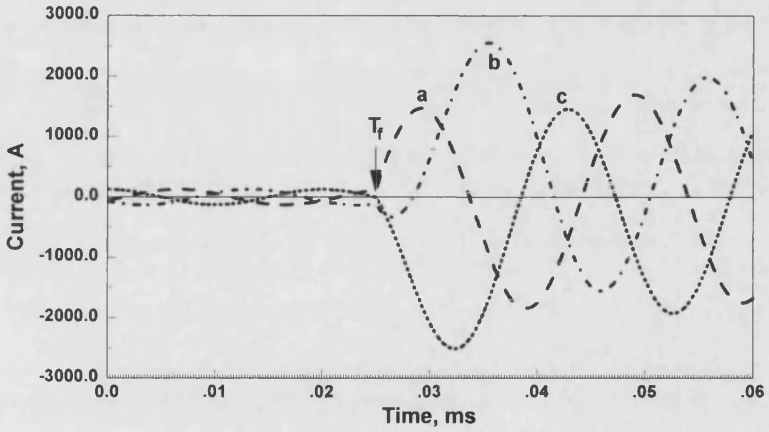

(b)

Figure 5.2 Voltage and current waveforms for a three-phase fault at 8.4 km for the system shown in Figure 5.1(a) (R_f=2 Ω).

(a) Voltage waveforms

(b) Current waveforms

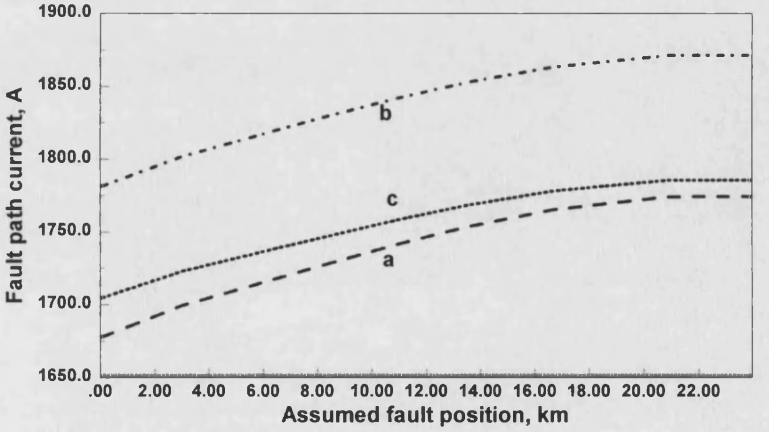

Figure 5.3 Fault path currents for a three-phase fault at 8.4 km from end P for the system shown in Figure 5.1(a) (R_f=2 Ω).

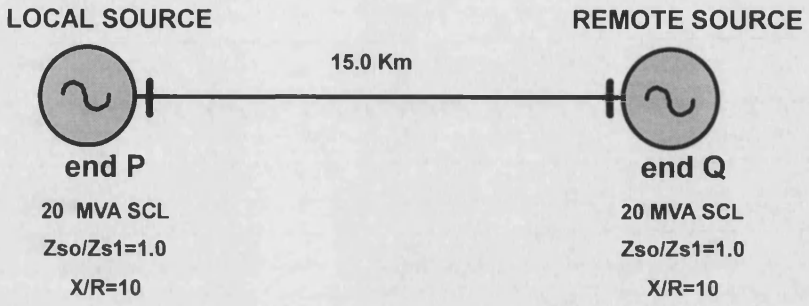

Figure 5.4 Simple distribution system with remote source.

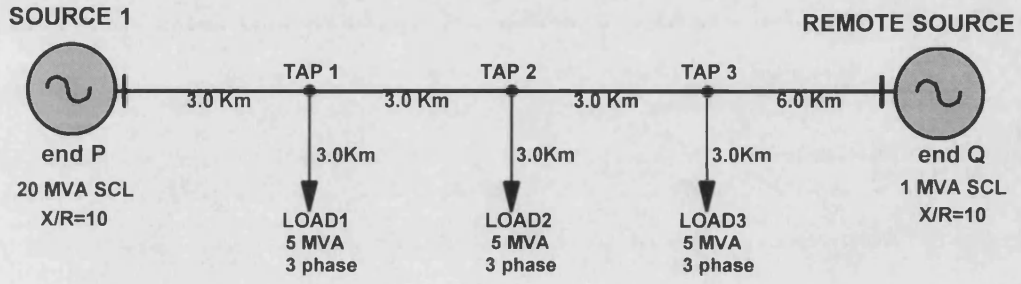

(a)

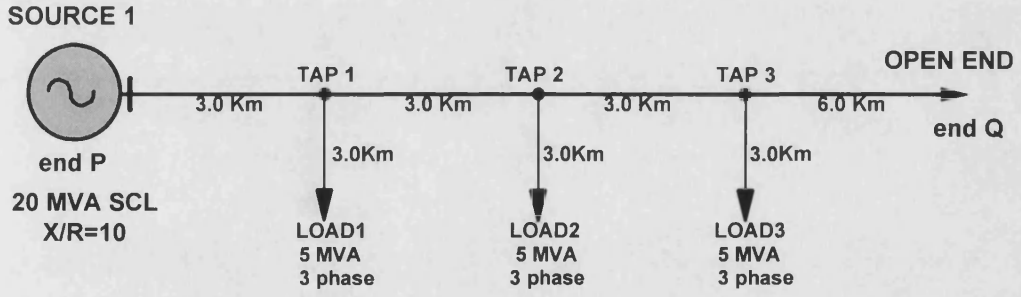

(b)

Figure 5.5 Experimental radial distribution systems studied.

(a) System with load taps and remote source.
(b) System with load taps and no remote source.

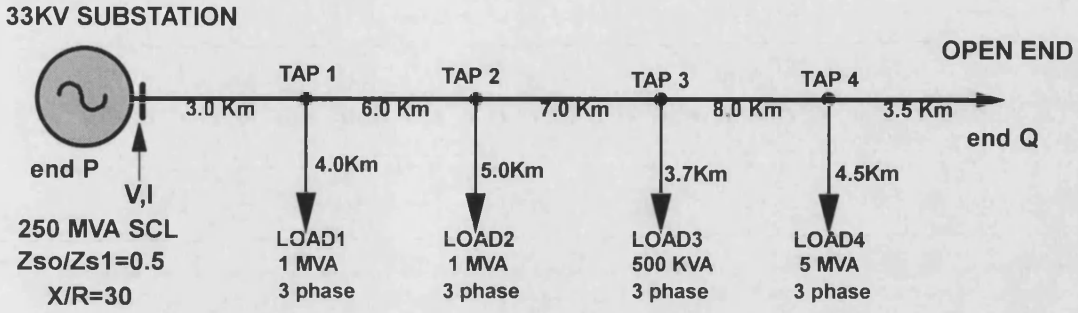

(a)

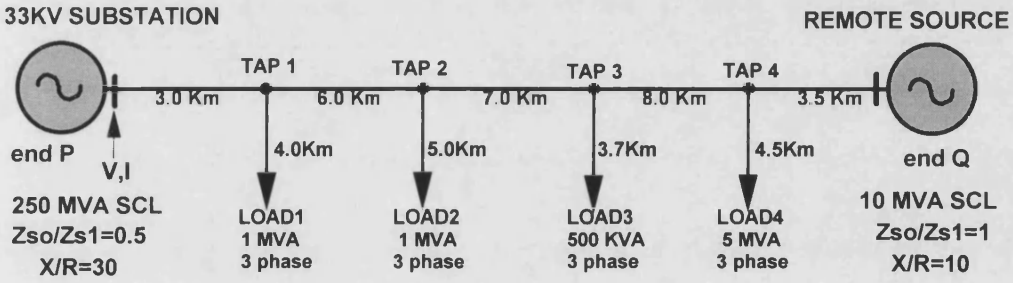

(b)

Figure 5.6 Typical 33 kV radial distribution systems studied.

(a) Distribution system with no remote source.
(b) Distribution system with remote source.
For all load taps, power factor P_f=0.9 lagging.

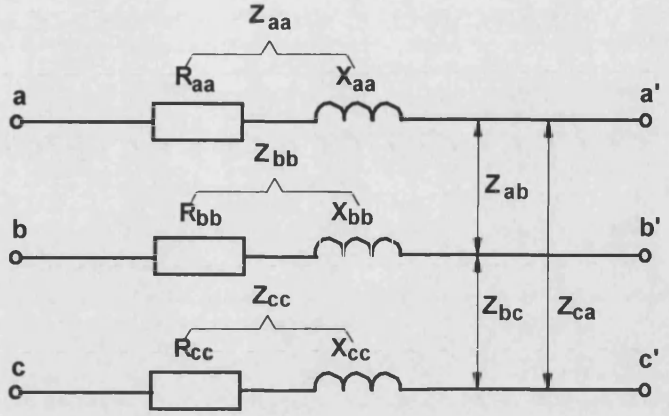

Figure 5.7 Line circuit diagrams

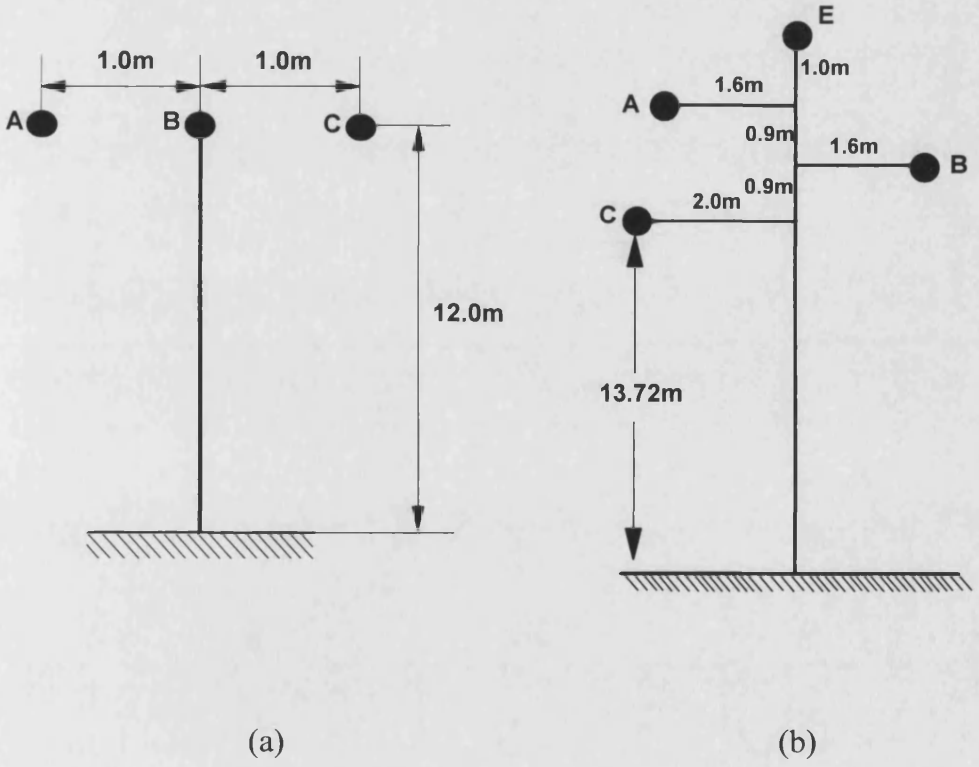

(a) (b)

Figure 5.8 11 kV and 33 kV pole configurations.

(a) 11 kV wooden pole configuration
(b) 33 kV pole configuration

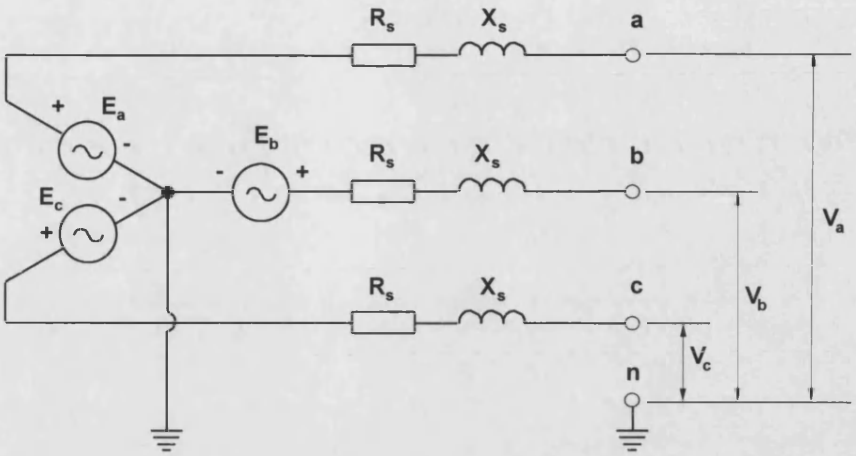

(a)

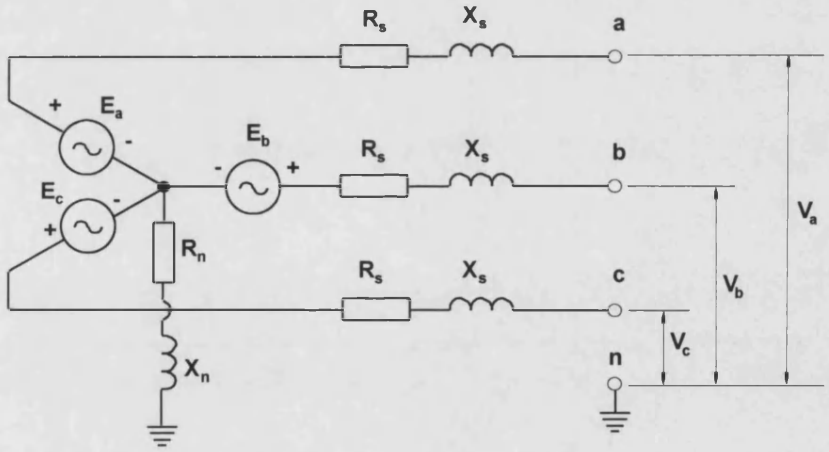

(b)

Figure 5.9 Source connections

(a) Source solidly grounded, $Z_{s0}/Z_{s1}=1.0$.
(b) Source grounded through an impedance, $Z_{so}/Z_{s1}=0.5$.

PERFORMANCE EVALUATION AND SENSITIVITY ANALYSIS

6.1 Introduction

This chapter has been divided into three main parts. The first part is concerned with the testing of the proposed algorithm on experimental distribution systems as shown in Figure 5.4 and 5.5. The second part presents the performance evaluation of the algorithm on a practical system as shown in Figure 5.1. In particular, the effect of fault position, fault type, fault resistance, source capacity etc. on accuracy are examined. In the third part sensitivity analysis of the fault locator algorithm is carried out; here non-algorithmic errors introduced by load and remote source impedance estimations and small variations in line length are investigated.

The ElectroMagnetic Transients Program (EMTP) was used to simulate the primary system faults and to produce discrete-time data for the busbar voltage and current signals.

6.2 Testing of the Fault Location Algorithm

The fault location algorithm developed is initially tested for a distribution system with remote infeed. At this stage the presence of load taps are not taken into consideration. As a second step, presence of load taps and the line sections between loads and tap points at the main line are taken into consideration. It should be mentioned that this procedure is adopted in order to facilitate the development of the technique.

In all the results presented herein, the percentage error relating to fault location is based on:

%Error = [estimated location-actual location]/[length of distribution feeder] × 100

6.2.1 Response of Algorithm on a System With No Load Taps

The technique initially has been tested by using a very simple system terminated with a remote source as shown in Figure 5.4 and the presence of load taps are not taken into account. Figure 6.1(a) shows the changes experienced in the fault path currents in the interactive approach for an actual 'a'-phase-earth fault at 10.0 km. As can be seen whilst the faulted phase superimposed fault path currents are very high at all assumed points the healthy 'b' and 'c' phase superimposed fault path currents pass through a minima at the actual fault point; beyond this point, they increase very rapidly. In marked contrast, the superimposed fault path current in faulted phase is significantly higher and changes very little with respect to the assumed fault position.

The algorithm is also tested for double-phase-earth ('a'-'b'-earth) and phase-phase ('a'-'b') faults and the changes in the superimposed currents in the fault paths for all the phases are illustrated in Figures 6.1(b) and Figure 6.1(c) respectively. As expected, the fault path currents in the healthy 'c' phase attains a minimum value at the actual fault point for both types of fault. It is interesting to note from the diagrams that the superimposed faulted phase fault path currents are highest in double-phase-earth faults followed by phase-phase fault and then single-phase-earth fault. However, the superimposed fault path currents associated with healthy phases (at all points other than the actual fault point) are highest for single-phase-earth faults, followed by double-phase-earth and then phase-phase faults.

Table 6.1 summarises the results obtained for the different types of fault considered, the faults being applied at two different fault points on the line. As

seen from the results for all types of fault and fault positions, a very high accuracy is attained and the error recorded is less than 1% in all cases. This can be largely attributed to the absence of any load taps on the system studied.

6.2.1.1 Effect of Fault Resistance for a Plain System

Figures 6.2(a) and 6.2(b) show the effect of fault resistance on the accuracies attained for the plain distribution system with remote source (shown in Figure 5.4) subjected to an 'a'-phase-earth fault at 10.0 km from end P. Figure 6.2(a) shows the change in superimposed fault path currents for a fault resistance of 100 ohm. As can be seen from the figure the healthy phase fault path currents attain the minimum values at fault points which are slightly different from each other. In this case, the average of the two is taken as the actual fault point. Figure 6.2(b) shows the behaviour of fault path currents for all phases when the fault resistance is increased to 200 Ω. As expected, the magnitudes of the fault path currents for all the phases decrease with the increase in the fault resistance and this is due to the attenuation by the large fault resistance. Moreover, the stagger between two minima relating to the healthy phase fault path currents is increased with the increase in fault resistance. Table 6.2 shows the accuracy attained for different fault resistances for single-phase-earth and double-phase-earth faults. As evident, there is a slight deterioration in accuracy in the case of the former with the increase of fault resistance, this is largely due to computational and quantization errors. In the case of double-phase-earth faults in the presence of higher fault resistance, however, the fault practically becomes a phase-phase fault at high fault resistances and therefore the zero phase sequence component in the fault path current becomes very small; the accuracy is thus is not very much affected of such high fault resistances.

6.2.2 Performance of the Algorithm on a System with Load Taps and Remote Source

To ascertain the effect of load taps on accuracy, the technique is tested on a distribution system with three load taps terminated with a remote source. Figure

6.3(a) shows the change of currents in fault paths for an 'a'-phase-earth fault at 4.5 km from end P for the system shown in Figure 5.5(a) As seen the currents in the healthy 'b' and 'c' phases attain the minimum values around 4.5 km while the faulted 'a'-phase fault path current remains high and changes little with a change of the assumed fault location. The effect of load taps can also be observed in the superimposed fault path currents associated with the healthy phases, in that a discontinuity in terms of a change in the slope of the currents occurs every time a load tap is surpassed and this is a direct consequence of presence of load tap admittance. The changes observed in fault path currents for 'a'-'b'-phase fault and 'a'-'b'-phase-earth faults are also shown in Figures 6.3(b) and 6.3(c). Again for these faults, similar performance is obtained in that the superimposed fault path currents associated with the healthy 'c' phase attains the minimum value at the actual fault position while 'a' and 'b' faulted phase fault path currents are very high at all times and change little with a change in the assumed fault position.

Table 6.3 gives a summary of the results for different fault types and locations for the system shown in Figure 5.5(a). As seen from the results, the error in fault location is increased slightly in comparison with the results given in Table 6.1 for a system with no load taps; this would be somewhat expected, but unlike conventional techniques this increase is only very marginal and this clearly illustrates the robustness of the algorithm developed herein.

6.2.2.1 Effect of Fault Resistance in the Presence of Load Taps

Effect of fault resistance has been tested in the presence of load taps and remote infeed. Figure 6.4(a) shows the change in fault path currents for an 'a'-phase-earth solid fault at 7.5 km from end P for the system shown in Figure 5.5(a). The same fault was repeated in the presence of 100 Ω fault resistance and the change in fault path currents are shown in Figure 6.4(b). It is clearly evident from both figures that despite a significant reduction in the fault path currents, the points at which the minima occur are close with each other in the two cases.

6.2.2.2 Performance of the Algorithm on a Open Ended System with Loads

The effect of load taps is also tested for an open ended system with three load taps as shown in Figure 5.5(b). The change of fault path currents for an 'a'-phase-earth fault at 4.5 km is depicted in Figure 6.5(a). As can be seen the currents in the healthy 'b' and 'c' phases attain minimum values at the actual fault point and once this point has been surpassed, the fault path currents in the healthy phases increase until the load tap 3. Beyond this point, the superimposed fault path currents for all the phases attain constant values and virtually remain unchanged. This can be attributed to the fact that since there is no remote source and the charging currents in a low voltage distribution system are very low, after load tap 3, the superimposed fault path current I_R' (as described in Section 3.2.1) that is fed into fault from end Q is almost zero. In this case, the superimposed fault path current I_f' is equal to the superimposed fault path current I_S' that is fed into the fault from end P and does not change with the change of assumed fault point beyond load tap 3. Figures 6.5(b) and 6.5(c) show the change of superimposed fault path currents for 'a'-'b'-phase and 'a'-'b'-phase-earth fault respectively, and similar performance is observed for the healthy 'c'-phase superimposed fault path current. Table 6.4 shows the effect of remote source on the accuracies attained for the experimental system shown in Figure 5.5(b). Results clearly show that there is small degradation in accuracy. This is due to fact the I_R' currents fed into the fault is lower. This leads to a lower I_f' current at the assumed fault point.

6.3 Performance Evaluation for Practical Distribution Systems

This section presents the performance evaluation of the fault locator algorithm under different fault conditions, for faults on typical 11 kV and 33 kV overhead distribution systems commonly found in the UK. Details of the line configuration

and the parameters that used are given in Chapter 5.

The results presented relate to distribution systems comprising of a number of load taps with differing loads, both with and without any remote infeed as shown in Figures 5.1 and 5.6 respectively. It should be noted that unlike the assumption made in the explanation of the basic principle of the technique, the tap line impedance for the practical system considered here is different from that of the main feeder and this has been taken into account when setting up the model of the distribution system.

6.3.1 Effect of Fault Type and Location

Figure 6.6 typifies the variations in the healthy-phases and the faulted phase currents in the fault paths for an 'a'-phase-earth fault, 'a'-'b'-phase-earth fault and 'a'-'b'-phase fault respectively at different locations for the radial feeder shown in Figure 5.1(a). First of all considering 'a'-phase-earth fault close to the source end i.e., between taps 1 and 2 , as expected, an incorrect fault position manifests itself into giving rise to currents in the fault paths of the two healthy phases; there is however, a fault point at which these currents are at a minima, as shown in Figure 6.6(a). It is apparent from the foregoing theory presented that the point on the line at which this minima occurs is the actual location of the fault. In this respect, it should be noted that at the minima, the healthy phase fault path currents should ideally be zero. However, in practice this is not always the case because of the presence of small algorithmic and/or non-algorithmic errors. As would be expected, the behaviour of the faulted-phase fault-path current is distinctly different from those associated with the healthy phases; its magnitude is much larger and varies relatively little irrespective of whether the fault is at the correct point. Similar behaviour of the fault-path currents can be observed for a fault close to the remote end, i.e. at load tap 6. As shown by Figure 6.6(b), the main difference between the two fault positions is that in the case of the latter, the increase in the levels of the incorrect fault path currents associated with the

healthy phases, particularly after the minima has been surpassed, is significantly less than in the case of the former. This is somewhat expected by virtue of the fact that as the fault moves closer to the open end, the infeed into the *pseudo* fault paths created by the incorrect fault positions, becomes progressively smaller. With regard to the faulted 'a'-phase fault-path current, like in the previous case, it more or less stays constant at a high level at all assumed fault positions.

The algorithm has been tested for 'a'-'b'-phase-earth and 'a'-'b'-phase faults at the same locations and the variations in the healthy phase ('c') and the faulted ('a' and 'b') phases are shown in Figures 6.6(c) to 6.6(f). As shown from the diagrams, similar performance to that for single-phase-earth fault is obtained for these faults; the main difference is in the magnitudes of the currents, in particular the faulted phase fault path currents. As expected, these are highest for double-phase-earth faults, followed by phase-phase faults which in turn are significantly larger than the single-phase-earth-fault.

Table 6.5 gives a summary of the performance achieved for different fault types at different fault positions for the system shown in Figure 5.1(a). It is apparent that as the fault moves closer to the open end, there is a small degradation in the performance attained. This can be attributed to the fact that for faults closer to the end of the system due to higher line impedance in the fault path, faulted phase fault path currents are relatively smaller and this leads to lower superimposed currents fed into the fault from end P. Moreover, the impedance seen at the fault point towards the end Q is higher due to a relatively lower number of load taps with lower capacities; in this case, the superimposed currents fed into the fault from end Q are relatively less. Under these circumstances, the superimposed fault path current which is a total of superimposed currents fed from end P and Q becomes small. The net result is that the levels of the fault-path currents associated with the healthy phases become quite small at the incorrect fault points, in particular after the minima has been surpassed. This leads to more quantization and computational errors for faults near end Q for an open end system.

When comparing the accuracies for different types of fault, it is evident that for the two fault positions considered, those obtained for double-phase-earth and phase-phase faults are slightly less than those for the corresponding single-phase-earth faults. It is apparent from Figure 6.6(a) to 6.6(f) that although the faulted phase superimposed fault path currents are higher for double-phase-earth and phase-phase faults, the magnitudes of superimposed pseudo fault path currents associated with healthy phases are the highest in single-phase-earth faults followed by double-phase-earth and phase-phase faults. This results in less quantization and computational errors in the case of single-phase-earth faults.

It is important to note that the fault location algorithm presented herein does not require any prior knowledge of the actual phase(s) involved in a fault since the technique is not based on fault classification.

6.3.2 Effect of Remote Infeed Source

Although hitherto the majority of distribution systems comprise of feeders with remote ends open, with the deregulation of the Electricity Supply Industry, more and more private generators are being connected into the system and this trend is likely to continue; a direct of consequence of this is an increase in the complexity of distribution systems and more importantly for such systems, any fault will also have remote infeed. It is well known that a remote infeed can adversely affect the accuracy of conventional fault locators. The performance of the technique described herein was examined for faults on the distribution system shown in Figure 5.1(b) and the results are summarised in Table 6.6. In comparison to the results attained for the radial feeder system shown in Figure 5.1(a), it is evident that the presence of a remote infeed has only a slight effect on accuracy. In fact the accuracy attained in the case of the latter interestingly shows a slight improvement over the former; this can be directly attributed to the fact that with a remote infeed, the currents arising in the *pseudo* fault paths (associated with the healthy phases) due to the location being incorrect, are relatively large in

comparison to those generated by the algorithm in the case of the open-ended system, particularly after the minima has been surpassed; this in turn enhances the performance of the fault locator in its ability to discern between the actual and assumed fault positions with greater accuracy. and this phenomenon is clearly evident from a comparison of Figures 6.6(b) and 6.7(a). These correspond to identical faults ('a'-phase-earth at 16.7 km from end P) on the two systems shown in Figure 5.1(a) and 5.1(b).

It is clearly evident from a comparison of Figures 6.6(b) and 6.7(a) that in the presence of remote source, the currents in pseudo fault paths (associated with the healthy phases) due to incorrect location is relatively large. As expected at the actual fault point, healthy phase fault path currents go to near zero values and subsequently after the fault point, they increase very rapidly. This leads to a very sharp change in the healthy phase currents at the actual fault point and therefore results in better accuracy for fault location, than is the case for a system with no remote infeed.

The effect of remote source was also tested for 'a'-'b'-phase-earth and 'a'-'b'-phase faults as shown in Figure 6.7(b) and 6.7(c) respectively. As shown from the figures, and Table 6.6, similar performance is achieved for these types of fault.

6.3.3 Effect of Fault Resistance

It is vitally important to ascertain if the fault location estimation is significantly influenced by changes in fault resistance. A series of tests were thus carried out with the proposed fault locator algorithm to examine its sensitivity to different fault resistances. The tests were carried out by varying the fault resistance from 1 to 200 Ω for both single-phase-earth and double-phase-earth faults. The effect of fault resistance is not studied for phase-phase faults because in practice the fault resistance for such type of faults rarely exceeds about 1 Ω.

Figure 6.8(a) to 6.8(d) shows the effect of fault resistance on the accuracies attained for the distribution system with no remote infeed (shown in Figure 5.1(a)) when subjected to an 'a'-phase-earth fault. It is evident that with an increase of fault resistance, the fault path currents get attenuated and the change in the healthy phase fault path currents at the actual fault point gets less discrete as a consequence. The same studies were performed for the distribution system with remote infeed (shown in Figure 5.1(b)) and the variations in fault path currents associated with healthy phases ('b' and 'c') and faulted phase ('a') are given in Figure 6.9(a) to 6.9(d) respectively. As seen for higher fault resistances, despite the fact that the currents in fault paths decrease with an increase in fault resistance, at the actual fault point the change in healthy phase fault path currents is still much sharper in comparison with the open ended system. Like in the previous case, this again leads to better accuracy in the presence of fault resistance in comparison with the open-ended system.

Tables 6.7 and 6.8 show the effect of fault resistance on the accuracies attained for the distribution systems shown in Figure 5.1 subjected to 'a'-phase-earth and 'a'-'b'-phase-earth faults respectively; Figure 6.10 depicts the effect on accuracy as the fault resistance is varied for a fixed fault position (in this case at 11.1 km) from end P. It is clearly evident from tables and Figure 6.10 that the fault locator gives an inherently accurate evaluation of fault position that is largely independent of the fault resistance. For double phase-earth faults, particularly in the presence of high fault resistance, the fault effectively becomes similar to a phase-phase fault and as seen from the table, after a certain value of the fault resistance, the percentage error does not change. In the case of single-phase-earth faults, however, there is a small degradation in performance especially when the fault resistance goes above about 100 Ω for open end systems. This can directly attributed to the fact in the presence of fault resistance, for all phases I_S' (as described in Section 3.2.1) that is fed into the fault from end P decreases; the superimposed voltage V_f' at the actual fault point decreases with an increase in fault resistance; this results in a lower I_R' that is fed into the fault from end Q

for all phases. Finally, the I_f' which is the total of superimposed currents fed into the fault at the assumed fault point decreases and in this case the effect of computational and quantization errors are accentuated.

In the case of systems with remote source, due to the presence of remote source impedance, the overall impedance seen at the fault point towards the end Q is significantly lower in comparison with open end systems. Hence the superimposed currents fed into the fault from end Q are higher for all phases. This leads to higher fault path currents in the presence of fault resistance for the systems with remote source.

It can be concluded from the foregoing results presented that the overall performance attained is significantly superior to that achieved with conventional techniques, particularly those based on impedance to fault measurements, which give rise to unacceptably large errors in the presence of fault resistance [31].

6.3.4 Effect of Source Capacity

Although the actual fault location algorithm is independent of source capacity at the end P, it is important to ascertain if the location estimation is significantly influenced by changes in source capacity. Which in practice can have an inherent effect on the level of unbalance in the system.

Figure 6.11 shows the fault path currents attained when the source capacity at end P is varied from a large value to a very small value for the system shown in Figure 5.1(a). Figure 6.11(a) shows the fault path currents for an 'a'-phase-earth fault at 11.1 km from end P when the source at that end was replaced with a much higher source of 250 MVA source; Figure 6.11(b) shows the corresponding fault path currents when the source was replaced with a lower capacity (10 MVA) source. In the case of latter, the fault path currents both in the healthy phases and faulted phase are lower in comparison to the former. As a direct consequence there is a slight decrease in the accuracy achieved due to the effect

of quantisation errors on the fault location algorithm increasing.

Table 6.9 summarises the effect of source capacity on the accuracies attained for the distribution system shown in Figure 5.1(a) for different source capacities. As mentioned above, although there is a slight deterioration in performance at lower source capacities, it can be clearly seen that for the fault considered ('a'-phase-earth fault 11.1 km from end P), the performance of the fault locator is largely immune to changes in the local source capacity, in this case at end P. This also is a major advantage particularly since source capacities constantly change according to the prevailing load conditions.

Figure 6.12 depicts the effect on accuracy when the source capacity at end P is varied from 0.25 MVA up to 60 MVA for two fault positions (in this case at 11.1 km and 16.7 km) for the system shown in Figure 5.1(b) under various types of fault. As can be seen, the accuracy is interestingly lower for faults close to end P when the source capacity at end P is decreased to 0.25 MVA. This is due to fact the I_S' (as described in Section 3.2.1) current fed into the fault from end P is significantly reduced in the presence of very weak source termination at end P. For the faults occur at 16.7 km, the accuracy is significantly higher; this is because the I_R' current that feeds into the fault from end Q is very high due to a relatively short fault path while the I_S' current fed into the fault from end P is much lower. Since the I_f' is the total of I_S' and I_R' currents, the resultant superimposed fault path current I_f' at the actual fault will be high and less affected from computational and quantization errors. When the source capacity at the end P is increased, the accuracy for all types of fault is increased significantly, as apparent from Figure 6.12.

Figure 6.13 shows the effect of remote source capacity on accuracy for two fault positions for the system shown in Figure 5.1(b). The source capacity at end Q is varied from 0.25 MVA up to 10 MVA and various types of faults are created at 11.1 km and 16.7 km respectively. As seen from the figures, in the case of faults

at 16.7 km, the error is higher when remote source capacity is very low. This is due to fact that the I_R' current fed into the fault from end Q is very low due to a much lower source capacity termination and the I_S' current that is fed into the fault from end P is also low due to a relatively longer fault path. Thus the I_f' current which is the total of two will be relatively low and subject to increased computational and quantization errors. When the source capacity at the remote end is increased, the accuracy for both fault positions is increased significantly. This can be directly attributed to the fact that with an increase in remote source capacity, especially for the faults closer to end Q, the I_R' current that is fed into the fault from end Q increases substantially.

In summary it is evident from the foregoing results that the accuracy is higher in the presence of remote source capacity than for the systems with remote end open, and this accuracy is increases as the remote source capacity goes up. Furthermore, in the case of the latter, the accuracy attained is significantly higher for faults occurring near the remote source.

6.3.5 Effect of Dynamic Load

The results presented so far relate to static load taps. However, in practice there can also be present dynamic load taps and it is thus important to establish the effect on accuracy in the presence of such loads. The dynamic load is a three phase 1.0 MVA star connected squirrel cage induction motor with four poles and is simulated within the EMTP. The motor has 2.5% slip and 85% efficiency at 0.84 lagging power factor. In the simulation, mechanical losses are taken into account. The mechanical part is converted into an equivalent electric network with lumped R,L,C which is then treated by the EMTP as if it were part of the overall electric network. The electromagnetic torque of the universal machine appears as a current source injection into the equivalent electric network. Figures 6.14(a) and 6.14(b) show the behaviour of the fault-path currents in the healthy phases ('b' and 'c') when an 'a'-phase-earth fault occurs (at 8.4 km and 13.6 km from end P

respectively) on the system shown in Figure 5.5(a), in which load tap 7 has been replaced by a dynamic load. As shown in figures the healthy phase fault path currents attain the minimum values around the actual fault point and increase quite sharply thereafter. Table 6.10 shows the effect of dynamic load on the accuracies attained for various types of faults. It is apparent that for the two different fault positions considered, i.e. faults near taps 3 (8.4 km from end P) and 5 (12.35 km from end P), the fault locator gives a high accuracy for 'a'-phase-earth faults corresponding to errors of 0.62% and 1.05% respectively. This corresponds to an additional increase in error of 0.42% and 0.15% respectively, when the results are compared with Table 6.5 which applies to the same system with static loads The accuracy of fault location algorithm was also tested in the presence of two and three dynamic loads. The performance attained was little different from that achieved with the one dynamic load.

As seen from the Table 6.10 in the case of double-line-earth faults and line to line faults, accuracy is again slightly degraded. The results summarised in the table clearly demonstrate that the technique described herein is little affected by the presence of dynamic load taps on the system.

6.3.6 Effect of Fault Cycle

In the fault location algorithm, the DFT technique ignores the first cycle of post-fault data since the transients are most prominent during this period. However, there can be situations particularly under high speed fault clearance when only the first cycle of fault information is available to the fault location and it is no longer possible to ignore the first cycle of fault information; all the post-fault information must be taken into account. It is thus important to ascertain the affect on performance of the algorithm for such cases.

A comparison of accuracies attained between utilising the first and second cycle of data following a fault for various types of fault is investigated and the results

are summarised in Table 6.11. It shows the accuracies attained for different types of fault for the system illustrated in Figure 5.1(a). The results clearly show that for single-phase-earth and double-phase-earth faults, the accuracy is not significantly affected. In the case of phase-phase faults, however, the accuracy is slightly decreased when the first cycle of information is utilised. This can be attributed to the fact that when the first cycle of fault information is used there is still some DC off-set and distortion present both in voltage and current waveforms as evident from Figure 6.16; this effectively means that the extraction of the fundamental phasors via the DFT filter causes some errors. It is evident from figures 6.6(a) to 6.6(f) that the *pseudo* fault path currents associated with healthy phases produced by the algorithm are lowest for phase-phase faults for the same location. In this case phase-phase faults are more affected from slight distortions in waveforms in comparison with other fault types.

6.3.7 Three Phase Faults

As mentioned in Section 3.2.1, the fault location algorithm presented here is based on utilizing information from the healthy phases and therefore cannot locate three phase faults since no healthy phase is present during such type of fault. Hence, in order to locate the three-phase faults a separate algorithm (as described in Section 5.2.1) has been developed. To test this algorithm, three-phase faults are created at various points on the distribution system shown in Figure 5.1(a) and the results are summarised in Table 6.12. As seen from the results, satisfactory performance in terms of accuracy is attained in fault location for three-phase faults. This is the case for a majority of faults on the line except for a small section towards the end of the line where the accuracy is slightly degraded. This can be directly attributed to the fact that, although load impedances are much higher in comparison with the fault resistance, for faults towards end of the system, the total load impedance begins to have some influence on accuracy. Nonetheless as evident from the table, even for a three-phase fault right at the end of the distribution system (as shown in Figure 5.1(a) which is 23.9 km long) the alternative algorithm indicates a

location at 23.1 km; this corresponds to 3.2% estimation error which is still within the acceptable limits.

6.3.8 Effect of Capacitor Bank

It is a well-known fact that shunt power capacitors are the most economical source to meet the reactive power requirements of inductive loads and power distribution lines operating at a lagging power factor. When reactive power is provided by only substations, each system component (i.e., transformers, distribution lines, switchgear, and protective equipment) has to be increased in size accordingly. Capacitors can minimise these requirements by decreasing the reactive power demand all the way, back to substations. As a result, losses and loadings are reduced in distribution lines and substation transformers. Furthermore, the current reduction in transformers, distribution equipments and lines reduces the load and consequently delays the need for new installation of new facilities. In general, the economic benefits force capacitor banks to be installed on the primary distribution system rather than on the secondary. Hence it is essential to investigate the effects of capacitor banks on the fault location algorithm.

To test the effects of a capacitive load, load tap 4 in the system shown in Figure 5.1(a) was replaced with a delta connected capacitor bank with a capacity of 250 kvar and the results are presented in Table 6.13. The results clearly show that algorithm is virtually immune to the presence of a capacitive load.

6.3.9 Effect of DFT Filter and Fault Inception Time

The majority of results presented hitherto, relate to faults at an instant corresponding to maximum voltage for the faulty phase or phases. In practice faults can occur at any point on wave i.e. the fault inception angle cannot be defined in advance. It is thus important to ascertain the algorithm's performance for faults at inception angles other than those near voltage maximum. This section analyses the effect of the fault inception angle on the accuracies attained. Tests

were performed on the distribution system shown in Figure 5.1(a) for different inception angles ranging from 0^0 to 180^0, in steps of 45^0. Figure 6.15 typifies the primary system fault voltage and current waveforms obtained at the fault locator end (end P) for 'a'-phase-earth, 'a'-'b'-phase-earth and 'a'-'b'-phase faults that occurred at tap 3 (8.4 km from end P) on the distribution system shown in Figure 5.1(a) with the remote end open. As seen from waveforms both high frequency distortion and DC offset are apparent. Figure 6.16(a) typifies the response of the DFT filter when both digitised voltage and current waveforms for an 'a'-phase-earth fault near voltage zero are inputted into it. As would be expected, there is little high frequency distortion on the input waveforms but the DC offset particularly on the current waveform is quite significant. It is apparent from the output waveforms that the DFT is not very effective in rejecting the DC offset during the first cycle of fault information but gives an accurate indication of the fundamental components subsequently. In the case of a fault near voltage maximum, the severe attenuation of the high frequency components on the digitised waveforms, particularly on the voltage waveform, by the transducers/antialising filters, etc. is clearly evident from Figure 6.16(b). However, unlike the previous fault case, there is little DC offset on the current waveforms and hence the error in the extraction of the fundamental components even in the first cycle of fault information is significantly less than that obtained for a voltage zero fault. Whilst this error manifests itself into causing significant errors in accuracy in fault location when employing conventional techniques, particularly those based on impedance measuring principles, It is apparent from the results presented in Table 6.14 (these are for various faults and inception angles at a distance 9.75 km from end P) that the algorithm maintains a high degree of accuracy which is virtually independent of fault inception angle.

6.3.10 Effect of Different Line Impedance

As explained in Chapter 1, in radial distribution systems, the current magnitude is the highest near the substation and decreases towards the end of system. With

a decrease in current magnitude, the size of the conductor is also reduced, by many distribution authorities principally to cut the costs down. It is thus vitally important to ascertain that the algorithm is not significantly affected when a particular line comprises of a number of conductors of different sizes i.e. the line is non-homogenous. Tests were therefore carried on the system shown in Figure 5.1 but with the line section between load tap 2 and load tap 4 replaced with a conductor of impedance (0.25+j0.38) ohm/km and the section after the load tap 4 of the main feeder was replaced with a conductor having an impedance of (0.36+j0.38) ohm/km; these are compared to the original studies based on a homogenous feeder comprising of a single conductor impedance. For non-homogenous applications, the algorithm is supplied with the differing conductor impedance for each section.

Table 6.15 summarises the results for different types of fault and fault positions for the system shown in Figure 5.1(a). As can be seen, the accuracy is slightly reduced in comparison with the results presented in Table 6.5 which shows the performance for the same system but with a homogenous main feeder impedance. This can be attributed to the fact that since after the load tap 2 the impedance of the main feeder is gradually increased, for the faults beyond that tap, lower levels of fault currents are obtained. This inevitably leads to higher quantization and computational errors.

The same system was also tested with a remote source connected i.e., faults were applied on the system shown in Figure 5.1(b) but with sections of line replaced by different conductors as stated above; the results are summarised in Table 6.16 for different fault types and fault positions. As evident from the results, the accuracy attained is significantly higher in comparison with the open ended systems (Table 6.15) but the accuracy is still lower than when compared with the equivalent system in which line impedance is the same throughout the main feeder (see Table 6.6); the error is increased by about 0.4% for single-phase-earth faults, 0.7% for phase-phase faults and 1.9% for double-phase-earth faults at 16.7 km

from end P.

In conclusion, it can be said that the performance of the algorithm is not too adversely affected when applied to a non-homogeneous line.

6.3.10.1 Effect of Fault Resistance for a System with Different Line Sections

The effect of fault resistance was also tested on the aforementioned distribution system with different line sections i.e., that shown in Figure 5.1(a) but modified to accommodate line sections of different conductor sizes. Table 6.17 summarises the results obtained for both 'a'-phase-earth and 'a'-'b'-phase-earth faults at 11.1 km from end P. As can be seen from the results, the fault locator gives an inherently high accuracy in the presence of fault resistance for such a non-homogenous system. However, there is a small decrease in accuracy for single-phase earth faults (in comparison to the previously studied homogenous system (see Table 6.7)) especially when the fault resistance exceeds 100 Ω. In the case of double-phase-earth faults, the accuracy is increased slightly with an increase of fault resistance.

6.3.11 Faults on Laterals

In the fault location technique described herein; although the presence of load taps is taken into account, in the fault location process only the main feeder is scanned to locate the faults. It is thus important to investigate the effect on accuracy of faults at load taps and load lines. Various faults were created at load terminals and on lines between taps and main feeder. Table 6.18 shows the effect on accuracies of various such faults. For an 'a'-phase-earth fault that is created right at load 1, the algorithm shows the fault between load tap 1 and load tap 2 i.e., at 4.45 km from end P as compared to it being actually at 3 km. When the same

fault is repeated at 1 km on branch line 1, again the algorithm shows it between load tap 1 and load tap 2 this time at 3.6 km from end P. This clearly shows the effect of branch line reactances on fault location. For faults that occur close to main feeder can be localized to the nearest tap. Likewise, for an 'a'-phase-earth fault created at load 6, again the algorithm shows the location between load tap 6 and load tap 7 i.e., at 19.4 km from end P instead of the actual location at 16.7 km from end P. It is thus apparent from the foregoing that the algorithm has some difficulty in accurately discerning faults occurring at or on the spurs themselves. However, for such faults, it is able to localise the fault between the two nearest taps thereby significantly narrowing the region that needs to be scanned manually in order to pinpoint the location of the fault.

6.3.12 Implementation and Testing of the Algorithm on a 33 kV Distribution System

Although the algorithm has been extensively tested for 11 kV distribution system, it can be equally implemented for various distribution levels such as 6.6 kV, 22 kV, 33 kV and 66 kV. In order to show the flexibility and robustness of the algorithm, it was also tested for a 33 kV system with four load taps and with remote source as shown in Figure 5.6.

6.3.12.1 Implementation of Algorithm on a 33 kV Distribution System With no Remote Source

The algorithm was tested for the system with four load taps and no remote source as shown in Figure 5.6(a) and various faults were created at different positions. Figure 6.17 shows the changes in the superimposed fault path currents for various types of fault at 16 km from end P on system which is 27.5 km long. As can be seen, the superimposed fault path currents associated with healthy phases attain the minimum values around the actual fault point. However, in the case of 'a'-

phase-earth fault the superimposed fault path currents associated with the healthy phases attain the minimum values at slightly different positions. This can be attributed to the fact that the capacitive effects (which have not been taken into consideration within the algorithm) become more prominent as the voltage levels go up and thereby the levels of shunt-path currents increase; these in turn have some bearing on the accuracy. Table 6.19 summarises the performance of the algorithm for different fault positions. As seen from the results, the algorithm maintains its high accuracy for the 33 kV system. In fact the accuracies attained are relatively higher in comparison with the 11 kV system with no remote source (see Table 6.5). This can be attributed to the fact that in the 33 kV system, the loads and substation capacities are considerably higher. The net effect is that for faults particularly towards the end of system, higher superimposed currents are obtained and these in turn mitigate the effects of quantization and computational errors.

6.3.12.2 Testing of the Algorithm on a 33 kV System With Remote Source Infeed

Figures 6.18(a) to 6.18(c) show the change of superimposed fault path currents for different types of fault and fault positions for a 33 kV system with four load taps which is terminated with a remote source as shown in Figure 5.6(b). As seen from the diagrams in the presence of remote source, the I_R' (as described in Section 3.2.1) currents fed into the fault from end Q are much higher and this results into an overall increase of I_f' currents which are the total of the superimposed currents fed into the fault from ends P and Q; the quantization and computational errors are thus less effective. Table 6.20 shows the accuracies attained for different types of fault at different fault positions. As can be seen from the results, the accuracy is always higher for a system with remote infeed than that with the remote end open. This once again reinforces the significant advantage this algorithm has over conventional fault locators whose accuracy is adversely affected by the presence of a remote-end source infeed.

6.3.12.3 Effect of Fault Resistance on 33 kV Distribution Systems

Table 6.21 shows the effect of fault resistance on the fault locator's accuracy for a 33 kV system with no remote source as shown in Figure 5.6(a). As seen from the results, the algorithm is largely immune to the changes in fault resistance for both phase-earth and phase-phase-earth faults. Although in the case of phase-earth fault the error is increased with an increase in fault resistance, the overall performance obtained is again superior to that achieved with conventional techniques. Table 6.22 summarises the effect of fault resistance when a remote source is connected to the system as shown in Figure 5.6(b) which clearly shows that the accuracy is slightly better in comparison with the results presented for an open ended system. As explained previously, this is attributed to the fact the magnitude of superimposed fault path currents associated with healthy phases is much higher once the minima has been surpassed, due to the presence of remote infeed.

6.4 Sensitivity Analysis

6.4.1 Effect of Load and Remote Source Capacity Estimation Errors

In practice the load taps and the remote source are subjected to variations with the time of day and this effectively means that the values can only be approximated when applying the fault locator to a particular fault recorded dataset. Since such non-algorithmic errors can have a detrimental effect on the fault locator's performance, it is vitally important to ascertain as to what extent the locator's accuracy is affected as a result of errors in load estimations.

For this study, voltage and current datasets were generated for a fault at 8.4 km and 11.1 km from end P for the systems shown in Figure 5.1. Tables 6.23 to 6.31 summarise the locator's performance when the load taps and remote source

capacity were then subjected to changes by varying degrees of error. Table 6.23 shows the results for an 'a'-phase-earth fault with no estimation error. Table 6.24 shows the corresponding results when all the load capacities associated with load taps are subjected to a +5% estimation error; as can be seen this leads to an error in fault location of ≈3%. Likewise, when all the load taps are subjected to an estimation error of -5%, again an error of about 3% is attained as shown in Table 6.25.

Table 6.26 gives the results when different load taps were subjected to different errors; here load taps 1, 3,5 and 7 were subjected to +5% estimation error and load taps 2, 4 and 6 were subjected to -5% error. In this case, unlike the previous case, the error obtained is slightly low ≈2%. Results have shown that even with, an increase in load tap estimation error to 10% the error in fault location was little different from that obtained for the previous case as shown in Table 6.27.

As seen from the results, although the percentage error in fault location increases with an increase in the load estimation error, more importantly the increase in inaccuracy is still relatively small; this finding once again highlights the significant advantage of the technique presented herein.

Table 6.28 shows the results relating to faults at 11.1 km from end P on the distribution system with remote infeed (Figure 5.1(b)) and these are with no estimation errors in loads. In Table 6.29, the remote source capacity estimate is reduced by 5% and in Table 6.30 it is increased by 10% higher. As seen from the tables, in both cases the fault locator algorithm maintains its high accuracy in that the errors arising are always less than 1%.

In order to ascertain how the performance of the fault locator would be affected for a more realistic situation, both load and remote source capacities are approximated for the system shown in Figure 5.1(b). Table 6.31 shows the performance when an estimation error of ±10% is introduced into the load

capacities and at the same time, the remote source capacity is varied from a range ±10% to ±50% .

It is apparent from the results shown in Table 6.31 that the fault locator maintains its high accuracy for these various combination of errors introduced into both remote source and load taps. The error in fault location remains less than 3% in all the cases except when the remote source capacity is increased by 50%; in this case, the error in fault location increases to about 8%.

These results clearly indicate the robustness of the fault location algorithm described herein and this is a major advantage when applying the technique to real fault datasets recorded from practical distribution systems.

6.4.2 Effect of Line Length Setting Errors

As emphasised in Chapter 3, although the proposed technique is based on Computer Aided Design (CAD) studies, practical considerations such as effect of transducers, interface modules and analog filters, quantisation, digital filtering, etc. are included in the fault location process, so that the fault data processed through the algorithm is very close to that encountered in practice. However, in practice with regard to the line lengths, some non-algorithmic errors are inevitable. It is thus important to determine as to what extent the proposed algorithm is affected from line length setting errors.

In this section the effect of line length errors on the accuracy attained is analyzed. An error of ± 5% introduced in to line sections for the system shown in Figure 5.1. Table 6.32 shows the effect of line length setting errors for the open ended radial system shown in Figure 5.1(a). As can be seen from the results, the accuracy is little affected by line length setting errors except for faults at the 16.7 km. In this case, the worst performance is obtained for double-phase-earth faults resulting in 7.7% error recorded when line length is estimated as 5% higher. This

is an additional increase of about 4.2% over and above that when no setting error is considered for the same fault (see Table 6.5). In the case of single-phase-earth and phase-phase faults, 5.9% and 3.3% error recorded respectively for this same fault location. This can be attributed to the fact that, since the current signals in healthy phase fault paths are lower towards the end of the system, faults occurring towards the end of system are significantly affected from the line length setting errors.

Table 6.33 gives the estimation error in the presence of ±5% line setting errors for the system with remote source shown in Figure 5.1(b). As seen from the results, better performance is obtained in comparison with the open ended system and the error in the majority of cases remains less than 3%. Here again the highest errors are recorded and for 'a'-phase-earth fault and 'a'-'b'-phase-earth faults for faults at 16.7 km and there are 3.1% and 3.8% error recorded respectively. These are again additional errors of 2.9% and 3.6% over and above those attained when no setting errors are considered for the same faults (see Table 6.6).

In summary it can be said that although there is a small degradation in the performance for the faults towards the end of systems both with open end and with remote source, in general the results attained clearly show that the fault location algorithm described is not significantly affected by the line length setting errors.

Table 6.1: Effect of fault position on the fault locator's accuracy for a plain feeder (R_f=1 Ω).

Type of fault	Actual distance from end P(km)	Estimated distance from end P(km)	Error (%)
a-e	5.00	5.01	0.06
b-e	5.00	5.02	0.13
c-e	5.00	5.01	0.06
a-b-e	5.00	5.08	0.53
a-b	5.00	5.02	0.13
a-e	10.00	9.98	-0.13
b-e	10.00	10.01	0.06
c-e	10.00	10.00	0.00
a-b-e	10.00	9.96	-0.27
a-b	10.00	9.98	-0.13

Table 6.2: Effect of fault resistance on the fault locator's accuracy for a plain feeder.

Fault resistance (Ω)	a-e fault		a-b-e fault	
	Estimated distance from end P(km)	Error (%)	Estimated distance from end P(km)	Error (%)
2.0	9.98	-0.13	9.96	-0.27
50.0	9.92	-0.53	9.88	-0.80
100.0	9.95	-0.33	9.90	-0.66
150.0	9.90	-0.66	9.98	-0.01
200.0	9.82	-1.20	9.98	-0.01

Table 6.3: Effect of fault type and position on fault locator's accuracy for a system with three load taps and remote infeed (R_f=1 Ω).

Type of fault	Actual distance (km)	Estimated location (km)	Error (%)
a-e	1.50	1.50	0.00
a-b-e	1.50	1.55	0.33
a-b	1.50	1.50	0.00
a-e	3.00	3.05	0.33
a-b-e	3.00	3.05	0.33
a-b	3.00	3.00	0.00
a-e	4.50	4.53	0.20
a-b-e	4.50	4.55	0.33
a-b	4.50	4.40	-0.66
a-e	6.00	6.08	0.53
a-b	6.00	5.95	-0.33
a-b-e	6.00	6.05	0.33
a-e	7.50	7.45	-0.33
a-b	7.50	7.35	-1.00
a-b-e	7.50	7.40	-0.66
a-e	9.00	8.95	-0.33
a-b	9.00	8.85	-1.00
a-b-e	9.00	8.85	-1.00
a-e	12.00	11.80	-1.33
a-b	12.00	11.65	-2.33
a-b-e	12.00	11.60	-2.67

Table 6.4: Effect of fault type and fault position on locator's accuracy for a system with three load taps and no remote infeed (R_f=1 Ω).

Type of fault	Actual distance (km)	Estimated location (km)	Error (%)
a-e	1.50	1.50	0.00
a-b-e	1.50	1.55	0.33
a-b	1.50	1.50	0.00
a-e	3.00	3.05	0.33
a-b-e	3.00	3.05	0.33
a-b	3.00	3.00	0.00
a-e	4.50	4.53	0.20
a-b-e	4.50	4.45	-0.33
a-b	4.50	4.40	-0.66
a-e	6.00	6.08	0.53
a-b	6.00	5.95	-0.33
a-b-e	6.00	6.05	0.33
a-e	7.50	7.45	-0.33
a-b	7.50	7.25	-1.67
a-b-e	7.50	7.40	-0.67
a-e	9.00	8.90	-0.66
a-b	9.00	8.70	-2.00
a-b-e	9.00	8.80	-1.33

Table 6.5: Effect of fault position on fault locator's accuracy for a typical system with no remote infeed (R_f=2 Ω).

Type of fault	Actual distance from end P(km)	Estimated distance from end P(km)	Error (%)
a-e	1.50	1.50	0.00
b-e	1.50	1.58	0.33
a-b-e	1.50	1.55	0.21
a-b	1.50	1.55	0.21
a-e	4.80	4.85	0.21
b-e	4.80	5.08	1.17
a-b-e	4.80	4.60	-0.84
a-b	4.80	5.05	1.05
a-e	8.40	8.45	0.21
b-e	8.40	8.90	2.09
a-b-e	8.40	8.20	-0.84
a-b	8.40	8.55	0.63
a-e	12.35	12.58	0.96
b-e	12.35	12.95	2.51
a-b-e	12.35	12.15	-0.84
a-b	12.35	12.10	-1.05
a-e	16.70	17.10	1.67
b-e	16.70	17.80	4.60
a-b-e	16.70	17.55	3.55
a-b	16.70	16.10	-2.51

Table 6.6: Effect of remote infeed on fault locator's accuracy for a typical system (R_f=2 Ω).

Type of fault	Actual distance from end P(km)	Estimated distance from end P(km)	Error (%)
a-e	1.50	1.53	0.12
b-e	1.50	1.50	0.00
a-b-e	1.50	1.55	0.21
a-b	1.50	1.60	0.42
a-e	4.80	4.73	-0.13
b-e	4.80	4.85	0.21
a-b-e	4.80	4.75	-0.21
a-b	4.80	4.80	0.00
a-e	8.40	8.35	-0.21
b-e	8.40	8.43	0.13
a-b-e	8.40	8.30	-0.42
a-b	8.40	8.45	0.21
a-e	12.35	12.30	-0.21
b-e	12.35	12.40	0.42
a-b-e	12.35	12.15	-0.84
a-b	12.35	12.30	-0.21
a-e	16.70	16.63	-0.29
b-e	16.70	16.80	0.42
a-b-e	16.70	17.75	0.21
a-b	16.70	16.50	-0.84

Table 6.7: Effect of fault resistance on fault locator's accuracy for 'a'-earth and 'a'-'b'-earth faults on a typical system with no remote infeed.

Fault resistance (Ω)	a-e fault		a-b-e fault	
	Estimated distance from end P(km)	Error (%)	Estimated distance from end P(km)	Error (%)
1.0	11.25	0.63	11.30	0.84
20.0	11.30	0.83	10.90	-0.84
50.0	11.40	1.25	11.00	-0.42
100.0	11.55	1.88	11.00	-0.42
150.0	11.85	3.13	10.85	-1.05
200.0	12.10	4.18	10.95	-0.63

Table 6.8: Effect of fault resistance on fault locator's accuracy for 'a'-earth and 'a'-'b'-earth faults on a typical system with remote infeed.

Fault resistance (Ω)	a-e fault		a-b-e fault	
	Estimated distance from end P(km)	Error (%)	Estimated distance from end P(km)	Error (%)
1.0	11.05	-0.21	10.95	-0.63
20.0	11.05	-0.21	10.70	-1.67
50.0	10.85	-1.05	10.95	-0.63
100.0	10.65	-1.88	10.95	-0.63
150.0	10.60	-2.09	10.95	-0.63
200.0	10.60	-2.09	10.95	-0.63

Table 6.9: Effect of sending-end source capacity on fault locator's accuracy for a typical system with no remote infeed.

Type of fault	Source SCL (MVA)	located distance from end P (km)	Error (%)
a-e	10	11.48	1.58
a-b-e	10	12.00	3.76
a-b	10	10.70	-1.67
a-e	60	11.25	0.72
a-b-e	60	11.25	0.72
a-b	60	11.05	-0.25
a-e	250	11.25	0.72
a-b-e	250	11.20	0.47
a-b	250	11.05	-0.23

Table 6.10: Effect of dynamic load on fault locator's accuracy.

Type of fault	Actual distance from end P(km)	Estimated distance from end P(km)	Error (%)
a-e	8.40	8.25	-0.62
a-b-e	8.40	8.15	-1.05
a-b	8.40	8.10	-1.25
a-e	12.35	12.10	-1.05
a-b-e	12.35	12.05	-1.25
a-b	12.35	12.00	-1.50

Table 6.11: Effect of fault cycle on fault locator's accuracy for a typical system with no remote infeed.

Type of fault	Actual location from end P (km)	Estimated location using 1.cycle	Error (%)	Estimated location using 2.cycle	Error (%)
a-e	3.00	3.05	0.21	3.10	0.42
a-b	3.00	2.65	-1.46	2.90	-0.42
a-b-e	3.00	2.75	-1.05	3.10	0.42
a-e	11.10	11.33	0.92	11.25	0.63
a-b	11.10	9.85	-5.23	10.85	-1.05
a-b-e	11.10	10.95	-0.63	-11.05	-0.21
a-e	13.60	14.18	2.42	13.98	1.56
a-b	13.60	11.75	-7.54	13.30	-1.25
a-b-e	13.60	13.55	-0.21	13.85	1.05

Table 6.12: Fault estimation under three phase fault conditions.

Actual location from end P(km)	Estimated location from end P (km)	Error (%)
3.00	3.06	0.25
6.60	6.67	0.28
8.40	8.45	0.21
11.10	11.16	0.25
13.60	13.55	0.21
16.70	16.54	0.67
20.90	20.46	1.84
23.90	23.14	3.20

Table 6.13: Effect of capacitor bank on locator's accuracy for a typical system with no remote infeed.

Type of fault	Actual location (km)	Estimated location (km)	Error (%)
a-e	6.60	6.68	0.33
a-b-e	6.60	6.65	0.21
a-b	6.60	6.15	-1.89
a-e	11.10	11.30	0.84
a-b-e	11.10	11.35	1.05
a-b	11.10	10.60	-2.09
a-e	13.60	13.80	0.84
a-b-e	13.60	13.90	1.25
a-b	13.60	12.80	-3.35

Table 6.14: Effect of fault inception angle on fault locator's accuracy.

Type of fault	Fault inception angle (degree)	Estimated location (km)	Error (%)
a-e	0^0	9.90	0.63
a-e	45^0	9.88	0.54
a-e	90^0	9.80	0.21
a-e	135^0	9.90	0.63
a-e	180^0	9.98	0.96
a-b	0^0	9.15	-2.51
a-b	45^0	9.35	-1.67
a-b	90^0	9.40	-1.46
a-b	135^0	9.10	-2.71
a-b	180^0	9.20	-2.30
a-b-e	0^0	10.10	1.46
a-b-e	45^0	10.00	1.05
a-b-e	90^0	9.80	0.21
a-b-e	135^0	10.00	1.05
a-b-e	180^0	10.30	2.31

Table 6.15: Effect of fault type and fault position on fault locator's accuracy for a typical system comprising different line impedances with no remote infeed.

Type of fault	Actual distance from end P(km)	Estimated distance from end P(km)	Error (%)
a-e	4.80	4.45	-1.46
a-b-e	4.80	4.90	0.42
a-b	4.80	4.75	-0.21
a-e	8.40	8.63	0.96
a-b-e	8.40	8.95	2.30
a-b	8.40	8.10	-1.25
a-e	13.60	13.98	1.59
a-b-e	13.60	14.30	2.92
a-b	13.60	13.40	-0.83
a-e	16.70	17.40	2.93
a-b-e	16.70	17.65	3.97
a-b	16.70	17.45	3.14

Table 6.16: Effect of fault type and fault position on fault locator's accuracy for a typical system comprising different line impedances with remote infeed.

Type of fault	Actual distance from end P(km)	Estimated distance from end P(km)	Error (%)
a-e	4.80	4.90	0.42
a-b-e	4.80	4.65	-0.63
a-b	4.80	4.70	-0.42
a-e	8.40	8.32	-0.29
a-b-e	8.40	8.30	-0.42
a-b	8.40	8.35	-0.21
a-e	13.60	13.52	-0.33
a-b-e	13.60	13.30	-1.25
a-b	13.60	13.35	-1.05
a-e	16.70	16.53	-0.71
a-b-e	16.70	16.20	-2.09
a-b	16.70	16.25	-1.46

Table 6.17: Effect of fault resistance on fault locator's accuracy for a typical system comprising different line impedances with no remote infeed.

Fault resistance (Ω)	a-e fault		a-b-e fault	
	Estimated distance from end P(km)	Error (%)	Estimated distance from end P(km)	Error (%)
2.0	11.38	1.17	11.70	2.51
50.0	11.43	1.38	10.85	-1.05
100.0	11.65	2.30	10.95	-0.63
150.0	12.45	5.60	10.95	-0.63
200.0	12.55	6.06	10.95	-0.63

Table 6.18: Effect of faults occurring along tapped feeders.

Type of fault	Tap no	Distance between tap and end P(km)	Distance between tap and fault (km)	Estimated location (km)
a-e	1	3.00	2.10	4.45
a-b	1	3.00	2.10	4.00
a-b-e	1	3.00	2.10	4.25
a-e	1	3.00	1.00	3.63
a-b	1	3.00	1.00	3.45
a-b-e	1	3.00	1.00	3.50
a-e	2	6.60	1.60	6.78
a-b	2	6.60	1.60	6.60
a-b-e	2	6.60	1.60	5.95
a-e	4	11.10	3.10	11.00
a-b	4	11.10	3.10	11.05
a-b-e	4	11.10	3.10	11.80
a-e	6	16.70	1.80	19.38
a-b	6	16.70	1.80	18.15
a-b-e	6	16.70	1.80	17.80

Table 6.19: Effect of fault type and position on the fault locator's accuracy for a 33 kV system with no remote infeed.

Type of fault	Actual distance from end P(km)	Estimated distance from end P(km)	Error (%)
a-e	4.50	4.40	-0.36
a-b-e	4.50	4.60	0.36
a-b	4.50	4.70	0.73
a-e	9.00	9.13	0.47
a-b-e	9.00	9.32	1.16
a-b	9.00	9.25	0.91
a-e	16.00	16.23	0.84
a-b-e	16.00	16.63	2.29
a-b	16.00	16.35	1.27
a-e	20.00	20.42	1.53
a-b-e	20.00	20.75	2.73
a-b	20.00	20.65	2.36

Table 6.20: Effect of fault type and position on the fault locator's accuracy for a 33 kV system with remote infeed.

Type of fault	Actual distance from end P(km)	Estimated distance from end P(km)	Error (%)
a-e	4.50	4.65	0.54
a-b-e	4.50	4.58	0.29
a-b	4.50	4.60	0.36
a-e	9.00	9.23	0.84
a-b-e	9.00	8.85	-0.55
a-b	9.00	8.75	-0.91
a-e	16.00	16.18	0.65
a-b-e	16.00	15.75	-0.91
a-b	16.00	15.65	-1.27
a-e	20.00	19.73	-0.98
a-b-e	20.00	19.52	-1.52
a-b	20.00	19.60	-1.45

Table 6.21: Effect of fault resistance on fault locator's accuracy for a 33 kV system with no remote infeed.

Fault resistance (Ω)	a-e fault		a-b-e fault	
	Estimated distance from end P(km)	Error (%)	Estimated distance from end P(km)	Error (%)
2.0	16.23	0.84	16.63	2.29
50.0	16.33	1.20	16.55	2.00
100.0	16.42	1.53	16.48	1.74
150.0	16.53	1.93	16.40	1.45
200.0	16.78	2.83	16.35	1.27

Table 6.22: Effect of fault resistance on fault locator's accuracy for a 33 kV system with remote infeed.

Fault resistance (Ω)	a-e fault		a-b-e fault	
	Estimated distance from end P(km)	Error (%)	Estimated distance from end P(km)	Error (%)
2.0	16.18	0.65	15.75	-0.91
50.0	16.28	1.01	15.70	-1.09
100.0	16.35	1.27	15.40	-2.18
150.0	16.43	1.56	15.65	-1.27
200.0	16.78	2.83	15.75	-0.91

Table 6.23: Effect of load capacity estimation on fault locator's accuracy, for faults at 8.4 km from end P for the typical system shown in Figure 5.1(a), 0 % estimation error for all load capacities.

Type of fault	Estimated location from end P (km)	Error (%)
a-e	8.45	0.21
a-b	8.20	-0.84
a-b-e	8.55	0.63

Table 6.24: Effect of load capacity estimation on fault locator's accuracy, for faults at 8.4 km from end P for the typical system shown in Figure 5.1(a), +5 % estimation error for all load capacities.

Type of fault	Estimated location from end P (km)	Error (%)
a-e	7.60	-3.34
a-b	7.75	-2.71
a-b-e	7.85	-2.30

Table 6.25: Effect of load capacity estimation on fault locator's accuracy, for faults at 8.4 km from end P for the typical system shown in Figure 5.1(a), -5 % estimation error for all load capacities.

Type of fault	Estimated location from end P (km)	Error (%)
a-e	9.27	3.64
a-b	8.30	-0.42
a-b-e	9.30	3.76

Table 6.26: Effect of load capacity estimation on fault loacator's accuracy, for faults at 8.4 km from end P for the typical system shown in Figure 5.1(a), ± 5 % estimation error for all load capacities.

Type of fault	Estimated location from end P (km)	Error (%)
a-e	8.08	-1.33
a-b	7.80	-2.51
a-b-e	8.25	-0.63

Table 6.27: Effect of load capacity estimation on fault locator's accuracy, for faults at 8.4 km from end P for the typical system shown in Figure 5.1(a), ±10 % estimation error for all load capacities.

Type of fault	Estimated location from end P (km)	Error (%)
a-e	7.68	-3.01
a-b	7.50	-3.76
a-b-e	7.90	-2.09

Table 6.28: Effect of remote source capacity estimation on fault locator's accuracy for faults at 11.1 km from end P for the typical system shown in Figure 5.1(b), 0 % estimation error for the remote source capacity.

Type of fault	Estimated location from end P (km)	Error (%)
a-e	10.95	-0.63
a-b	11.15	0.21
a-b-e	10.95	-0.63

Table 6.29: Effect of remote source capacity estimation on fault locator's accuracy for faults at 11.1 km from end P for the system shown in Figure 5.1(b), -5 % estimation error for the remote source capacity.

Type of fault	Estimated location from end P (km)	Error (%)
a-e	11.13	0.10
a-b	11.05	0.21
a-b-e	10.95	-0.63

Table 6.30: Effect of remote source capacity estimation on fault locator's accuracy, for faults at 11.1 km from end P for the system shown in Figure 5.1(b), +10 % estimation error for the remote source capacity.

Type of fault	Estimated location from end P (km)	Error (%)
a-e	11.20	0.42
a-b	11.05	0.21
a-b-e	10.90	-0.84

Table 6.31: Effect of load and remote source capacity estimation on fault locator's accuracy, for 'a'-earth faults at 11.1 km from end P for the radial system shown in Figure 5.1(b).

Source capacity	Load capacity	Estimated distance	Error (%)
-10	-10	10.78	-1.36
-10	+10	11.00	-0.42
+10	-10	11.13	0.13
+10	+10	11.38	1.17
-25	-10	10.60	-2.09
-25	+10	10.85	-1.05
+25	-10	11.60	2.09
+25	+10	11.82	3.01
-50	-10	10.45	-2.71
-50	+10	10.73	-1.55
+50	-10	12.90	7.53
+50	+10	13.05	8.16

Table 6.32: Effect of line setting errors on fault locator's accuracy for the radial system shown in Figure 5.1(a) (R_f=2 Ω).

Type of fault	Line setting error	Actual distance from end P(km)	Estimated distance from end P(km)	Error (%)
a-e	+5	4.80	4.80	0.00
a-e	-5	4.80	4.85	0.21
a-b	+5	4.80	5.00	0.84
a-b	-5	4.80	5.01	0.88
a-b-e	+5	4.80	4.55	-1.05
a-b-e	-5	4.80	4.60	0.84
a-e	+5	7.50	7.53	0.01
a-e	-5	7.50	7.58	0.33
a-b	+5	7.50	7.40	-0.42
a-b	-5	7.50	7.30	-0.84
a-b-e	+5	7.50	7.60	0.42
a-b-e	-5	7.50	7.65	0.63
a-e	+5	12.35	12.30	0.21
a-e	-5	12.35	12.58	0.96
a-b	+5	12.35	12.05	-1.25
a-b	-5	12.35	12.05	-1.25
a-b-e	+5	12.35	12.20	-0.63
a-b-e	-5	12.35	12.40	0.21
a-e	+5	16.70	16.40	-1.25
a-e	-5	16.70	18.12	5.94
a-b	+5	16.70	15.90	-3.34
a-b	-5	16.70	16.60	-0.42
a-b-e	+5	16.70	17.85	4.81
a-b-e	-5	16.70	18.55	7.74

Table 6.33: Effect of line setting errors on fault locator's accuracy for the radial system shown in Figure 5.1(b) (R_f=2 Ω).

Type of fault	Line setting error	Actual distance from end P(km)	Estimated dist from end P(km)	Error (%)
a-e	+5	1.50	1.53	0.13
a-e	-5	1.50	1.50	0.00
a-b	+5	1.50	1.65	0.63
a-b	-5	1.50	1.40	-0.42
a-b-e	+5	1.50	1.55	0.21
a-b-e	-5	1.50	1.55	0.21
a-e	+5	8.40	8.65	1.05
a-e	-5	8.40	7.95	-1.88
a-b	+5	8.40	8.75	1.46
a-b	-5	8.40	8.10	-1.25
a-b-e	+5	8.40	8.65	1.05
a-b-e	-5	8.40	7.95	-1.88
a-e	+5	12.35	12.83	2.00
a-e	-5	12.35	11.75	-2.51
a-b	+5	12.35	12.85	2.09
a-b	-5	12.35	11.65	-2.92
a-b-e	+5	12.35	12.65	1.25
a-b-e	-5	12.35	11.95	-1.67
a-e	+5	16.70	17.33	2.63
a-e	-5	16.70	15.95	-3.14
a-b	+5	16.70	16.75	0.21
a-b	-5	16.70	16.20	-2.09
a-b-e	+5	16.70	17.13	1.80
a-b-e	-5	16.70	15.80	-3.76

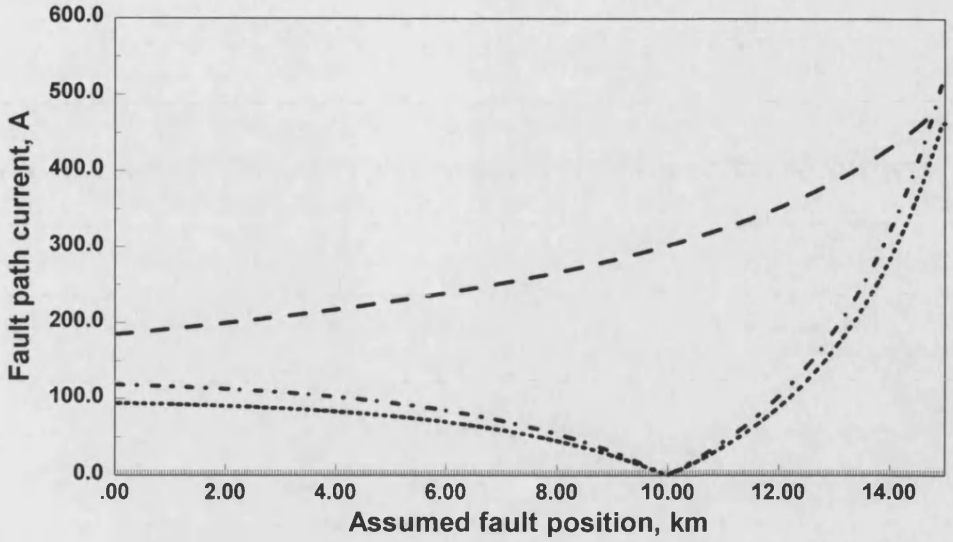

Figure 6.1(a) Fault path currents for an 'a'-phase-earth fault at 10.0 km from end P for the sysem shown in Figure 5.4 (R_f=2 Ω).

_ _ _ _ _ a - phase (scale x 5 of that shown)

_._._._._ b - phase

..... c - phase

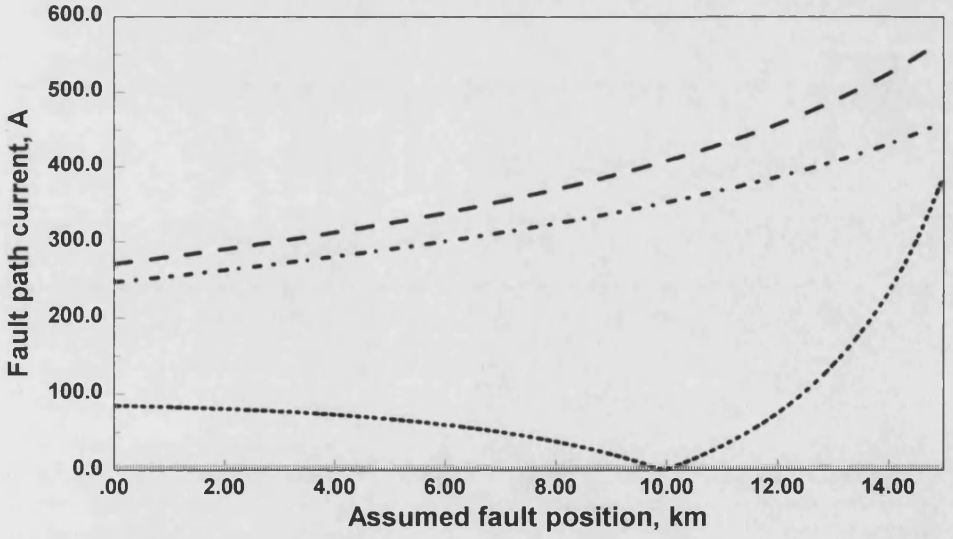

Figure 6.1(b) Fault path currents for an 'a'-'b'-phase-earth fault at 10.0 km from end P for the system shown in Figure 5.4 (R_f=2 Ω).

_ _ _ _ a - phase (scale x 5 of that shown)

_._._._._ b - phase (scale x 5 of that shown)

..... c - phase

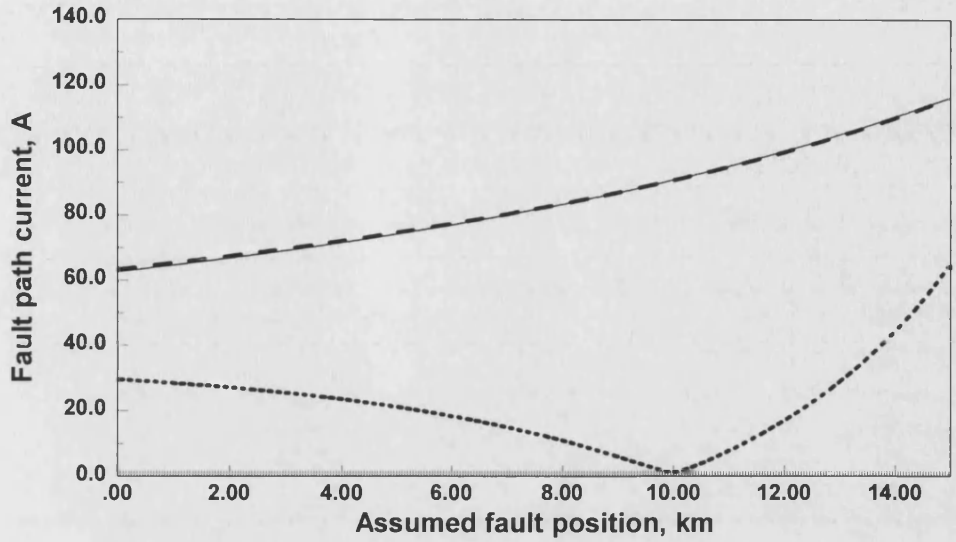

Figure 6.1(c) Fault path currents for an 'a'-'b'-phase fault at 10.0 km from end P for the system shown in Figure 5.4.

_ _ _ _ a - phase (scale x 20 of that shown)

_ . _ . _ . b - phase (scale x 20 of that shown)

..... c - phase

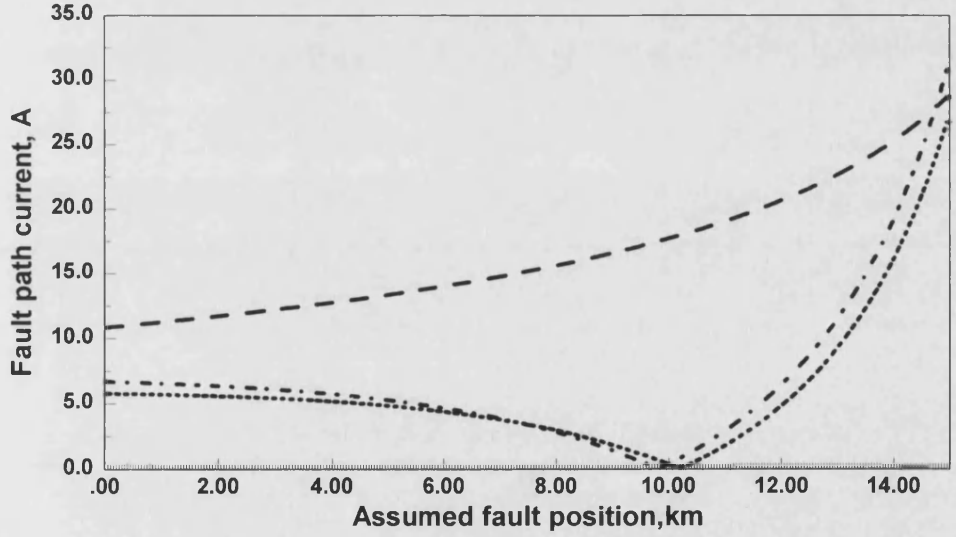

Figure 6.2(a) Fault path currents for an 'a'-phase-earth fault at 10.0 km from end P for the system shown in Figure 5.4 (R_f=100 Ω).

_ _ _ _ _ a - phase (scale x 5 of that shown)

_ . _ . _ . b - phase

..... c - phase

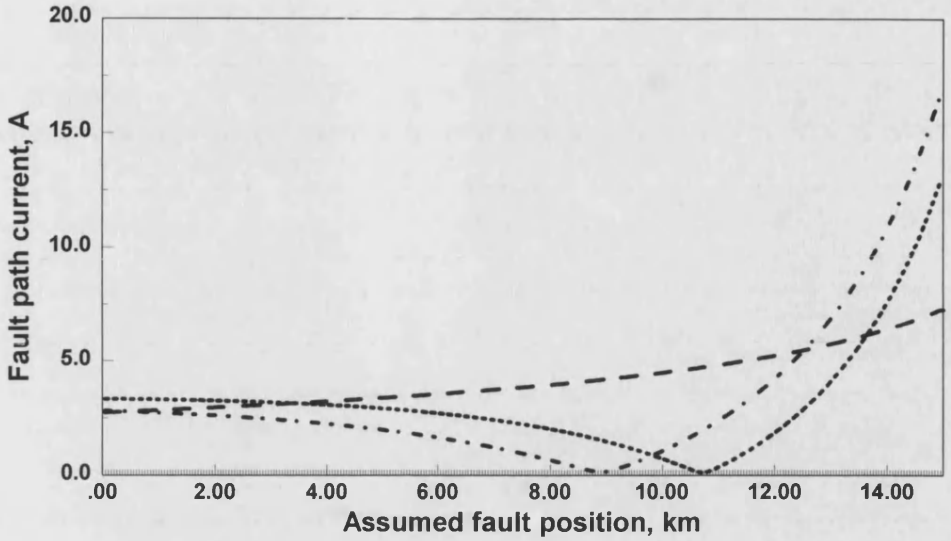

Figure 6.2(b) Fault path currents for an 'a'-phase-earth fault at 10.0 km from end P for the system shown in Figure 5.4 (R_f=200 Ω).

a - phase (scale x 10 of that shown)

b - phase

c - phase

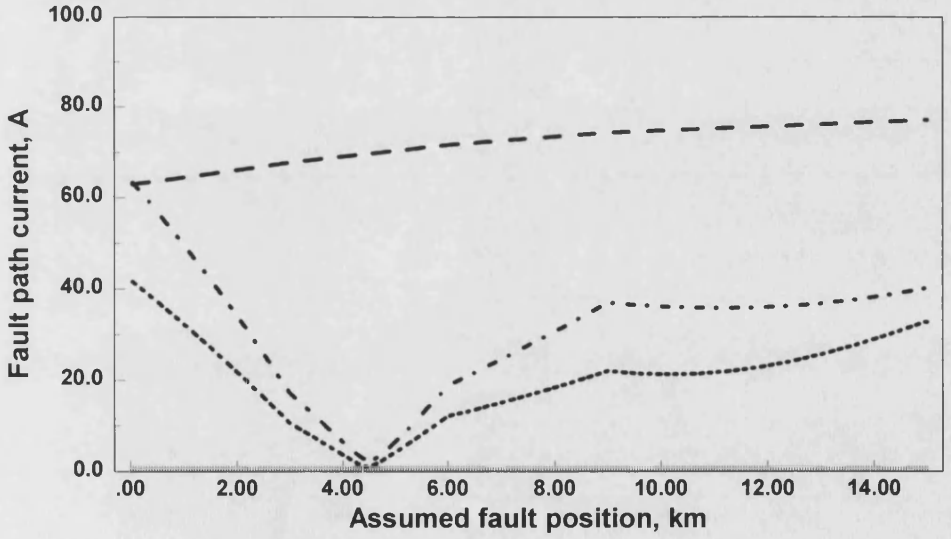

Figure 6.3(a) Fault path currents for an 'a'-phase-earth fault at 4.5 km from end P for the system shown in Figure 5.5(a) (R_f=2 Ω).

a - phase (scale x 20 of that shown)

b - phase

c - phase

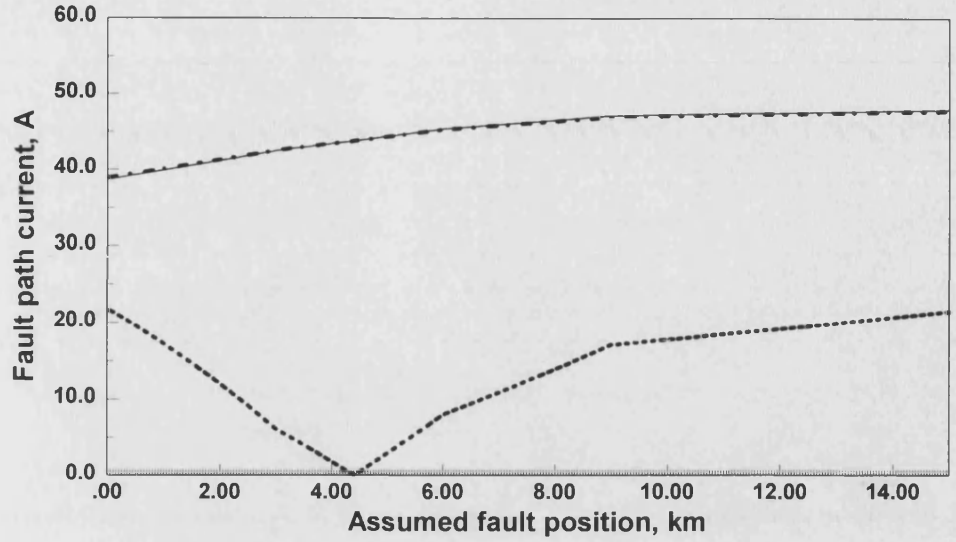

Figure 6.3(b) Fault path currents for an 'a'-'b'-phase fault at 4.5 km from end P for the system shown in Figure 5.5(a).

_ _ _ _ a - phase (scale x 50 of that shown)

_ . _ . _ . b - phase (scale x 50 of that shown)

..... c - phase

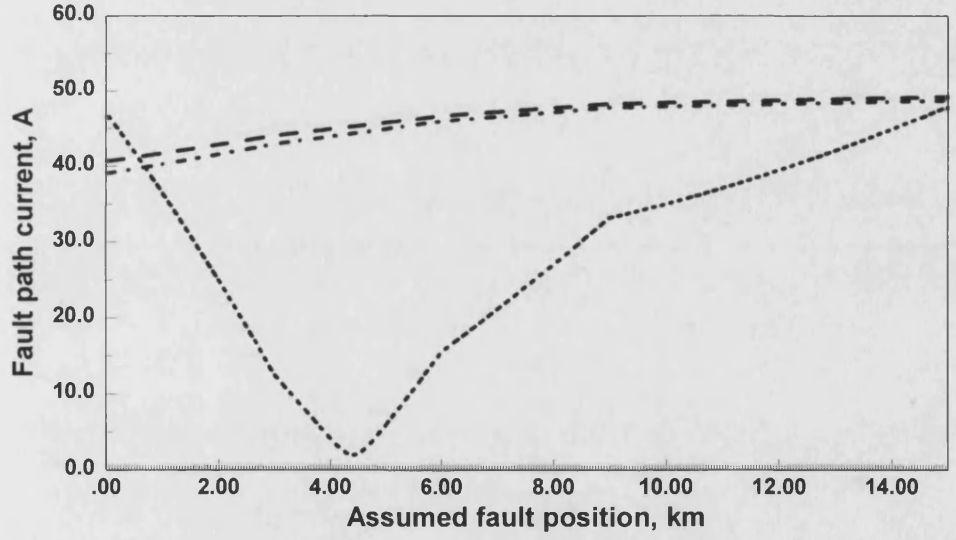

Figure 6.3(c) Fault path currents for an 'a'-'b'-phase-earth fault at 4.5 km from end P for the system shown in Figure 5.5(a) (R_f=2 Ω).

_ _ _ _ a - phase (scale x 50 of that shown)

_ . _ . _ . b - phase (scale x 50 of that shown)

..... c - phase

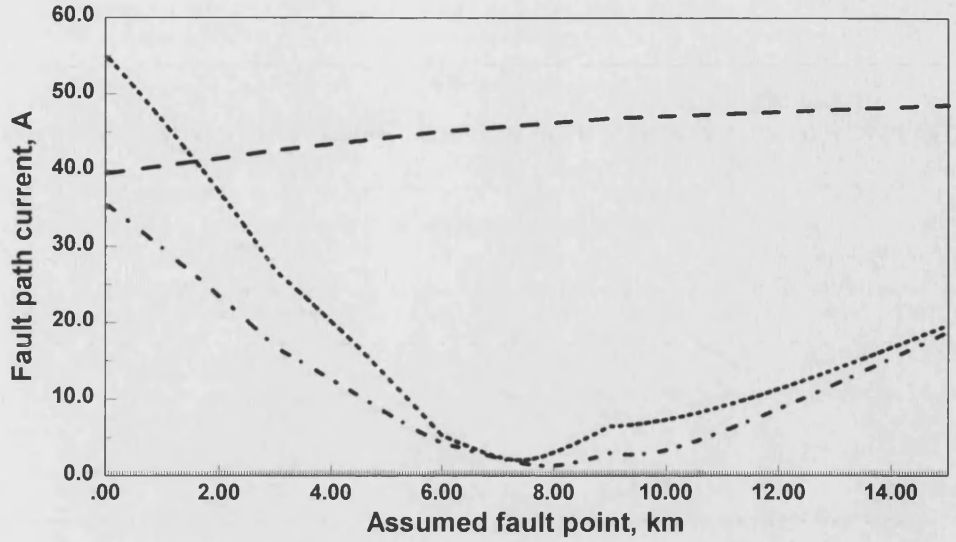

Figure 6.4(a) Fault path currents for an 'a'-phase-earth fault at 7.5 km from end P for the system shown in Figure 5.5(a) (R_f=2 Ω).

a - phase (scale x 20 of that shown)
b - phase
c - phase

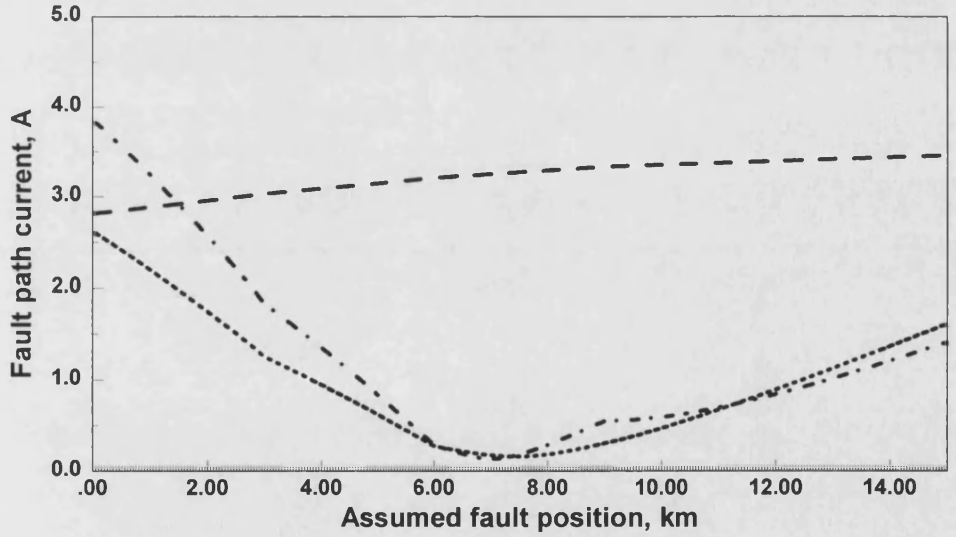

Figure 6.4(b) Fault path currents for an 'a'-phase-earth fault at 7.5 km from end P for the system shown in Figure 5.5(a) (R_f=100 Ω).

a - phase (scale x 20 of that shown)
b - phase
c - phase

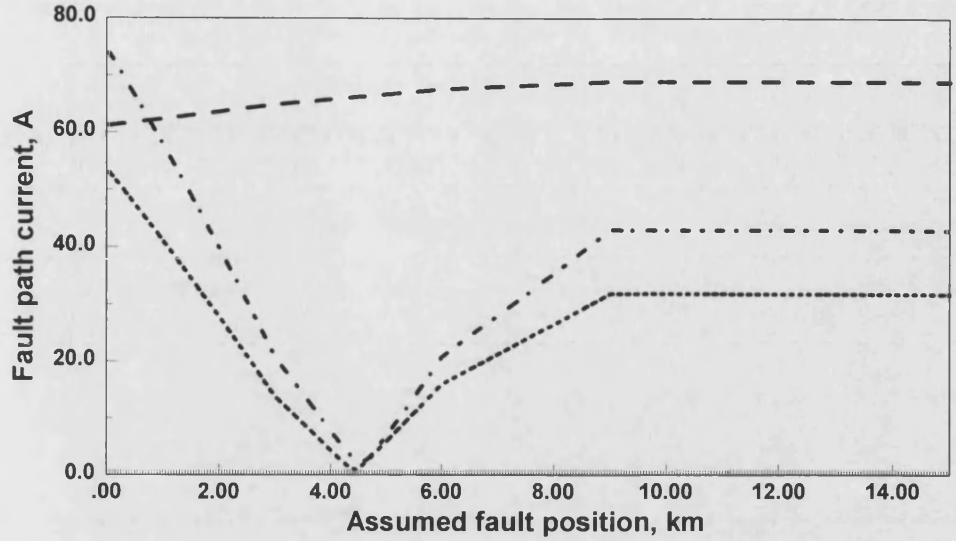

Figure 6.5(a) Fault path currents for an 'a'-phase-earth fault at 4.5 km from end P for the system shown in Figure 5.5(b) (R_f=2 Ω).

a - phase (scale x 20 of that shown)

b - phase

c - phase

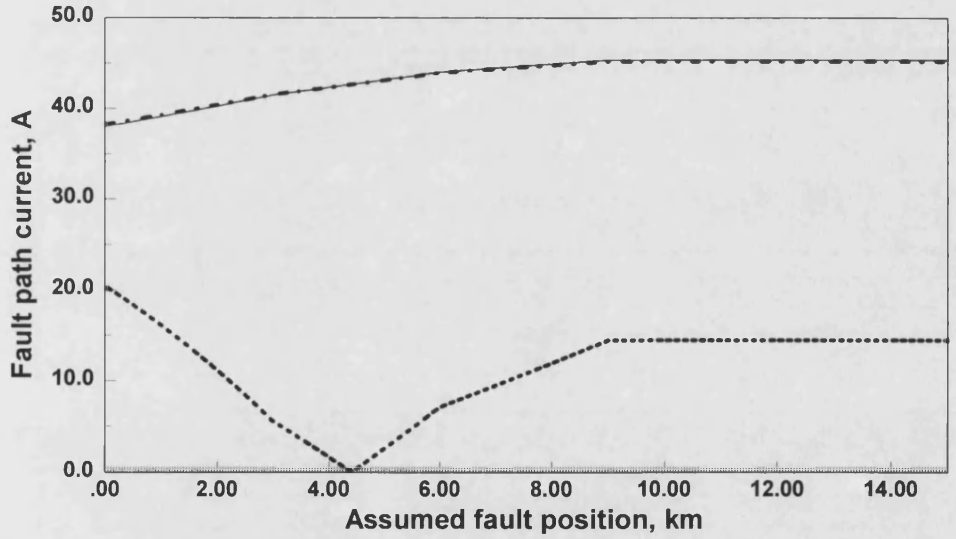

Figure 6.5(b) Fault path currents for an 'a'-'b'-phase fault at 4.5 km from end P for the system shown in Figure 5.5(b) (R_f=2 Ω).

a - phase (scale x 50 of that shown)

b - phase (scale x 50 of that shown)

c - phase

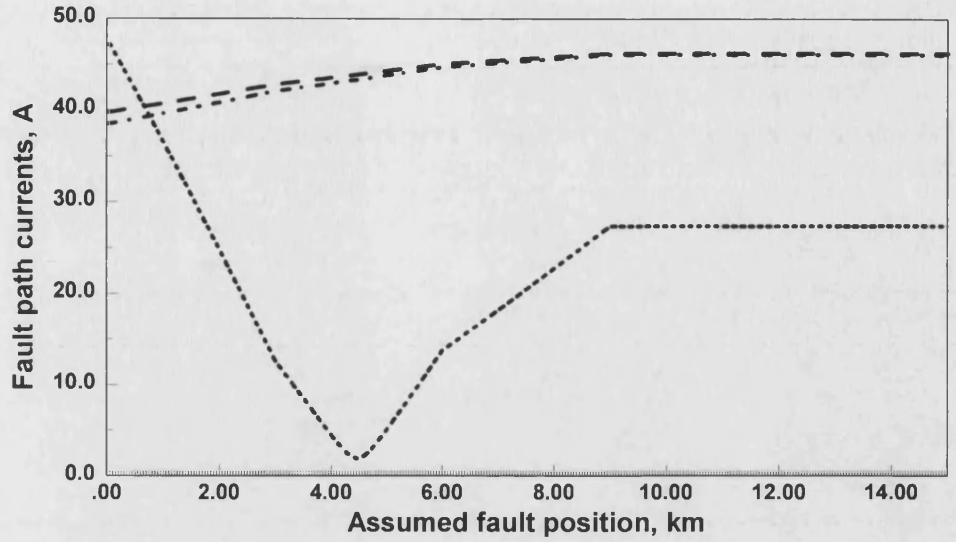

Figure 6.5(c) Fault path currents for an 'a'-'b'-phase-earth fault at 4.5 km from end P for the system shown in Figure 5.5(b) (R_f=2 Ω).

_ _ _ _ a - phase (scale x 50 of that shown)

_ . _ . _ . _ b - phase (scale x 50 of that shown)

..... c - phase

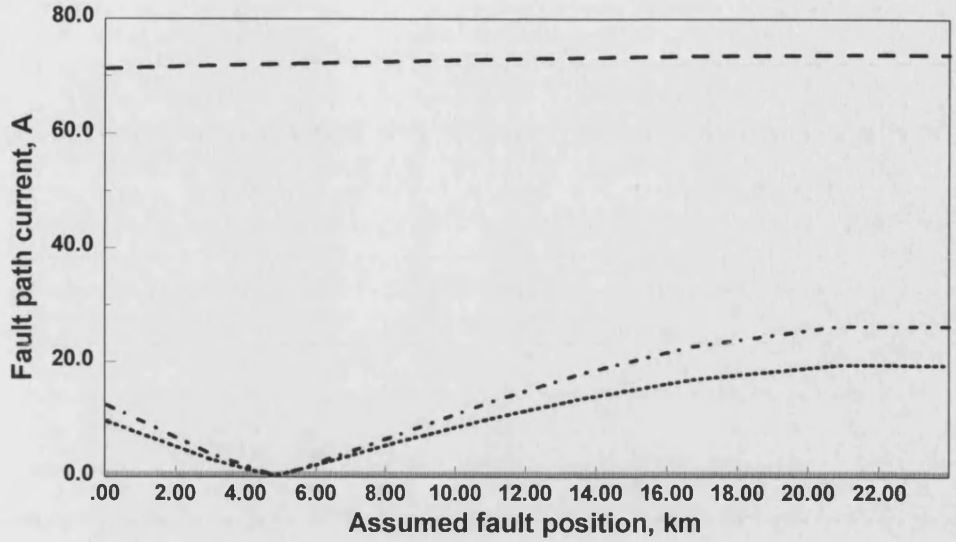

Figure 6.6(a) Fault path currents for an 'a'-phase-earth fault at 4.8 km from end P for the system shown in Figure 5.1(a) (R_f=2 Ω).

a - phase (scale x 20 of that shown)

b - phase

c - phase

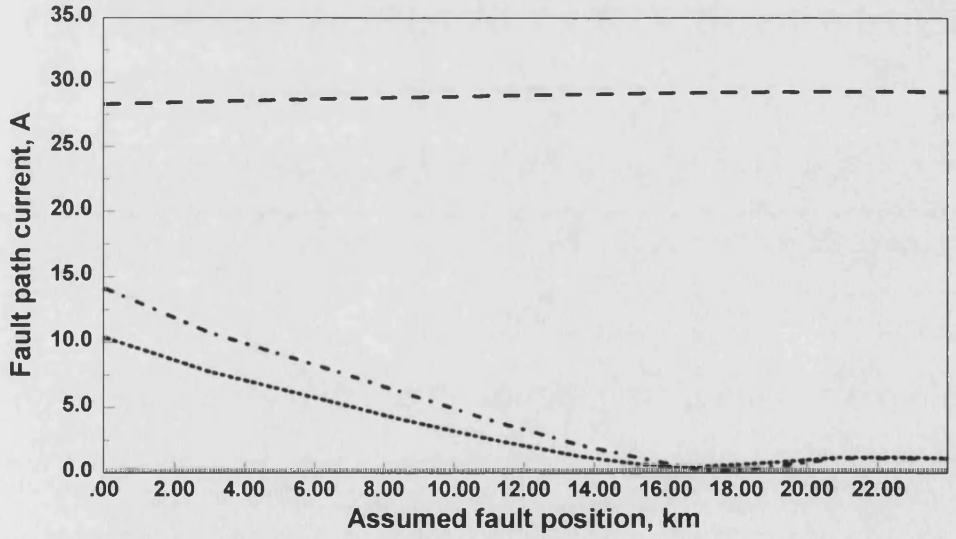

Figure 6.6(b) Fault path currents for an 'a'-phase-earth fault at 16.7 km from end P for the system shown in Figure 5.1(a) (R_f=2 Ω).

a - phase (scale x 10 of that shown)

b - phase

c - phase

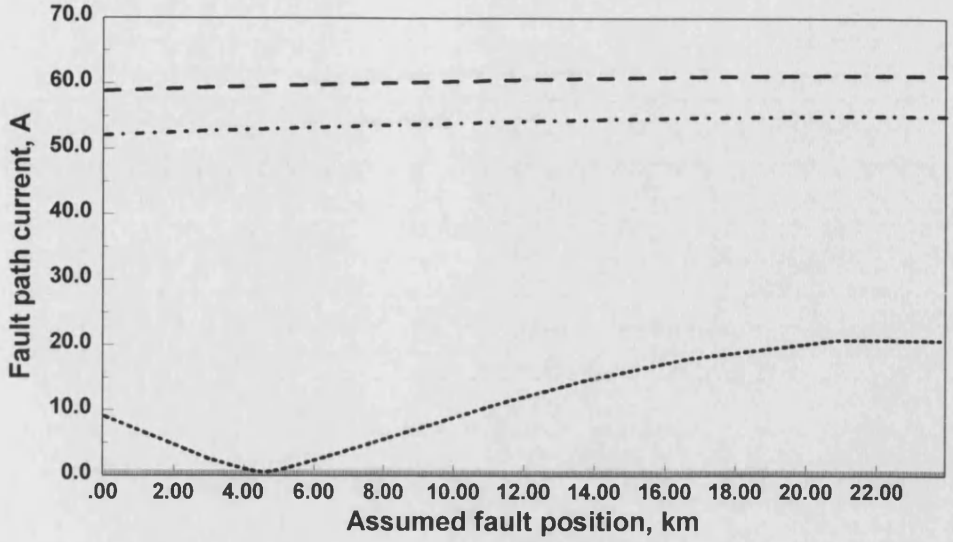

Figure 6.6(c) Fault path currents for an 'a'-'b'-phase-earth fault at 4.8 km from end P for the system shown in Figure 5.1(a) (R_f=2 Ω).

_ _ _ _ a - phase (scale x 40 of that shown)

. . . . . b - phase (scale x 40 of that shown)

..... c - phase

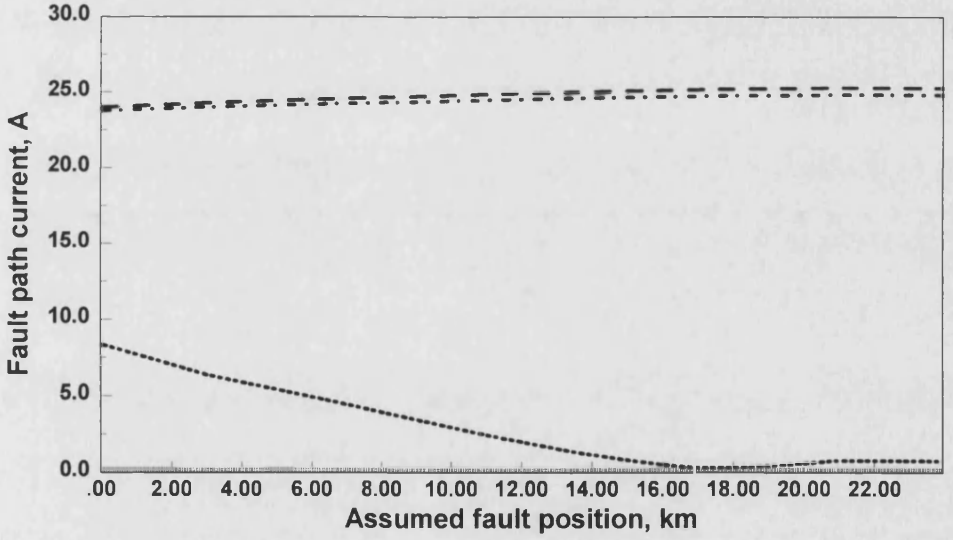

Figure 6.6(d) Fault path currents for an 'a'-'b'-phase-earth fault, at 16.7 km from end P for the system shown in Figure 5.1(a) (R_f=2 Ω).

_ _ _ _ a - phase (scale x 40 of that shown)

. . . . . b - phase (scale x 40 of that shown)

..... c - phase

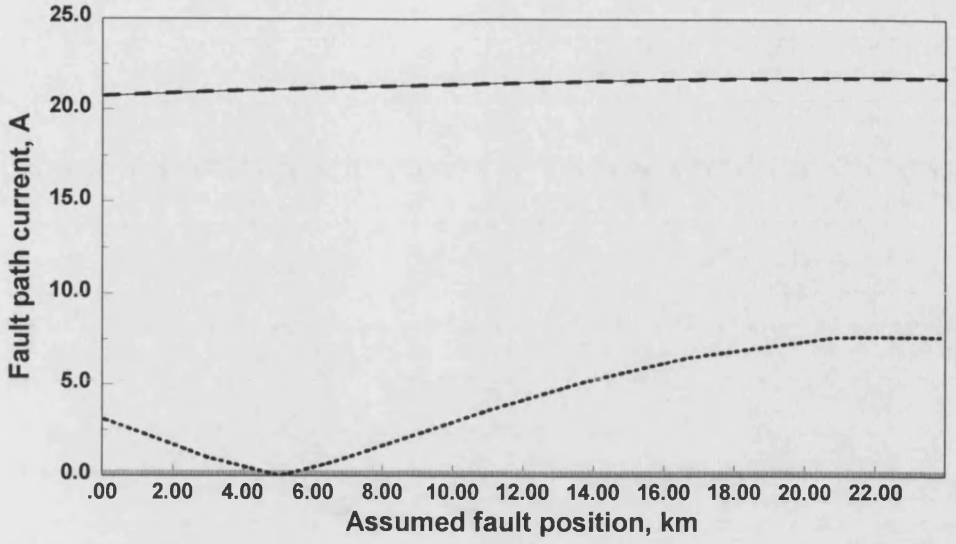

Figure 6.6(e) Fault path currents for an 'a'-'b'-phase fault, at 4.8 km from end P for the system shown in Figure 5.1(a).

_ _ _ _ a - phase (scale x 100 of that shown)
. . . . . b - phase (scale x 100 of that shown)
..... c - phase

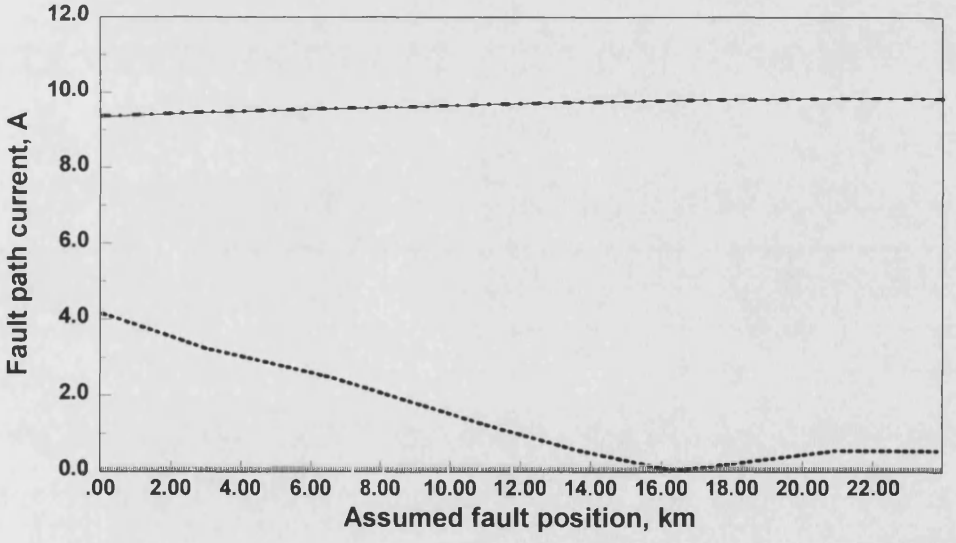

Figure 6.6(f) Fault path currents for an 'a'-'b'-phase fault at 16.7 km from end P for the system shown in Figure 5.1(a).

_ _ _ _ a - phase (scale x 100 of that shown)
. . . . . b - phase (scale x 100 of that shown)
..... c - phase

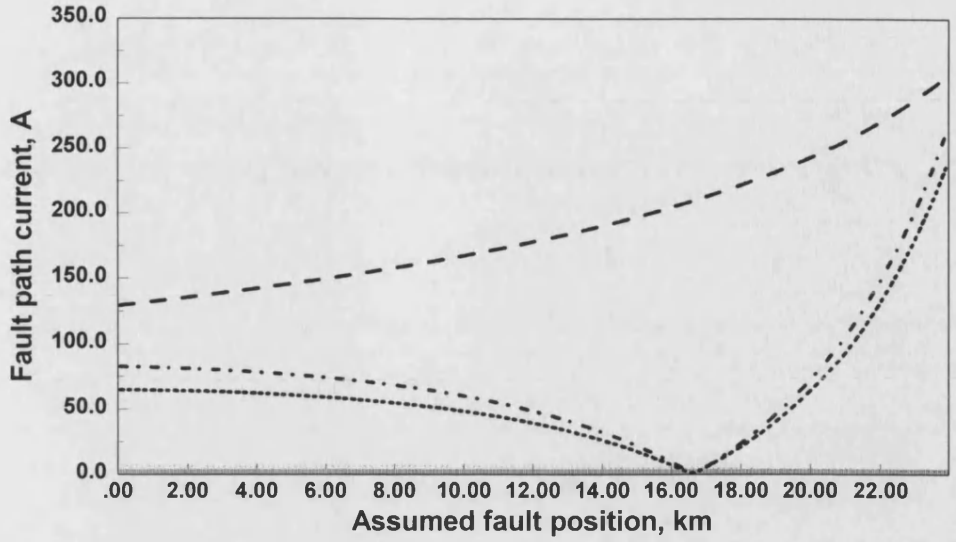

Figure 6.7(a) Fault path currents for an 'a'-phase-earth fault, at 16.7 km from end P for the system shown in Figure 5.1(b) (R_f=2 Ω).

_ _ _ _ _ a - phase (scale x 5 of that shown)

_ . _ . _ . _ b - phase

..... c - phase

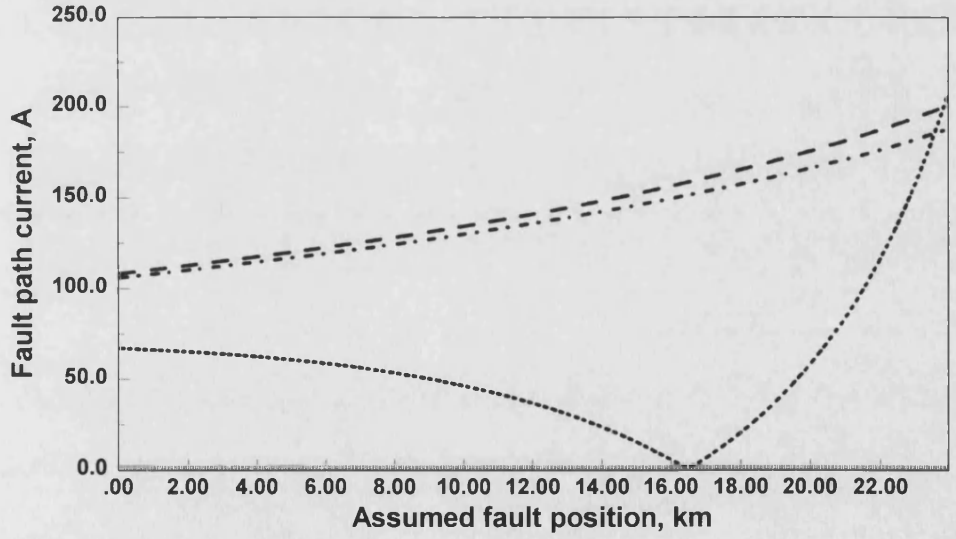

Figure 6.7(b) Fault path currents for an 'a'-'b'-phase-earth fault, at 16.7 km from end P for the system shown in Figure 5.1(b) (R_f=2 Ω).

_ _ _ _ a - phase (scale x 10 of that shown)

_ . _ . _ . b - phase (scale x 10 of that shown)

..... c - phase

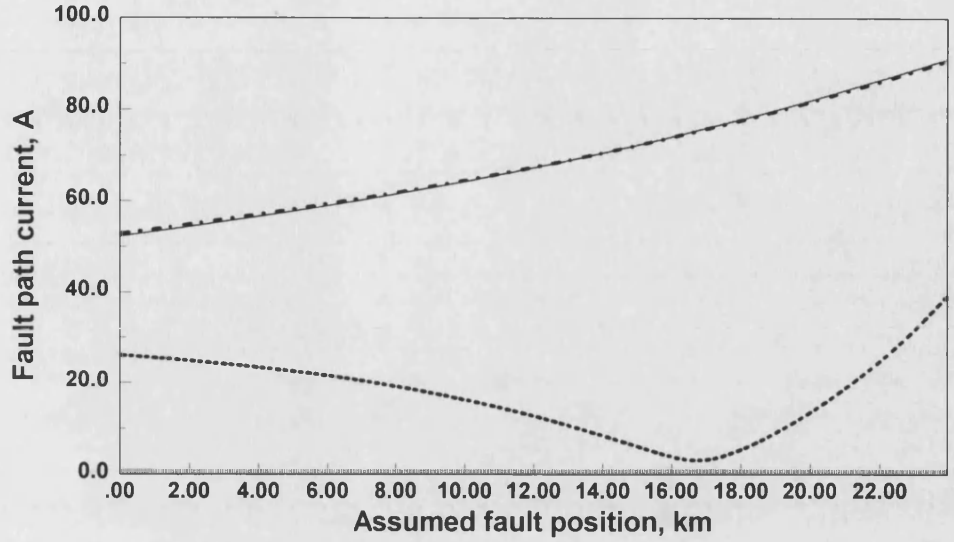

Figure 6.7(c) Fault path currents for an 'a'-'b'-phase fault, at16.7 km from end P for the system shown in Figure 5.1(b).

_ _ _ _ a - phase (scale x 20 of that shown)

_ . _ . _ . b - phase (scale x 20 of that shown)

..... c - phase

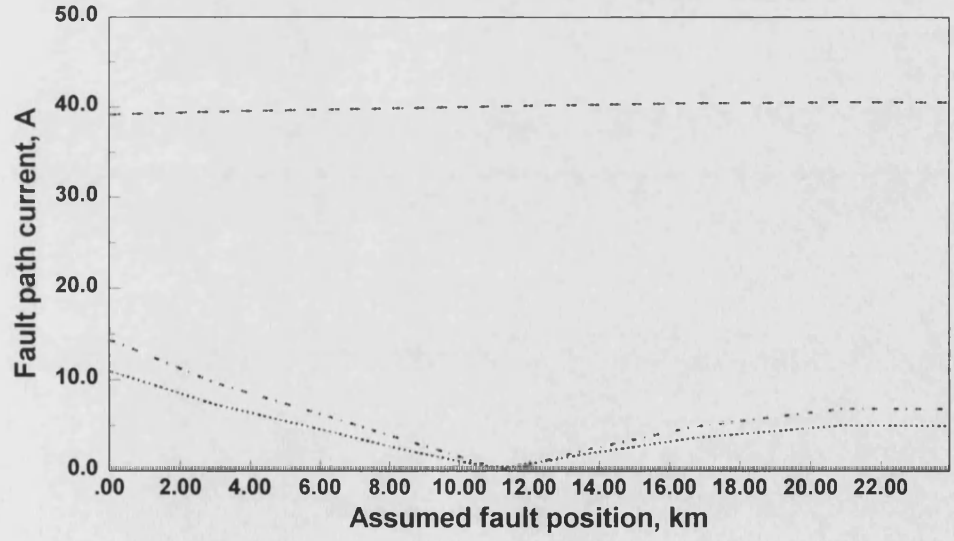

Figure 6.8(a) Fault path currents for an 'a'-phase-earth fault at 11.1 km from end P for the system shown in Figure 5.1(a) (R_f=2 Ω)

_ _ _ _ _ a - phase (scale x 20 of that shown)

_ . _ . _ . b - phase

..... c - phase

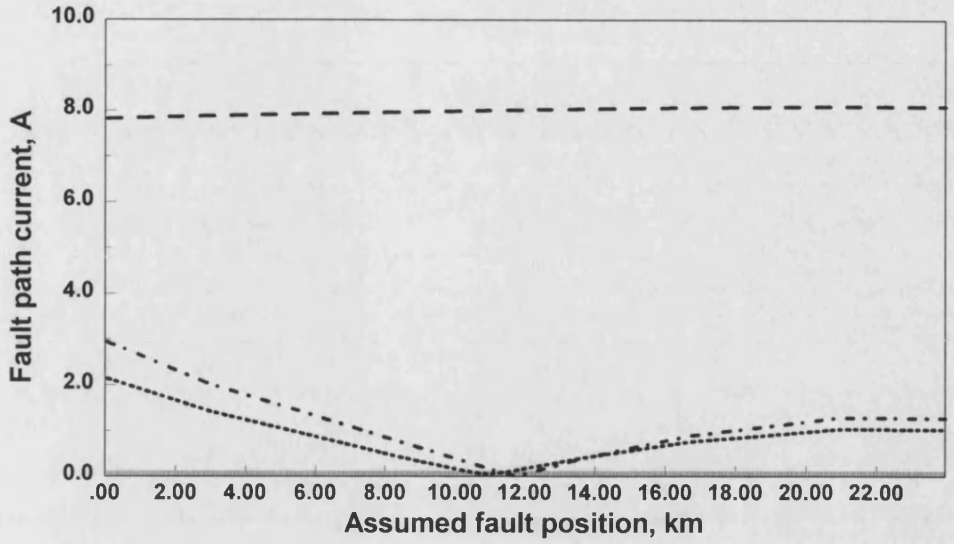

Figure 6.8(b) Fault path currents for an 'a'-phase-earth fault at 11.1 km from end P for the system shown in Figure 5.1(a) (R_f=50 Ω).

_ _ _ _ _ a - phase (scale x 20 of that shown)

_._._._._ b - phase

..... c - phase

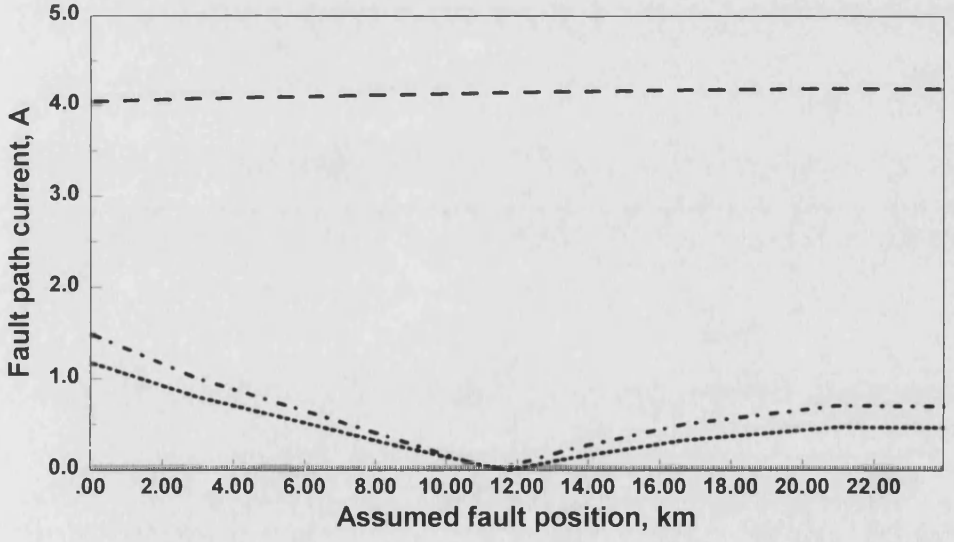

Figure 6.8(c) Fault path currents for an 'a'-phase-earth fault at 11.1 km from end P for the system shown in Figure 5.1(a) (R_f=100 Ω).

_ _ _ _ _ a - phase (scale x 20 of that shown)

_._._._._ b - phase

..... c - phase

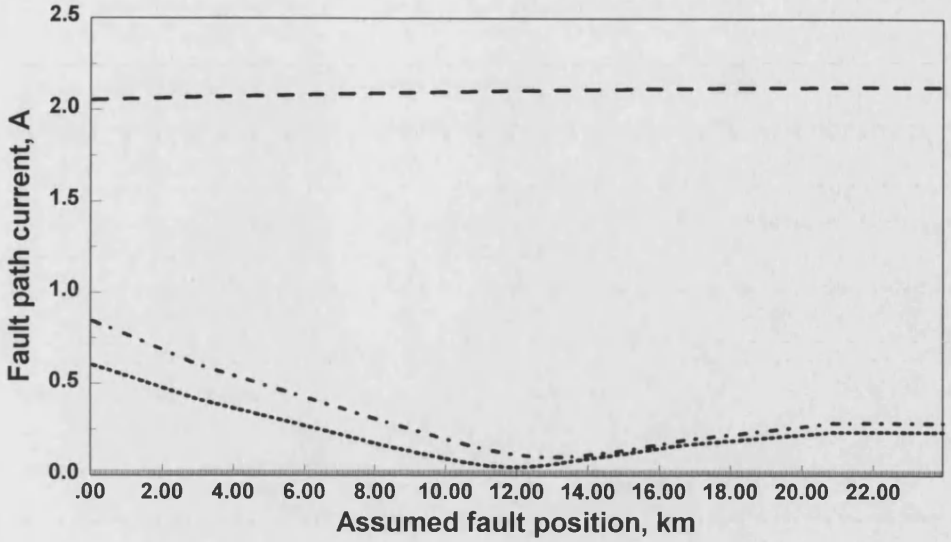

Figure 6.8(d) Fault path currents for an 'a'-phase-earth fault at 11.1 km from end P for the system shown in Figure 5.1(a) (R_f=200 Ω).

a - phase (scale x 20 of that shown)

b - phase

c - phase

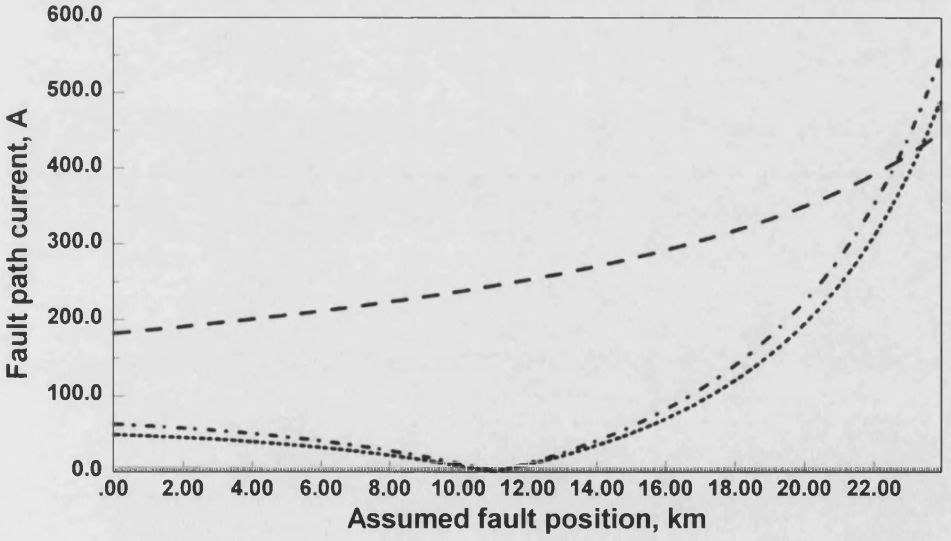

Figure 6.9(a) Fault path currents for an 'a'-phase-earth fault at 11.1 km from end P for the system shown in Figure 5.1(b) (R_f=2 Ω).

a - phase (scale x 5 of that shown)

b - phase

c - phase

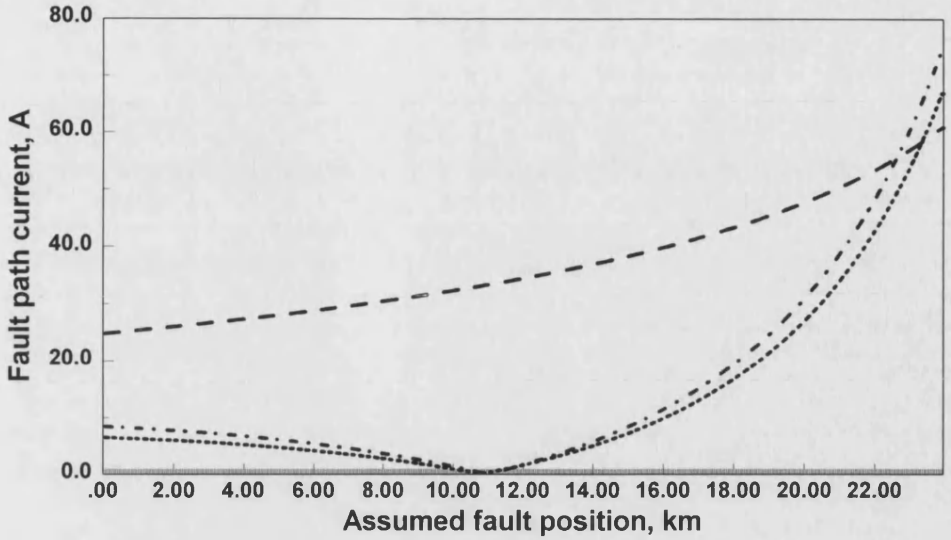

Figure 6.9(b) Fault path currents for an 'a'-phase-earth fault at 11.1 km from end P for the system shown in Figure 5.1(b) (R_f=50 Ω).

_ _ _ _ _ a - phase (scale x 5 of that shown)

_._._._._ b - phase

..... c - phase

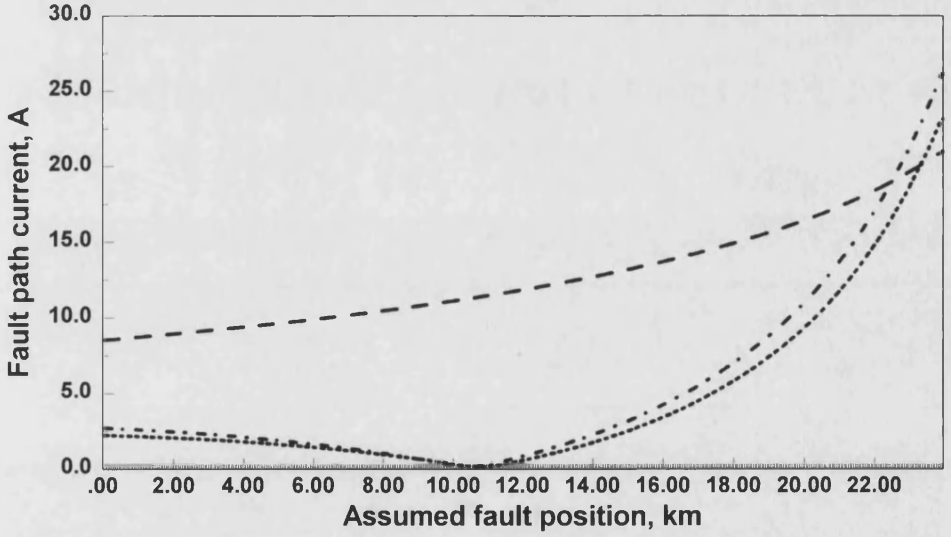

Figure 6.9(c) Fault path currents for an 'a'-phase-earth fault at 11.1 km from end P for the system shown in Figure 5.1(b) (R_f=100 Ω).

_ _ _ _ _ a - phase (scale x 5 of that shown)

_._._._._ b - phase

..... c - phase

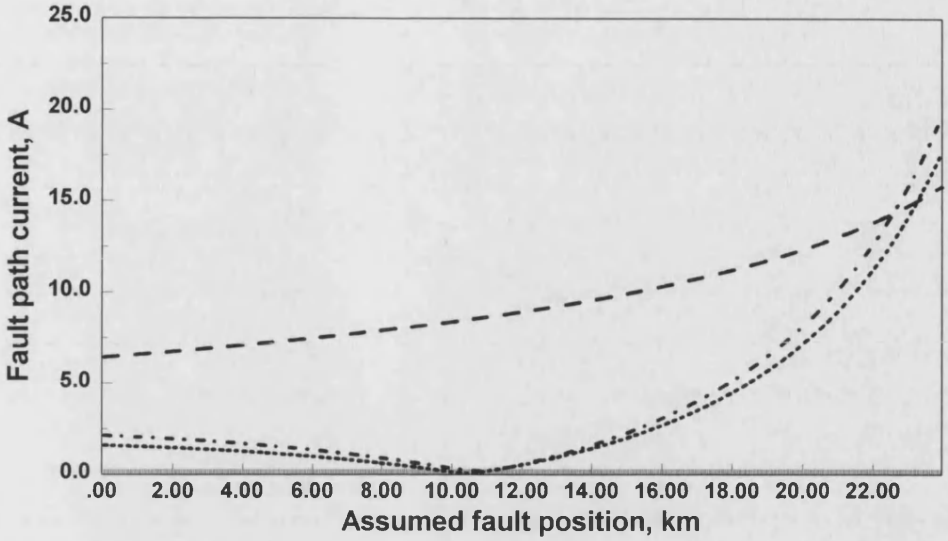

Figure 6.9(d) Fault path currents for an 'a'-phase-earth fault at 11.1 km from end P for the system shown in Figure 5.1(b) (R_f=200 Ω)

- a - phase (scale x 5 of that shown)
- b - phase
- c - phase

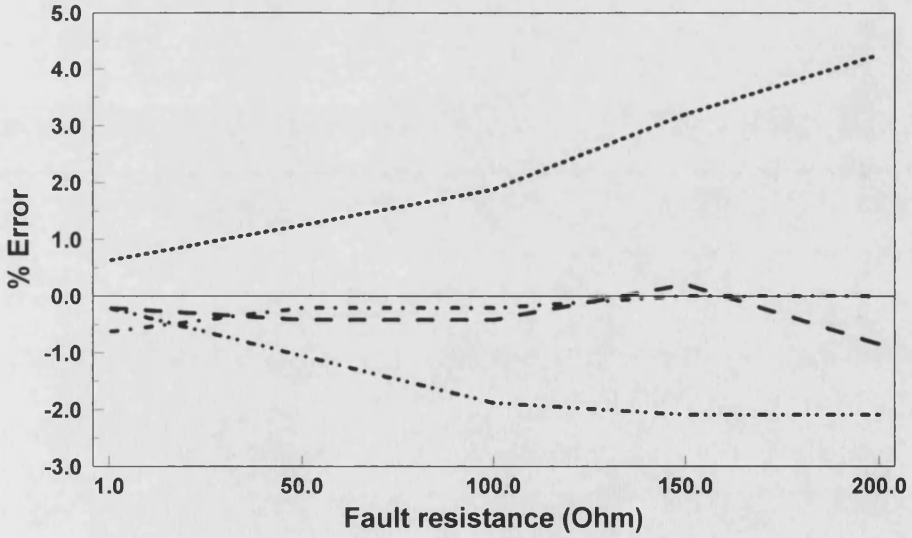

Figure 6.10 Effect of fault path resistance on fault locator's accuracy.

- SLGF for system with remote-end open
- SLGF for a system with remote infeed
- DLGF for system with remote-end open
- DLGF for a system with remote infeed

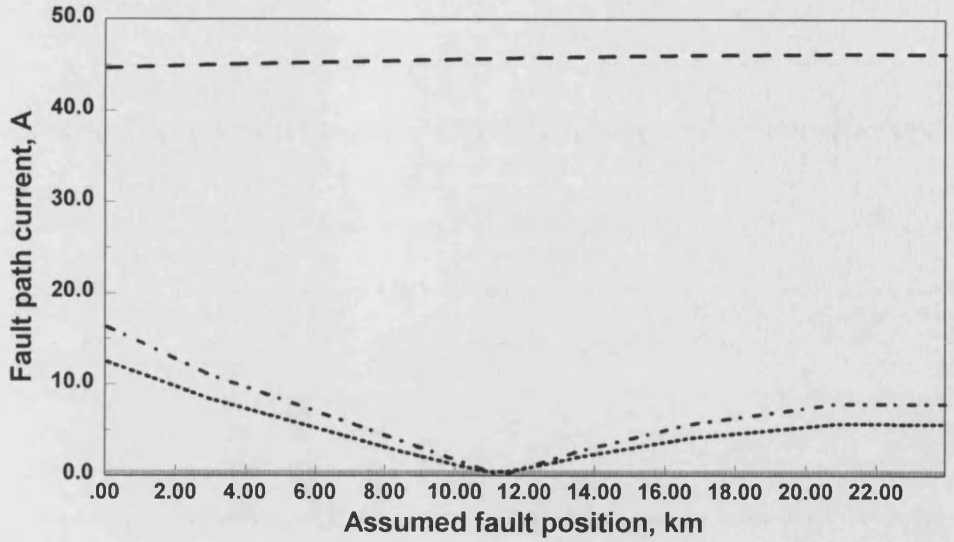

Figure 6.11(a) Fault path currents for an 'a'-phase-earth fault at 11.1 km from end P for the system shown in Figure 5.1(a) (250 MVA SCL at end P, R_f=2 Ω).

- - - - - a - phase (scale x 20 of that shown)
- . - . - . b - phase
..... c - phase

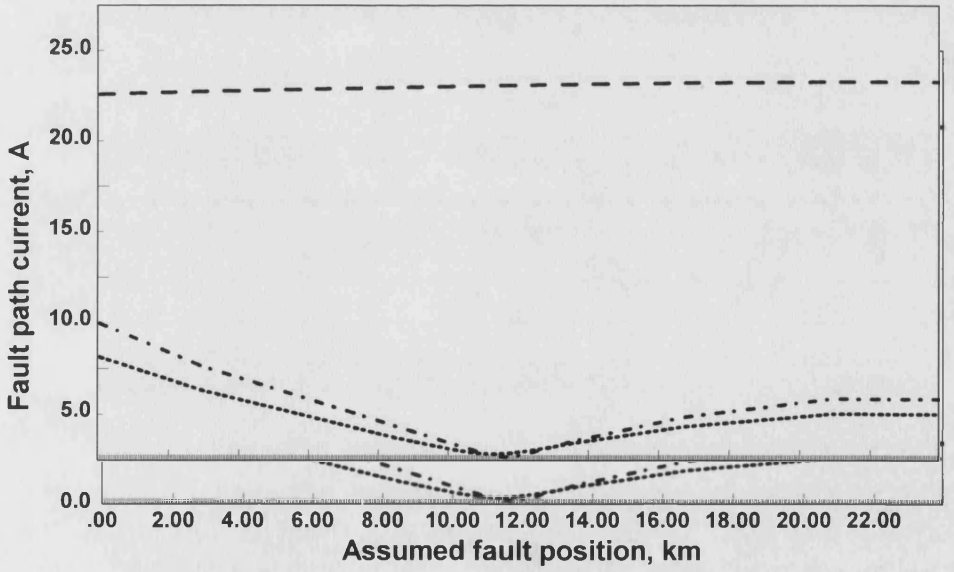

Figure 6.11(b) Fault path currents for an 'a'-phase-earth fault at 11.1 km from end P for the system shown in Figure 5.1(a) (10 MVA SCL at end P, R_f=2 Ω).

- - - - - a - phase (scale x 20 of that shown)
- . - . - . b - phase
..... c - phase

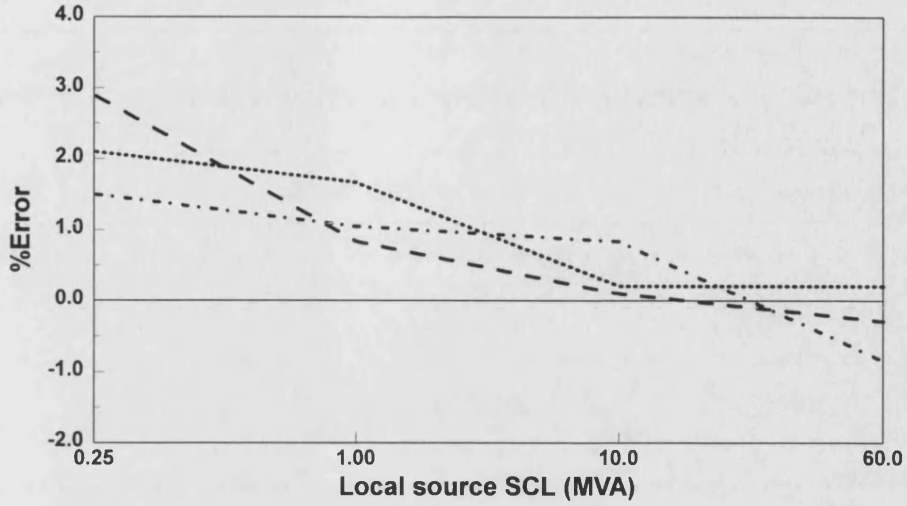

(a)

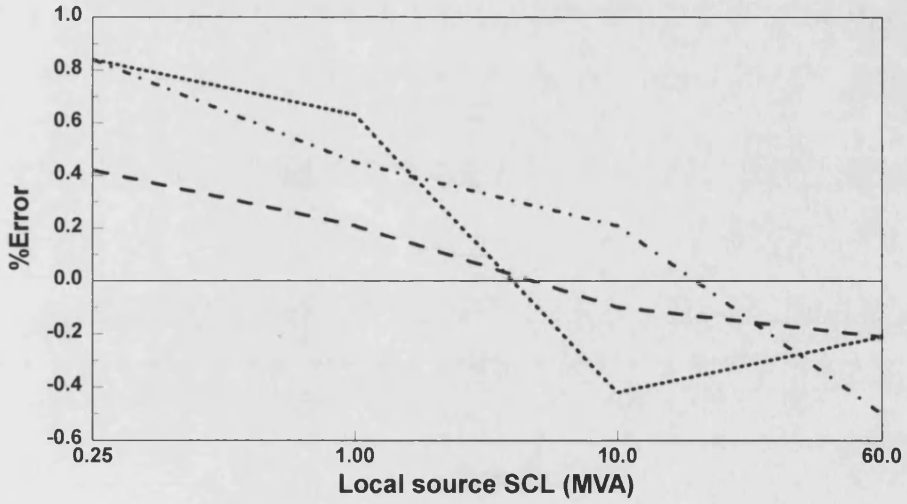

(b)

Figure 6.12 Effect of local source capacity on accuracy for the system shown in Figure 5.1(b) (R_f=2 Ω), remote source SCL = 10 MVA.

(a) Faults created at 11.1 km
(b) Faults created at 16.7 km.

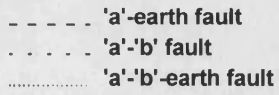

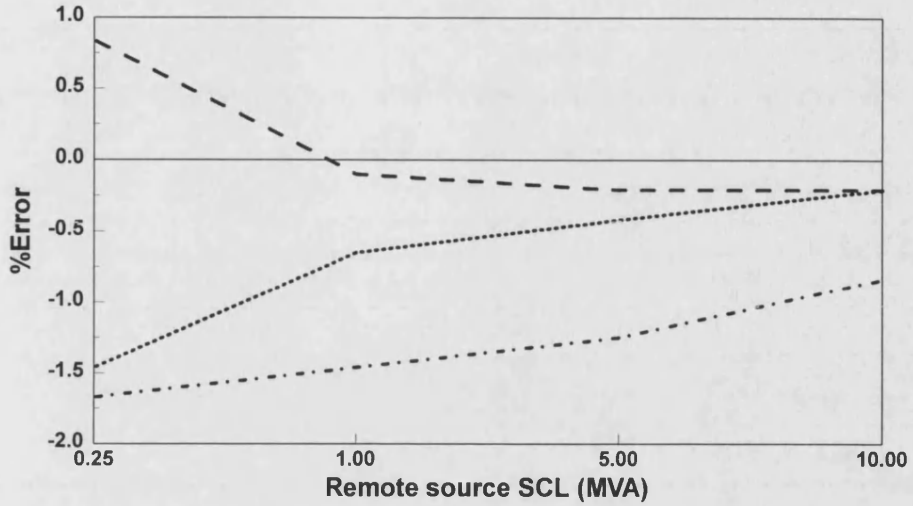

(a)

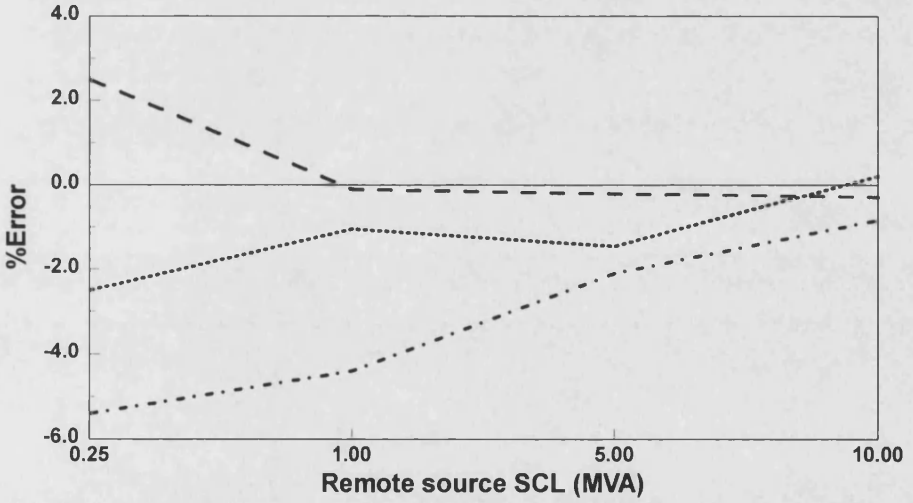

(b)

Figure 6.13 Effect of remote-end source capacity on accuracy for the system shown in Figure 5.1(b) (R_f=2 Ω), local source SCL = 58 MVA.

(a) Faults created at 11.1 km.
(b) Faults created at 16.7 km.

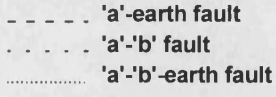

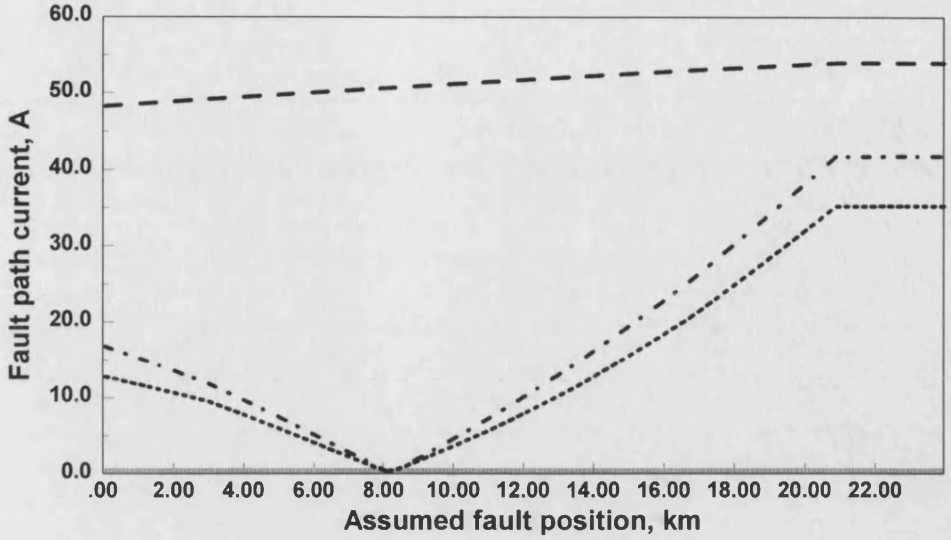

Figure 6.14(a) Effect of dynamic load on accuracy for an 'a'-phase-earth fault at 8.4 km from end P for the system shown in Figure 5.1(a) (R_f=2 Ω).

- - - - - a - phase (scale x 20 of that shown)
- . - . - . b - phase
..... c - phase

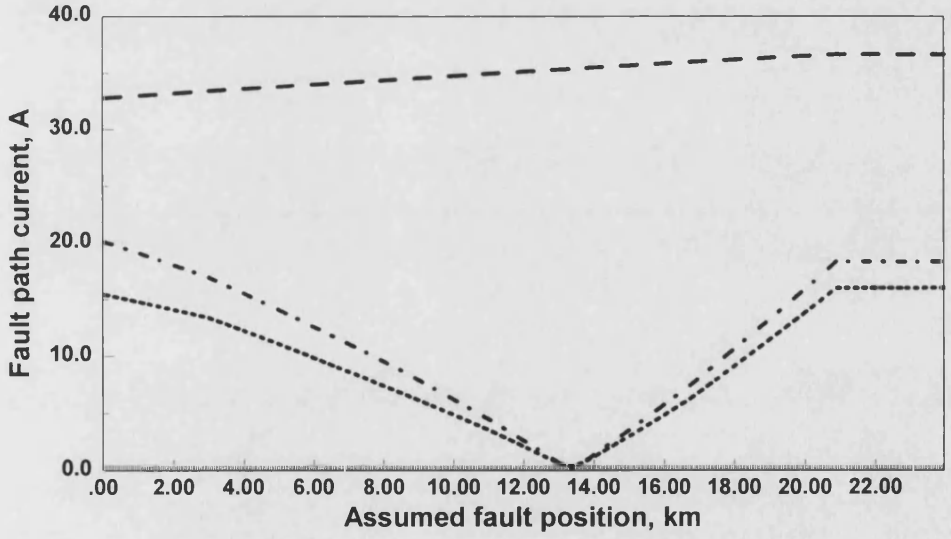

Figure 6.14(b) Effect of dynamic load on accuracy for an 'a'-phase-earth fault at 13.6 km from end P for the system shown in Figure 5.1(a) (R_f=2 Ω).

- - - - - a - phase (scale x 20 of that shown)
- . - . - . b - phase
..... c - phase

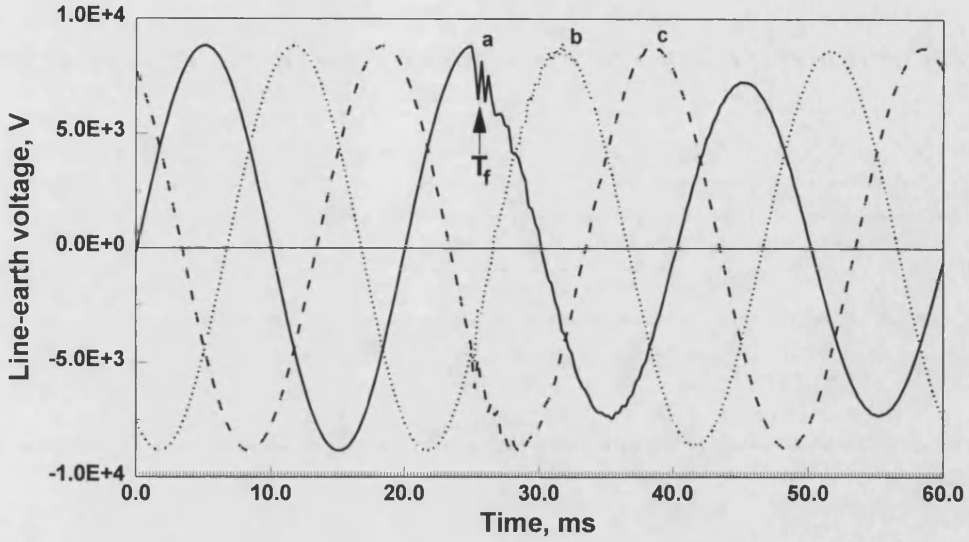

i. Voltage waveforms

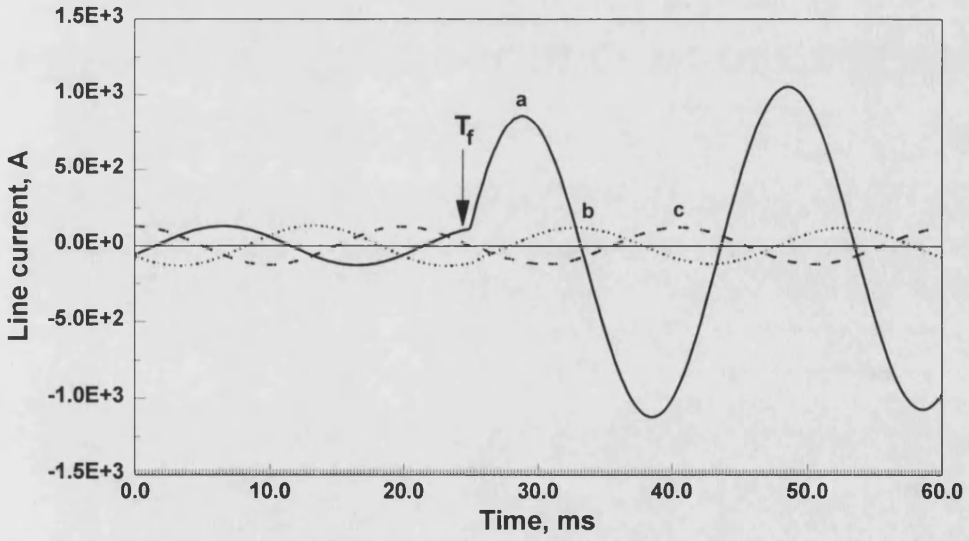

i. Current waveforms

Figure 6.15(a) Voltage and current waveforms for an 'a'-phase-earth fault at 8.4 km of the system shown in Figure 5.1(a) (T_f=fault inception time, R_f=2 Ω).

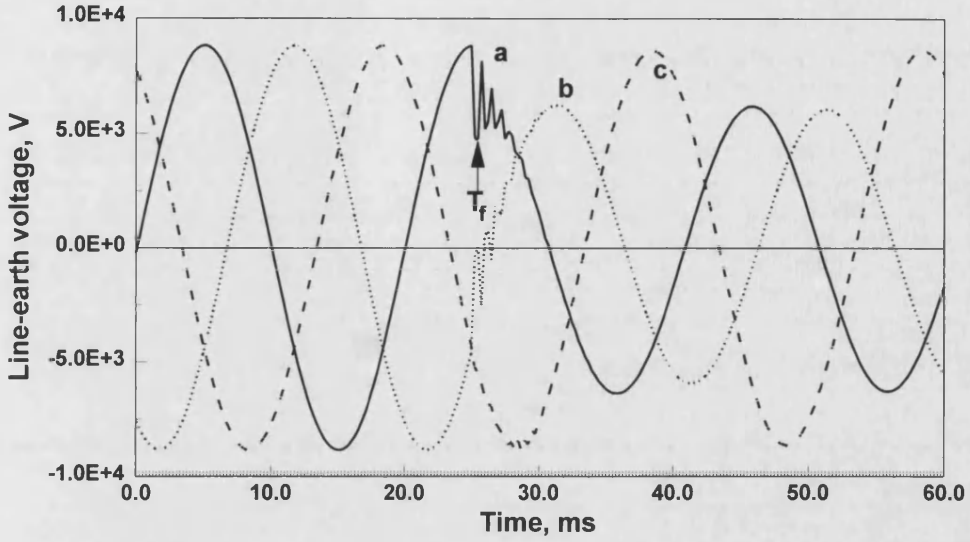

i. Voltage waveforms

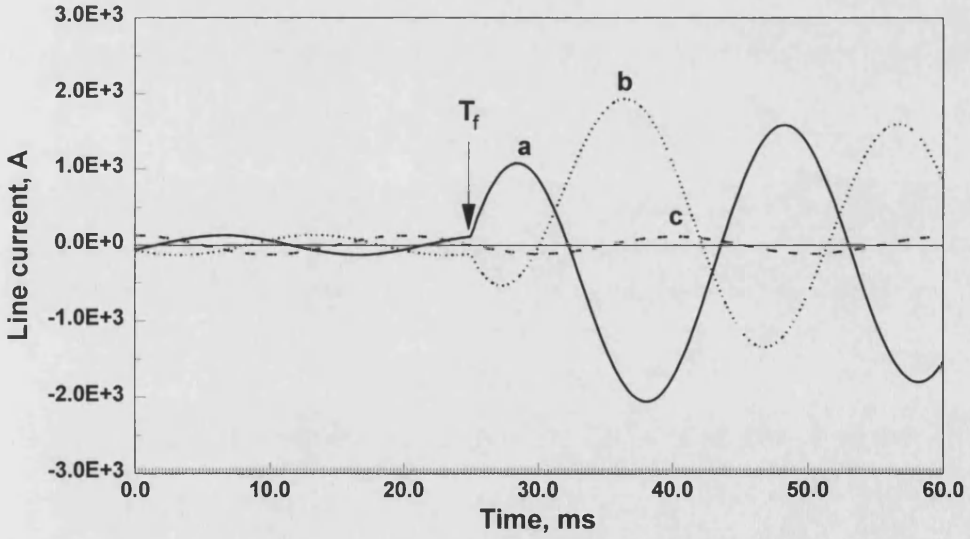

ii. Current waveforms

Figure 6.15(b) Voltage and current waveforms for an 'a'-'b'-phase-earth fault at 8.4 km of the system shown in Figure 5.1(a) (T_f=fault inception time, R_f=2 Ω).

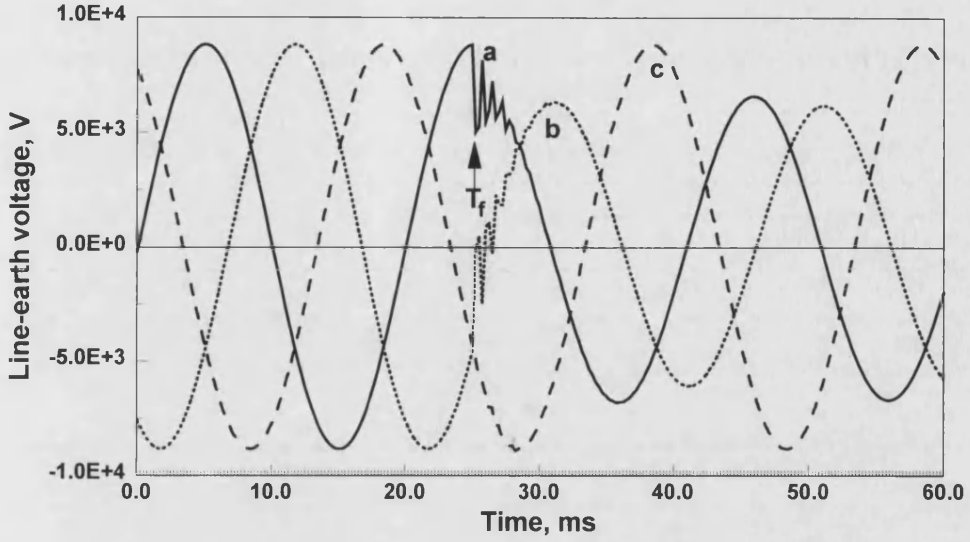

i. Voltage waveforms

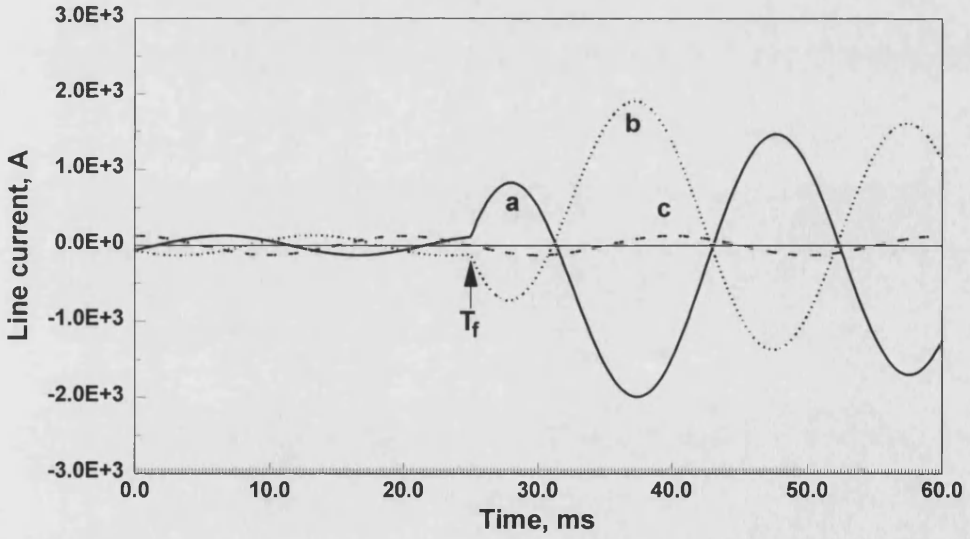

ii. Current waveforms

Figure 6.15(c) Voltage and current waveforms for an 'a'-'b'-phase fault at 8.4 km of the system shown in Figure 5.1(a) (T_f=fault inception time, R_f=2 Ω).

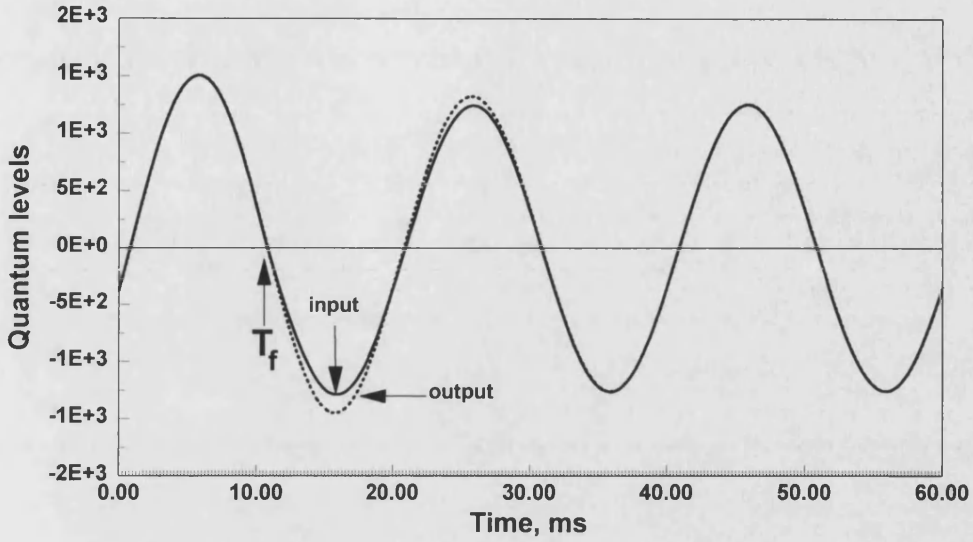

i. Voltage measurements

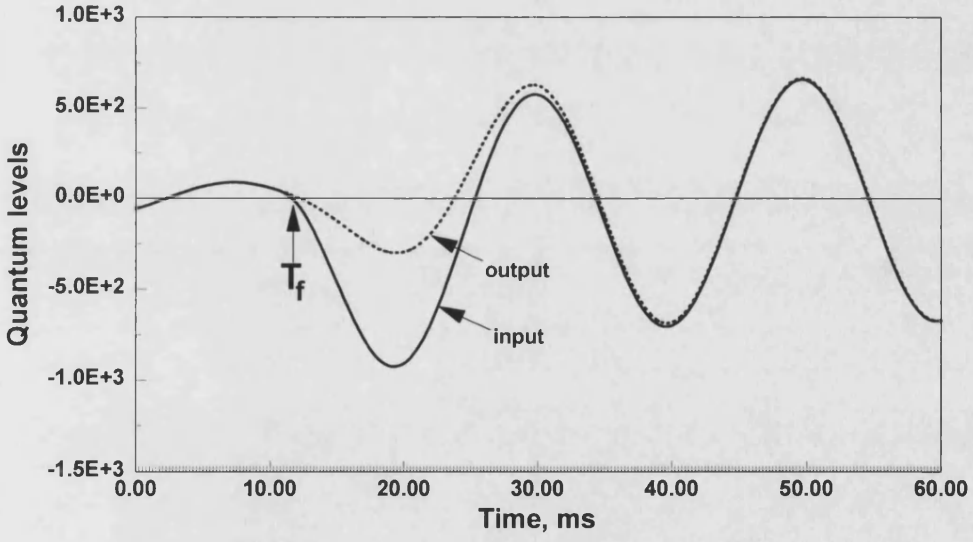

ii. Current measurements

Figure 6.16(a) Input and output of the DFT Filter for an 'a'-earth fault at 8.4 km from end P for the system shown in Figure 5.1(a) (T_f=fault inception time, Rf=2 Ω).

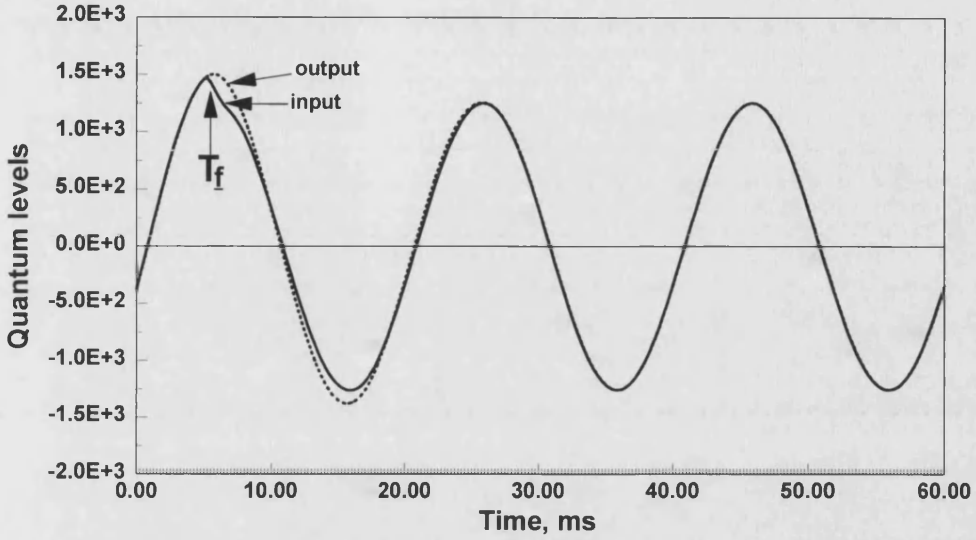

i. Voltage measurements

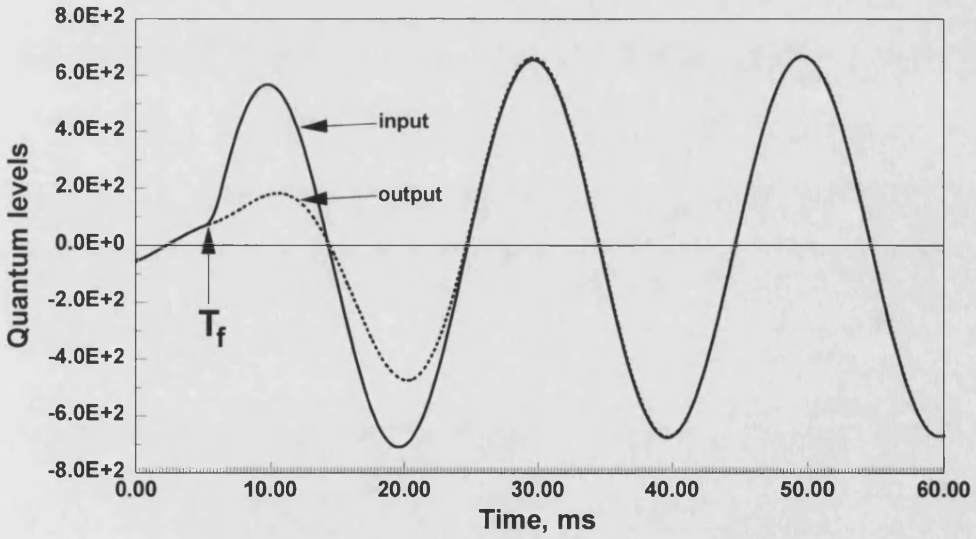

ii. Current measurements

Figure 6.16(b) Input and output of the DFT Filter for an 'a'-earth fault at 8.4 km from end P for the system shown in Figure 5.1(a) (T_f=fault inception time,Rf=2 Ω).

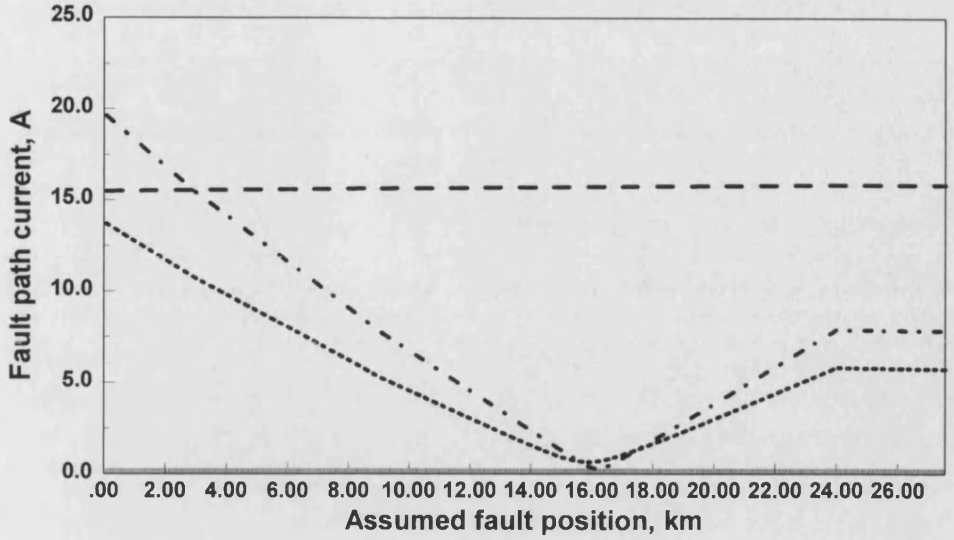

Figure 6.17(a) Fault path currents for an 'a'-phase-earth fault at 16.0 km from end P for the system shown in Figure 5.6(a) (R_f=2 Ω).

a - phase (scale x 100 of that shown)
b - phase
c - phase

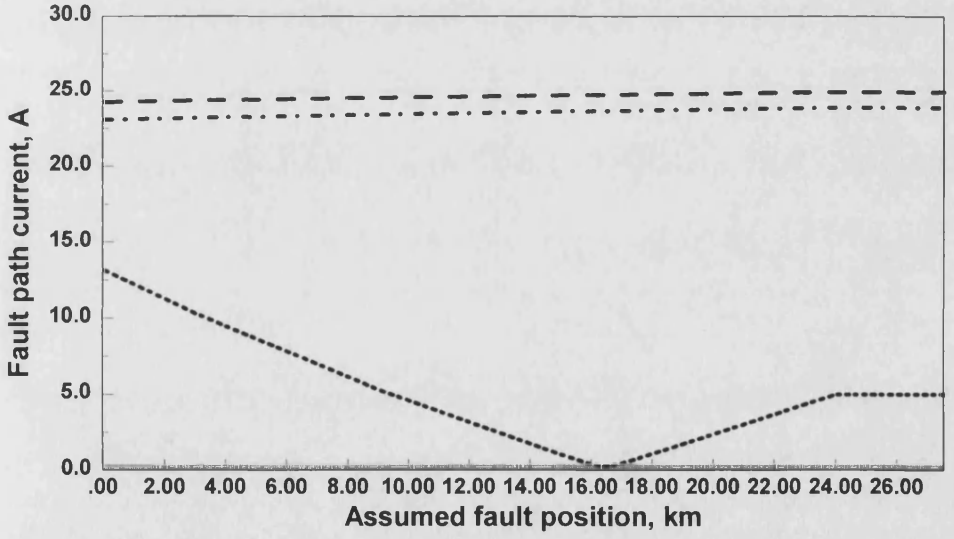

Figure 6.17(b) Fault path currents for an 'a'-'b'-phase-earth fault at 16.0 km from end P for the system shown in Figure 5.6(a) (R_f=2 Ω).

a - phase (scale x 100 of that shown)
b - phase (scale x 100 of that shown)
c - phase

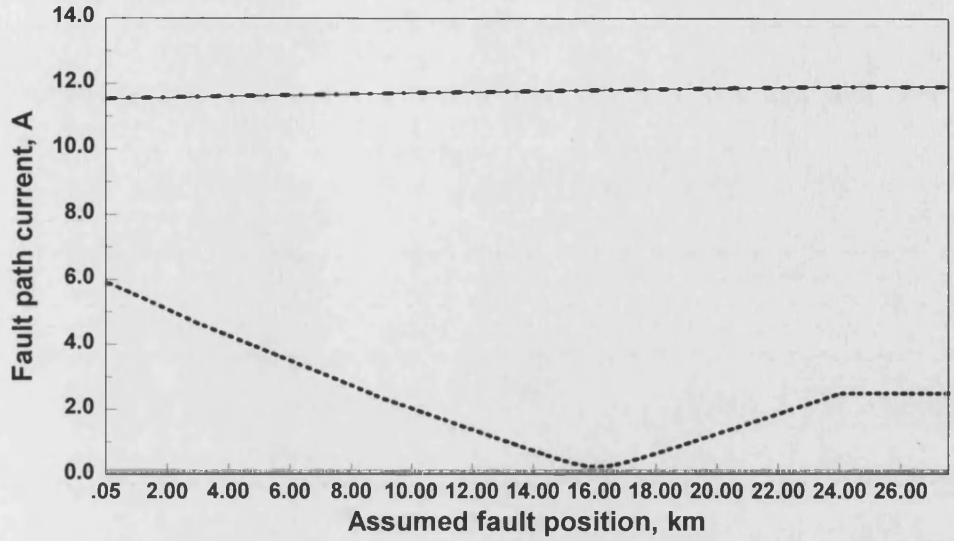

Figure 6.17(c) Fault path currents for an 'a'-'b-phase' fault at 16.0 km from end P for the system shown in Figure 5.6(a).

a - phase (scale x 200 of that shown)
b - phase (scale x 200 of that shown)
c - phase

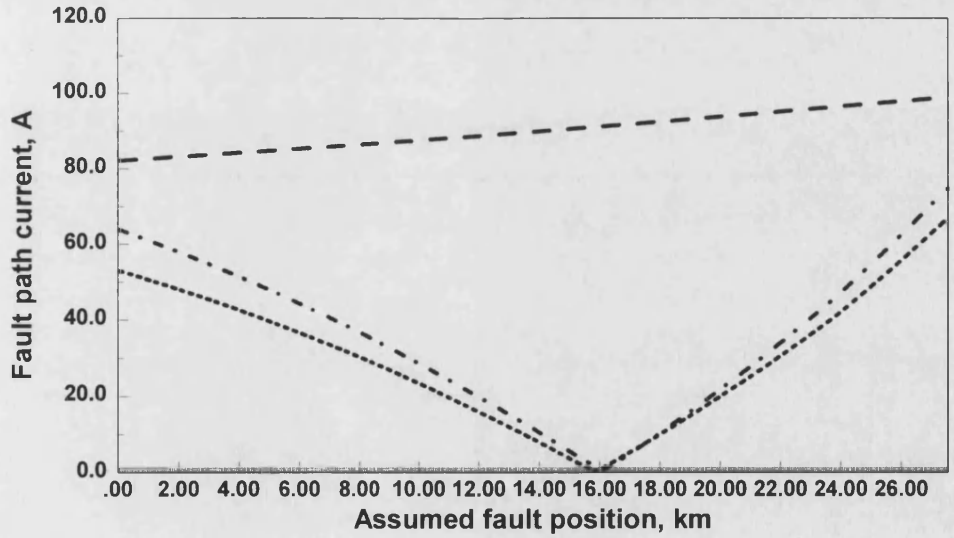

Figure 6.18(a) Fault path currents for an 'a'-phase-earth fault at 16.0 km from end P for the system shown in Figure 5.6(b) (R_f=2 Ω).

a - phase (scale x 20 of that shown)
b - phase
c - phase

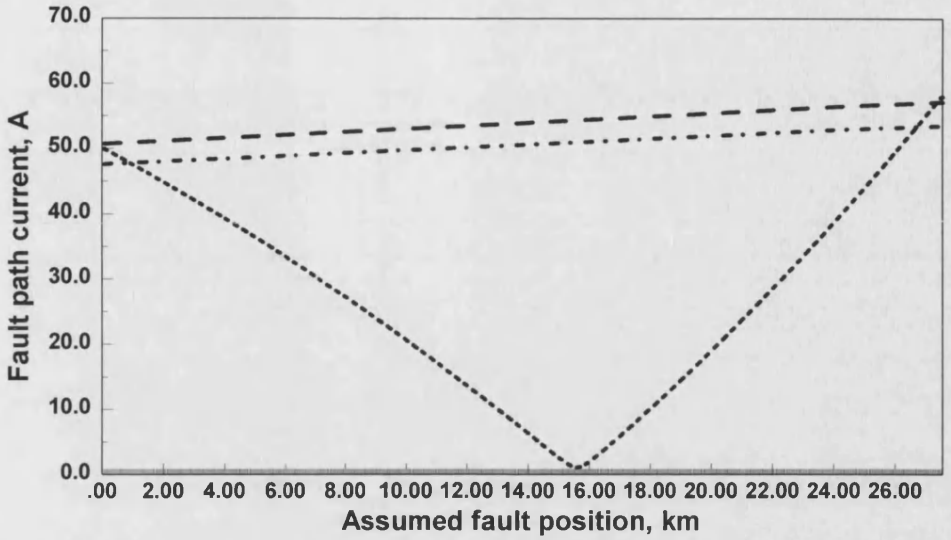

Figure 6.18(b) Fault path currents for an 'a'-'b'-phase-earth fault at 16.0 km from end P for the system shown in Figure 5.6(b) (R_f=2 Ω).

- - - - - a - phase (scale x 50 of that shown)
-.-.-.-. b - phase (scale x 50 of that shown)
..... c - phase

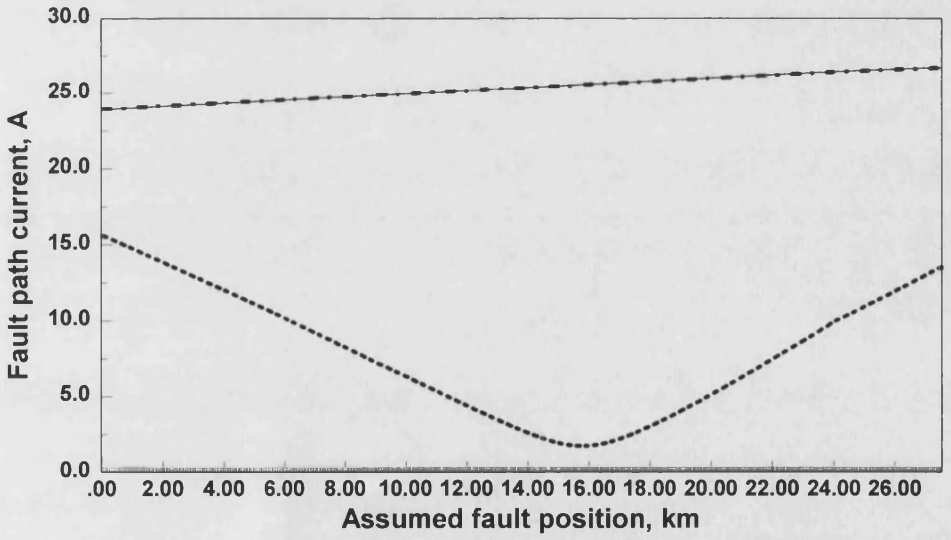

Figure 6.18(c) Fault path currents for an 'a'-'b'-phase fault at 16.0 km from end P for the system shown in Figure 5.6(b).

- - - - a - phase (scale x 100 of that shown)
-.-.-.-. b - phase (scale x 100 of that shown)
..... c - phase

SUMMARY, CONCLUSIONS AND SUGGESTIONS FOR FUTURE WORK

7.1 Summary of Work

This thesis presents an alternative approach to accurately locating faults on overhead radial distribution lines with or without remote source infeed. In the fault location algorithm, the presence of multiple load taps and the change in load capacities with the time of the day are taken into account. It can be applied to the vast majority of practically encountered overhead radial distribution systems and fault conditions.

A general literature review of fault locator techniques for distribution lines has been outlined in Chapter 2. They are divided into three groups: (i) techniques based on travelling waves and high frequency components (ii) techniques based on fundamental frequency components (iii) techniques based on knowledge based approaches. The merits and drawbacks of using each of the methods are also summarised.

The basis of the proposed fault locator has been presented in Chapter 3. The method is based on utilising voltage and current waveforms at one end of a typical distribution system, which are then filtered using Discrete Fourier Transform (DFT) techniques, to extract power frequency components of voltages and currents. The technique described makes use of superimposed components rather than total values of voltages and currents.

Although the fault location technique is based on Computer Aided Design (CAD) studies, however, practical considerations such as the effect of transducers, interface modules/analog filters, quantisation errors, etc. on primary system fault data are also included in the simulation, so that the data processed through the algorithm is very close to that attained from actual fault locators.

In Chapter 4 implementation of the algorithm for a typical distribution system with multiple load taps and possible remote source is explained. In this chapter, evaluation of load and remote source admittance matrices, and calculation of superimposed fault voltages and fault path currents at the assumed fault point are explained.

The interactive nature of the technique based on scanning a particular distribution system comprising of practical 11 kV overhead radial lines is explained in Chapter 5. Also in this chapter, various variables such as static and dynamic loads, line parameters, source configurations that studied are outlined.

An overall performance evaluation of the fault locator algorithm under different fault conditions is presented in Chapter 6. In particular, the effect of fault type and position, fault resistance, remote infeed, fault cycle and source capacity on the accuracy attained are examined. Finally, a sensitivity analysis of the fault locator algorithm to such non-algorithmic errors such as load tap and source capacity estimations, line lengths, etc. is also presented in Chapter 6.

7.2 Conclusions

The basis of a new approach in single-ended fault location for overhead distribution systems is described. The fault location algorithm is based on utilising superimposed phase signals and special filtering techniques are utilised to

accurately extract the fundamental phasors from the measured fault signals.

The technique, based on an interactive approach whereby an assumed fault point is varied systematically until the actual fault point is found, has culminated in a fault locator design that gives a high accuracy for the vast majority of practically encountered system and fault conditions; these include different source impedances (local and remote), the presence of load taps (static and dynamic), fault resistance, etc. The results presented also show the locator's robustness to large errors in the estimation of load taps and remote source capacity (if present).

Although the algorithm has been tested using CAD techniques, emphasis is placed on examining its performance using data as though it were captured through actual fault recorders; it is clearly demonstrated that with this approach, the algorithm retains its high accuracy in the presence of errors introduced by transducers and hardware, the errors attained being less than about 3 % for the majority of system and fault conditions studied.

The algorithm is initially tested on a plain distribution system with no load taps. As a second step the technique is extended to a more realistic distribution system with load taps.

Finally the algorithm is implemented on a typical 11 kV overhead distribution system with horizontal line configuration encountered in the UK. In this system presence of loads tapped off from the main feeder throughout the system are taken into account and also faults on systems with remote infeed are studied in details. The algorithm is also tested on a 33 kV distribution system both with and without remote source.

The fault location algorithm is firstly extensively tested for different fault positions and types for a practical 11 kV system without any remote-end infeed. In this process, various types of fault are created throughout the system i.e. at tap

points, in between taps, etc. It is shown that as the fault moves to the open end, there is a small degradation in the performance attained. When comparing the accuracies for different types of fault, it is shown that those obtained for double-phase-earth and phase-phase faults are slightly less than those for the corresponding single-phase-earth faults. It is important to note that the fault location algorithm presented herein does not require fault classification.

The performance of the technique described herein is also examined for faults on the distribution system with remote-end infeed. It is shown that in comparison to the results attained for the open ended radial feeder system the presence of remote infeed improves the accuracy slightly. This is a significant advantage and in marked contrast to conventional fault location algorithms, particularly those based on impedance measurements, whose accuracy deteriorates in the presence of any remote infeed.

It is shown that the fault locator gives an inherently accurate evaluation of fault position that is not significantly influenced by the changes in fault resistance. In the case of single-phase-earth faults, however, there is small degradation in performance (more so in the case of systems with remote end open), especially when the fault resistance goes above about 100Ω. Nevertheless, the overall performance attained is significantly superior to that achieved with conventional techniques, particularly those based on impedance to fault measurements, which tend to produce excessive errors when dealing with resistive faults.

In this technique, rather than total values of currents and voltages superimposed components are used. Thus the effect of preloading conditions and source impedance on accuracy is virtually eliminated. Hence the proposed algorithm does not require any local source impedance setting, and therefore any inaccuracies (or changes) in source parameters are of no consequence to this technique. This is a significant advantage over other techniques, since in distribution systems source capacities and load currents change with the time of day.

The effect of dynamic loads on the fault locator's accuracy has been tested for a system with no remote infeed source. In the fault location algorithm developed, any transients caused by the switching of dynamic loads are filtered-out by the DFT technique employed. From the results attained in Chapter 6, it is seen that the accuracy is slightly degraded for phase-to-phase faults. However, the accuracy attained is found to be well within acceptable limits (± 2.9 %, see Table 6.10).

The developed fault location algorithm cannot operate under three phase short circuit conditions. As a consequence, an alternative technique is proposed in this work for estimating the distance to fault under three phase short circuit conditions. From the limited investigations carried out in Chapter 6 on this alternative algorithm, it was found that the proposed technique can locate the distance to faults with acceptable accuracy for practical systems (Table 6.12).

For the practical distribution systems studied, different conductor sizes are employed for the main feeder and tap lines. The results presented in Chapter 6 show that the algorithm can cope with these differing line sections and X/R ratios in distribution system, i.e. its accuracy is not unduly affected for such faults (Table 6.15).

The effect of source capacity on fault locator's accuracy has been tested for a system terminated with a remote infeed source. It was found that for faults close to the sources, the accuracy is slightly affected. From the analysis of the studies conducted under different source conditions and as given in Chapter 6, it was found that the fault location is estimated with higher accuracy as the fault moves closer to stronger source. This effectively means that for faults closer to the remote-end weak source, the accuracy of estimation is found to be slightly less accurate than for faults closer to the strong source. For systems with remote-end open, it is found that the accuracy of fault location estimation gets better as the capacity of the local source is increased.

In distribution systems, for power factor improvement, capacitor banks are used. Capacitor banks pose problems to fault location techniques which are based on high-frequency components. In the technique developed in this work, the presence of capacitance on its own or as part of a load, makes little difference to the accuracy attained.

The faults can occur at any point on the voltage waveforms and thus tests were carried out to check the effect of fault inception angle. From the analysis of the results obtained in Chapter 6 for this condition, it was found that there is some effect of point on wave fault inception on the accuracy of the developed fault location algorithm, the accuracy attained was the highest when faults occur at the crest values of the voltage waveforms and the error was found to be a maximum at the zero point on wave.

An extensive sensitivity analysis was carried out to investigate the effects of non-algorithmic errors originating from source and load capacity estimations on the fault location algorithm developed in this thesis. For open end distribution systems, up to ±10 % errors were introduced in estimation of the loads. This condition led to around 3 % error in fault location estimation under single line to ground faults (see Tables 6.23-6.27).

The effect of estimations of the line length errors on the accuracy of the developed fault location algorithm has been analyzed. Line lengths between the taps and tapped lines were subjected to ±5 % error. It is clearly evident from the results presented in Chapter 6 that the algorithm detects the fault location with high accuracy and very small error. Of all the tests performed, a ±5 % error in the line sections, the highest error was found to be for a-b fault of 7.7 % (see Tables 6.32-6.33).

7.3 Suggestions For Future Work

The work described in this thesis shows rigorous testing of the fault location algorithm under different fault conditions and for different system configurations. However, the developed algorithm requires further investigations using real data captured from systems operating in the real time mode.

The fault location technique developed herein can localise faults with a high degree of accuracy when faults occur between taps or on the tap points themselves. However, for faults on the lines feeding the tap loads, it has difficulty in the sense that it indicates the faults between the two nearest taps. As part of the future work, the algorithm needs to be further developed to cater for this drawback i.e., there is a need to be able to localise the fault on the tap line itself when such a fault occurs.

The algorithm described in this thesis is developed for overhead distribution lines. There are many distribution systems with underground cables. The accurate measurement of distance to fault in distribution systems with underground cables is very important, because the cost involved in the repair of the fault is much higher than on overhead lines. In order to conduct a proper search for the faulty part of the cable, there are many obstructions mainly due to the nature of city streets. Inaccurate estimation could result into unnecessary digging up of streets/roads which could be very costly. Hence as part of future work, a logical step would be to develop the algorithm further in order to implement it for distribution underground cables or composite systems comprising sections of cables and overhead lines.

Finally, it can be concluded that the fault location technique developed in the research work presented in this thesis, is suitable for a vast majority of practically encountered different system and fault conditions in overhead distribution systems.

The novel approach presented is relatively simple to use in comparison to other traditional techniques and has many significant advantages over the latter.

In essence, it signifies a major breakthrough in accurate fault location on low voltage distribution systems, the complexity of which is increasing.

References

1. T. Gönen: *Electric Power Distribution System Engineering*, Text Book, McGraw-Hill, 1986.

2. Westinghouse Electric Corporation: *Electrical Transmission and Distribution Reference Book*, East Pittsburgh, 1964.

3. E Openshaw Taylor, G.A. Boal: *Electric Power Distribution 415V-33kV*, Text Book, Chapter:3, published by Edward Arnold Ltd, 1966.

4. L.V. McCall: "Distribution automation demonstration project", *IEEE Transactions on Power Apparatus and Systems,* vol. PAS-100, No.4, April 1981, pp.1744-1751.

5. P.C. Lyons and S.A. Thomas: "Microprocessor - based control of distribution systems", *IEEE Transactions on Power Apparatus and Systems*, vol. PAS-100, No.12, December 1981, pp. 4893-4899.

6. T.W. Stringfield, D.J. Marihart, and R.F. Stevens: "Fault location methods for overhead lines", *Transactions of the AIEE, Part III - Power Apparatus and Systems*, vol. 76, August 1957, pp.518-530.

7. A.A. Girgis, D.G. Hart, W.L. Peterson: "A new fault location technique for two and three terminal lines", *IEEE Transactions on Power Delivery*, vol.7, No.1, 1992, pp.98-107.

8. *Protective Relays Application Guide*, GEC ALSTHOM Measurements Ltd,

1987.

9. L. Erikson, M.M. Saha, G.D. Rockefeller: "An accurate fault locator with compensation for apparent reactance in the fault resistance resulting from remote-end infeed", *IEEE Transactions on Power Apparatus and Systems*, vol. PAS-104, No.2, February 1985, pp. 424-435.

10. T. Takagi, Y. Yamakoshi, M. Yamura, R. Kondow, T. Matsushima: "Development of a new type fault locator using the one-terminal voltage and current data", *IEEE Transactions on Power Apparatus and Systems*, vol PAS-101, No.8 August 1982, pp 2892-2898.

11. M.S. Sachdev, R. Agarwal: "A technique for estimating transmission line fault locations from digital impedance relay measurements", *IEEE Transactions on Power Systems*, vol. PWRD-1, No.2, April 1986, pp.242-451.

12. D.J. Lawrence, D.L. Waser:"Transmission line fault location using digital fault recorders.", *IEEE Transactions on Power Delivery*, vol.3, No 2, April 1988, pp 496-502.

13. A.A. Girgis, Christopher M. Fallon, David L. Lubkeman:"A fault location technique for rural distribution feeders.", *IEEE Transactions on Industry Applications*, vol. 29, No.6, November 1993, pp.1170-1175.

14. A.A. Girgis, Christopher. M Fallon: "Fault location techniques for radial and loop transmission systems using digital fault recorded data", *IEEE Transactions on Power Delivery*, vol. 7, No.4, October1992, pp 1936-1945.

15. R. Das, M.S. Sachdev, T. S. Sidhu: "A technique for estimating location of shunt faults on distribution lines.", Proc IEEE, Wescanex'95.

16. J. Zhu, D.L. Lubkeman, A.A. Girgis: "Automatic fault location and diagnosis on electric power distribution feeders.", IEEE Winter Meeting, 1996.

17. R.K. Aggarwal, D.V. Coury, A.T. Johns and A. Kalam: "A practical approach to accurate fault location on extra high voltage teed feeders", *IEEE Transactions on Power Delivery*, vol 8, No.3, July 1993, pp 874-883.

18. G.J. Clarke H.E. Horn: "Monitoring and protection systems suited distribution systems.", *Proc. Third Int. Conference Developments in Power Systems Protection*, 1985, pp 199-203.

19 . M. El-Hami, L.L. Lai, D.J. Daruvvala and A.T. Johns: "A new travelling-wave based scheme for fault detection on overhead power distribution feeders", *IEEE Transactions on Power Delivery*, vol.17, No.4, October 1994, pp 1825-1833.

20. A.T. Johns, L.L. Lai, M. El-hami and D.J. Daruvala: "A new approach to directional fault locator for overhead power distribution feeders", *IEE Proceedings*, Pt. C, vol.138, July 1991, 351-357.

21. W. Tenschert: "Fault location in Radial Networks", *Transmission and Distribution International*, Third quarter, 1994.

22. H. Kakimoto, T. Hayashi, H. Handa, K. Yukihira, Y. Okamura and N. Odaka: "Development of automatic fault point locating and sectional isolating system for power distribution line", *Electrical Engineering in Japan*, vol.115, No.5, 1995, pp 75-87.

23. Yuan-Yih Hsu, F.C. Lu, Y. Chien, J.P. Liu, J.T. lin, H.S. Yu, R.T. Kuo: "An expert system for locating distribution system faults", *IEEE Transactions on Power Delivery*, vol. 6, No.1, January 1991, pp 336-372.

24. P. Jarventausta, P. Verho, J. Partanen: "Using fuzzy sets to model the uncertainity in the fault location process of distribution networks", *IEEE Transactions on Power Delivery*, vol. 9, No.2. April 1994, pp 954-960.

25. A.T. Johns, P.J. Moore, R. Whittard: "New technique for the accurate location of earth faults on transmission systems", Proc. IEE, Gener., Transm., Distrib., vol 142, No 2, March 1995, pp 119-127.

26. E.B. Makram, M.A. BOU-RABEE and A.A. Girgis: "Three-phase modeling of unbalanced distribution systems during open conductors and/or shunt fault conditions using the bus impedance matrix", *Electric Power Systems Research*, No.13, 1987, pp 173-183.

27. T. Gönen, : *Electric Power Transmission System Engineering*, Text Book, McGraw-Hill, 1986.

28. D. Novosel, D.G. Hart, E. Udren and M. M. Saha: "Fault location using digital relay data", *IEEE Computer Applications in Power*, July 1995, pp 45-50

29. D. H. Sheingold: *Digital Conversion Handbook*, 3. edition, Prentice-Hall, 1986.

30. P. Bornard, J.M Tesseron, J.C Bastide, M. Nourris: "Field experience of digital fault recorders and distance relay in EHV substations." *IEEE Transactions on Power Apparatus and Systems*, vol. PAS-103, No.1, January 1984, pp 133-137.

31. V. Cook: "Fundamental aspects of fault location algorithm used in distance protection": *IEE Proceeding*, No.133, Pt.5, 6 Sept. 1986, pp 359-368.

32. K. Srinivasan, A. St-Jacques: "A new fault location algorithm for radial transmission lines with loads," *IEEE Transactions on Power Delivery*, vol.4, No.3, July 1989, pp 1676-1682.

33. C. Concordia, S. Ihara:" Load representation in power system stability studies." *IEEE Transactions on Power Apparatus and Systems*, vol. PAS-101, No.4 April 1982, pp 969-977.

PUBLISHED WORK

The following papers are based on the work described in this thesis:

1. Y. Aslan, R. K. Aggarwal, and A. T. Johns, "Fault location in Overhead Distribution Systems Using Superimposed Components", 30th Universities Power Engineering Conference 1995 at University of Greenwich, UK, September, 1995.

2. R. K. Aggarwal, Y. Aslan, and A. T. Johns, "An Interactive Approach to Fault Location on Overhead Distribution Lines with Load Taps", to be presented at Sixth International Conference on Developments in Power System Protection, University of Nottingham, 24-27 March, 1997.

2. R. K. Aggarwal, Y. Aslan, and A. T. Johns, "A New Concept in Fault Location for Overhead Distribution Systems Using Superimposed Components", In print, Proceedings of IEE, Part C: Generation, Transmission and Distribution. UK.

FAULT LOCATION IN OVERHEAD DISTRIBUTION SYSTEMS USING SUPERIMPOSED COMPONENTS

Y ASLAN R K AGGARWAL A T JOHNS

School of Electronic & Electrical Engineering
University of Bath
Bath BA2 7AY, UK

ABSTRACT

This paper presents the basis of a new digital fault location technique for locating faults in overhead distribution systems. An 11kV distribution line with taps is simulated using the well known Electro-Magnetics Transients Program (EMTP) software and embedded into the simulation is transducer/hardware errors associated with practical digital fault locators. The technique developed, based on an interactive approach, utilises fault voltages and currents at one end only of a typical distribution system, with and without remote infeed, and also takes into account the presence of three-phase, two-phase and single phase taps.

The paper concludes by illustrating the performance of the fault-locator developed under a variety of different system and fault conditions, including differing source impedances, types of fault, fault resistance, and different types of load taps.

1. INTRODUCTION

Distribution systems constitute the major link between subtransmission systems and customers. Because of simplicity of construction, maintenance advantages, low cost in instalment, etc., the majority of distribution systems are overhead systems. Overhead distribution systems are subject to abnormal weather conditions such as heavy winds, falling trees, heavy snow, ice, lightning, outages caused by accidents, fires, foreign objects, tree trimming and so on. In overhead distribution systems 60-80% of faults are transient in nature and can be cleared without permanent damage to plant and equipment by high-speed clearance of the fault. Normal service can be restored by means of auto-reclosing facilities. The need to locate permanent and transient faults in distribution systems has been essential for power companies to provide a service without any outages.

In EHV transmission lines fault location has been recognized as an essential requirement and relatively little work has been done on distribution lines. A technique has been developed by Girgis [1] for location of faults in rural distribution systems. This technique is based on the apparent impedance, in which the current and voltage information is obtained at a single location. The taps are taken into account and voltages and currents are updated at tap points. By using EMTP very accurate results are obtained. However in this technique remote infeed and interface errors are not considered.

Another technique is reported in references [2,3]. In these techniques rather than the power frequency, high frequency components are used, which are injected by the fault at the fault point and propagate up and down the line. By using specially designed line trap and stack tuners, the required high frequency spectrum is obtained and the direction and location of the fault is found.

Clarke and Horn have introduced a fault location technique for overhead distribution systems using a new sensor[4]. The overhead line mounted sensor relies on a newly developed single phase integrated current and voltage transformer. By measuring the phase angle between the resultant voltage and current vectors, the direction of the fault is detected.

Another technique is developed by Austria distribution authority to locate the faults in composite distribution systems[5]. Composite systems comprise of both overhead lines and underground cables. In this technique, impedances of line sections are stored in a computer and during the fault, the impedance measured by the relay is compared with the stored data. Again since this technique depends on the apparent impedance seen by the relay, the presence of a remote infeed introduces unacceptable errors and moreover during the fault, the remote infeed is disconnected to convert the system into a radial system. In conventional fault algorithms based on apparent impedance measurement, existence of a remote infeed and the presence of taps cause unacceptable errors[6].

A new concept in digital fault location for overhead radial distribution systems with taps is presented here and is based on superimposed components. By the use of superimposed components rather than total quantities, the adverse effect of line loading and source impedance on accuracy is virtually eliminated[7]. In this digital fault location technique, voltage and current information is obtained at a single location and presence of single, two and three phase taps are taken into account for an overhead distribution system with or without remote infeed. To increase the accuracy of location, prefault and postfault current and voltages are filtered at the power frequency by using Discrete Fourier (DFT) digital filtering techniques.

2. FAULT LOCATION TECHNIQUE

A digital fault location technique for overhead radial distribution lines as described here, uses voltage and current information obtained from a single location and is based on superimposed components.

Superimposed components are simply the difference between prefault and postfault current or voltage components. In the calculation of superimposed voltage and current components at the fault point, using measured voltages and currents, capacitive reactance of the line is ignored since the length of distribution systems are short and the voltage is low.

In this technique, superimposed voltages are calculated at the assumed fault point and then back injected to check the fault path currents in the healthy phase or phases as seen in Fig.1. When a

zero or near to zero value is obtained for the healthy phase or phases, this particular point is assumed as the fault point which in turn gives the distance to the fault.

A fault location algorithm is developed to locate the faults in a distribution system in an interactive fashion. For the entire line length at every 50 metres, superimposed voltages are evaluated and then injected back to find the fault path currents. The fault path currents are written into an output file for further inspection. When any of the current or currents become a zero or near zero value, then this gives the fault point and hence the distance to the fault.

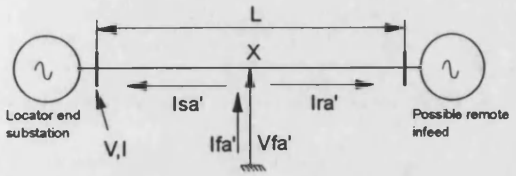

Fig.1 Injection of superimposed fault voltages

$$Ifa' = Isa' + Ira' \quad (1)$$

Ifa'	Superimposed fault path current at the assumed fault point
Vfa'	Superimposed fault path voltage at the assumed fault point.
Isa'	Superimposed sending end current
Ira'	Superimposed receiving end current
X	Assumed fault point
V,I	Recorded voltage and current

This technique is insensitive to fault resistance, source impedance and unbalance conditions which are very common in distribution lines. In order to attain a high degree of accuracy in the location of a fault, it is important to be able to accurately extract the power frequency voltage and current phasors from the post fault waveforms which in practice can have significant transients ranging from high frequencies down to DC levels (Fig.3,4 are typical examples). Since these transients are quite severely attenuated after about a cycle after the occurrence of a fault, extensive series of studies have shown that the application of filtering techniques based on Fourier transform methods produces very accurate voltage and current fundamental phasors, provided that the first cycle of post-fault data is ignored.

The effect of transducers (CTs and CVTs) and hardware errors such as antialiasing filters and quantisation are taken into account, so that the information processed throughout the fault locator is very close to real-life situation. The complete schematic of fault location algorithm is shown in Fig.2.

3. DISTRIBUTION SYSTEM SIMULATION:

The simulation of the 11KV distribution system is carried out using the well proven software EMTP. The overhead distribution lines employed in this work are based on a single circuit 11KV horizontal construction line currently used on the UK distribution system.

The conductor configuration is such that the conductors are located 1m from each other with a height of 12m at poles from the ground. The lines are assumed to be untransposed and line parameters are calculated using the distributive line model. The earth resistivity is taken between 100 and 300 Ωm which is the typical variation in UK distribution systems. System frequency is taken as 50Hz.

The overhead distribution systems studied with three or single phase taps are as shown in figure 7. Radial and remote infeed distribution systems are simulated and the source capacities varied throughout the simulations in the range of 1.0MVA - 60.0MVA.

The power source was represented by a simple lumped equivalent circuit with parameters set to produce a given symmetrical short circuit level at the bus-bar and a reactance to resistance ratio of 10 at power frequency. The ratio of the zero to positive sequence is unity. The source capacity at each line end was modelled using a series impedance.

In the fault location algorithm, where a line is terminated by a primary substation, the source admittance matrix is calculated in terms of the short circuit level and ratio of Z_{s0}/Z_{s1} .

4. RESULTS:

i. Effect of fault type: The distribution system shown in Fig.7 is simulated by using a distributive line model. The results for different types of faults as shown in Table 1 show satisfactory performance for all the cases. In the case of a single line to ground fault (SLGF), two healthy phase fault path currents are checked. In this case the average of the two is taken as the fault point.

ii. Effect of no remote infeed: Various type of faults are simulated in the distribution system shown in Fig.7 with source2 (remote source) disconnected and results are given in Table 2. Results clearly show that the absence of a remote infeed does not affect the accuracy of fault location. The only problem is, if any fault occurs after the last tap, due to the negligible capacitive effect of line, superimposed currents from the open end would be zero. In this case, faults occurring between last tap and open end can not be located accurately.

iii. Effect of fault resistance: Fig.5 shows the change of fault path currents in the healthy phases when a SLGF involving the 'A'-phase, with a fault resistance of 50 ohms occurs at 7.5. Km on a distribution line as shown in Fig.7. The same fault was repeated for a solid fault and the change in fault path currents are given in Fig.6. Results clearly show that in the presence of fault resistance, fault path currents are reduced but as seen from Table 3, faults with a fault resistance of 200.0 ohms have been located with very high accuracy. In the case of a 400.0 ohm fault resistance, the percentage of error has increased due to very low superimposed sending and receiving end currents.

iv. Position of the fault: In the distribution system shown in Fig.7, at two different locations various types of faults are simulated and results are given in Table 1. In the case of faults at 12.0 Km; accuracy is decreased. This is because superimposed currents from the remote infeed are low due to the low capacity of the source, and in this case computational errors and errors originated from the interface are more pronounced.

5. CONCLUSIONS:

The results obtained so far are very promising for 11KV radial overhead distribution systems with or without remote infeed. The results show the technique presented is virtually non sensitive to load types, source capacity and fault resistance. In this technique, errors originating from fault resistance, taps and remote infeed which cause unacceptable errors in conventional techniques are virtually eliminated.

6. REFERENCES:

[1] Girgis,A.A. Christopher,M.F. David, L.L. "A fault location algorithm for rural distribution systems." IEEE Summer Meeting. 1991.

[2] El-Hami,M Lai,L.L. Daruvvala,D.J. Johns,A.T. "Anewtravelling-wave based scheme for fault detection on overhead power distribution feeders." IEEE Trans. on Power Delivery. Vol.7,No.4, October 1992.

[3] Burdi,M.K. ElKatep, M.M. Johns,A.T. "Developments in the design of a fault locator for distribution systems". 28 UPEC Conference, September 93, Staffordshire University, pp.89-93.

[4] Clarke,G.J. Horn, H.E.,"Monitoring and protection systems suited to overhead distribution systems". IEEE Proc. third international Conference Developments in power systems protection. 1985.

[5] Tenschert,W. "Fault location in radial networks" Transmission and Distribution International, Third quarter, 1994, AUSTRIA.

[6] Salman,S.K. and Jiang. F.Rogers,W.J.S, "Investigation of using remotely connected embedded generators to regulate local voltage network.", 29 UPEC Conf, September 1994, University College Galway, pp 90-93 .

[7] AggarwaL,R.K. Coury,D.V. Johns,A.T. KALAM,A. "A Practical approach to accurate fault location on extra high voltage teed feeders." IEEE 1992 Summer meeting on Power Delivery.

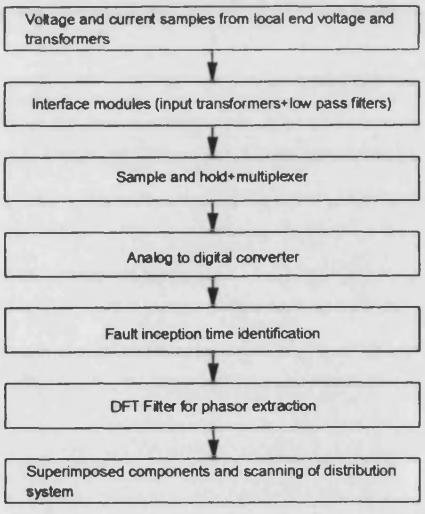

Fig .2 A block schematic of complete process.

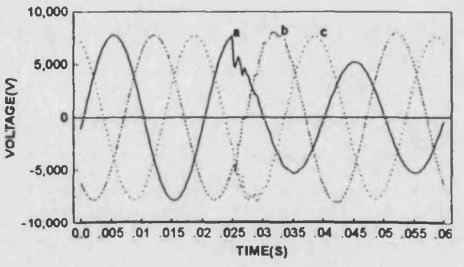

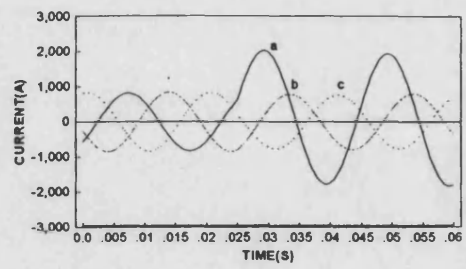

Fig.4 Typical current waveforms for a line to ground (A-G) fault on a 11 KV distribution system.

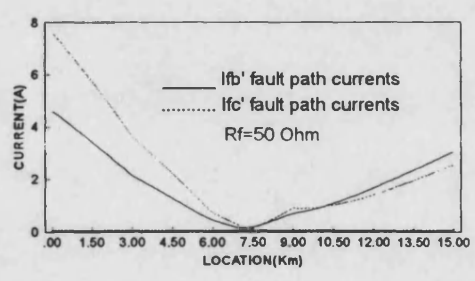

Fig.5 Change of faulth path currents for a line to ground (A-G) fault with 50.0 Ohm fault resistivity.

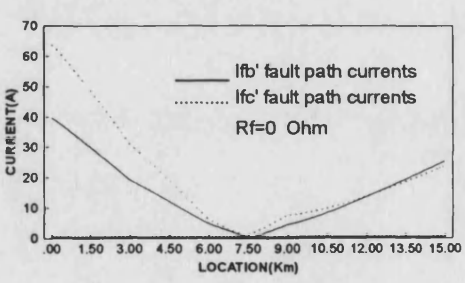

Fig.6 Change of fault path currents for a solid line to ground (A-G) fault.

Fig.3 Typical voltage waveforms for a line to ground (A-G) fault on a 11 KV distribution system.

Figure 6: 11KV Distribution system with taps and remote infeed.

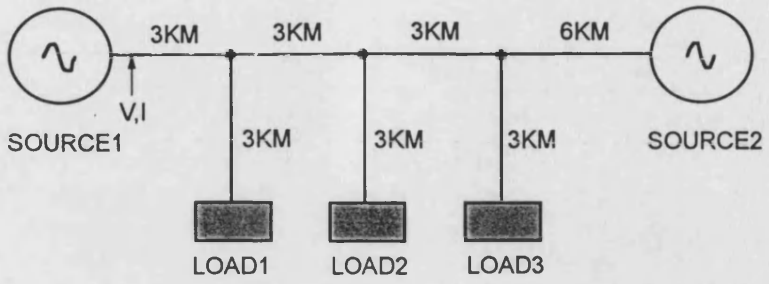

Table 1

Source1 (MVA)	Source2 (MVA)	Load1 (MVA)	Load2 (MVA)	Load3 (MVA)	Fault res. (Rf)	Type of fault	Actual distance	Estimated location	Error%
60.00	1.00	5.0 3phs	5.0 3phs	5.0 3phs	0.00	AG	7.5	7.55	0.333
60.00	1.00	5.0 3phs	5.0 3phs	5.0 3phs	0.00	ABG	7.5	7.60	0.667
60.00	1.00	5.0 3phs	5.0 3phs	5.0 3phs	0.00	AB	7.5	7.35	1.00
60.00	1.00	5.0 3phs	5.0 3phs	5.0 3phs	0.00	AG	12.0	11.80	1.33
60.00	1.00	5.0 3phs	5.0 3phs	5.0 3phs	0.00	ABG	12.0	11.40	4.00
60.00	1.00	5.0 3phs	5.0 3phs	5.0 3phs	0.00	AB	12.0	11.05	6.33

Table 2

Source1 (MVA)	Source2 (MVA)	Load1 (MVA)	Load2 (MVA)	Load3 (MVA)	Fault res. (Rf)	Type of fault	Actual distance	Estimated location	Error%
60.00	no source	5.0 3phs	5.0 3phs	5.0 3phs	0.00	AG	7.50	7.55	0.333
60.00	no source	5.0 3phs	5.0 3phs	5.0 3phs	0.00	ABG	7.50	7.80	2.000
60.00	no source	5.0 3phs	5.0 3phs	5.0 3phs	0.00	AB	7.50	7.55	0.333

Table 3

Source1 (MVA)	Source2 (MVA)	Load1 (MVA)	Load2 (MVA)	Load3 (MVA)	Fault res. (Rf)	Type of fault	Actual distance	Estimated location	Error%
60.00	1.00	1.6 1phs	5.0 3phs	1.6 1phs	0.00	AG	7.50	7.550	0.333
60.00	1.00	1.6 1phs	5.0 3phs	1.6 1phs	50.00	AG	7.50	7.700	1.333
60.00	1.00	1.6 1phs	5.0 3phs	1.6 1phs	100.0	AG	7.50	7.800	2.000
60.00	1.00	1.6 1phs	5.0 3phs	1.6 1phs	200.0	AG	7.50	7.850	2.333
60.00	1.00	1.6 1phs	5.0 3phs	1.6 1phs	400.0	AG	7.50	8.975	9.833

AG : Phase 'A' to ground fault
ABG : Phase 'A' to phase 'B' and ground fault
AB: Phase 'A' to phase 'B' fault

AN INTERACTIVE APPROACH TO FAULT LOCATION ON OVERHEAD DISTRIBUTION LINES WITH LOAD TAPS

R K Aggarwal, Y Aslan and A T Johns
School of Electronic & Electrical Engineering, University of Bath, Claverton Down, Bath BA2 7AY

INTRODUCTION

The demand and importance for a cost effective method for accurately locating faults on distribution systems, essentially to expedite the restoration of service and pinpoint potentially trouble areas, has increased in many parts of the world; a major cause of this is the challenge facing many utilities resulting from de-regulation, the privatisation of the Electricity Supply Industry in Britain being one example. It is generally well known that a conventional fault locator scheme leads to large unacceptable errors in the case of radial distribution lines with a number of load taps. The problem is further compounded if there is a remote infeed due, for example, to a private generator being connected into the system. In any new development of a fault locator, it is thus essential to include the effect of load taps and any remote infeed to obtain an estimate of the fault location with a high degree of accuracy.

Although double-ended fault location techniques which utilise fault data from both ends of a feeder, give reliable and accurate results, the data from the two ends has to be brought together via data communications. In this respect, single-ended fault locators are often more attractive both from an operational and overall cost points of view. A number of impedance-based algorithms for single-ended fault locators have been proposed[1,2]. However, all these have either limited application or they suffer from an increase in inaccuracy due to certain assumptions being made. More recently, a new technique utilising the high frequency (HF) signals generated under arcing faults has been developed[3]. However, the latter requires specialised equipments to capture the HF signals.

This paper presents a novel technique in single-ended fault location for overhead distribution systems based on the concept of superimposed components of voltages and currents rather than total quantities. It is shown that the fault locator is highly insensitive to variations in source impedances (both local and remote) and to the presence of taps with variable loads; this permits accurate fault location under a much wider range of system/fault conditions than has hitherto been possible.

FUNDAMENTAL PRINCIPLES

The Technique For A Plain Feeder

The algorithm developed works on the principle of determining from pre-fault and post-fault values of voltage and current measured, the *superimposed* voltage (this is simply the difference between the total post-fault voltage and pre-fault steady state voltage) at any assumed fault point. This voltage is then back injected at the assumed fault point to check currents in the unfaulted phases. Only when the fault point is correct do the sound phase injected currents at the actual fault point attain a near zero value. A very simple example involving a plain feeder with no taps is shown in Fig 1. Assuming a lumped parameter model of the line, the *total* voltage V_f at the assumed fault point β is related to the *total* measured voltages and currents by:

$$\begin{bmatrix} V_{fa}(\beta) \\ V_{fb}(\beta) \\ V_{fc}(\beta) \end{bmatrix} = \beta \begin{bmatrix} Z_s & Z_m & Z_m \\ Z_m & Z_s & Z_m \\ Z_m & Z_m & Z_s \end{bmatrix} \begin{bmatrix} I_{sa} \\ I_{sb} \\ I_{sc} \end{bmatrix} + \begin{bmatrix} V_{sa} \\ V_{sb} \\ V_{sc} \end{bmatrix} \quad (1)$$

Eqns 2-4 show how the *superimposed* voltages can be attained from the total voltage and current data recorded at a particular end.

$$V'_{fa,b,c}(\beta) = V_{fa,b,c}(\beta) - V_{fa,b,c(pf)}(\beta) \quad (2)$$

$V'_{fa,b,c}(\beta)$, $V_{fa,b,c}(\beta)$ and $V_{fa,b,c(pf)}(\beta)$ and are respectively, the superimposed, post-fault and pre-fault voltages at the prospective fault point. In eqn 2, $V_{fa,b,c(ss)}(\beta)$ is given by:

$$[V_{fa,b,c(pf)}(\beta)] = \beta\,[Z]\,[I_{sa,b,c(pf)}] + [V_{sa,b,c(pf)}] \quad (3)$$

It will be necessary to obtain, from the pre-fault and post-fault measurands, the superimposed voltages and currents at the measuring end P (see Fig 1). These are given by:

$$V'_{sa,b,c} = V_{sa,b,c} - V_{sa,b,c(pf)}\ ,\ I'_{sa,b,c} = I_{sa,b,c} - I_{sa,b,c(pf)} \quad (4)$$

The *superimposed* system model is then as shown in Fig 2, from which we can easily evaluate the *superimposed* currents $I'_{ra,b,c}$ fed into the fault from end Q. This then gives the *superimposed* fault-path currents at the assumed fault point as:

$$I'_{fa,b,c} = I'_{sa,b,c} + I'_{ra,b,c} \quad (5)$$

Essentially, the assumed fault position is shifted in an interactive fashion in order to find the minimum value of $I'_{fb,c}$ (for an 'a'-earth fault, say) and this corresponds to the actual fault point α as shown in Fig 1.

Feeder With Multiple Load Taps

The computational process for a feeder with multiple taps is considerably more complex than the previously shown technique for plain feeders. However, the same principle can be applied. The accuracy attainable will nonetheless be dependent upon the extent to which the system model representing the remote infeed corresponds to the real system. However, unlike transmission systems, there is much less variation in source characteristics for a distribution system.

Load representation. In a typical distribution system, it is common to have a mix of 3-phase and single-phase taps terminating a length of tap. In the case of a single tap, it is adequate to take the nominal transformer rating M and from that assume a load P_f of *0.95*. Thus the impedance referred to the primary of the transformer will be given by:

$$Z_L = |V_{LP}|^2 / M \angle Cos^{-1} P_f \qquad (6)$$

where V_{LP} is the voltage at the load point.
For a 3-phase tap, the load impedance will be a Δ connected impedance between phases given by:

$$Z_L = 3|V_{LP}|^2 / M \angle Cos^{-1} P_f \qquad (7)$$

Depending upon the type of load, it is then relatively easy to set up the appropriate load impedance matrix. Where a line is terminated by a primary substation, the source impedance matrix can be defined in terms of the symmetrical short circuit level and ratio Z_{s0}/Z_{s1}.

It will be seen from the *Plain Feeder* technique that it is necessary to calculate the impedance on each side of the assumed fault point in order to *force* the network.

DISTRIBUTION SYSTEM MODELLING AND BASIC CONSIDERATIONS

System Modelling

The modelling of the distribution system, including all the load taps and source representations, was carried out using the ElectroMagnetic Transients Program; the results presented relate to a typical 11 kV overhead Distribution System (commonly found in the UK) comprising of a number of load taps with differing loads, both with and without any remote infeed as shown in Fig 3.

Basic Considerations

The aforementioned method described is designed to work with measured busbar voltage and current signals in a phasor form at the fundamental frequency; the method for accurately extracting these phasors is based on one cycle of information using the Discrete Fourier Transform (DFT)[4]. Moreover, since the technique utilises *superimposed* components, these are attained by simply taking the difference between the total fault and pre-fault fundamental phasors.In the technique described herein, important aspects of practical fault recorders/locators such as VT and CT responses, analogue interface effects and quantisation errors, have been taken into account in the CAD of the fault locator; this is to ensure that the performance obtained is close to a real-life situation.

PERFORMANCE EVALUATION

Effect Of Fault Type And Fault Location

Fig 4 typifies the primary system fault voltage and current waveforms obtained at the fault locator end (end P) when an 'a'-earth fault occurs between taps 3 and 4 (11km from end P) on the distribution system shown in Fig 3 with the remote end open. Both high frequency distortion and DC offset are apparent in the waveforms and hence the necessity to apply DFT filters to accurately extract the fundamental phasors. Fig 5 depicts the corresponding variations in the healthy phase ('b' and 'c') and the faulted 'a' phase currents in the fault paths. As expected, an incorrect fault position manifests itself into giving rise to currents in the fault paths of the two healthy phases; there is, however, a fault point at which these currents are at a minima. It is apparent from the foregoing theory presented that the point on the line at which this minima occurs is the actual fault location. As would be expected, the behaviour of the faulted-phase fault path current is distinctly different from those associated with the healthy phases, particularly its magnitude which is much higher.

The algorithm was also tested for other fault positions and for other types of fault, and its performance is summarised in Table 1. First of all considering the effect of fault position, it is apparent that as the fault moves further away from the local end (end P in Fig 3), there is a degradation in the performance attained. This is so by virtue of the fact that the levels of the fault path currents associated with the healthy phases become progressively small as the fault approaches the remote end (which in this case is open), in particular after the minima has been surpassed. Studies have shown that for a fault very close to the open end, the magnitudes of these erroneous currents are only slightly higher than those at the minima. When comparing the accuracies for different types of fault, it is evident from Table 1 that for the two fault positions considered, those obtained for double-phase-earth and phase-phase faults are less than those for the corresponding single-phase-earth fault.

Effect Of Remote Infeed

In view of the fact that more and more private

generators are being connected into distribution systems (and this trend is likely to continue), it is important to examine the performance of the algorithm developed when a distribution system has remote infeed. For this study, the same distribution system as that shown in Fig 3 was employed but with the remote source connected. Fig 6 typifies the behaviour of the healthy and faulted phase fault path currents. Like the previous study involving a system with remote end open (Fig 5), here again a minima in the case of the healthy phase fault path currents signifies the actual fault position. However, in marked contrast, the magnitudes of these currents are much higher once the minima has been surpassed, and this is due to the presence of the remote infeed; more importantly, the accuracy attained is much higher, ≈0.12% in comparison to 1.5% as in the previous case. In fact, for the fault location technique presented herein, the accuracy is always higher for a system with remote infeed than that with the remote end open; this is a significant advantage over conventional fault locators whose accuracy is adversely affected by the presence of a remote infeed.

Effect Of Fault Resistance

It is apparent from Fig 7 (fault at 8.4 km from end P) that the fault locator gives an inherently high accuracy in fault location in the presence of fault resistance; this is particularly so for double-phase-earth faults. In the case of single-phase earth faults, however, there is a small increase in inaccuracy (particularly in the case of a system with remote end open), especially when the fault resistance exceeds about 100Ω. Nonetheless, the overall performance obtained is superior to that achieved with conventional techniques, particularly those based on impedance to fault measurements.

Sensitivity To Load Tap Variations

In practice, the load taps and source capacities are subjected to variations with the time of day and this effectively means that their values can only be approximated when applying the fault locator to a particular fault recorded dataset. It is thus important to ascertain as to what extent the locator's accuracy is affected due to non-algorithmic errors emanating from load estimations. For this study, voltage and current datasets were generated for faults 8.4 km from end P for the distribution system shown in Fig 3 with the remote end open. Table 2 summarises the fault locator's performance when the load taps were subjected to changes by varying degrees. It is apparent from the results that although the percentage error in fault location increases. more importantly, the increase in inaccuracy is relatively small and this is the case for different types of fault. These results clearly indicate the robustness of the fault locator algorithm and this is a major advantage when applying the technique to real fault datasets recorded from practical distribution systems.

CONCLUSIONS

The basis of a novel approach in single-ended fault location for overhead distribution systems is described. The fault location algorithm is based on superimposed phase values and special filtering techniques are incorporated to accurately extract the fundamental phasors from the measured fault signals. The technique, based on an interactive approach has culminated in a fault locator design that gives high accuracy for the vast majority of practically encountered system and fault conditions, including the presence of load taps and remote source infeed. The results presented also show the locator's robustness to errors in the estimation of load taps.

REFERENCES

1.A.A. Girgis and C.M. Fallon:"Fault location technique for radial and loop transmission systems", IEEE Trans on Power Delivery, vol 7, No 4, October 1992, pp 1936-1945.

2.R. Das, M.S. Sachdev and T.S. Sidhu:"A technique for estimating location of shunt faults on distribution lines", Proc IEEE, Wescanex'95.

3.M. El-Hami, L.L. Lai, D.J. Daruvvala and A.T. Johns:" A new travelling-wave based scheme for fault detection on overhead power distribution feeders", IEEE Trans on Power Delivery, vol 17, no 4, October 1994.

4.R.K. Aggarwal, D.V. Coury, A.T. Johns and A. Kalam:" A practical approach to accurate fault location on extra high voltage teed feeders", ibid, vol 8, no 3, July 1993.

Table 1: Effect of fault position and fault type on fault location

Type of fault	Actual dist.(km)	Estimated dist(km)	%Error	Actual dist(km)	Estimated dist.(km)	%Error
SLGF(a)	6.60	6.70	0.49	15.40	15.62	1.09
DLGF(ab)	6.60	6.75	0.74	15.40	15.70	1.49
LLF(ab)	6.60	6.80	0.99	15.40	15.90	2.48

Table 2: Effect of load capacity estimation on accuracy.

Type of fault	%load error (0%) est. loc.	%error	%load error (5%) est. loc	%error	%load error (10%) est. loc.	%error
SLGF(a)	8.55	0.74	8.70	1.49	8.90	2.48
DLGF(ab)	8.65	1.24	8.85	2.20	9.05	3.23
LLF(ab)	8.70	1.49	8.80	2.00	8.95	2.73

SLGF = Single line to ground fault, DLGF = Double line to ground fault, LLF = Line to line fault.

Loads 1 & 3 +5%(or +10%) error
Loads 2 & 4 -5%(or -10%) error

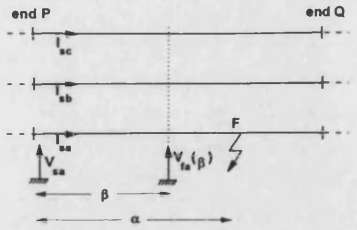

Fig.1 Simplified faulted system model

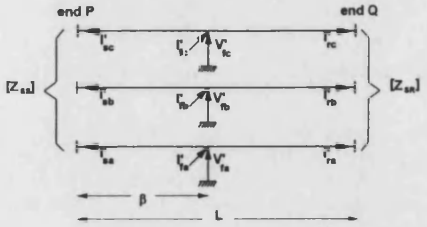

Fig.2 Superimposed - component circuit

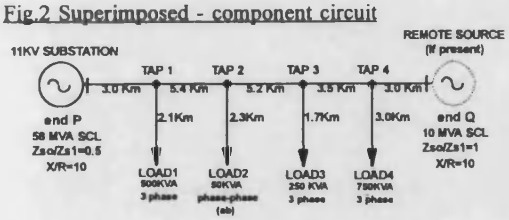

Fig.3 A typical 11kV radial distribution system

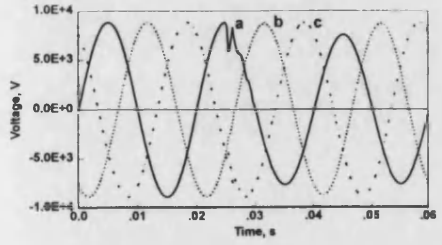

Fig.4a Voltage waveforms

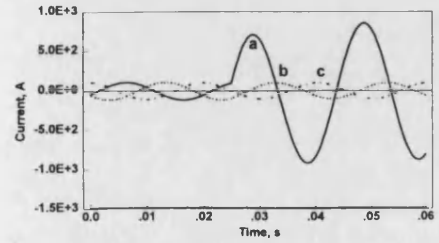

Fig. 4b Current waveforms

Fig 4 Typical primary system waveforms

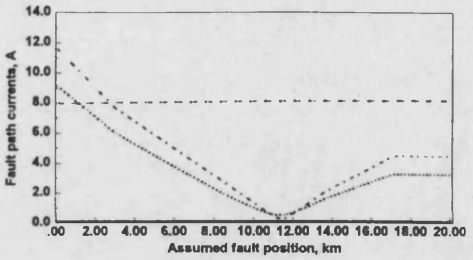

Fig. 5 Fault path currents for the system with remote end open.

a - phase (scale x 100 of that shown)
b - phase
c - phase

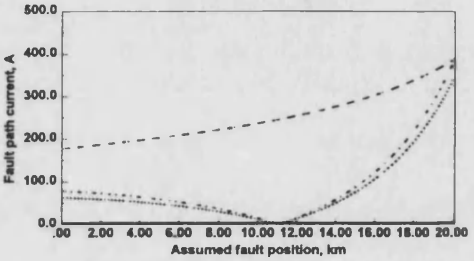

Fig.6 Fault path currents for the system with remote source connected.

a - phase (scale x 5 of that shown)
b - phase
c - phase

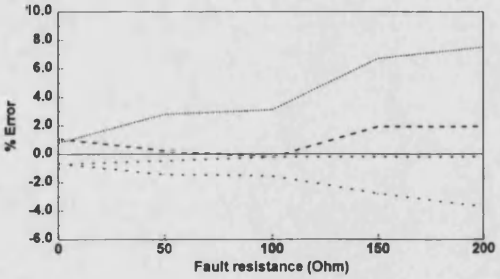

Fig.7 Effect of fault path resistance on accuracy.

SLGF for system with remote-end open
SLGF for a system with remote infeed
DLGF for system with remote-end open
DLGF for a system with remote infeed

A NEW CONCEPT IN FAULT LOCATION FOR OVERHEAD DISTRIBUTION SYSTEMS USING SUPERIMPOSED COMPONENTS

R.K. Aggarwal
Y. Aslan
A.T. Johns

School of Electronic and Electrical Engineering, University of Bath, Claverton Down, Bath BA2 1HU

Indexing terms: *fault location, distribution systems, superimposed components*

Abstract: Due to the challenges facing many Utilities worldwide as a result of de-regulation, the demand and importance of accurate fault location in distribution systems has increased, principally to minimise line outages through effecting repairs expeditiously. This paper presents a novel approach in single-ended fault location for overhead distribution systems based on the concept of *superimposed* voltages and currents. It is clearly shown that the technique, which is interactive in nature, is highly robust to changes in local and remote source capacities and to the presence of load taps.

1 INTRODUCTION

The development of fault location techniques using digital fault recorder data to expedite the restoration of service and pinpoint potentially troubled areas on EHV transmission systems has been identified as an essential requirement for Power Companies. However, until recently, relatively little work has been done in the development of fault locating techniques for distribution systems; this stems from the fact that hitherto, fault locators on such systems have been considered useful but not essential. However, the demand and importance for a cost effective method for accurately locating faults on distribution systems has increased (and is likely to gather momentum) in many parts of the world; a major cause of this is the challenge facing many utilities resulting from de-regulation, the privatisation of the Electricity Supply Industry in Britain being one example. The consequences of the latter are resulting in a need to effect repairs more quickly through location of faults via purpose-built fault locators.

It is generally well known that a conventional fault locator scheme leads to large unacceptable errors in the case of radial distribution lines with a number of load taps. The problem is compounded if there is a remote infeed due, for example, to a private generator being connected into the system.

Although double-ended fault location techniques which utilise fault data from both ends of a feeder give reliable and accurate results, single-ended fault locators are often more attractive both from an operational and overall cost points of view since they obviate the need for communication links or fault recording equipment at both ends of the distribution line. A number of algorithms for single-ended fault locators have been proposed; these show a trend towards impedance measuring fault locators where the *apparent impedance* may be compensated for the effect of fault resistance. However, all of these have either limited applications (in terms of providing the required accuracy when system and/or fault conditions change) or they suffer from an increase in inaccuracy due to certain assumptions being made. For example, the technique proposed by Girgis [1] gives good accuracy provided there is no remote infeed ie, that the fault-path current is co-phasal with the locally recorded current data, and the load taps are constant. The technique proposed in reference [2] is based on high frequency (HF) measurements and requires special equipments in order to capture the HF signals. More recently, the technique outlined by Das et al [3], gives high accuracy in the presence of dynamic load taps but the distribution line model used is based on lumped π sections and results relating to a system with remote infeed are not considered.

This paper presents a new technique in single-ended fault location for overhead distribution systems and is based on the concept of superimposed components of voltages and currents rather than total quantities. It is shown that the fault locator is highly insensitive to variations in local and remote source impedances and to the presence of taps with variable loads; this permits fault location under a much wider range of system/fault conditions than has hitherto been possible.

2 FAULT LOCATION TECHNIQUE

The underlying principles of the technique presented are essentially the same as those developed for plain transmission lines [4], except that the algorithm has been significantly

modified to specifically deal with the much higher complexity encountered in distribution systems; this arises principally due to the presence of many load taps in the case of the latter.

2.1 Fundamental principles as applied to a plain feeder

The methodology outlined is based on determining the *superimposed* values of voltage and current at any assumed fault point from the measured pre-fault and fault values. It should be noted that the superimposed values are simply the differences between the total fault and pre-fault steady-state voltage/current signals. Using a specified model of the distribution system under consideration, these superimposed voltages and currents are employed to ascertain the voltage at an assumed fault position; this is then back injected at the assumed fault point in order to check the fault-path currents in the unfaulted phases. Only when the fault point is correct will the healthy-phase(s) at the actual fault point in the model attain a near zero value.

The fundamental principle can best be illustrated with reference to the simple example shown in Fig 1 which is for a plain feeder with no load taps. Assuming a lumped parameter model of the line, the *total* voltage V_f at the assumed fault point is related to the measured *total* voltages and currents by:

$$\begin{bmatrix} V_{fa}(\beta) \\ V_{fb}(\beta) \\ V_{fc}(\beta) \end{bmatrix} = \beta \begin{bmatrix} Z_s & Z_m & Z_m \\ Z_m & Z_s & Z_m \\ Z_m & Z_m & Z_s \end{bmatrix} \begin{bmatrix} I_{Sa} \\ I_{Sb} \\ I_{Sc} \end{bmatrix} + \begin{bmatrix} V_{Sa} \\ V_{Sb} \\ V_{Sc} \end{bmatrix} \qquad (1)$$

$$\longleftarrow Z \longrightarrow$$
$$\longleftarrow Z_\beta \longrightarrow$$

where β is the assumed fault position, α is the actual fault position, and Z_s, Z_m are the line self and mutual impedances/unit length respectively.

Eqn 1 is a relationship involving the total voltage and current measurands under fault conditions. The superimposed quantities are effectively the information available on a de-energised system. Eqns 2-4 show how the superimposed voltages at position β can be obtained from the total voltage and current data measured at a particular busbar; since these are simply the difference between the fault and pre-fault fundamental phasors, it is essential to accurately extract them from the measured values before applying the algorithm. we have:

$$[V'_{fa,b,c}(\beta)] = [V_{fa,b,c}(\beta)] - [V_{fa,b,c(ss)}(\beta)] \quad (2)$$

Where $[V'_{fa,b,c}(\beta)]$, $[V_{fa,b,c}(\beta)]$ and $[V_{fa,b,c(ss)}(\beta)]$ are the superimposed, total, and pre-fault voltages at the assumed position, respectively.

Now in eqn 2, the pre-fault voltage at the assumed fault position is given by:

$$[V_{fa,b,c(ss)}] = [Z_\beta]\ [I_{Sa,b,c(ss)}] + [V_{Sa,b,c(ss)}] \quad (3)$$

The superimposed voltages and currents at the measuring end P (see Fig 1) are given by:

$$[V'_{Sa,b,c}] = [V_{Sa,b,c}] - [V_{Sa,b,c(ss)}]\ ,\quad [I'_{Sa,b,c}] = [I_{Sa,b,c}] - [I_{Sa,b,c(ss)}] \quad (4)$$

The superimposed system model is shown in Fig 2, from which it is apparent that the superimposed currents at the remote end Q are given by:

$$\begin{bmatrix} I'_{Ra} \\ I'_{Rb} \\ I'_{Rc} \end{bmatrix} = \left[(L-\beta) \begin{bmatrix} Z_s & Z_m & Z_m \\ Z_m & Z_s & Z_m \\ Z_m & Z_m & Z_s \end{bmatrix} + [Z_{SR}] \right]^{-1} \begin{bmatrix} V'_{fa} \\ V'_{fb} \\ V'_{fc} \end{bmatrix} \quad (5)$$

$\leftarrow Z \rightarrow$

$\leftarrow\!\!\!

2.2 Extension of the principle to a feeder with multiple load taps

The computational process for a feeder with multiple taps is considerably more complex than for the previously shown technique for plain feeders; however, the same principle can be applied. In order to locate the actual fault point, the fault is first assumed to be at a point close to the local end (in this case end P). The most accurate fault location is then found interactively by systematically varying the assumed fault position until such time as the fault-path current(s) in the healthy phase(s) attain a minima.

2.2.1 Load representations

In a typical distribution system, it is common to have a mix of 3-phase and single-phase loads terminating a length of tap. In the case of a single-phase load tap, it is adequate to take the nominal transformer rating M and from that assume a load power factor p_f which in practice, varies typically from about 0.8→0.95. Thus with reference to Fig 3a, the impedance referred to the primary of the transformer will be given by:

$$Z_L = \left[|V_L|^2 / M\right] \angle \cos^{-1} p_f \qquad (7)$$

where V_L is the voltage at the load point.

For a 3-phase load tap, in the majority of cases the load impedance can be approximated by a Δ-connected impedance between phases, as shown in Fig 3b, which is given by:

$$Z_L = \left[3|V_L|^2 / M\right] \angle \cos^{-1} p_f \qquad (8)$$

From a computational point of view, it is more convenient to represent each load tap by a load matrix $[Y_L]$ which in turn is dependent upon the type of load; this can be either three-phase, single-phase or, in some cases two-phase, and can be relatively easily set up via the load impedance relationships for Z_L as shown in eqns 7 and 8.

As mentioned previously, although the majority of low voltage distribution systems comprise of radial feeder with the remote end open, there can be situations when a line section is terminated by a primary sub-station. In the general case shown in Fig 4, we can define a source impedance matrix $[Y_{SR}]$ (or $[Y_{SS}]$) in terms of the symmetrical short circuit level and

the ratio Z_{S0}/Z_{S1}.

In setting up the load impedance, as in eqns 7 and 8, we need to take account of the variation of the load with time of day; although this can only be done approximately, pre-fault voltages and currents can be utilised to establish, to a fair degree of accuracy, the active power fed to the feeder at the measuring point. This can be calculated from:

$$P_{ss} = \sqrt{3}\ |V_{Lss}|\ |I_{Lss}|\ \cos\Phi \qquad (9)$$

where V_{Lss} and I_{Lss} are the pre-fault line voltage and line current at the measuring end respectively; ϕ = angle between V_{Lss} and I_{Lss}.

Note that if the line losses are neglected then P_{ss} is the actual summated load power.
We then take the sum of the rated load powers on the feeder to determine the maximum total load, which is given by:

$$P_{Lmax} = (M_1+M_2+...+M_N)\cos\Phi \qquad (10)$$

Where N is the number of load taps and M is the nominal transformer rating as defined in eqns 7 and 8.
It should be noted that the power factor for all the load taps is assumed to be the same.
The load *level* is then defined as:

$$L_{level} = P_{ss}/P_{Lmax} \qquad (11)$$

It is now possible to define an approximate level of an active load at each load tap; for example, for load tap 1 of rating M_1 the load impedance (assuming a single phase load) is given as:

$$Z_{L1} = \left[|V_{L1}|^2/(L_{level}\ M_1)\right]\angle\cos^{-1}p_f \qquad (12)$$

This is essentially the same as that described in eqn 8; the other load impedances are likewise derived.

2.2.2 Fault location calculation

It will be seen from Section 2.1 that it is necessary to calculate the impedance on each side

of the assumed fault point in order to force the network. The technique for determining the driving impedances can best be illustrated by considering the specific example shown in Fig 4, which shows a network comprising of four load taps; it can be seen that each leg is terminated in an effective load impedance derived via the load matrix $[Y_L]$.

As an example, suppose we wanted to set up an assumed fault position at tap point 4. In this case, the admittances of interest $[Y_{ES}]$ and $[Y_{ER}]$ for the system shown in Fig 4 would have to be formed. It is shown in Appendix 6.1 that these are given as:

$$[Y_{ER}] = [Y_{L4}][U + l_4 Z Y_{L4}]^{-1} + [Y_{45}] = [Z_{ER}]^{-1} \quad (13)$$

$$[Y_{ES}] = [Y_{3S}][U + l_{34} Z Y_{3S}]^{-1} = [Z_{ES}]^{-1} \quad (14)$$

Having determined the two admittance matrices on either side of the assumed fault position, the procedure for evaluating the superimposed fault-path currents$[I'_{fa,b,c}]$ is essentially the same as that outlined in eqns 1-6 except that in eqn 1, the impedance matrix $[Z_\beta]$ is simply replaced by $[Z_{ES}]$ and in eqn 5 the impedance matrix $[Z_{L-\beta}]$ by $[Z_{ER}]$.

It should be noted that the computational process of fault location for feeders with multiple taps is highly complex and can as a consequence, impose a heavy burden on computer requirements. However, the technique presented herein facilitates the process by assuming a fault position in the first instance and then shifting this position systematically and in an interactive manner until such time as the requisite criterion is satisfied. Although this approach involves a number of steps (in the algorithm developed here this is at 50m intervals) and for each new step, the two driving matrices (as shown in eqns 13 and 14) have to be recalculated, an extensive series of studies have shown that for a typical distribution system with up to ten load taps, the whole process of fault location is completed in about 30s on a 486 PC.

2.3 Extraction of fundamental phasors

The algorithm described above is designed to work with the measured busbar voltage and current signals in phasor form. In practice, the six analogue signals from the power transducers (VTs and CTs) are recorded by microprocessor-based hardware; this converts the

signals into discrete-time values by a sampling process through the use of an analogue-to-digital converter (ADC). Subsequent processing of the recorded dataset converts the discrete-time values into phasor form by the use of the Discrete Fourier transform (DFT). In this respect, it should be mentioned that although in practice, the fault data measured on distribution systems comprises of predominantly power frequency components with relatively little of either high frequency or DC components (this is primarily so by virtue of the fact that firstly the line lengths involved are very short and secondly because the line X:R ratios are very low, typically about 2-3 for an 11 kV overhead line), nonetheless it is vitally important to be able to accurately extract the fundamental frequency phasors from the fault voltage and current waveforms.

The method used here is based on one cycle of information and the general DFT equation which gives both magnitude and phase of a fundamental phasor is as given in reference [4].

2.4 Superimposed component extraction

As mentioned previously, since the technique described herein is based on superimposed components, the latter are attained by simply taking the difference between the total fault and pre-fault fundamental phasors. The principal advantage of this approach is that any errors arising in fault location due to variations in line loading either at the feeder source ends or load taps are very significantly reduced.

2.5 Practical considerations

Since the fault location technique described is designed to work with recorded voltage and current signals (via VTs and CTs) which are subsequently digitised within the digital hardware associated with a practical fault recorder, it is crucial to take into account any transducer/hardware errors. In this respect, the principal sources of error are: (i) the frequency responses of the CTs and VTs, together with the analogue interface modules within the hardware, (ii) the response of the anti-aliasing filters, and (iii) the quantisation errors arising as a result of converting analogue signals into sampled values through the ADC.

In the technique described here, these effects have been taken into account by including

within the simulation, models of VTs, CTs and interface modules. Furthermore, the dataset is quantised to a 12-bit resolution (at a sampling rate of 4 kHz) before it is processed through the fault location algorithm. It is vitally important to adopt this approach in order to ensure that the performance attained from the technique pertains to an actual practical situation.

3 PERFORMANCE EVALUATION

The performance of the new fault locator was examined for faults on an 11kV overhead distribution system commonly found in the UK; details of the line configuration are given in Appendix 6.2. The ElectroMagnetic Transients Program (EMTP) was used to simulate the primary system faults and to produce discrete-time data for the local busbar voltage and current signals. The simulation included both the distributive nature of the line and its frequency dependent parameters.

The results presented relate to a typical distribution system comprising of a number of load taps with differing loads, both with and without any remote infeed, as shown in Fig 5. The relevant data used is:

(i) Earth resistivity (assumed homogeneous) = 100 Ωm
(ii) Source: X/R ratio = 10, $Z_{S0}/Z_{S1} = 0.5$
(iii) Diversity factor for the load taps = 0.5
(iv) Main feeder impedance = (0.18+j0.34) Ω/km
(v) Tap line impedance = (0.54+j0.38) Ω/km

It should be noted that unlike the assumption made in the explanation of the basic principle of the technique, the tap line impedance for the practical system considered here is different from that of the main feeder and this has been taken into account when setting up the model of the distribution system.

In all the results presented herein, the percentage error relating to fault location is based on:

% error = [estimated location - actual location]/[length of distribution feeder] × 100

3.1 Effect of fault type and fault location

Fig 6 typifies the variations in the healthy-phases ("b" and "c") and the faulted "a" phase currents in the fault paths for an "a"-earth fault on the radial feeder shown in Fig 5 with remote end open. First of all considering the fault close to the source end ie, between taps 1 and 2, as expected, an incorrect fault position manifests itself into giving rise to currents in the fault paths of the two healthy phases; there is however, a fault point at which these currents are at a minima, as shown in Fig 6a. It is apparent from the foregoing theory presented that the point on the line at which this minima occurs is the actual location of the fault. In this respect, it should be noted that at the minima, the healthy phase fault path currents should ideally be zero. However, in practice this is not always the case because of the presence of small algorithmic and/or non-algorithmic errors. As would be expected, the behaviour of the faulted-phase fault-path current is distinctly different from those associated with the healthy phases; its magnitude is much larger and varies relatively little irrespective of whether the fault is at the correct point. Similar behaviour of the fault-path currents can be observed for a fault close to the remote end, ie between load taps 6 and 7. As shown by Fig 6b, the main difference between the two fault positions is that in the case of the latter, the increase in the levels of the incorrect fault path currents associated with the healthy phases, particularly after the minima has been surpassed, is significantly less than in the case of the former. This is somewhat expected by virtue of the fact that as the fault moves closer to the open end, the infeed into the *pseudo* fault paths, created by the incorrect fault positions, becomes progressively smaller. With regard to the faulted "a"-phase fault-path current, like in the previous case, it more or less stays constant at a high level at all assumed fault positions.

The algorithm was also tested for other types of fault and Table 1 gives a summary of the performance achieved. It is apparent that as the fault moves closer to the open end, there is a small degradation in the performance attained. This would again be somewhat expected because of the aforementioned reasons ie, in that the levels of the fault-path currents associated with the healthy phases become quite small at the incorrect fault points, in particular after the minima has been surpassed. When comparing the accuracies for different types of fault, it is evident that for the two fault positions considered, those obtained for double-phase-earth and phase-phase faults are slightly less than those for the corresponding

single-phase-earth faults.

It is important to note that the fault location algorithm presented herein does not require any prior knowledge of the actual phase(s) involved in a fault.

3.2 Effect of remote infeed

Although hitherto the majority of distribution systems comprise of feeders with remote ends open, with the deregulation of the Electricity Supply Industry, more and more private generators are being connected into the system and this trend is likely to continue; a direct of consequence of this is an increase in the complexity of distribution systems and more importantly for such systems, any fault will also have a remote infeed. It is well known that a remote infeed can adversely affect the accuracy of conventional fault locators. The performance of the technique described herein was examined for faults on the distribution system shown in Fig 5 but with the remote source connected and the results are summarised in Table 2. In comparison to the results attained for the radial feeder system with remote end open (see Table 1), it is evident that the presence of a remote infeed has only a slight effect on accuracy. In fact the accuracy attained in the case of the latter interestingly shows a slight improvement over the former; this can be directly attributed to the fact that with a remote infeed, the currents arising in the pseudo fault paths (associated with the healthy phases) due to the fault location being incorrect, are relatively large in comparison to those generated by the algorithm in the case of the open-ended system, particularly after the minima has been surpassed; this in turn enhances the performance of the fault locator in its ability to discern between the actual and assumed fault positions with greater accuracy and this phenomenon is clearly evident from a comparison of Figs 6b and 7.

3.3 Effect of fault resistance

It is apparent from Fig 8 that the fault locator gives an inherently accurate evaluation of fault position that is largely independent of the fault resistance; this is particularly so for double-phase-earth faults. In the case of single-phase-earth faults, however, there is a small degradation in performance (more so in the case of systems with remote ends open), especially when the fault resistance goes above about 100Ω. Nevertheless, the overall

performance attained is significantly superior to that achieved with conventional techniques, particularly those based on impedance to fault measurements, which give rise to unacceptably large errors in the presence of fault resistance [5].

3.4 Sensitivity to load variations

In practice the load taps and the remote source are subjected to variations with the time of day and this effectively means that the values can only be approximated when applying the fault locator to a particular fault recorded dataset. Since such non-algorithmic errors can have a detrimental effect on the fault locator's performance, it is vitally important to ascertain as to what extent the locator's accuracy is affected as a result of errors in load estimations; for this study, voltage and current datasets were generated for a fault at 8.4 km from end P for the system shown in Fig 5 without and with remote source connected. Tables 3 and 4 summarise the locator's performance when the load taps and remote source capacity were then subjected to changes by varying degrees of error.

First of all considering the effect on accuracy due to errors in load tap estimations, although the percentage error in fault location increases as the load estimation error increases, more importantly, the increase in inaccuracy is still relatively small. Likewise, in the case of errors in the estimation of the remote source capacity, the fault locator maintains its high accuracy even when a 50% error is introduced. These results clearly indicate the robustness of the fault location algorithm described herein and this is a major advantage when applying the technique to real fault datasets recorded from practical distribution systems.

The results presented so far relate to static load taps. However, in practice there can also be present dynamic load taps and it is thus important to establish the effect on accuracy in the presence of such loads. Fig 9 shows the behaviour of the fault-path currents in the healthy phases ("b" and "c") when an "a"-phase-earth fault occurs on the system shown in Fig 5 with remote end open, in which load tap 7 has been replaced by a dynamic load; this comprises of a 1.2 MVA star-connected asynchronous motor which has been modelled within the EMTP simulation. It is apparent that for the two different fault positions considered, ie faults near taps 3 and 5, the fault locator gives a high accuracy corresponding to errors of 0.9% and 1% respectively. This clearly demonstrates that the technique described herein is little affected by

the presence of dynamic load taps on the system.

It should be mentioned that, although not shown here, the performance of the fault locator is largely immune to changes in the local source capacity, in this case at end P. This also is a major advantage particularly since source capacities constantly change according to the prevailing load conditions.

4 CONCLUSIONS

The basis of a new approach in single-ended fault location for overhead distribution systems is described. The fault location algorithm is based on utilising superimposed phase signals and special filtering techniques are utilised to accurately extract the fundamental phasors from the measured fault signals.

The technique, based on an interactive approach whereby an assumed fault point is varied systematically until the actual fault point is found, has culminated in a fault locator design that gives a high accuracy for the vast majority of practically encountered system and fault conditions; these include different source impedances (local and remote), the presence of load taps (static and dynamic), fault resistance, etc. The results presented also show the locator's robustness to large errors in the estimation of load taps and remote source capacity (if present).

Although the algorithm has been tested using CAD techniques, emphasis is placed on examining its performance using data as though it were captured through actual fault recorders; it is clearly demonstrated that with this approach, the algorithm retains its high accuracy in the presence of errors introduced by transducers and hardware, the errors attained being less than about 3% for the majority of system and fault conditions studied.

5 REFERENCES

1. A.A. Girgis and C.M. Fallon:"Fault location techniques for radial and loop transmission systems", IEEE Trans. on Power Delivery, vol 7, No 4, October 1992,

pp 1936-1945.

2. M. El-Hami, L.L. Lai, D.J. Daruvvala, A.T. Johns:"A new travelling-wave based scheme for fault detection on overhead power distribution feeders", Ibid, Vol 17, No 4, October 1992.

3. R. Das, M.S. Sachdev, T.S. Sidhu:"A technique for estimating location of shunt faults on distribution lines", Proc IEEE, Wescanex'95.

4. A.T. Johns, P.J. Moore, R.Whittard:"New technique for the accurate location of earth faults on transmission systems", Proc. IEE, Gener.,Transm.,Distrib., vol 142, No 2, March 1995, pp 119-127.

5. V. Cook:"Fundamental aspects of fault location algorithm used in distance protection", Proc IEE, Vol 133, Pt C, No 6, September 1986.

6 APPENDIX

6.1 Admittance matrix evaluation

In order to evaluate the two driving admittance matrices $[Y_{ER}]$ and $[Y_{ES}]$ (as given in eqns 13 and 14 in Section 2.2.2) on either side of the assumed fault position shown in Fig 4, it is necessary in the first instance to evaluate the equivalent admittance matrix associated with a particular load tap. The derivation of such a matrix can best be illustrated with a general example as in Fig 10, which shows a load tap N relationship. It can be seen that:

$$V_{TN} = l_N Z I_{LN} + V_{LN} \tag{15}$$

Now $I_{LN} = I_{TN} = Y_{LN} V_{LN}$ where $Y_{LN} = [Z_{LN}]^{-1}$ (16)

Therefore $V_{TN} = [U + l_N Z Y_{LN}] V_{LN}$ (17)

where l_N = line length from tap point N to load tap L_N

U = unity matrix

Z = impedance matrix/unit length of tap line

Z_{LN} = load impedance matrix representation for load tap L_N

This then gives:

$$V_{LN} = [U + l_N Z Y_{LN}]^{-1} V_{TN} \tag{18}$$

By substituting eqn 18 into eqn 16 we thus get:

$$I_{LN} = I_{TN} = [Y_{LN}]\ [U + l_N Z Y_{LN}]^{-1} V_{TN} = [Y_{EN}] V_{TN} \tag{19}$$

It is apparent that $[Y_{EN}]$ is the equivalent admittance matrix looking into l_N from tap point 1 to load tap terminating in L_N (see Fig 4). The equivalent admittance matrices for the other load taps can be likewise derived.

6.1.1 Evaluation of the driving matrix $[Y_{ER}]$

With reference to Fig 4 which shows a fault assumed at tap point 4, we can say that:

$$[Y_{ER}] = [Y_{E4}] + [Y_{45}] \tag{20}$$

where

$$[Y_{E4}] = [Y_{L4}]\ [U + l_4 Z Y_{L4}]^{-1} \tag{21}$$

This is the equivalent admittance matrix looking into tap line l_4 from tap point 4 to load tap terminated in load L_4; it is derived using the same methodology as described in Section 6.1 above. Likewise:

$$[Y_{45}] = [Y_{SR}]\ [U + l_{45} Z Y_{SR}]^{-1} \tag{22}$$

This is the equivalent admittance matrix looking into main line l_{45} from tap point 4 to the remote source which in turn is represented by admittance $[Y_{SR}]$.

6.1.2 Evaluation of the driving matrix $[Y_{ES}]$

Again with reference to Fig 4, we can say that:

$$[Y_{1S}] = [Y_{E1}] + [Y_{10}] \tag{23}$$

where

$$[Y_{E1}] = [Y_{L1}]\,[U + l_1 Z Y_{L1}]^{-1}; \quad [Y_{10}] = [Y_{SS}]\,[U + l_{01} Z Y_{SS}]^{-1} \tag{24}$$

Now $[Y_{1S}]$ terminates tap point 2, so that with reference to Fig 4, $[Y_{2S}]$ is given by:

$$[Y_{2S}] = [Y_{E2}] + [Y_{21}] \tag{25}$$

where

$$[Y_{E2}] = [Y_{L2}]\,[U + l_2 Z Y_{L2}]^{-1}; \quad [Y_{21}] = [Y_{1S}]\,[U + l_{12} Z Y_{1S}]^{-1} \tag{26}$$

Now $[Y_{2S}]$ terminates tap point 3, so that with reference to Fig 4, $[Y_{3S}]$ is given by:

$$[Y_{3S}] = [Y_{E3}] + [Y_{32}] \tag{27}$$

where

$$[Y_{E3}] = [Y_{L3}]\,[U + l_3 Z Y_{L3}]^{-1}; \quad [Y_{32}] = [Y_{2S}]\,[U + l_{23} Z Y_{2S}]^{-1} \tag{28}$$

Finally $[Y_{3S}]$ terminates section 3-4 to give:

$$[Y_{ES}] = [Y_{3S}]\,[U + l_{34} Z Y_{3S}]^{-1} \tag{29}$$

(note: in this particular example, the effect of load tap 4 has been included in the evaluation of $[Y_{ER}]$).

6.2 Configuration of the 11 kV distribution line (wooden pole) used in the application studies

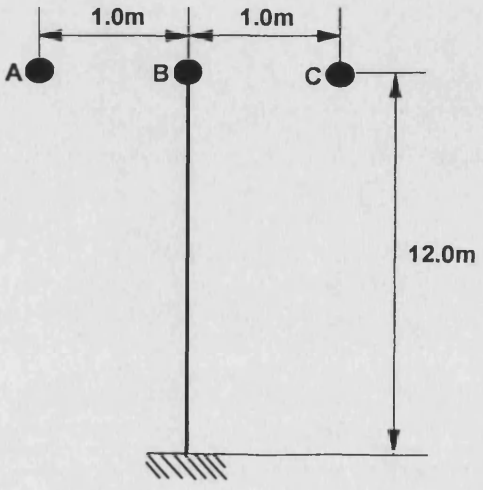

Table 1: Effect of fault position and fault type on fault location

Type of fault	Actual dist. (km)	Estimated dist (km)	% Error	Actual dist. (km)	Estimated dist. (km)	% Error
SLGF(a)	4.80	4.85	0.21	16.70	17.10	1.67
DLGF(ab)	4.80	4.90	0.42	16.70	17.30	2.51
LLF(ab)	4.80	5.05	1.05	16.70	16.10	2.51

Table 2: Effect of remote infeed

Type of fault	Actual distance (km)	Located distance(km)	% Error
SLGF (a)	16.70	16.63	0.29
LLF(ab)	16.70	16.75	0.21
DLGF(ab)	16.70	16.50	0.83

Table 3: Effect of tap load capacity estimation on accuracy.

Fault Type	0% Load estim. error		5% Load estim. error		10% Load estim. error	
	Estim loc	%Error	Estim loc	%Error	Estim loc	%Error
SLGF(a)	8.450	0.21	8.700	1.26	7.725	2.80
LLF(ab)	8.200	0.84	8.150	1.05	7.650	3.14
DLGF(ab)	8.550	0.65	8.850	1.88	7.900	2.09

(Actual fault at 8.4 km from end P; error in all tap loads)

Table 4: Effect of remote source capacity estimation on accuracy.
(SLGF)

Estimation error for remote source capacity	Actual distance (km)	Located distance(km)	% Error
+20%	16.70	16.55	0.62
-20%	16.70	16.55	0.62
+50%	16.70	17.48	3.24
-50%	16.70	16.95	1.05

SLGF = Single line to ground fault.
DLGF = Double line to ground fault.
LLF = Line to line fault.

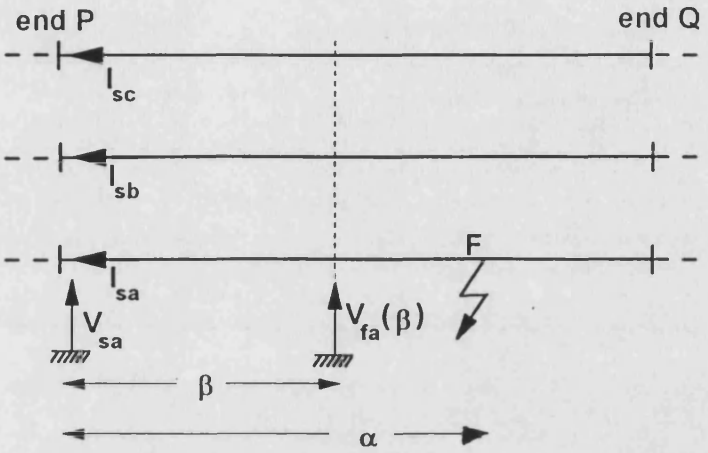

Fig 1 **Simplified faulted system model**

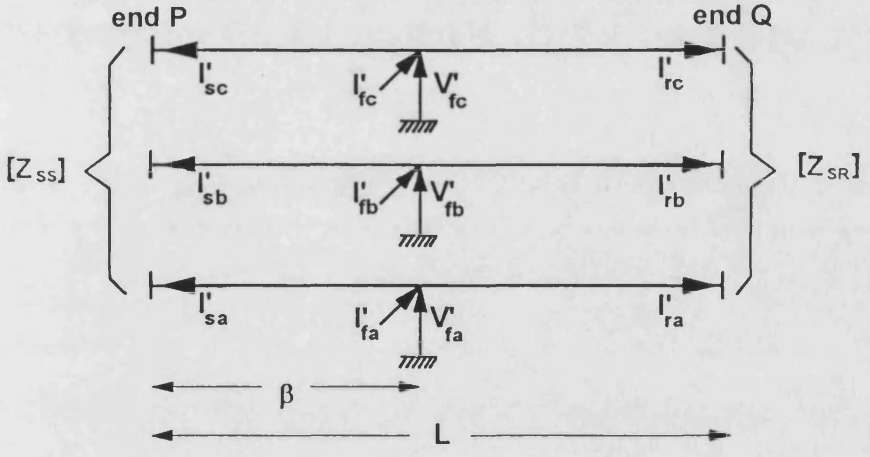

Fig 2 **Superimposed - component circuit**

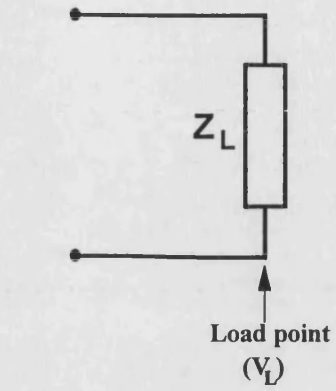

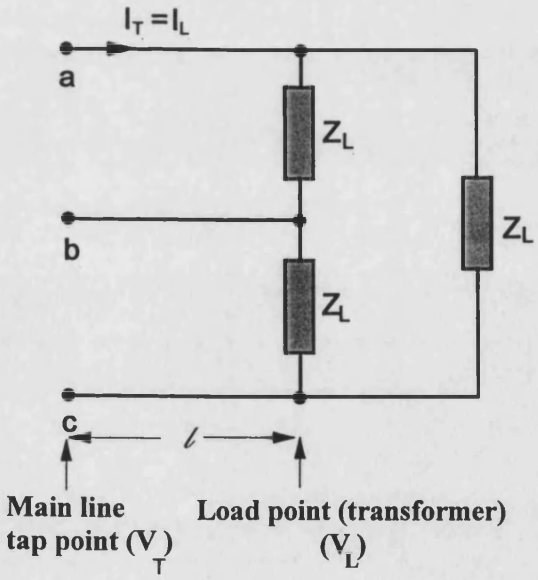

Fig 3 **Load-tap representation**

(a) Single-phase tap
(b) 3-phase tap

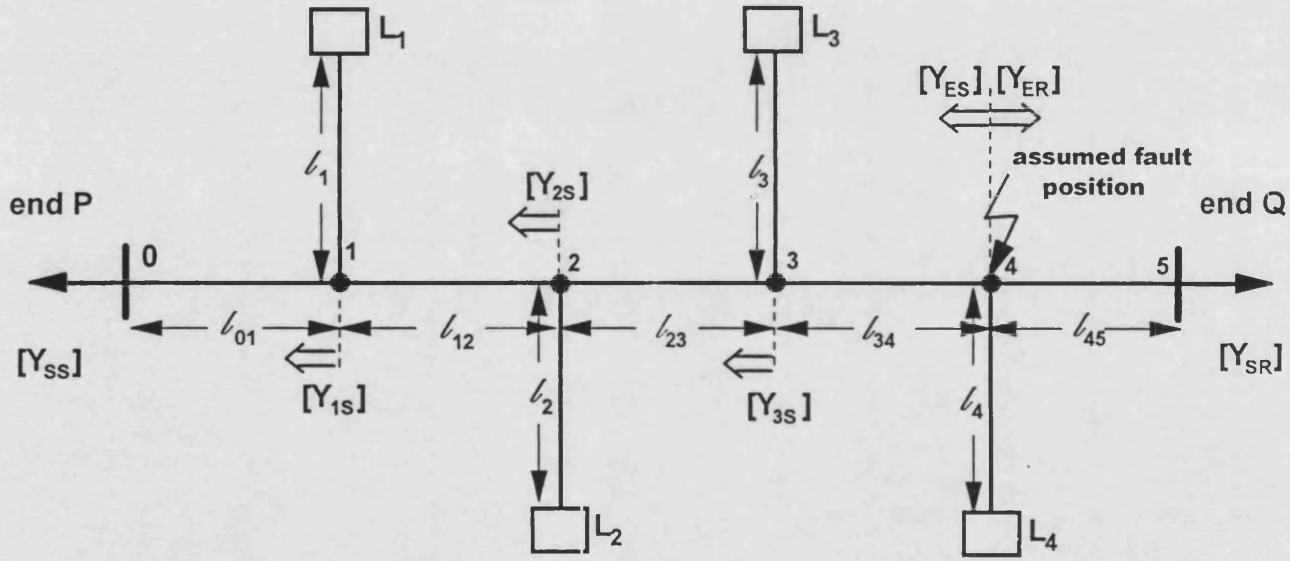

Fig 4 Faulted tapped line model

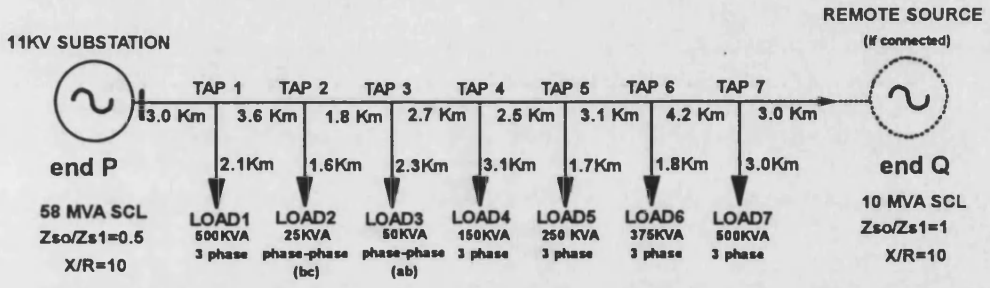

Fig. 5 **Typical 11kV radial distribution system studied.**

For all load taps, power factor P_f=0.9 lagging.

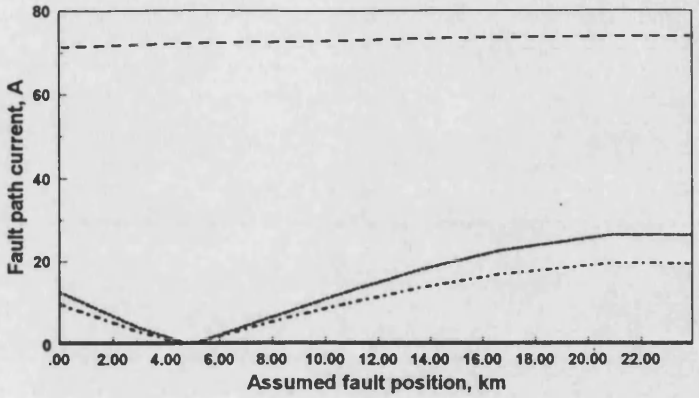

Fig 6a

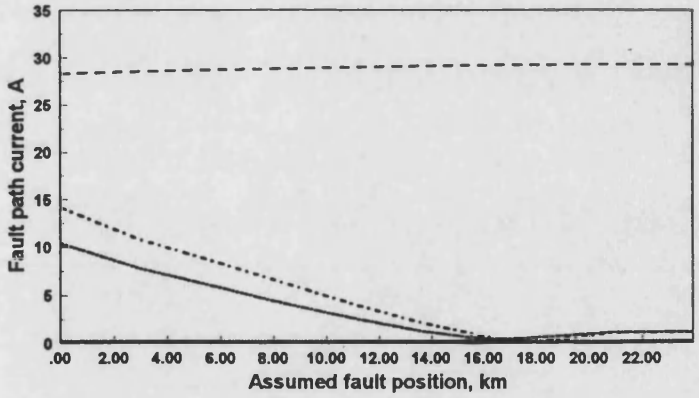

Fig 6b

Fig 6 **Fault path currents for the radial system with remote end open**

(a) a-phase earth fault 4.8 km from end P

(b) a-phase earth fault 16.7 km from end P

Fault resistance R_f=2Ω

- - - **a - phase (scale x 10 of that shown)**

-·-·-· **b - phase**

——— **c - phase**

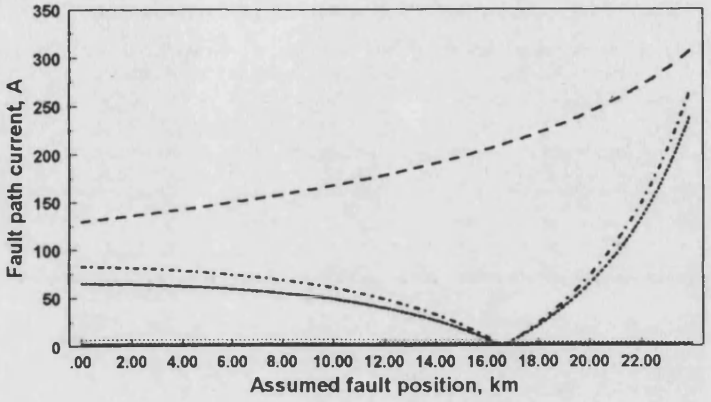

Fig.7 **Effect of remote infeed on fault path currents**
a - earth fault at 16.7km from end P. R_f=2.0 Ω
- - - - a - phase (scale x 5 of that shown)
-.-.-.- b - phase
——— c - phase

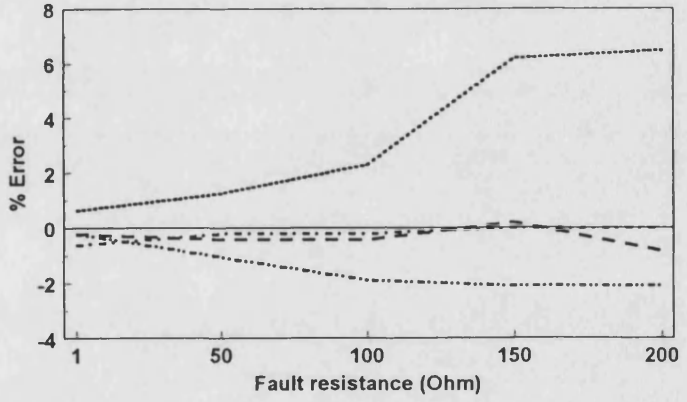

Fig. 8 **Effect of fault path resistance on accuracy.**

..... SLGF for system with remote-end open
-.-.-.- SLGF for a system with remote infeed
— — — DLGF for system with remote-end open
-.-.-.- DLGF for a system with remote infeed

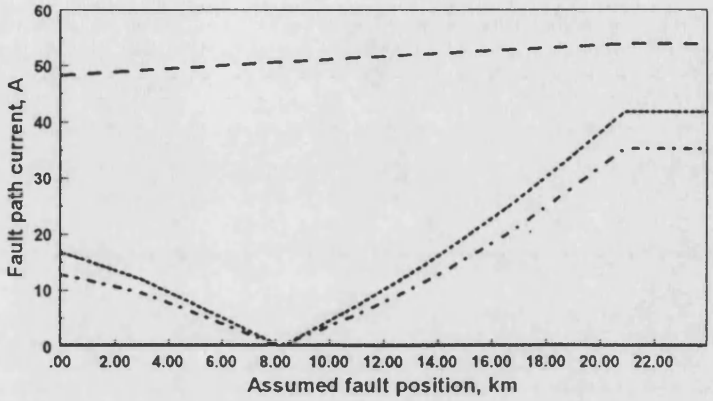

Fig. 9a

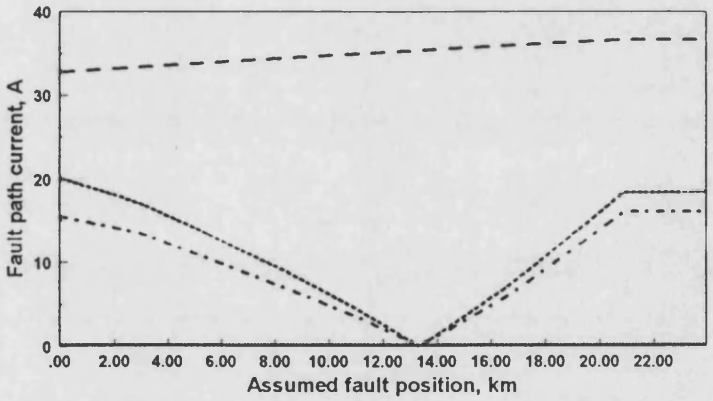

Fig. 9b

Fig. 9 **Effect of dynamic load on accuracy.**
(a) a - phase earth fault 8.4 km from end P
(b) a - phase earth fault 13.6 km from end P
Fault resistance R_f=2Ω
– – a - phase (scale x 20 of that shown)
..... b - phase
-.-.- c - phase

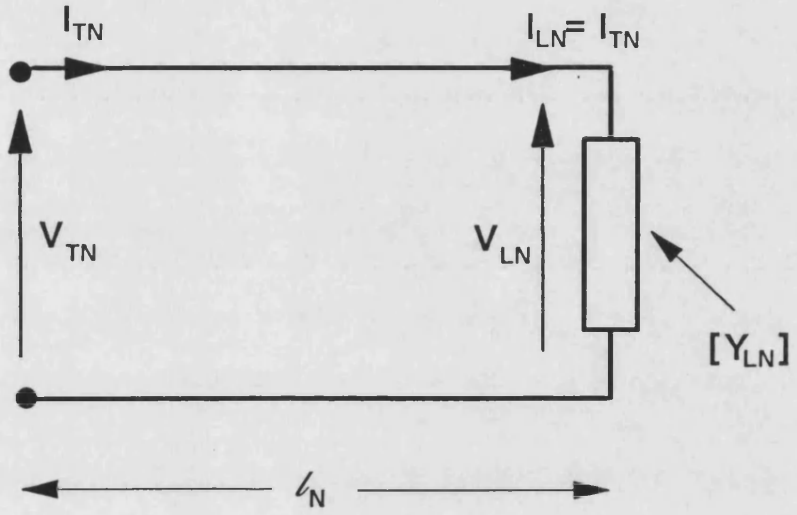

Fig 10 General load tap circuit